Evaluation of Compressibility and Hydraulic Characteristics of Soft Slurries and Tailings in 1g and Ng Environments based on Finite-Strain Consolidation

A thesis submitted in

Partial Fulfilment of the Requirements

for the degree of

Doctor of Philosophy

By

Akhila V

(Roll No. 186104002)

Under the Supervision of

Prof. T V Bharat



Department Of Civil Engineering,

Indian Institute of Technology Guwahati

Guwahati-781039, India

December 2024

TH-3534_186104002

DEDICATED

To

Maa Kaamakhya

and my Family

TH-3534_186104002

CERTIFICATE

It is certified that the thesis entitled "**Evaluation of Compressibility and Hydraulic Characteristics of Soft Slurries and Tailings in 1g and Ng Environments based on Finite-Strain Consolidation**" by Akhila V (Roll No. 186104002) a research scholar in the Department of Civil Engineering, Indian Institute of Technology, Guwahati, for the award of the degree of Doctor of Philosophy, is a record of an original research work carried out by her under my supervision and guidance. The thesis has fulfilled all the requirements as per the regulations of the institute and in my opinion, has reached the standard needed for submission. The results presented in this thesis have not been submitted to any other university or institute for the award of any degree or diploma.

Dr. T V Bharat
Professor
Department of Civil Engineering
Indian Institute of Technology
Guwahati, Assam, India

December, 2024

TH-3534_186104002

Acknowledgements

I am grateful to my PhD supervisor, Prof. T V Bharat, for his consistent support, patience, and guidance throughout this journey. Prof. Bharat has been a constant source of encouragement for me to explore various domains and acquire knowledge and expertise. I thank him from the bottom of my heart for his time and effort.

I thank my doctoral committee members, Prof. Gautam Barua and Dr. Arindam Dey from the Department of Civil Engineering and Dr. Arup Nandy from the Department of Mechanical Engineering, for their constructive comments and valuable suggestions during my annual progress seminars.

I am thankful to the members of my temporarily replaced doctoral committee, Prof. Rajan Choudhary, Dr. Kaling Taki, and Dr. Vivek Padmanabha from the Department of Civil Engineering, for their suggestions and support during my work progress seminars.

I am thankful to Upen Gohain, technical staff in the Mechanical Workshop, Department of Mechanical Engineering, IIT Guwahati, for his help in fabrication work.

I acknowledge Soroj Patowary, technical staff in the Computational Laboratory of the Department of Civil Engineering, IIT Guwahati, for his help with accessing the remote desktop facility.

I acknowledge Hariram Upadhyay from the Geotechnical Lab of the Department of Civil Engineering, IIT Guwahati, for his help and support during the experimental study.

I thank Himanshu Kaushik, Ganne Karthik, Alan Thomas, and Soutreya Kundu for helping me with research and literature review.

I thank Kenbi Riba and Divya Thakur for helping me with research and literature review.

I thank Sundaram Kumar and D Srinivasulu for their assistance with experimental and analytical work during my PhD research.

I am grateful to Suman for his help and support during the conduction of centrifuge experiments.

I acknowledge my lab research group - Pooja, Abhishek, Krishna, Sahil, Mahesh, and Sharad - for their lively interactions and support.

I thank my lab seniors Dr. Partha Das, Dr. Ankit Srivastava, and Mr. Bedabrata Ghose for sharing their guidance and support.

TH-3534_186104002

I am grateful to Himanshu Yadav for his moral support and encouragement during the difficult phases of this journey.

I am grateful to my seniors Dr. Anjaly Pillai, Dr. Sagar Mohan, and Dr. Dhanesh Singh Das for their invaluable guidance and mentorship.

I thank my friends Induchoodan T G, Akhila Das E K, Jenny Laura, Shyamili Sharma, Nicola Thonoujam, Riya Roy, Christy K Benny, and Vishnu G for their empathy, care, and support over the past six years.

I want to express my deepest gratitude to my family, whose unwavering support has been the cornerstone of my journey toward completing this PhD thesis.

To my beloved parents, Dr. E Vasudevan Nampoothiri and Dr. Gouri Antherjanam, whose endless encouragement, love, and sacrifices have been the driving force behind my academic pursuits. I am forever indebted for instilling in me the values of perseverance and determination.

To my cherished in-laws, Kanhaiya Lal Singh and Sashi Kala Singh, gratitude is extended for continuous support and understanding throughout this journey. Their belief in my abilities has been a source of inspiration, and it is an honour to be part of their family.

To my dear husband, Vinay Kumar Singh, who has been a constant source of support. His unwavering belief in my capabilities, patience, and understanding have been instrumental in navigating the highs and lows of doctoral research.

To my beloved brother-in-law, Vipul Kumar Singh, appreciation is expressed for his support and encouragement. His insightful discussions and unwavering faith in my abilities have provided valuable perspectives and motivation to persevere through challenges.

I am extremely grateful to Milli and her family, Army, Rahul, Pluto, Fluffy, Krish, Jebi, and Pilli for offering mental support during the stressful times of my journey.

Guwahati, December 2024 Akhila V

TH-3534_186104002

Abstract

Global technological advancements and industrial developments have prompted the generation of large quantities of slurry wastes such as mine tailings and dredged clays. The frequent tailings dam failures and excessive subsidence problems in capital-intensive land reclamation projects using dredged slurries necessitate strict guidelines and protocols for the safe and efficient management of these waste slurries. These high-water content materials experience significant deformation under the self-weight, and therefore, the structural stability and operational efficiency of facilities designed to store these materials are contingent upon the consolidation behaviour of the settling slurry. The finite strain consolidation theory offers a suitable framework for analysing the self-weight consolidation under field conditions. The compressibility and hydraulic conductivity functions are the constitutive function parameters influencing the finite strain consolidation behavior of slurries.

The routine tests conducted for the measurement of these functions are tedious and laborious. In this study, the experimental capabilities of a tailor-made benchtop centrifuge as an alternative to the conventional oedometer for the determination of compressibility function parameters were explored. The non-linear stress distribution within the centrifuge model gives rise to linear variation in the acceleration scale factor within the model. Past studies established four distinct ‘effective radii’ to guarantee optimal similarity between the model and prototype. The present study established effective scale factors by using the effective radius values. A numerical analysis was carried out to examine the discrepancy between the prototype's final settlement value and the value estimated by utilising effective scale factors to scale the centrifuge consolidation data. Additionally, a quantitative examination of the relationship between the degree of consolidation and the exponent value for the scale factor used to scale the model settlement time to prototype settlement time was presented. These aspects were studied for different model height to centrifuge radius ratios and for increasing acceleration scale factor values of the sample.

The present study further presented the inverse analyses using the temporal settlement from centrifuge tests for the first time to predict the model parameters of the conductivity function using the available time-invariant compressibility data. Two graphical methods for the estimation of hydraulic conductivity parameters from the 1g settlement versus time data were extrapolated for the first time for the settlement data from the centrifuge FSC tests. Further, the back-estimation of the compressibility and hydraulic conductivity functions from 1g and Ng

TH-3534_186104002

settlement data, using metaheuristic optimisation algorithms, was explored. The study proposed three novel algorithms namely Hybrid Particle Swarm Optimisation (HPSO), Modified Artificial Bee Colony (MABC) and Hybrid Artificial Bee Colony (HABC) for the improvement of robustness and reliability of optimal solutions while ensuring faster convergence. The performances of these algorithms were compared with the standard PSO and ABC algorithms. In addition to these five algorithms, the performance efficiency of the Quantum behaved PSO (QPSO), an advanced variant of PSO, was tested for the back prediction of constitutive function parameters.

For the first time, the measured pore pressure data at the base of the settling slurry was proposed as an alternative to temporal settlement data as input for inverse analysis of hydraulic conductivity function coefficients in case of highly turbid slurries. The graphical and optimisation-based inverse approaches successfully back-predicted the hydraulic conductivity function parameters from the 1g and Ng pore pressure data. All proposed methods of inverse analysis were first tested using synthetically simulated settlement or pore pressure data. The published settlement and pore pressure data from various literature studies were used to validate these approaches. The predicted constitutive functions were observed to be in good agreement with the experimental data from past studies. This study offers relatively fast and robust methods for the reliable estimation of constitutive function parameters under various laboratory conditions to evaluate the safety of the facilities in field conditions. This study facilitates seamless monitoring of the containment structures and secure handling of waste slurries.

TH-3534_186104002

TH-3534_186104002

Contents

Certificate i

Acknowledgement ii

Abstract iv

Contents vi

List of Figures xi

List of Tables xxiii

List of Important Symbols xxix

List of Abbreviations xxxi

Chapter 1 Introduction 1

1.1 Background 1

1.2 Organisation of the thesis 5

Chapter 2 Literature Review 8

2.1 General 8

2.2 Finite Strain Consolidation Analysis 8

2.3 FSC Analysis for Centrifuge Environment 10

2.4 Constitutive Relationships for FSC Theory 11

2.5 Experimental Studies on FSC 12

2.6 Estimation of Constitutive Functions By Indirect Methods 16

2.7 Optimisation Algorithms 17

2.7.1 Particle Swarm Optimisation 18

2.7.2 Artificial Bee Colony Algorithm 20

2.8 Objectives of the study 22

Chapter 3 Theoretical Background 23

3.1 General 23

3.2 Terzhagi's Theory of Consolidation -A review 23

3.2.1 Consequences of Terzaghi's assumptions 24

3.3 Finite Strain Consolidation Theory 26

3.4 Coordinate Systems 27

3.5 Settling column test 30

3.6 Centrifuge modelling 31

3.6.1 Scaling laws in centrifuge modelling 32

3.6.2 Concept of effective radius 33

TH-3534_186104002

3.6.3 Finite Strain Consolidation Theory for Centrifuge Environment 36

Chapter 4 Materials and Methodology 38

4.1 General 38

4.2 Materials 38

4.2.1 General 38

4.2.2 Materials Used for Experimental Study 38

4.2.3 Materials considered from past studies 39

4.3 Experimental Methods 45

4.3.1 General 45

4.3.2 Oedometer Test 45

4.3.3 Benchtop Centrifuge Test 48

4.4 Methodology for Numerical Analyses 50

4.4.1 General 50

4.4.2 Numerical solution of FSC equation using Explicit Finite Difference Method (EFDM) 50

4.4.3 Concept and implementation of effective scale factor 54

4.4.4 Numerical analysis of time-scale factor exponent 57

4.4.5 Graphical Methods of Inverse Analysis from Centrifuge Settlement Data 57

4.5 Optimisation-Based Inverse Analysis 66

4.5.1 General 66

4.5.2 Inverse Analysis Procedure 66

4.5.3 Fmincon 69

4.5.4 Fminsearch 69

4.5.5 Particle Swarm Optimization (PSO) 70

4.5.6 Quantum Particle Swarm Optimization (QPSO) 72

4.5.7 Hybrid Particle Swarm Optimization Algorithm (HPSO) 74

4.5.8 Artificial Bee Colony Algorithm (ABC) 75

4.5.9 Modified Artificial Bee Colony Algorithm (MABC) 76

4.5.10 Hybrid Artificial Bee Colony Algorithm (HABC) 78

4.6 FEM formulation for Centrifuge FSC 79

TH-3534_186104002

4.6.1 General 79
4.6.2 FEM model for centrifuge FSC 79
4.7 Summary 82
Chapter 5 Experimental Analysis of Soft-Soil Consolidation Behavior 83
5.1 General 83
5.2 Oedometer Test Results 83
5.2.1 General 83
5.2.2 Conventional consolidation test on soil slurries 83
5.3 Benchtop Centrifuge Test Results 92
5.3.1 General 92
5.3.2 FSC testing of slurries in Benchtop Centrifuge 92
5.4 Challenges and Limitations 96
5.5 Summary 97
Chapter 6 Scaling Effects in Centrifuge 99
6.1 General 99
6.2 Influence of Effective Centrifuge Radius on Scaling 99
6.2.1 General 99
6.2.2 Numerical study using synthetic prototype data 99
6.2.3 Numerical study using experimental prototype data 104
6.3 Numerical Study on the exponent of Time Scale Factor 112
6.3.1 General 112
6.3.2 Time Scale Exponent Versus Degree of Consolidation 112
6.4 Summary 116
Chapter 7 Graphical Estimation of Hydraulic Characteristics 118
7.1 General 118
7.2 Prediction of Hydraulic Conductivity Characteristics 118
7.2.1 Prediction Using Synthetic Settlement Data 118
7.2.2 Prediction Using Settlement Data from Literature 127
7.2.3 Inverse analysis using 50% of the measured data 134
7.3 Summary 135

Chapter 8 Inverse Analysis Using 1g Settlement Data 137
8.1 General 137

TH-3534_186104002

8.2 Inverse analysis for hydraulic conductivity parameters 137
8.2.1 Performance of initial value-based algorithms 137
8.2.2 Swarm based algorithms and tuning parameters 140
8.2.3 Back estimation using synthetic settlement data 141
8.2.4 Back estimation using measured settlement data 146
8.2.5 Discussion on significant observations 150
8.2.6 Summary 155
8.3 Simultaneous estimation of compressibility and hydraulic characteristics 156
8.3.1 General 156
8.3.2 Back estimation using synthetic settlement data 157
8.3.3 Back estimation using experimental settlement data 164
8.3.4 Discussion on significant observations 170
8.3.5 Summary 172
8.4 Strategies for Reliable Optimal Solutions 172
Chapter 9 Inverse AnalysisUsing Ng Settlement Data 174
9.1 General 174
9.2 Estimation of Hydraulic Conductivity Parameters 174
9.2.1 General 174
9.2.2 Tuning Parameters 175
9.2.3 Inverse analysis using synthetic settlement data 175
9.2.4 Inverse analysis using experimental settlement data 180
9.2.5 Summary 187
9.3 Simultaneous estimation of compressibility and permeability characteristics 188
9.3.1 General 188
9.3.2 Back-estimation Using Synthetic Data 188
9.3.3 Back-estimation Using Experimental Data 194
9.3.4 Summary 202
9.4 Strategies for Reliable Optimal Solutions 203
Chapter 10 Inverse Analysis Using Pore Pressure Data 204
10.1 General 204
10.2 Inverse Analysis by Graphical Approach Using 1g Data 204
10.2.1 General 204

TH-3534_186104002

10.2.2 Inverse analysis using Synthetic Data 205
10.2.3 Inverse Analysis Using Experimental Data 209
10.2.4 Summary 211
10.3 Back-estimation using Optimisation Algorithms from 1g Tests 212
10.3.1 General 212
10.3.2 Configuration of tuning parameters 212
10.3.3 Back-prediction using synthetic pore pressure data 213
10.3.4 Back-prediction using experimental pore pressure data 217
10.3.5 Discussion on Significant observations 220
10.3.6 Summary 222
10.4 Inverse Analysis Using Pore Pressure Data from Centrifuge 223
10.4.1 General 223
10.4.2 Back-estimation using the synthetic and experimental pore pressure data 224
10.4.3 Summary 230
Chapter 11 Conclusions and Future Scope 231
11.1 Conclusions 231
11.2 Future Scope 237
Appendix 239
List of Publications 248
References 250

TH-3534_186104002

List of Figures

Figure	2.1	Illustrating the No Free Lunch Theorem	17
Figure	3.1	Soil layer of infinite lateral extend	24
Figure	3.2	Soil element with boundaries fixed in space	24
Figure	3.3	Lagrangian and convective coordinate systems (a) Initial configuration at t=0 and (b) Configuration at time t >0	27
Figure	3.4	Details of the coordinate systems involved	28
Figure	3.5	Illustration of simple settling column test	30
Figure	3.6	Illustration of a geotechnical centrifuge and its important parts	31
Figure	3.7	Variation of acceleration scale factor with depth on centrifuge model and the stress at the base of the sample	33
Figure	3.8	Comparison of stress distribution in the field and in a centrifuge	34
Figure	4.1	Samples used in the oedometer test in Chapter 5 (a) BCS (b) RS (c) MBC (d) Kao-I	39
Figure	4.2	Oedometer set up at IIT Guwahati	46
Figure	4.3	(a) conical flask of slurry prepared for mixing in the shaker (b) top-view of the centrifuge set up (c) the centrifuge experimental set up.	49
Figure	4.4	(a) finite difference mesh used for the EFDM solution of the FSC governing equation. (b) Sample under 1g FSC	51
Figure	4.5	Flow chart of numerical analysis of FSC equation using MATLAB code.	54
Figure	4.6	Illustration of the impact of model heights on the variation in acceleration scale factor value (N) from top to bottom, (b) illustration of conversion of model data to prototype data	55

TH-3534_186104002

Figure 4.7 Flow chart for the steps for the numerical study on the influence of effective scale factor on scaling of centrifuge FSC data to prototype data 56

Figure 4.8 Comparison of Ng and 1g settlement versus time curves, numerically generated using the material properties of Rutgers, for (a) different *P* values (b) different *M* values 59

Figure 4.9 Translation of the arbitrary settlement versus time curves, using two pairs of initial guesses, (M1, P1) and (M2, P2), through four points (H, I, J, and K) on a synthetic settlement versus time curve (a) translation of (M1, P1) and (M2, P2) through H (b) (M1, P1) and (M2, P2) through I (c) (M1, P1) and (M2, P2) through J (d) (M1, P1) and (M2, P2) through K 60

Figure 4.10 Illustration of Method 1 (a) Iteration history for three runs of a swarm based stochastic optimisation algorithm for back analysis on centrifuge settlement data of SMC (f) Linear relationships in the P-lnM space obtained for various data points (H, I, J, and K) on the synthetic curve 61

Figure 4.11 Simulated excess pore pressure at base dissipation curves simulated for Antwerpen Soil (a) Effect of *M*-value (*M* in m/s) on the curve, for a constant P-value (b) Effect of *P*-value on the curve, for a constant *M*-value 62

Figure 4.12 For Phosphatic Clay (a) Iteration history for three runs of a swarm-based stochastic optimization algorithm for back analysis on simulated base excess pore pressure dissipation data(b) Linear relationships in the *P*-ln *M* space obtained for various data points on the synthetic base excess pore pressure dissipation curve. 63

Figure 4.13 Illustrating Method 2 (a) Points considered from the simulated settlement curves and the measured settlement curve used for the calculation of variance b) proposed correlation fitted to power versus variance data c) showing the shifting of settlement curve generated using arbitrary *M* value and predicted power value (*P_pred*). 65

TH-3534_186104002

Figure	4.14	FSC Settlement curves simulated for Rutgers by varying the (a) value of coefficient A and (b) value of coefficient C from the compressibility function	67
Figure	4.15	(a) illustration of the objective function used for the optimization (b) flow chart for the inverse analysis procedure for the simultaneous estimation of hydraulic conductivity and compressibility function coefficients	68
Figure	4.16	Illustration of the updation of the position of a particle in PSO algorithm	71
Figure	4.17	Numerical grid for FEM formulation (a) details of the mesh with nodes (b) mapping the physical element (element (i)) to one dimensional quadratic master element.	81
Figure	5.1	Oedometer test conducted on BCS (a) Change in height with time at different load steps (b) settlement plots under various loads	84
Figure	5.2	Constitutive relationships from the oedometer observations (a) Effective stress versus void ratio relationship for BCS (b) Hydraulic Conductivity versus void ratio relationship for BCS	85
Figure	5.3	Oedometer test conducted on RS (a) Change in height with time at different load steps (b) settlement plots under various loads	86
Figure	5.4	Constitutive relationships from the oedometer observations (a) Effective stress versus void ratio relationship for RS (b) Hydraulic Conductivity versus void ratio relationship for RS	87
Figure	5.5	Oedometer test conducted on MBC (a) Change in height with time at different load steps (b) settlement plots under various loads	88
Figure	5.6	Constitutive relationships from the oedometer observations (a) Effective stress versus void ratio relationship for MBC (b) Hydraulic Conductivity versus void ratio relationship for MBC	89
Figure	5.7	Oedometer test conducted on Kao-I (a) Change in height with time at different load steps (b) settlement plots under various loads	90

TH-3534_186104002

Figure	5.8	Constitutive relationships from the oedometer observations (a) Effective stress versus void ratio relationship for Kao-I (b) Hydraulic Conductivity versus void ratio relationship for Kao-I	91
Figure	5.9	Based on benchtop centrifuge FSC test on BCS (a) Measured settlement versus time curves for various RPMs (b) Comparison of effective stress relationships from oedometer and benchtop centrifuge	93
Figure	5.10	Based on benchtop centrifuge FSC test on RS (a) Measured settlement versus time curves for various RPMs (b) Comparison of effective stress relationships from oedometer and bench-top centrifuge	94
Figure	5.11	Based on benchtop centrifuge FSC test on MBC (a) Measured settlement versus time curves for various RPMs (b) Comparison of effective stress relationships from oedometer and benchtop centrifuge	94
Figure	5.12	Based on benchtop centrifuge FSC test on Kao-I(a) Measured settlement versus time curves for various RPMs (b) Comparison of effective stress relationships from oedometer and benchtop centrifuge	95
Figure	5.13	(a) Kaolinite sample leaking from the mould due to sudden loading (b) Kaolinite slurry sample undergoing slow sedimentataion- without properly visible settling boundary	96
Figure	6.1	Comparison of the scaled settlement curves of SMC, with the prototype behaviour for No=60 when (a) Hm/R=0.1, (b) Hm/R=0.15, (c) Hm/R=0.2, and, (d) Hm/R=0.25	101
Figure	6.2	Comparison of the scaled settlement curves of SMC, with the prototype behaviour for No=90 when (a) Hm/R=0.1, (b) Hm/R=0.15, (c) Hm/R=0.2, and, (d) Hm/R=0.25	102
Figure	6.3	Comparison of the scaled settlement curves of SMC, with the prototype behaviour for No=104.6 when (a) Hm/R=0.1, (b) Hm/R=0.15, (c) Hm/R=0.2, and, (d) Hm/R=0.25	103
Figure	6.4	Comparison of the scaled settlement curves of PA-MFT, with the prototype behaviour for N=60g when (a) Hm/R=0.1, (b) Hm/R=0.15, (c) Hm/R=0.2, and, (d) Hm/R=0.25	105

TH-3534_186104002

Figure	6.5	Comparison of the scaled settlement curves of PA-MFT, with the prototype behaviour for N=100 when (a) Hm/R=0.1, (b) Hm/R=0.15, (c) Hm/R=0.2, and, (d) Hm/R=0.25	106
Figure	6.6	Comparison of the scaled settlement curves of PA-MFT, with the prototype behaviour for N=150 when (a) Hm/R=0.1, (b) Hm/R=0.15, (c) Hm/R=0.2, and, (d) Hm/R=0.25	107
Figure	6.7	Comparison of the scaled settlement curves of Phosphatic Clay, with the prototype behaviour for N=80 when (a) Hm/R=0.1, (b) Hm/R=0.15, (c) Hm/R=0.2, and, (d) Hm/R=0.25	109
Figure	6.8	Comparison of the scaled settlement curves of Phosphatic Clay, with the prototype behaviour for N=100 when (a) Hm/R=0.1, (b) Hm/R=0.15, (c) Hm/R=0.2, and, (d) Hm/R=0.25	110
Figure	6.9	Comparison of the scaled settlement curves of Phosphatic Clay, with the prototype behaviour for N=120 when (a) Hm/R=0.1, (b) Hm/R=0.15, (c) Hm/R=0.2, and, (d) Hm/R=0.25	111
Figure	6.10	For a given prototype (a) effect of varying the scale factor *N* on the settlement versus time plot (b) Settlement versus time plots or various *N* values converted into degree of consolidation versus time plots (illustrated using data from Phosphativ Clay, at Hm/R=0.25)	113
Figure	7.1	Settlement versus time behaviour simulated numerically for (a) Rutgers, (b) OFT (c) MFT 5 and (d) MFT 6, using initial guess values of M and P given in Table 7.1 and the synthetic data points simulated using hydraulic conductivity function parameters from Table 4.3 for Method 1 (Qi and Simms, 2020)	119
Figure	7.2	Settlement versus time curves showing the synthetic data points and corresponding points from the simulated curves for initial guesses considered in group 1 for predicting the power P using Method 2 (Qi et al.2020) for (a) Rutgers (b) OFT (c) MFT5 and (d) MFT6	121
Figure	7.3	Comparison of the average of predicted hydraulic conductivity functions with functions used for generating synthetic settlement data for (a) Rutgers (b) OFT (c) MFT 5 (d) MFT 6	125

TH-3534_186104002

Figure 7.4 Synthetic settlement versus time curve data points and the curves generated using the average predicted values of hydraulic conductivity parameters using Method 1 and Method 2 for (a) Rutgers (b) OFT (c) MFT5 (d) MFT6 126

Figure 7.5 Settlement versus time plots generated for different initial guess values of M and P given in Table 7.1 and the data points measured from centrifuge for (a) SMC (b) Kaolinite (c) TT50 and (d) AL15 for Method 1 129

Figure 7.6 Settlement versus time curves showing the data points measured from the centrifuge consolidation test and corresponding points from the simulated curves for initial guesses considered in group 1 for predicting the power P value using Method 2 for (a) SMC (b) Kaolinite (c) TT50 (d) AL15 130

Figure 7.7 Comparison of the average of predicted permeability functions with data from the literature for (a) SMC (b) Kaolinite (c) TT50 (d) AL15 131

Figure 7.8 Measured settlement versus time curve data points and the curves generated using the average predicted values of hydraulic conductivity parameters using Method 1 and Method 2 for (a) SMC (b) Kaolinite (c) TT50 (d) AL15 133

Figure 7.9 Testing Method 1 and Method 2 using 50% of the settlement versus time data points for (a) Rutgers (b) OFT 135

Figure 8.1 Comparison of worst-case predictions obtained using fmincon and fminsearch with settlement versus time data for (a) Phosphatic Clay (b) Rutgers (c) Antwerpen Slurry, and in terms of hydraulic conductivity function for (d) Phosphatic Clay (e) Rutgers (f) Antwerpen Slurry 139

Figure 8.2 The objective function value (RMSE) versus the number of iterations plotted for the best run of each of the algorithms employed for inverse analysis using synthetic settlement data of (a) MFT5 (b) MFT6 and (c) Rutgers 143

TH-3534_186104002

Figure 8.3 Comparison of optimised power (P) and Multiplier (M) values from various algorithms with the actual values in the form of hydraulic conductivity function for (a) MFT5 (b) MFT6 and (c) Rutgers 144

Figure 8.4 Comparison of synthetically generated settlement data points given as input for inverse analysis using the algorithms considered and settlement curves simulated using the hydraulic conductivity function parameters predicted by inverse analysis for (a) MFT5 (b) MFT6 and (c) Rutgers 145

Figure 8.5 Comparison of the objective function value (RMSE) with progressing iterations of the best of three runs of the inverse analysis algorithms using experimental settlement data cases (a) PA-MFT (b) Phosphatic Clay and (c) Antwerpen Slurry 147

Figure 8.6 Comparison of hydraulic conductivity functions reported in the literature for the experimental data cases and the same predicted using inverse analysis from the algorithms considered for (a) PA-MFT (b) Phosphatic Clay (c) Antwerpen Slurry 149

Figure 8.7 Comparison of experimental data points given as input for inverse analyses using the algorithms considered and settlement curves simulated using the hydraulic conductivity function parameters predicted by inverse analysis for (a) PA-MFT (b) Phosphatic clay and (c) Antwerpen Slurry 150

Figure 8.8 (a) M and P values from successive iterations converging to a straight line leading to the optimal pair of values when settlement data for Phosphatic clay was used for inverse analysis (b) Three-dimensional error surface for the optimisation problem derived for the Phosphatic Clay sample 151

Figure 8.9 (a) Iteration versus RMSE plotted for three runs of PSO for Phosphatic Clay to show the variation in convergence (b) Comparison of hydraulic conductivity function using the parameters obtained from best and worst runs of PSO with the same from literature for Phosphatic Clay 152

TH-3534_186104002

Figure 8.10 For the case of inverse analysis Phosphatic Clay from settlement data (a) Iteration history of Power (P) in run 1 (Worst run) and run 2 (Best run) of PSO (b) Iteration history of Multiplier (M) in run 1 (Worst run) and run 2 (Best run) of PSO (c) Influence of erroneous prediction of hydraulic conductivity function parameters on simulated hypothetical field observation of percentage settlement 153

Figure 8.11 Illustration of the effect of choice of the number of iterations on the convergence for Antwerpen Slurry using (a) HPSO (b) HABC 155

Figure 8.12 Comparison of the objective function value (RMSE) with progressing iterations of the best of three runs of the inverse analysis algorithms using synthetic settlement data cases (a) MFT5 (b) MFT6 and (c) Rutgers 160

Figure 8.13 Comparison of hydraulic conductivity functions of the synthetic data cases and the same predicted using inverse analysis from the algorithms considered for (a) MFT5 (b) MFT6 and (c) Rutgers 161

Figure 8.14 Comparison of compressibility functions of the synthetic data cases and the same predicted using inverse analysis from the algorithms considered for (a) MFT5 (b) MFT6 and (c) Rutgers 162

Figure 8.15 Comparison of synthetically generated settlement data points given as input for inverse analysis using the algorithms considered and settlement curves simulated using the constitutive function parameters predicted by inverse analysis for (a)MFT 5 (b) MFT 6 and (c) Rutgers 163

Figure 8.16 Comparison of the objective function value (RMSE) with progressing iterations of the best of three runs of the inverse analysis algorithms using experimental settlement data cases (a) Antwerpen Slurry (b) PA-MFT and (c) Phosphatic Clay 165

Figure 8.17 Comparison of hydraulic conductivity functions reported in the literature for the experimental data cases and the same predicted using inverse analysis from the algorithms considered for (a) Antwerpen Slurry (b) PA-MFT (c) Phosphatic Clay 167

TH-3534_186104002

Figure 8.18 Comparison of compressibility functions reported in the literature for the experimental data cases and the same predicted using inverse analysis from the algorithms considered for (a) Antwerpen Slurry (b) PA-MFT (c) Phosphatic Clay 168

Figure 8.19 Comparison of experimental data points given as input for inverse analyses using the algorithms considered and settlement curves simulated using the constitutive function parameters predicted by inverse analysis for (a) Antwerpen Slurry (b) PA-MFT and (c) Phosphatic clay 169

Figure 8.20 The M and P values obtained from consecutive iterations of PSO, QPSO and HPSO forming a linear relationship, finally converging to the optimal pair of values for (a) Rutgers and (b) PA-MFT. 171

Figure 9.1 The objective function value (RMSE) versus the number of iterations plotted for the best run of each of the algorithms employed for inverse analysis using Ng synthetic settlement data of (a) MFT5 (b) MFT6 and (c) Rutgers 177

Figure 9.2 Comparison of power (*P*) and Multiplier (*M*) values predicted using centrifuge settlement data from various algorithms with the actual parameter values used to generate the synthetic data points for (a) MFT5 (b) MFT6 and (c) Rutgers 178

Figure 9.3 Comparison of synthetically generated settlement data points given as input for inverse analysis using the algorithms considered and settlement curves simulated using the hydraulic conductivity function parameters predicted by inverse analysis for (a) MFT5 (b) MFT6 and (c) Rutgers 179

Figure 9.4 The objective function value (RMSE) versus the number of iterations plotted for the best run of each of the algorithms employed for inverse analysis using *N*g experimental settlement data of (a) AL15 (b) Kaolinite (c) TT50 and (d) TT60 183

TH-3534_186104002

Figure 9.5 Comparison of power (P) and Multiplier (M) values predicted using experimental Ng settlement data as input from various algorithms with corresponding actual values in the literature for samples of (a) AL15 (b) Kaolinite (c) TT50 and (d) TT60 184

Figure 9.6 Comparison of experimental Ng settlement data points given as input for inverse analysis using the algorithms considered and settlement curves simulated using the hydraulic conductivity function parameters predicted by inverse analysis for (a) AL15 (b) Kaolinite (c) TT50 and (d) TT60 185

Figure 9.7 The objective function value (RMSE) versus the number of iterations plotted for the best run of each of the algorithms employed for simultaneous back-estimation of constitutive function parameters using Ng synthetic settlement data of (a) MFT5 (b) MFT6 and (c) Rutgers 190

Figure 9.8 Comparison hydraulic conductivity parameters predicted using centrifuge settlement data reported for various algorithms with the actual parameter values used to generate the synthetic data points for (a) MFT5 (b) MFT6 and (c) Rutgers 191

Figure 9.9 Comparison compressibility function predicted using centrifuge settlement data reported for various algorithms with the actual parameter values used to generate the synthetic data points for (a) MFT5 (b) MFT6 and (c) Rutgers 192

Figure 9.10 Comparison of settlement curves simulated using the predicted constitutive function parameters reported for various algorithms with the observed settlement data from literature for (a) MFT5 (b) MFT6 and (c) Rutgers 193

Figure 9.11 The objective function value (RMSE) versus the number of iterations plotted for the best run of each of the algorithms employed for inverse analysis using Ng experimental settlement data of (a) AL15 (b) Kaolinite (c) TT50 and (d) TT60 197

TH-3534_186104002

Figure 9.12 Comparison of hydraulic conductivity functions predicted using experimental Ng settlement data as input from various algorithms with corresponding actual values in the literature for samples of (a) AL15 (b) Kaolinite (c) TT50 and (d) TT60 198

Figure 9.13 Comparison of compressibility functions predicted using experimental Ng settlement data as input from various algorithms with corresponding actual values in the literature for samples of (a) AL15 (b) Kaolinite (c) TT50 and (d) TT60 199

Figure 9.14 Comparison of experimental Ng settlement data points given as input for inverse analysis using the algorithms considered and settlement curves simulated using the constitutive function parameters predicted by inverse analysis for (a) AL15 (b) Kaolinite (c) TT50 and (d) TT60 200

Figure 10.1 Base excess pore pressure dissipation curves simulated using various initial guess values and the synthetic data sets simulated for (a) Antwerpen Slurry (b) Phosphatic Clay 206

Figure 10.2 Comparison of base excess pore pressure dissipation data simulated using the average of predicted values of hydraulic conductivity parameters with the synthetic data for (a)Antwerpen slurry (b) Phosphatic Clay 207

Figure 10.3 Comparison of settlement curve simulated using the average of predicted values of hydraulic conductivity parameters with the settlement data from the literature for (a)Antwerpen slurry (b) Phosphatic Clay 207

Figure 10.4 Comparison of the average of predicted permeability functions with the data from the literature for (a) Antwerpen slurry (b) Phosphatic Clay 208

Figure 10.5 Base excess pore pressure dissipation curves simulated using various initial guess values and the synthetic data sets simulated for (a) AS-II (b) Gold Tailings 210

Figure 10.6 Comparison of the average of predicted permeability functions with the data from the literature for (a) AS-II (b) Gold Tailings 210

TH-3534_186104002

Figure 10.7 Comparison of base excess pore pressure dissipation data simulated using the average of predicted values of hydraulic conductivity parameters with the experimental data for (a) AS-II (b) Gold Tailings 211

Figure 10.8 Comparison of the objective function value (RMSE) with progressing iterations of the best of three runs of the inverse analysis algorithms using synthetic excess pore pressure data for (a) Antwerpen Slurry (b) Phosphatic Clay. 214

Figure 10.9 Comparison of hydraulic conductivity functions for synthetic excess pore pressure data cases (a) Antwerpen Slurry (b) Phosphatic Clay 215

Figure 10.10 Comparison of settlement versus time data in literature and the curves simulated using the hydraulic conductivity function parameters predicted by inverse analysis from excess pore pressure data for (a) Antwerpen Slurry (b) Phosphatic Clay 216

Figure 10.11 Comparison of excess pore pressure dissipation data points given as input for inverse analyses and the curves simulated using the hydraulic conductivity function parameters predicted by inverse analysis for a) Antwerpen Slurry (b) Phosphatic Clay (c) Gold Tailings and (d) AS-2 216

Figure 10.12 Comparison of the objective function value (RMSE) with progressing iterations of the best of three runs of the inverse analysis algorithms using experimental excess pore pressure data for (a) AS-2 and (b) Gold Tailings 217

Figure 10.13 Comparison of hydraulic conductivity functions for experimental excess pore pressure data cases (a) Gold Tailings and (b) AS-2 218

Figure 10.14 Comparison of settlement versus time data in literature and the curves simulated using the hydraulic conductivity function parameters predicted by inverse analysis from excess pore pressure data for (a) Gold Tailings and (b) AS-2 219

Figure 10.15 Comparison of excess pore pressure dissipation data points given as input for inverse analyses and the curves simulated using the 219

TH-3534_186104002

hydraulic conductivity function parameters predicted by inverse analysis for (a) Gold Tailings and (b) AS-2

Figure 10.16 (a) M and P values from successive iterations converging to a straight line leading to the optimal pair of values when base excess pore pressure dissipation data for Phosphatic clay was used for inverse analysis. (b) Error surface showing the valley and straight-line formation in ln M versus P plane for inverse analysis using excess pore pressure dissipation data for Antwerpen Slurry 221

Figure 10.17 Iteration number versus RMSE value plots for the inverse analysis using synthetic pore pressure data set simulated for Ng FSC tests for the cases (a) AL15 (b) TT50 225

Figure 10.18 Comparison of hydraulic conductivity data reported in literature with the hydraulic conductivity function parameters predicted using optimisation algorithms through inverse analysis with synthetic total pore pressure data from Ng FSC tests for (a) AL15 (b) TT50 225

Figure 10.19 Comparison of settlement versus time data in literature and the curves simulated using the hydraulic conductivity function parameters predicted by inverse analysis from Ng pore pressure data for (a) AL15 and (b) TT50 227

Figure 10.20 Comparison of pore pressure dissipation data generated synthetically and the curves simulated using the hydraulic conductivity function parameters predicted by inverse analysis from Ng pore pressure data for (a) AL15 and (b) TT50 227

Figure 10.21 Observations from the inverse analysis using experimental pore pressure data from the benchtop centrifuge test on Kao-III: (a) comparison of RMSE versus iteration number plots for various algorithms (b) comparison of predicted hydraulic conductivity parameters with the available literature data (c) comparison of predicted settlement behaviour and, (d) comparison of simulated pore pressure dissipation curves with the corresponding experimental data 228

TH-3534_186104002

List of Tables

Table	3.1	Scaling of various parameters in centrifuge models	32
Table	3.2	Definitions of effective radius values	36
Table	4.1	Characteristics of slurries used for experimental study	38
Table	4.2	Properties of various slurries considered in the present study used for testing and validation in 1g environment	43
Table	4.3	Properties of various slurries considered in the present study used for testing and validation in centrifuge environment	44
Table	5.1	Initial properties of the slurries used to conduct the oedometer tests	83
Table	5.2	Consolidation Parameters estimated from oedometer tests on BCS	85
Table	5.3	Consolidation Parameters estimated from oedometer tests on RS	87
Table	5.4	Consolidation Parameters estimated from oedometer tests on MBC	89
Table	5.5	Consolidation Parameters estimated from oedometer tests on Kao-I	91
Table	5.6	Properties of slurry sample after complete consolidation	92
Table	5.7	Initial properties of the slurries used to conduct the centrifuge tests	93
Table	6.1	Influence of Hm/R ratio on the error in ultimate settlement when different factors are used to convert model settlement data to prototype data	100
Table	6.2	Influence of Hm/R ratio on the error in ultimate settlement when different factors are used to convert model settlement data to prototype data for PA-MFT	104
Table	6.3	Influence of Hm/R ratio on the error in ultimate settlement when different factors are used to convert model settlement data to prototype data for Phosphatic Clay	108
Table	6.4	Time scale exponent values for different degree of consolidation for Phosphatic Clay, at different Hm/R values	114
Table	6.5	Time scale exponent values for different degree of consolidation for PA-MFT Clay, at different Hm/R values	115

TH-3534_186104002

Table	6.6	The average value of exponent for full consolidation at different Hm/R values for various scale factors	116
Table	7.1	Initial guess values used for simulating arbitrary settlement curves for applying the graphical methods	120
Table	7.2	*M* and *P* values predicted for synthetic data cases using Method 1	122
Table	7.3	Values of *M* (m/s) and *P* predicted using Method 2, using the equations connecting the power and variance of settlement versus log time curves, formed for different groups, each containing different numbers of points considered from the synthetic settlement versus time data and the corresponding points from the curves of initial guesses given in 1.	123
Table	7.4	*M* and *P* values predicted for synthetic data cases using Method 1	128
Table	7.5	Values of *M* (m/s) and *P* predicted using Method 2, using the equations connecting the power and variance of settlement versus log time curves, formed for different groups, each containing different numbers of points considered from the experimental settlement versus time data and the corresponding points from the curves using the initial guesses given in 1	132
Table	7.6	*M* (m/s) and *P* values predicted using Method 1 and Method 2 considering only 50% of the data points for the analysis	134
Table	8.1	Hydraulic conductivity parameters -power (*P*) and multiplier (*M*), predicted using fmincon and fminsearch	138
Table	8.2	Performance of different inverse analysis algorithms using synthetic settlement data as the input for predicting the power (*P*) and multiplier (*M*)	142
Table	8.3	Performance of different inverse analysis algorithms using experimental settlement data as the input for predicting the power (*P*) and Multiplier (*M*) parameters	148

TH-3534_186104002

Table 8.4 Inverse analysis performance of various algorithms in predicting compressibility and hydraulic conductivity function parameters using synthetic settlement data as the input 159

Table 8.5 Inverse analysis performance of various algorithms in predicting compressibility and hydraulic conductivity function parameters using experimental settlement data as the input 166

Table 9.1 Performance of different inverse analysis algorithms using Ng synthetic settlement data as the input for predicting the hydraulic conductivity function coefficients -power (P) and multiplier (M) 176

Table 9.2 Performance of different inverse analysis algorithms using Ng experimental settlement data as the input for predicting the hydraulic conductivity function coefficients -power (P) and multiplier (M) 181

Table 9.3 Performance of different inverse analysis algorithms using Ng synthetic settlement data as the input for predicting the constitutive relation coefficients 189

Table 9.4 Performance of different inverse analysis algorithms using Ng synthetic settlement data as the input for predicting the constitutive relation coefficients 195

Table 10.1 Hydraulic conductivity function parameters predicted from synthetic base excess pore water pressure data using the graphical method 205

Table 10.2 Hydraulic conductivity function parameters predicted from experimental base excess pore water pressure data using the graphical method 209

Table 10.3 Performance of different inverse analysis algorithms using synthetic excess pore pressure data as the input for predicting the Power (P) and Multiplier (M) parameters 213

Table 10.4 Performance of different inverse analysis algorithms using experimental excess pore pressure data as the input for predicting the Power (P) and Multiplier (M) parameters 218

TH-3534_186104002

Table 10.5 Performance of optimisation algorithms for the inverse analysis of hydraulic conductivity function parameters using Ng pore pressure data 224

TH-3534_186104002

List of Important Symbols

k	Hydraulic conductivity (m/s)
σ'	Effective Stress (kPa)
σ	Total Stress (kPa)
e	Void ratio
V_f	Fluid velocity
V_s	Velocity of solids
u	Excess pore pressure (kPa)
t	time
ρ_f	Density of Fluid (kg/m^3)
ρ_s	Density of solids (kg/m^3)
C_v	Coefficient of consolidation (m^2/s)
m_v	Coefficient of volume compressibility (m^2/kN)
a_v	Coefficient of compressibility (m^2/kN)
c_c	Compression Index
$\Delta l/l$	Lagrangian Strain
ξ	Distance in convective system(m)
z	Distance in Material coordinates (m)
ω	Angular velocity (rad/s)
R	Centrifuge Radius(m)
R_e	Effective Centrifuge Radius(m)
N	Scale Factor
N_0	Acceleration scale factor at base
G_s	Specific gravity of solids
Δ	Space Step(m)
τ	Time Step (s)
T_v	Time Factor
γ_w	Unit weight of water (kN/m^3)
γ_s	Unit weight of solids (kN/m^3)
σ'_b	Effective Stress at Base (kPa)
L_s	Height of Solids
$k(e)$	Hydraulic conductivity function

TH-3534_186104002

$\sigma'(e)$	Compressibility function
M, P	Coefficients of Hydraulic Conductivity Function
A, B, C	Coefficients of Compressibility Function
H_m	Height of the model
H_p	Height of the prototype
a,b,Ψ	Coefficients of Variance function
P_{pred}	Predicted Power Value
M_{arb}	Predicted Multiplier Value
P^{best}	Personal Best Position Value in PSO
G^{best}	Global Best Position Value in PSO
M^{best}	Mean of Personal Best Values in QPSO
M	Global Mass Matrix in FEM
K	Global Stiffness Matrix in FEM
Iter_max	Maximum number of iterations
Obj_val	Objective function value

TH-3534_186104002

List of Abbreviations

FSC	Finite Strain Consolidation
1g	Normal gravity conditions
Ng	Centrifuge gravity condition
ABC	Artificial Bee Colony Algorithm
MABC	Modified Artificial Bee Colony Algorithm
DE	Differential Evolution
GA	Genetic Algorithm
ACO	Ant Colony Algorithm
HABC	Hybrid Artificial Bee Colony
PSO	Particle Swarm Optimisation
QPSO	Quantum behaved Particle Swarm Optimisation
EFDM	Explicit Finite Difference Method
RPM	Revolutions per minute
FEM	Finite element method
MBC	Black Cotton Soil-Jabalpur
RS	Red Soil
BCS	Black Cotton Soil
Rutgers	Newark Bay Clay
CRD	Constant rate of deformation
PA-MFT	Polymer Amended Matured Fine Tailings
LL	Liquid Limit
PL	Plastic Limit
AS	Antwerpen Slurry
SMC	Singapore Marine Clay
Kao-I	Kaolinite
LSCT	Large Strain Consolidation Test
TT50	Thickened oil sands tailings with 50% fines
TT60	Thickened oil sands tailings with 60% fines
AL15	Albian Tailings
MFT	Matured Fine Tailings
OFT	Overflow Tailings
RMSE	Root Mean Square Error

TH-3534_186104002

1. INTRODUCTION

1.1 Background

Soft soils are geological materials that are characterised by high compressibility, high water content, and a susceptibility to undergo excessive settlement under self-weight. Major industrial wastes, such as mine tailings and dredged clay sediments, are examples of soft soils. Storage and management of such waste slurries is a global concern. The tailings storage facilities (TSF) designed to store the tailings are one of the largest artificial geotechnical structures in the world (Adamo et al., 2020). Stored mine tailings undergo significant consolidation over time under self-weight, which in turn influences the long-term stability and storage capacity of the TSF. The Mount Polley mine disaster in 2014 is a tragic example of the devastating consequence of tailings dam failure, highlighting the need for appropriate design, monitoring, and management of TSFs (Chambers, 2015). Clay slurries dredged from waterways and contaminated industrial undersea environments are stored on land inside confined disposal facilities (CDFs) for safety. The non-contaminated dredged spoils are used for land reclamation in lakes and other water bodies, where the spoils gain strength with consolidation (Rakshith and Singh, 2017). In the storage facilities, sufficient resident time has to be provided for these deposits to avoid spillage. When the land reclamation process utilises soft soils for filling, the fill has to achieve sufficient strength through consolidation before the land can be used for construction purposes (de Lillis et al. 2020).

Consolidation reduces the volume of materials due to the dissipation of excess pore water/fluid pressure. Therefore, these materials possessing high moisture content, fine-grained particles, and low permeability undergo large volume reductions, over long time (Carrier et al., 1983; Abu-Hejleh et al., 1996). The consolidation behaviour of such soft soils under self-weight, is not governed by the conventional consolidation theory given by Terzaghi (1923). The considerable strain due to self-weight-induced settlement makes it impossible to apply Terzaghi's infinitesimal strain assumption. The void ratio of the material changes significantly with progress in consolidation, causing a change in its permeability characteristics as well as compressibility. Gibson et al. (1967) provided a one-dimensional finite strain consolidation (FSC) model incorporating the change in permeability as well as compressibility during the process of consolidation. The example of the substantial settlement of the Kansai International Airport in Japan highlights the potential consequences of the long term consolidation aspect of

TH-3534_186104002

the reclaimed lands (Puzrin et al., 2010). Understanding the consolidation behaviour of these slurry materials in the FSC framework is therefore critical for developing sustainable management practices that ensure the safety and stability of reclaimed lands and storage or disposal facilities.

Regular consolidation tests for slurry materials, like seepage-induced consolidation tests and slurry consolidation tests frequently fail to simulate field stress conditions (Sorta, 2015). These laboratory tests require continuous monitoring and are time-consuming due to the low permeability and high water content of the consolidating slurries. Further, The FSC theory considers the non-linear variation of hydraulic conductivity and effective stress with the void ratio for accurate settlement estimations. The estimation of these two material functions or constitutive relationships is critical to engineering practice. Though many sophisticated instruments are used for conventional 1g testing, oedometer tests on slurry are not reported commonly, mainly because of the difficulty in the sample preparation and loading without triggering the expulsion of material at such high water contents. A geotechnical centrifuge offers a viable alternative to conventional experimental methods by reducing the testing time considerably and simulating the field stress conditions better (Taylor, 1995). The centrifuge provides a testing environment where the slurry sample, scaled down to N times the prototype height, experiences an acceleration equivalent to N times the normal acceleration due to gravity along its depth. Numerous literatures are available on FSC testing in centrifuges (Bloomquist, 1982; Robinson et al., 2003; Sorta et al., 2016; Reid et al., 2012). A better understanding of the experimental capabilities of a benchtop centrifuge for exploring the FSC behaviour of slurries can be gained through comparison with oedometer tests.

The acceleration due to gravity is constant within perceivable depths and, therefore, produces a linear distribution of stress within a vertical column of slurry undergoing self-weight consolidation. However, the non-linear variation of gravity-equivalent acceleration within a centrifuge model, due to its dependency on the distance from the centre of rotation, poses significant challenges in the scaling of various phenomena. The effect of the scale factor on consolidation time and settling value must be considered when converting centrifuge model observations to 1g prototype data for comparison with field observations. The time of consolidation in the centrifuge was shown to be multiplied by the square of scale factor N for comparison with prototype data by Croce et al. (1985). However, the exponent for the time scale was observed to show variation with from the established value, showing some

TH-3534_186104002

dependence on the degree of consolidation of the slurry sample (Sorta, 2015). Schofield (1980) and Taylor (1995) showed that in the centrifuge, the acceleration factor is not a constant for the whole model and varies with distance from the centre of rotation. Fox et al., (2005) reported that the *Hm/R* ratio (model height to centrifuge radius) influences the error induced by assuming the acceleration scale factor to be a constant with depth. All the studies essentially suggest that the centrifuge model test results show a lack of compatibility when a constant *N* value is considered. Besides, defining the effective radius values based on initial model dimensions might be erroneous since consolidation can result in the reduction of the model height, and the effective radius will change during the consolidation process.

Comparison and validation of centrifuge experimental data with the real field data of complete consolidation are difficult when the self-weight consolidation of slurries and slow-settling materials is studied, as it would take years for the process to complete. This calls for a numerical simulation of the process. Multiple analytical and numerical solutions to Gibsons's equation can be seen in the literature for 1g condition. Fox et al. (2005) developed a numerical model using the piecewise linear method (CC1) to simulate the process of consolidation in a centrifuge environment. This method was found to be effective but computationally expensive (Sorta et al. 2016). Recently, Bharat and Ubaid (2019) developed an analytical model for consolidation in a centrifuge environment, considering that the acceleration factor varies with the depth of the model. The model proposed solved the analytical governing equation using the explicit finite difference method and was found to be robust and efficient. Only brief studies are available on the variation of time scale exponent value and its dependency on the concentration of solids. A numerical study on the influence of various definitions of effective radius on the scaling of finite strain consolidation behaviour of slurries has not been reported yet. These aspects of centrifuge modelling need further exploration.

Indirect determination of hydraulic conductivity function parameters by inverse analysis is currently an area of great interest. The constitutive function parameters can be determined by inverse analysis using consolidation curves from settling column tests (Bharat & Sharma, 2011; He et al., 2017; Qi et al., 2020; Qi & Simms, 2020). However, these methods are computationally expensive and are dependent on the objective function formulation (Qi and Simms, (2020)). Recently, Qi and Simms (2020) developed a graphical method of inverse analysis to determine the hydraulic conductivity function when the time-invariant compressibility function was known. The method used the settlement versus time curve from

TH-3534_186104002

settling column tests as the input for inverse analysis. This technique uses settlement curves simulated by forward analysis using at least two pairs of assumed hydraulic conductivity function parameters. Further, the function parameters were obtained by a few hand calculations. Qi et al.(2020) proposed a graphical method, modifying the method given by Qi and Simms (2020) using combined sedimentation and consolidation settlement data for inverse analysis. These methods focus on the shape and variance of the settlement plots and the relative position of the graph with respect to the time axis for back-predicting the hydraulic conductivity parameters. The application of these methods using settlement data from centrifuge FSC tests is not yet available. Pore pressure dissipation data is another set of observations available from routine FSC tests. The effectiveness of pore pressure data as input for these procedures is not reported anywhere.

The indirect prediction or inverse analysis of constitutive function parameters involves two steps: forward analysis using a numerical model of FSC and backward analysis using an optimisation method. Bharat and Sharma (2011) used a piecewise linear model of FSC (Fox & Bearles, 1997) for the forward analysis and Particle Swarm Optimisation (PSO) for inverse analysis of constitutive function parameters from FSC data. Qi and Simms (2020) used the settlement data from slurry column tests for the back-prediction exercise using the Nelder-Mead Simplex algorithm for optimisation and the piecewise linear FSC model formulation for forward analysis. The Bharat and Ubaid model (2019) based on the explicit finite difference method (EFDM) offers a better alternative in terms of computational effort for the forward analysis part. Swarm intelligence-based optimisation algorithms, such as Particle Swarm Optimisation (PSO) and Artificial Bee Colony (ABC), are observed to be highly adaptable based on various literature (Bharat et al. (2008; 2009a; 2009b; 2012)). These algorithms show a lack of repeatability of results due to inherent randomness. The accuracy of conventional deterministic optimisation algorithms, such as the Nelder Mead simplex algorithm, shows heavy dependency on the initial point values supplied by the user. However, these algorithms converge fast when appropriately initialised. Hybrid algorithms combining stochastic and deterministic optimisation algorithms can help overcome shortcomings. The use of such hybrid optimisation algorithms for inverse analysis along with the EFDM solution for forward analysis needs to be investigated for the indirect estimation of hydraulic conductivity and compressibility function parameters from FSC observations from 1g and *Ng* testing conditions.

TH-3534_186104002

In the present work, a combination of experimental and extensive numerical studies has been carried out to understand the FSC behaviour of soft soils under normal and centrifuge gravity conditions. Oedometer tests and centrifuge tests were carried out on a few slurry samples to study the applicability of benchtop centrifuge for FSC experimentation. The concepts of effective centrifuge radius and time scaling exponent were explored, and the influence of these parameters in predicting the FSC behaviour of prototypes in the field from centrifuge FSC observations was studied numerically. Further, using appropriate data from the literature, various methods for the indirect estimation of constitutive function parameters were thoroughly explored. The existing graphical methods of inverse analysis that back-predicted the hydraulic conductivity function parameters from 1g settlement column tests were tested on centrifuge settlement data from the literature as well as synthetically generated centrifuge settlement data. Swarm-based stochastic algorithms such as PSO, ABC, and Quantum behaved PSO (QPSO) were combined with the EFDM model of FSC to back-predict the constitutive function parameters from FSC tests under 1g conditions. Three novel optimisation algorithms- Modified ABC (MABC), Hybrid PSO (HPSO), and Hybrid ABC (HABC) were proposed to improve the speed of convergence and to overcome issues of robustness associated with the original algorithms. The performances of these algorithms were tested using settlement and pore pressure data from normal and centrifuge FSC tests. Further, the influence of dimensionality on these algorithms was studied by simultaneous estimation of hydraulic conductivity and compressibility function parameters.

1.2 Organisation of the Thesis

The thesis consists of ten chapters, including six contributing chapters

Chapter 1 presents a general introduction to the problem, the motivation behind the research work.

Chapter 2 presents a thorough literature review elaborating the problem domain. Existing numerical and experimental methodologies associated with finite strain consolidation of soft soils are explained in this chapter. Inverse analysis methods currently existing and optimisation algorithms in use, along with shortcomings of the same, are discussed. The identified research gaps are also presented in this chapter. Well-defined objectives of the work are also presented in this chapter.

TH-3534_186104002

Chapter 3 presents a theoretical background of the consolidation behaviour of slurry materials. The governing differential equations and the numerical modelling of 1g and centrifuge cases are explained, and an overview of the effective radius and time scale exponent in centrifuge testing is explained.

Chapter 4 The basic characteristics of the slurries used for experiments and materials whose literature data were used in this study are presented in this chapter. The experimental methodologies adopted, including the oedometer FSC test and benchtop centrifuge test, are discussed. FSC models and various inverse analysis methods used in this study are explained. A detailed explanation of optimisation algorithms and the corresponding pseudocodes associated with this study are also presented in this chapter. Contributions from the present work are presented in chapters 5-10.

Chapter 5 presents an experimental study of the consolidation behaviour of four soil slurries tested in an oedometer as well as a benchtop centrifuge under different levels of gravity. The expedition of FSC of slurries through the use of a centrifuge is discussed. Further, the compressibility function derived from both methods is compared in this chapter.

Chapter 6 presents a numerical study on the effect of using the scale factor defined by various effective radius definitions in the literature in scaling the FSC settlement versus time data from centrifuge to prototype. The variation of the exponent of the scale factor for the time data with the degree of consolidation is also discussed in this chapter.

Chapter 7 presents the inverse analysis of hydraulic conductivity function parameters using synthetic centrifuge FSC data and data from literature by applying two existing graphical methods, which were originally defined for 1g settling column tests.

Chapter 8 presents inverse analysis using optimisation algorithms with synthetic 1g FSC settlement data and the settlement from the literature. The application of three novel optimisation algorithms proposed in this study, along with three conventional optimisation algorithms for the estimation of hydraulic conductivity function parameters, is presented. Simultaneous estimation of hydraulic conductivity and compressibility function parameters using these algorithms are also discussed in this chapter.

TH-3534_186104002

Chapter 9 presents inverse analysis using optimisation algorithms with synthetic *Ng* FSC settlement data and the *Ng* FSC settlement data from the literature. The application of three novel optimisation algorithms proposed in this study, along with three conventional optimisation algorithms for the estimation of hydraulic conductivity function parameters, is presented. Simultaneous estimation of hydraulic conductivity and compressibility function parameters from *Ng* FSC data using these algorithms are also discussed in this chapter.

Chapter 10 presents the separate and simultaneous estimation of hydraulic conductivity and compressibility function parameters using synthetic pore pressure data and the same from literature under 1g and *Ng* conditions through various methods of inverse analysis.

Chapter 11 discusses important conclusions and the scope of future studies based on detailed analyses of the results and gaps in the present work.

TH-3534_186104002

2. Literature Review

2.1 General

In this section, the relevant literature reviewed for this study is discussed.

2.2 Finite Strain Consolidation Analysis

The one-dimensional small strain theory proposed by Terzaghi (1923) was limited by its inherent assumptions. Slurry materials like mine tailings and dredged slurries show considerable volumetric deformation under self-weight, which cannot be analysed using Terzaghi's theory (Ahmed & Siddiqua 2014). Gibson et al. (1967) developed the finite strain theory for the consolidation of thin layers of clay material. He also accounted for the variation in permeability and compressibility during the process of consolidation. A thin, homogeneous, saturated clay layer was considered. A partial differential equation that governs the large strain consolidation process with the void ratio as the dependent variable was developed. Darcy's law is applied in such a way that the relative velocity of pore fluid and the soil skeleton is related to the gradient in the pore fluid pressure. However, the work is mathematical and also did not study various relationships between the void ratio and effective pressure.

Gibson et al. (1981) considered a thick consolidating layer, which integrated the self-weight effect into the consolidation process. A material coordinate system was used to manage the moving boundary (Ortenbald,1930). Using the Lagrangian coordinates and rearranging the fluid relationships, Koppula (1970) came up with a governing equation. Lee (1979) incorporated the convective coordinate system and redefined the governing differential equation in terms of porosity. However, the approach is computationally costly as the convective coordinate system necessitates updating the geometry at each step (Ito, 2013; Jeervipoolvarn, 2010). Somogyi (1980) integrated Koppula's formulation into the theory and derived the governing equation in terms of the excess pore pressure. Monte and Krizek (1976) presented a mathematical model of one-dimensional large strain consolidation, considering variable compressibility and permeability characteristics of homogeneous saturated clay. The term fluid limit is coined for the initial no-stress state of the soil in the slurry. The Lagrangian coordinate system was used. Lee and Sills (1981) studied the consolidation during and after the deposition of soft soil, using Gibson's large strain consolidation governing equation, recognizing the effect of self-weight. Permeability is assumed to be proportional to the void

TH-3534_186104002

ratio. Lagrangian and Eulerian coordinates are related through the void ratio. Consolidation of dredged fill, normally consolidated stratum, stratum formed by continuous deposition under different timings of deposition are studied. The effect of self-weight was observed to be less pronounced in cases where extra load is applied on the soil surface. However, since the majority of the compression of the layer happens while the effective stresses reach equilibrium with the weight of the soil, the effect of self-weight is very significant. Schiffman (1980) demonstrated that the small strain theory, together with its fundamental linear and nonlinear variants, are specific cases inside the finite strain theory. This establishes the finite strain theory as a comprehensive and all-encompassing theory for one-dimensional consolidation. Though subsequent studies have made multiple modifications to the basic FSC theory to suit various problem statements, the theory has been identified as useful for the consolidation analysis of waste slurries. (Caldwell et al.,1984; Koppula & Morgenstern, 1982; Schiffmann & Cargill, 1981; Krizek & Somogyi, 1984; Bromwell, 1984).

Cargill (1982) derived a solution for the nonlinear governing equation for large strain consolidation using the explicit finite difference method. The coefficients are updated in each time step, applying appropriate initial and boundary conditions for dredged fill and normally consolidated soft soil. The progress of consolidation is studied in terms of pore pressure, settlement, and stress. The determination of these relationships from oedometer testing was also studied, considering a case of a semipermeable boundary. A program CSLFS (Consolidation of Soft Layers, Finite Strain) was developed in FORTRAN using the mathematical model and its solution to solve a few typical cases of consolidation of soft layers.

Townsend and Mcvay (1990) reviewed a variety of computer programs and solution techniques for solving the equation governing nonlinear large strain consolidation. These involved implicit and explicit finite differences, material-based, and spatial-based methods. Piecewise linear programs were observed to have handled initial non-uniform void ratio conditions and multilayer conditions with some assumptions in place. Spatial coordinate-based piecewise linear programs predicted various scenario boundary conditions compared to material coordinate-based programs. However, this is at the expense of a much greater run time required for the solution compared to the finite difference programs in material coordinates.

Fox and Berls (1997) proposed a dimensionless, piecewise linear numerical model called Consolidation Settlement 2 (CS2) to model the large strain consolidation behaviour of compressible layers. This model accounts for a finite value of strain, the self-weight of the soil, the relative velocity of the solid and fluid phases, and variable compressibility and hydraulic

TH-3534_186104002

conductivity during the process of consolidation. The constitutive relationships are specified using discrete data points without requiring mathematical approximations or calculation of any derivative functions. The CS2 source code was also discussed, and its effectiveness was demonstrated in examples of problems with infinitesimal strain, finite strain, self-weight, and nonlinear constitutive relationships.

2.3 FSC Analysis for Centrifuge Environment

Fox *et al.* (2005) developed a numerical model, based on Gibson *et al.* (1967), for one-dimensional large-strain self-weight consolidation of soft soils in a geotechnical centrifuge. The acceleration factor of the model varies with the depth of the sample. The results of centrifuge tests on Singapore marine clay were used to verify their numerical model. The numerical model was found to closely match the experimental data. To study the effect of non-uniform acceleration, several numerical simulations were run using varying model heights, acceleration levels, effective radius, and the ratio of height to the effective radius. The numerical simulations were compared with the experimental centrifuge time-settlement curve. Results indicated that the effect of non-uniform acceleration is greatly controlled by the ratio of specimen height at the start to the radius of the centrifuge. The numerical simulation of Fox *et al.* (2005) indicated that an effective radius to the initial mid-height of the specimen results in a good match to the settlement-time curves obtained from the centrifuge test.

Bharat and Ubaid (2019) derived the governing equation for large strain consolidation under self-weight in a centrifuge environment. This was based on the FSC theory by Gibson et a*l.* (1981). The solution for the equation was obtained using the finite difference method, and settlement versus time plots were obtained. Data from some slurries were used to study the effect of varying acceleration along with the depth of the sample, as well as the effect of sample size and centrifuge radius. The model was validated with experimental data from Singapore marine clay, which was in agreement.

Srinivasulu (2023) formulated the finite element method-based numerical technique adopting the implicit time integration scheme to simulate the centrifuge finite strain consolidation. The formulation incorporates the nonlinearities arising from the hydraulic conductivity, compressibility, and acceleration factor *N*. Through comparative analysis with the explicit-based finite difference method, the computational efficiency of the FEM approach was demonstrated in terms of time steps and computational time.

TH-3534_186104002

Malengier (2016) presented a mathematical model for the FSC in a bench-top centrifuge. The model is not based on the scaling laws and allows the use of multiple boundary conditions. A lines-based approach is proposed to solve the mathematical model.

Cooke (1991) investigated an effective radius to be used in calculating average acceleration in a centrifuge. The effective radius from the central axis to 40% of the model height was found to minimize the vertical stress distribution error in centrifuge modelling.

Taylor (1995) studied the scaling laws using standard methods using either the dimensional analysis or the governing differential equation. The most common errors in centrifuge modelling scaling laws were discussed in detail. The effect of variable acceleration throughout the sample depth was described. He derived the effective centrifuge radius to minimize errors in stress calculation in a sample. The effective centrifuge radius, which is the distance from the centre of rotation of the centrifuge to the one-third depth of the sample, was suggested for use in calculating the angular rotation speed. Schoefield (1990) presented similar observations.

Croce et al. (1985) developed scaling relationships for centrifuge modelling by taking into consideration mechanical similarities, which allowed for the comparison between models and prototypes. It was found that the self-weight consolidation of soils adheres to a time-scaling exponent of 2. However, the modelling of model tests by Sorta (2015) revealed that during certain phases of consolidation, the exponent of the time scale factor is not equal to the theoretical value. The scale exponent was observed to be dependent on the degree of consolidation. Consistent with the findings of this study, prior simulations conducted by Scully et al. (1984) and Bloomquist and Townsend (1984) also demonstrate that the rate of time-scaling is not consistent and tends to increase in relation to the degree of consolidation. Croce et al.'s research (1985) indicates that the time exponent for the centrifugal modelling of consolidation in kaolinite clay is 2.0. However, their findings are based on samples with a very low starting void ratio. Additionally, the scaling law was only assessed at 50% and 100% of consolidation rather than during the whole consolidation process. Based on this, we may infer that the time-scaling exponent seems to be influenced by the level of consolidation and the relative acceleration employed in modelling.

2.4 Constitutive Relationships for FSC Theory

The hydraulic conductivity and compressibility functions are identified as the important characteristics that control the process of consolidation. These constitutive relations are obtained by fitting appropriate function forms on experimental data. These functions are

TH-3534_186104002

relevant for the numerical solution of the FSC governing differential equation to obtain the void ratio profile (Carrier et al.,1983; Somogyi, 1980; Barthelomuseen et al., 2002; Cargill, 1982). The power form of hydraulic conductivity function is introduced by Somogyi (1980). A logarithmic function form is proposed by Barthelomuseen et al. (2002). Znidarcic et al. (2011) confirmed the effectiveness of the power form for fitting the nonlinear relation between hydraulic conductivity and void ratio in the case of matured fine tailings of oil sands. Though many other forms of hydraulic conductivity functions are proposed by various researchers, such power form of hydraulic conductivity is widely used (Townsend & McVay, 1990; Jeeravipoolvarn et al., 2008; Yao & Znidarcic, 1997).

The nonlinear correlation between effective stress and the void ratio is termed the compressibility function. This relation is critical in understanding the long-term behaviour of the consolidating material. Some of the commonly used functional forms for the compressibility function are the Weibull function (Jeeravipoolvarn et al., 2008), the power function (Townsend & McVay, 1990) and the extended power function (Liu & Znidarcic, 1991). The Weibull function was shown to be effective when the consolidation is associated with creep, while the modified power function incorporates the boundary value of effective stress at which the sedimentation ends and the self-weight consolidation starts.

With multiple options available to represent the constitutive function fitting the experimental data, it is crucial to identify the form that can simulate the actual behaviour of the slurry materials accurately.

2.5 Experimental Studies on FSC

The Modified Conventional Oedometer Test utilises a modified apparatus to deliver minimal starting pressures and evaluate the relationship between void ratio and effective stress at the completion of each load increment. The measurement of hydraulic conductivity is conducted by a falling head test (Hong et al. (2010), Xu et al. (2015a, 2015b) and Tavenas et al. (1983a, 1983b). However, this approach has several drawbacks, such as the possibility of sample leakage affecting the accuracy of hydraulic conductivity measurements, the use of small samples that may not be representative, and the potential for seepage-induced consolidation, especially at low-stress levels (Suthaker, 1995; Tavenas et al., 1983a; Tavenas et al.,1983b).

The Multi-step Loading Large Strain Consolidation Test estimates volume compressibility and hydraulic conductivity by applying multiple load steps. The load is applied manually up to 8

TH-3534_186104002

kPa, and then a bellofram air pressure system is used for higher pressures. It employs a constant head test to measure hydraulic conductivity at each load step. (Jeervipoolvarn, 2010; 2005; Jeervipoolvarn et al., 2005, Azam, 2011; He et al., 2017) Limitations include long test durations (6-12 months), potential internal erosion at high gradients, and wall friction concerns at higher pressures (Jeervipoolvarn, 2010).

The Constant Rate of Deformation Test involves deforming specimens at a constant rate while measuring axial load and deformation, providing detailed data on the void ratio-effective stress and hydraulic conductivity relationships (Znidarcic et al., 1984; Gorman et al., 1978; Znidaric et al.,1986; Umehare & Zen, 1980; Lee 1981; Silvestri et al., 1986; Gorman et al., 1979) Challenges include selecting an appropriate rate of deformation and the small strain assumption, which makes it unsuitable for characterizing slurry-like soils (Umehara &Sun, 1980).

The Controlled Hydraulic Gradient Test maintains a constant hydraulic gradient by regulating the load through a feedback mechanism. It measures vertical effective stress and corresponding strain, utilizing Terzaghi's one-dimensional theory (Gorman et al., 1978; Lowe et al., 1969; Silvestri et al., 1986; Gorman et al., 1976; Lowe et al., 1969). This test is limited by the small strain theory assumptions, which restrict its applicability to soils experiencing significant deformation. The unknown initial rate of loading and inconsistent pore water pressure can also lead to errors.

The Seepage Induced Consolidation Test leverages effective stress differences induced by seepage pressures to initiate consolidation, measuring pore-water pressure distribution and void ratio changes along the specimen (Imai, 1979; Fox and Baxter, 1997; Tian et al., 2020). The hydraulic conductivity is measured by the constant head method. Though it is a widely used procedure (Estapho, 2014; Huerta et al., 1998; Berilgen et al., 2005; Janbaz & Maher, 2017), it requires sophisticated instrumentation and can suffer from potential specimen rebound, sidewall leakage, and operator-dependent data quality. Besides, it is a very slow test.

The Compressibility Standpipe/ Settling Column Test establishes the compressibility relation by directly measuring density, total stress, and pore water pressure using a self-weight consolidation column. This is one of the most common and simplest FSC experiments (Jeeervipoolvarn, 2010; Jeervipoolvarn et al., 2009; Been & Sills, 1981; Wickland & Willson, 2005; Scott et al., 1986; Babaoglu et al., 2020; Dromer et al., 2004; Miller, 2010; Li et al., 2013; Soleimani et al., 2014; Sun et al., 2009; Barthelomuseen et al., 2002). The consolidation

TH-3534_186104002

behaviour under self-weight conditions is simulated. Pore pressure dissipation data can be obtained by using pressure transducers. However, this test is time-consuming, especially for low hydraulic conductivity specimens, and can experience significant sidewall friction. Due to the length of the test, the potential of getting only limited data points exists.

The centrifuge-modelling approach is well-suited for studying geotechnical constructions that involve gravity-driven soil behaviour, such as embankment building, mining waste deposition and consolidation, and self-weight consolidation. (Schofield, 1980; Beasley & James, 1976; King and McCoughin, 1993; Lydon, 1985; Antonaki et al., 2014; Antonaki et al., 2018; Basset, 1973). The beam centrifuge test has been utilised by several researchers to forecast the field consolidation of phosphatic clays (Bloomquist, 1982; Lawver et al., 1983; Townsend & Hernadez, 1986) and the consolidation behaviour of flocculated clays (Wieland et al., 1994). Mikasa and Takada (1984) and other researchers (McVey et al., 1986; Croce et al., 1985) have undertaken theoretical investigations on the consolidation process under centrifuge settings to compare them with experimental findings. Dunmola et al. (2018) performed a beam centrifuge test on flocculated fine tailings of oil sands. Robinson et al. (2003) conducted a beam centrifuge test using Singapore Marine clay (SMC). Takada and Mikasa (1984) established the effective stress relation by analysing the distribution of moisture content throughout the depth of the model. The centrifuge-based hydraulic conductivity function determination needs multiple sets (McVey et al., 1987). Sorta (2015) used a centrifuge test with density and pore pressure transducers to determine the relationships between void ratio and effective stress, as well as void ratio and hydraulic conductivity, for both oil sands tailings and kaolinite slurry. This method allowed them to avoid the need for multiple tests on the same samples. Compared to conventional consolidation testing, the self-weight consolidation in the centrifuge test offers several advantages. Firstly, the self-weight consolidation process can be explored over a shorter time period. Secondly, centrifuge modelling is more regulated and allows for more accurate instrumentation. Lastly, centrifuge modelling is more reproducible than predictions based on the large strain theory, as it is highly sensitive to consolidation parameters like hydraulic conductivity.

A bench-top centrifuge is a compact device that can replicate severe stress conditions by rotating at high revolutions per minute (RPM). This overcomes the spatial limitations of the beam centrifuge. It is cost-effective. Centrifuge modelling is a widely recognised and established technique used to investigate the behaviour of soil. However, the use of bench-top centrifuges has been limited to a small number of research focused on investigating the

TH-3534_186104002

consolidation behaviour of slurry-like materials. McDermott and King (1998) performed an expedited consolidation test on Speswhite kaolin clay using a small-scale centrifuge to investigate how kaolin slurries with varying beginning moisture levels consolidate. The hydraulic conductivity was determined using the Mikasa-Takada method, whereas the compressibility relationship was constructed by measuring the solid content in slices obtained from the sample. El-Shall et al. (1996) examined the consolidation characteristics of phosphatic clays using a small-scale centrifuge. A mathematical model, utilising first-order kinetics, was used to determine the correlations between void ratio and effective stress, as well as void ratio and hydraulic conductivity. Reid et al. (2012) employed a customised bench-top centrifuge to investigate the consolidation characteristics of a kaolin slurry. The void ratio-effective stress profile was established by directly measuring the moisture content. The researchers created an iterative numerical model using the FLAC v7.0 finite-difference algorithm to calculate the effective stress-hydraulic conductivity profile of the tested samples in order to align with the observed pore water pressure dissipation data. Although the mentioned modifications have valid reasons for using a bench-top centrifuge to study the consolidation behaviour of slurry-like soil, the small radius of rotation can cause significant variation in the centrifugal acceleration level (*Ng*) across the test specimen (Muir Wood, 2017; Black, 2014; Anderson et al., 2015). According to Muir Wood (2017), if the height of the specimen in the centrifuged model is less than one-tenth of the radius of rotation, the fluctuation of centrifugal acceleration level (Ng) throughout the specimen is considered insignificant and may be assumed to be constant.

Gibson's finite strain consolidation theory is a suitable framework for understanding self-weight consolidation behaviour in mine tailings and dredged clays. FSC tests in a geotechnical centrifuge provide an alternative to conventional testing under normal gravity, with the potential for speed and simplicity in bench-top centrifuge testing. However, there is little literature on the experimental derivation of constitutive functions using bench-top centrifuge. In the present study, the experimental performance of the conventional oedometer is compared with the bench-top centrifuge in the analysis of the FSC behaviour of soil slurries.

Nonlinear stress distribution in the centrifuge model due to varying acceleration poses a scaling challenge. Effective radius concepts have been introduced, but their impact on predicting prototype settlement values needs deeper exploration from an FSC framework. The exponent for the scale factor in time values during consolidation varies between 1 and 2, depending on factors like consolidation degree and solid concentration. However, the influence of factors

TH-3534_186104002

such as centrifuge acceleration and model depth-to-radius ratio on these exponent values remains unstudied. The present study delves deep into these aspects through a numerical analysis using the EFDM solution developed by Bharat and Ubaid (2019).

2.6 Estimation of Constitutive Functions By Indirect Methods

Methods of indirect estimation of the compressibility and permeability functions reported in the literature are based on either regression analysis using correlation to properties like the Atterberg limits (Babaoglu & Simms, 2018; Chapuis & Aubertin, 2003; Morris, 2003; Samarasinghe et al., 1982) or back-calculation using the FSC formulations from simpler FSC test observations such as the data from settling column tests. (Hajihassani et al., 2018; Jin et al., 2016; Oberender & Puzrin, 2015; Qi et al., 2020; Qi & Simms, 2020; Yin et al., 2018). The regression analysis estimation of the permeability function has the advantage of being a more straightforward method as it uses the readily available existing database. However, the permeability function obtained by this process is not satisfactory for major design purposes due to the empirical nature of the approach (Qi & Simms, 2020). The approach based on back-calculation is performed using the trial-and-error method, which requires experience and expertise or by a combination of the numerical solution of FSC governing equations with the appropriate optimisation algorithm. (Bharat & Sharma 2011; Been & Sills 1981; He et al. 2017; Qi & Simms, 2020; Thiebot et al., 2011; Znidarčić et al., 1986). The second approach is complicated in terms of the computational cost involved. Qi and Simms (2020) proposed a graphical inverse analysis method incorporating the self-weight consolidation data, and Qi et al. (2020) modified the same to include the effect of sedimentation in the analysis.

Inverse analysis combines FSC forward modeling with optimization. Bharat and Sharma (2011) used a piecewise linear FSC model (Fox & Bearles, 1997) with PSO, while Qi and Simms (2020) used slurry column data and the Nelder-Mead Simplex algorithm. The piecewise linear method is computationally intensive (Sorta, 2015; Fox & Bearles, 1997).

Based on the literature review, it is clear that the constitutive functions (hydraulic conductivity and compressibility) heavily influence FSC behaviour in slurries. Indirect estimation methods from simpler experimental observations provide an alternative to time-consuming direct measurements. Existing graphical methods of inverse analysis were observed to successfully predict the hydraulic conductivity function parameters from the settlement observations of column tests under normal gravity conditions. The same model, if tested in a centrifuge, settles at a much faster rate and produces a different settlement curve. Therefore, in the present study,

TH-3534_186104002

the efficiency and accuracy of these existing methods are tested further by using settlement data from FSC tests conducted in a centrifuge.

Studies use various optimisation algorithms combined with the piecewise linear method of FSC analysis for the process of inverse analysis. The forward analysis steps involved in the back-prediction of constitutive function parameters can be significantly simplified by the use of EFDM instead of the piecewise linear method. Therefore, in this study, optimisation-based inverse analysis methods, combining swam-based algorithms and EFDM formulation of FSC, is explored to improve the speed of the inverse estimation process.

Pore pressure dissipation data taken at the base of the settling sample are more reliable compared to settlement data in the case of turbid slurries where the settling boundary is not comprehensible. The back prediction of constitutive function parameters from pore pressure data has not been reported yet. In the present study, this approach is attempted using the FEM model for the FSC in a centrifuge environment.

2.7 Optimisation Algorithms

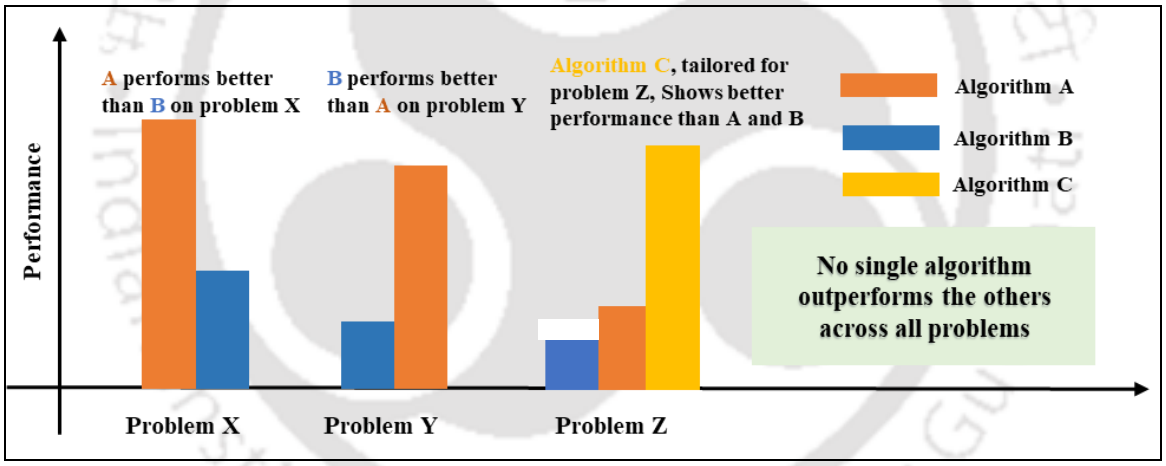


Figure 2.1 Illustrating the No Free Lunch Theorem

Wolpert and Macready (1997) coined the No-free-lunch theorem in the context of a comparison of the performance of optimisation algorithms. According to this theorem, if optimisation method "A" is superior to optimisation technique "B" on optimisation problem "X", then there exists an optimisation problem "Y" for which optimisation technique "B" surpasses optimisation technique "A". The no-free-lunch theorem asserts that when optimisation tool "C" is tailored to certain problems, it is likely to exhibit strong performance for those problems, but it is likely to exhibit poor performance for other problems. The no-free-lunch theorem asserts the challenge of creating a universally effective optimisation strategy that can perform well

TH-3534_186104002

across a diverse array of optimisation tasks. Specialised solutions are expected to surpass a generic optimisation approach when applied to a specific optimisation problem.

2.7.1 Particle Swarm Optimisation

Kennedy and Eberhart (1995) introduced the PSO algorithm closely mimicking the natural behaviour of swarms, such as the flocking behaviour of birds or the schooling behaviour of fish, to resolve nonlinear continuous optimization problems with improved accuracy. PSO is a highly adaptable optimization algorithm with broad applicability across a wide range of optimization problems, some of which were studied by Bharat et al. (2008; 2009a; 2009b; 2012). Over time, a number of variants for PSO have been developed, focusing on the tendency of premature convergence to local minima and the convergence rate. During the execution, certain particles may become inactive, rendering them unable to conduct searches and leading to a velocity close to zero. Adaptive PSO solves this issue by substituting inactive particles with fresh ones while preserving the PSO connections (Xie et al., 2002). In traditional PSO, the inertia weight remains constant for all particles within a generation. However, in adaptive PSO, distinct ω values are assigned to each particle based on their rankings, with the aim of improving the search capability (Panigrhi et al., 2008). The Global Best Particle Swarm Optimisation (GBPSO) (Engelbrecht, 2007) is a version of the regular Particle Swarm Optimisation (PSO) algorithm that incorporates velocity weights, including inertia weight, personal best weight, and global best weight. GBPSO, unlike traditional PSO (Kennady & Eberhart, 1995), incorporates an inertia weight and does not rely on c_1, but instead requires c_2 to be set to 2. Decreasing weight particle swarm optimisation (DWPSO) is a variant of GBPSO that gradually decreases the inertia weight over time. This approach aims to enhance variety in the first iterations and encourage convergence in the later ones (Engelbrecht, 2007). The Guaranteed Convergence PSO (GCPSO) algorithm assures that the particle with the best global solution searches within a radius that is dynamically adjusted. This approach addresses stagnation and improves local convergence by randomly modifying the search radius (Van den Bergh & Engelbrecht, 2002). Local best PSO (LBPSO) is distinguished from Global Best PSO (GBPSO) by utilising the optimal location of a subset of particles instead of a single global best position (Engelbrecht, 2007). The PSO algorithm, known as Fully Informed PSO (Jordan et al., 2008), organises particles into clusters in order to enhance the exchange of information. Attraction-repulsion PSO algorithm (Riget & Vesterstrøm, 2002) undergoes alternating attractive and repulsive phases, which are determined by the diversity of the swarm. It employs

TH-3534_186104002

two thresholds to transition between the convergence-focused phase (attractive phase) and the diversity-focused phase (repulsive phase).

Garg (2016) combined PSO with a Genetic Algorithm (GA) to handle constrained optimisation problems, which is efficient in global search. Abdel-Kader (2011) developed discrete PSO-GA, introducing two driving parameters controlling the optimisation. Niu et al. (2008) have presented a new global hybrid optimisation technique named PSODE, which combines the characteristics of PSO and DE. This strategy involves the simultaneous execution of PSO and Differential Evolution (DE) algorithms, resulting in regular information exchange throughout the population, which ultimately helps the population as a whole. Holden et al. (2007) introduced a new hybrid method called PSO/ACO to uncover classification rules in data mining. This technique combines the advantages of PSO and Ant Colony Optimisation (ACO). The revised PSO/ACO method was assessed on 16 publicly available real-world datasets using two distinct particle fitness functions, showcasing its higher performance in comparison to the original approach. In addition, Elloumi et al. (2014) introduced a hybrid method called PSO/ACO to solve the issue of travelling salesmen. This method offers the most efficient answers even in intricate search areas and has been empirically proven to be more time-efficient than traditional algorithms when assessed using TSP benchmarks.

In addition to these hybridizations, PSO has been integrated with other metaheuristic algorithms to tackle distinct application domains. The algorithms mentioned include Simulated Annealing (Laarhoven et al., 1987), Artificial Bee Colony (ABC)(Pham et a., 2005), Cuckoo Search (CS) (Yang & Deb, 2009), Bat Algorithm (Yang, 2010a), Firefly Algorithm (Yang, 2010b), Glowworm Swarm Optimisation Algorithm (Kalaiselvi et al., 2017), Grey Wolf Optimisation (Liu et al., 2011) and Moth Flame Optimisation (Mirjalili, 2005).

Integrating the principles of quantum mechanics and PSO, Sun et al. (2004) devised the probabilistic optimization algorithm called quantum-behaved particle swarm optimization (QPSO). Based on this idea, the QPSO algorithm uses the Schrödinger wave function $\Psi(x, t)$ to define a particle instead of exact position and velocity. QPSO assumes that each particle is subject to the effects of a quantum potential field. (Sun et al., 2004; Sun et al., 2012). The QPSO method enables particles to demonstrate quantum behaviour, as opposed to the conventional Newtonian dynamics employed in prior versions of PSO. Instead of adhering to a Newtonian random walk, the search process utilises "quantum motion." When evaluated using benchmark functions, QPSO demonstrated higher performance in comparison to traditional PSO, especially when dealing with large population sizes (Poli, 2007). One major

TH-3534_186104002

benefit of QPSO is its decreased number of control parameters, necessitating the tuning of only a single parameter.

Sun et al. (2004) conducted a probabilistic study of QPSO, whereas Fang et al. (2010a) examined its convergence behaviour. QPSO has demonstrated significant efficacy and versatility across a range of applications. The QPSO method is widely used because of its simplicity and straightforward implementation, making it accessible even to those without expertise in swarm intelligence. Users may easily employ QPSO in many areas and combine it with other approaches. Furthermore, QPSO possesses a remarkable capacity for performing global searches, resulting in very effective optimisation outcomes across various benchmark functions and diversified applications (Fang et al., 2010b). The potential of QPSO has been explored in a few engineering applications (Coelho, 2010; Bharat & Sharma, 2012; Bharat et al., 2019). Based on the abundant literature, there are multiple ways of improving the PSO. However, the hybrid approach seems to offer better global optimisation. The available combination of algorithms in the hybrid form of PSO works on complicated backgrounds combined with other metaheuristic optimisation methods. In this work, a novel hybrid optimisation algorithm combining the PSO with *fmincon* -a constrained optimisation algorithm in MATLAB optimisation toolbox is developed. This is a hybrid algorithm (HPSO) combining the benefits of deterministic algorithms in terms of exploitation with the exploration capacity of PSO. QPSO is an algorithm with immense potential that has not yet been applied in many engineering applications. Therefore, in this study, the efficiency of QPSO is explored when solving optimisation problems in an FSC framework. The PSO, QPSO, and HPSO are applied to estimate indirectly the compressibility and hydraulic conductivity function coefficients of slurry materials.

2.7.2 Artificial Bee Colony Algorithm

Artificial Bee Colony (ABC) is a metaheuristic algorithm mimicking the foraging behaviour of honey bees, introduced by Dervis Karaboga (2005). In certain instances, ABC has been observed to strike a balance between exploration and exploitation in its estimation of the global best, mean fitness, and standard deviations (Bharat, 2017). Karaboga and Gokremli (2012) introduced a method of neighbourhood determination by using the concept of Euclidean distance to modify the onlooker bee phase of the ABC. Akay and Karaboga (2012) incorporated a dynamic scale factor to control the perturbation given to the current solution to arrive at the neighbouring solution. A control parameter was introduced that determined the number of attributes in the solution that had to be modified to produce a neighbouring solution. Wang

TH-3534_186104002

(2015) incorporated the generalized opposition-based learning strategy proposed by Tiszoosh (2005) in all the phases of ABC, including population initialisation.

One of the regular approaches adopted for improving ABC's exploration and exploitation capabilities further involves modifying the position update equation and learning from the best available solution or the global best solution in the previous iteration. Gao et al. (2013) used an orthogonal learning strategy along with this approach to gain valuable insights from the algorithm. Luo et al. (2013) proposed a converged onlooker approach, which allowed for the guided movement of the onlooker bees directly to the global best value through successive updates. Kiran and Findik (2015) used this direction information to allow constriction of search space in consecutive iterations, which helped improve the speed of convergence. An elite vector-based guidance strategy, combined with a reduction of employed bees to one-fourth of the total bee colony size, helped improve the local searching capacity and speed of convergence of ABC (Ye et al., 2018). Gao et al. (2018) controlled the tendency of employed bees to oscillate between low-quality solutions repeatedly by combining the global best guidance with a turbulence control parameter.

Another approach adopted to improve the performance of ABC is hybridization with other algorithms. A combination of ABC with the Levenberq-Marquardt algorithm (Ozturk & Karaboga, 2011), pattern search (Kang et al., 2013), etc, for the exploration phase has been adopted in various works. Chung et al. (2014) improved the position update equation by hybridizing ABC with the particle swarm search strategy and a chaotic operator for the solution search. A comprehensive learning approach combined with Powell's search approach for local searching improved the performance of ABC in the work of Ma et al. (2016). The dynamic population sizing concept was also introduced to reduce the computational load.

Many studies have adopted the DE and GA principles to derive hybrid algorithms. Gao and Liu (2012) modified ABC using DE, chaotic systems, and opposition-based learning to achieve global convergence while omitting probabilistic selection and the scout bee phase. Some studies used the mutation and crossover phase from DE and global-best-based guidance to balance exploration and exploitation (Jadon et al.,2017; Ustun et al., 2022; Zhou et al., 2017). A hybrid of ABC and Non-Dominated Sorting Genetic Algorithm-ii was proposed for multi-objective optimization by Sutar and Jadhav (2022). The neighbourhood searching of ABC was improved by Sun et al. (2023) using global optimal solution information for guidance and a genetic model for enhancing the diversity of solutions through crossover and mutation.

TH-3534_186104002

The conventional stochastic algorithms tend to experience premature convergence and reduced robustness, which can be eliminated by combining these algorithms with deterministic optimisation algorithms appropriately. Such hybrid algorithms can be further used in the fast and reliable estimation of constitutive function parameters from FSC data. Based on the abundant literature on the attempts to improve ABC, two variants of ABC are proposed in the present study. The first is the modified ABC (MABC), which incorporates opposition-based learning for population initialization, an improved position update rule containing the information from global best value from the previous iterations, a modified probability calculation equation that acknowledges the previously estimated probabilities of the considered food source and Euclidean distance-based computing for determining the neighbourhood during the onlooker bee phase. The second algorithm is the hybrid ABC (HABC), which combines the ABC with *fmincon*, a function in MATLAB used for solving constrained nonlinear optimization problems to improve the convergence of ABC to robust solutions.

2.8 Objectives of the Research Work

Based on the research gaps identified from the literature review, the following objectives were defined for the present work:

- Experimental study of the finite strain consolidation behaviour of soft soils under normal and centrifuge gravity conditions.
- Numerical investigation of the influence of centrifuge effective radius and time scale exponent on predicting prototype finite strain consolidation behaviour
- Estimation of hydraulic conductivity function parameters from centrifuge-finite strain consolidation behaviour of slurries using graphical methods
- Estimation of constitutive function parameters from finite strain consolidation settlement data under normal gravity conditions using optimisation algorithms
- Estimation of constitutive function parameters from centrifuge- finite strain consolidation settlement data using optimisation algorithms
- Inverse analysis of constitutive function parameters using pore pressure dissipation data from FSC tests under normal and centrifuge gravity conditions.

TH-3534_186104002

3. Theoretical Background

3.1 General

In this chapter, the basic theory involved in the studies conducted as a part of the present work is explained for clarity. Short explanations of various concepts like conventional consolidation theory, Gibson's theory of consolidation and the centrifuge modelling of consolidation are presented.

3.2 Terzaghi's Theory of Consolidation -A review

A simple mechanism to explain the phenomenon of consolidation was first proposed by Karl Terzaghi in 1923. Along with his understanding of effective stress and the introduction of the fourth dimension-time, the era of modern Soil Mechanics began. Terzaghi's consolidation theory simplifies the process of volume reduction of compressible soils by releasing the pore fluid through a spring-dashpot analogy and provides a simple one-dimensional governing differential equation. However, few of the assumptions involved in the development of this equation resulted in the theory yielding unsatisfactory predictions when applied to soft soils and slurry materials. The following are the assumptions involved in the conventional consolidation theory:

- The soil voids are filled with water completely, i.e., the soil is fully saturated and homogeneous.
- The soil particles and water cannot be compressed
- Darcy's law is valid for various computations involved
- The permeability *k* remains constant throughout the consolidation
- The system is laterally confined, i.e., the deformation happens only in the vertical direction
- The void ratio and effective stress are uniquely related, and the relation remains a constant
- The strain is infinitesimal, and the effect of self-weight is not considered

TH-3534_186104002

3.2.1 Consequences of Terzaghi's assumptions

When uniform vertical stress is applied to a saturated thin layer of compressible soil, vertical drainage occurs following the development of an initial uniform excess pore water pressure throughout the layer, resulting in the volume reduction of the layer.

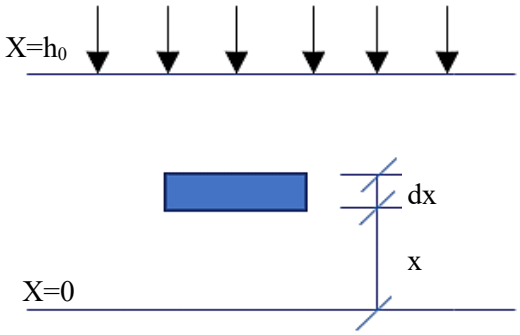


Figure 3.1 Soil layer of infinite lateral extend

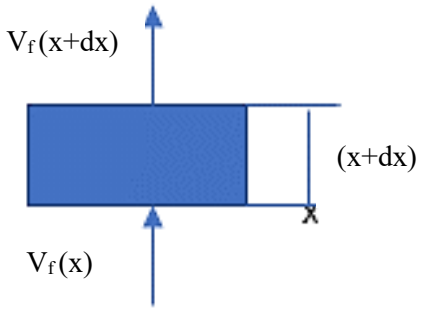


Figure 3.2 Soil element with boundaries fixed in space

Terzaghi considered a small soil element '*dx*' thickness, shown in Figure 3.1, of unit cross-sectional area normal to the direction of flow, from the layer shown in Figure 3.1, possessing fixed boundary coordinates' *x*' and '*x+dx*'. According to the law of conservation of mass, the net flow happening in the element must be balanced by the volume change in the element, which can be expressed as $net\ flow = -\frac{\partial V_f}{\partial x}$ where V_f is the flow velocity, and the rate of change of volume of the element is $\frac{\partial V}{\partial t}$ where V is the volume of water in this element. Therefore,

$$-\frac{\partial V_f}{\partial x} = \frac{\partial V}{\partial t} \tag{3.1}$$

Equation 3.1 is the continuity equation. However, this equation considers only fluid movement. As the fluid moves out, the solid particles also move relative to the fluid particles. Terzaghi ignores this relative movement. To couple the fluid flow to pore pressure, Darcy's law was used, which can be expressed as:

$$V_f = -\frac{k}{\gamma_f}\frac{\partial u}{\partial x} \tag{3.2}$$

TH-3534_186104002

Where k is the hydraulic conductivity coefficient, u is the excess pore water pressure, and γ_f is the unit weight of water. Here, the absolute velocity of water flow is taken, neglecting soil skeleton movement. However, the excess pore water pressure can be linked to the relative velocity, not the absolute velocity.

In a conventional consolidometer sample tested in a single drainage condition, the base is non-draining. At the non-draining surfaces, the gradient of excess pore water pressure is zero as there is no fluid flow or $V_f=0$. However, for a double-drained condition with drainage at the bottom, when consolidation gets started, the loading plate will move, and so will the water and soil particles near it without causing an excess pore pressure gradient. This goes against Equation 3.2. However, if we couple the excess pore pressure with the relative velocity between fluid and soil solids, in this case of bottom drainage, both soil and water will move in along with the cap, making their relative velocity zero.

The error due to this is introduced at each stage and depends on the strain. Therefore, in the case of infinitesimal strain, this is not observable. Gibson et al. (1967) pointed out that by combining equations 3.1 and 3.2 in the consequent step, the effect of this error gets cancelled out. That is

$$\frac{\partial V}{\partial t} = \frac{\partial}{\partial x}\left(\frac{k}{\rho_f}\frac{\partial u}{\partial x}\right) \tag{3.3}$$

Terzaghi postulated that the change in the volume of water is equal to the compressional strain in the element, which is applicable only in cases where the Lagrangian strain ($\Delta l/l_0$) is very small or negligible, which, in turn, is because the boundaries of the element are fixed in space. The coefficient of volume consolidation' m_v' is used to connect strain to effective stress. Assuming constant total stress, he reached the governing equation

$$\frac{\partial u}{\partial x} = c_v \frac{\partial^2 u}{\partial x^2} \tag{3.4}$$

Where the coefficient of consolidation can be expanded as $C_v = \frac{k}{\rho_f m_v}$ where 'k and m_v are assumed to be constants throughout the process of consolidation. However, the values of k and m_v are dependent on instantaneous void ratio values, which change as the consolidation progresses at each point within the layer.

TH-3534_186104002

Applying the governing Equation 3.4 to the soil layer, bound in space by $x=0$ and $x=h_0$ before the consolidation process, Terzaghi obtained a solution that satisfies this equation within fixed boundaries. However, these boundaries, in reality, can only be fixed if the strain is very small. In case of finite deformation, when consolidation progresses, the soil layer compresses, and the boundaries will move to accommodate the new volume of the soil layer. So, the solution should satisfy the moving boundaries, not the initial fixed boundaries.

The slurry materials like dredged clay slurries and mine tailings possess considerable specific gravity. Therefore, the self-weight of these materials becomes significant. The self-weight-imposed load contributes significantly to the strain on these materials during storage. Terzaghi's theory neglects this aspect, which results in underestimating consolidation characteristics.

The assumptions of Terzaghi's theory, therefore, limit the usage of the conventional consolidation theory for large-strain conditions

3.3 Finite Strain Consolidation Theory

Gibson et al. (1967) presented the finite strain consolidation theory to address the consolidation of thin clay layers in one dimension, considering finite strains and the variation of soil parameters during consolidation. Gibson et al. (1981) extended this framework to thick clay layers, focusing on the self-weight of the consolidating material. Given below is the governing differential equation

$$\left(\frac{\rho_s}{\rho_f}-1\right)\frac{d}{de}\left[\frac{k(e)}{1+e}\right]\frac{\partial e}{\partial z}+\frac{\partial}{\partial z}\left[\frac{k(e)}{\rho_f(1+e)}\frac{d\sigma'}{de}\frac{\partial e}{\partial z}\right]+\frac{\partial e}{\partial t}=0 \qquad (3.5)$$

In the above equation, ρ_s and ρ_f are the densities of the solid particles and pore fluid present in the slurry, respectively. The variable e stands for the void ratio, $\sigma'(e)$ and $k(e)$ are the compressibility and hydraulic conductivity functions. The space coordinate z is expressed in the material coordinate system.

The following modifications have been made to Terzaghi's assumptions :

- The theory does not restrict itself to small strains, hence enabling more accurate prediction of slurry behaviour when subjected to substantial load increments
- The coefficients of compressibility and hydraulic conductivity undergo variation throughout the process of consolidation. This takes into consideration alterations in the void

TH-3534_186104002

ratio and soil structure that occur during the process of consolidation. The compressibility and hydraulic conductivity are therefore considered as functions of void ratio

- A redefined Darcy's Law, based on the relative velocity between the solid and pore fluid particles, holds good
- The self-weight of the material undergoing consolidation is significant and is accounted for.
- The movement of the settling boundary during consolidation is incorporated by using the material coordinate

3.4 Coordinate Systems

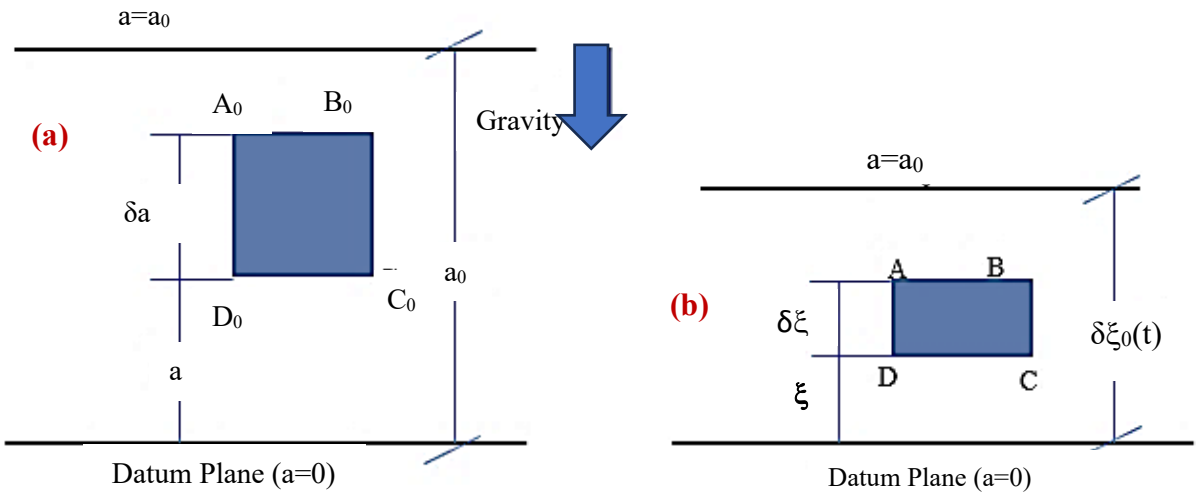


Figure. 3.3 Lagrangian and convective coordinate systems (a) Initial configuration at t=0 and (b) Configuration at time t >0

The Eulerian coordinate system is generally used in conditions where material deformations are related directly to planes fixed in space. For example, the excess pore pressure within a consolidating soft soil layer is measured at a point fixed with respect to a fixed datum. In the Eulerian coordinate system, a piezometer located at a point in the clay layer is denoted in space to a fixed datum. The distance from the datum to the piezometer is always taken to remain constant. This can be applied when the clay layer is thin and the compression involved is very small.

In the case of large strain consolidation, the deformations involved are large compared to the clay layer thickness, and hence, the Eulerian system cannot be used. For example, a piezometer that is fixed in space but near the clay layer boundary may be outside the layer after some

TH-3534_186104002

progress in consolidation. In this case, the convective coordinate system can be used. This is a real measuring system that moves along with the material particles. Therefore, the piezometer will always be surrounded by the same material points. It would measure the pore water pressure of that particular part of the skeleton, and it will be a function of time and the momentary position of the piezometer.

Consider a clay layer having an initial configuration, as given in Figure 3.3 (a) that is, before the consolidation starts. The lower boundary is considered to be fixed in space, for example, a rock layer beneath a soft clay layer. Within this layer, a thin layer $A_0B_0C_0D_0$ has a coordinate position' a' from the datum and has a thickness' $\delta a'$. $a=0$ at the bottom boundary while $a=a_0$ at the top boundary. The distance $'a'$ is the Lagrangian coordinate of the point concerned. Figure 3.3(b) shows the configuration of the clay layer as consolidation progresses. The datum plane is fixed while the top surface moves. This causes the sample to take up the new position *ABCD* at a distance $'\xi'$ which is a function of time. This distance is the convective coordinate. $'\xi'$ is a function of 'a' as well as time *'t'*. It is convenient to express the dependent variable, like excess pore pressure, in terms of the convective coordinate system. However, the dependence on time makes it mathematically inconvenient to use this system. However, the Lagrangian system coordinates $'a'$ is independent of time. So, it is easier to use. Therefore, the Eulerian system is fixed in space for the entire time of consolidation, and the Lagrangian system will refer all events to the initial configuration at $t=0$. Events that occur with time can be expressed in either Lagrangian $(a,1)$ or convective system (ξ, t)

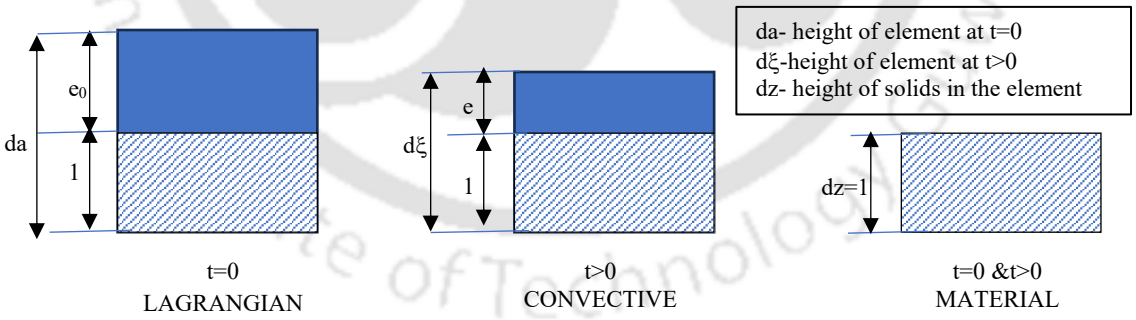


Figure. 3.4 Details of the coordinate systems involved

For simplification of the mathematics involved, another coordinate system that moves with the layer can also be used. In order to satisfy this condition, coordinates can be defined in terms of the volume of solid particles contained within the layer, which is independent of time. It remains a constant quantity throughout the consolidation process. The Lagrangian and Convective systems consider both pore fluid and soil solids in the layers. The material or reduced coordinates (Ortenbald, 1930) are suited for use in time-dependent consolidation. The

TH-3534_186104002

Lagrangian and material systems remain constant with time, making them more mathematically convenient for developing the governing equations.

Lagrangian System: This system considers the entire matrix of the consolidating slurry, including the solid and liquid particles, defined at the beginning of the process of consolidation, i.e., *t=0.* The Lagrangian system always starts at the initial boundary.

Convective System: This is a coordinate system used to describe the condition of a slurry at any time t >0, particularly useful when the flow itself affects the measured properties, which are the volume or height of the sample, pore pressure, void ratio, in this case. This system starts at the current solid-liquid boundary at any given point in time after the consolidation has started.

Material Coordinate System: This system is defined on the basis of the volume of solids, which is constant and independent of the time and strain values. In a fixed coordinate system, the datum is the solid-liquid boundary that moves continuously downwards with settlement. However, below this moving boundary, the volume of solids present in the sample does not change during consolidation.

The observed values of properties are in the convective system of coordinates, which in turn is a function of the Lagrangian coordinates, but the mathematical calculations are convenient in the material system or reduced system. Consider Figure 3.4 for deriving a relationship between these three coordinate systems. The material coordinate cannot be directly measured. Therefore, we can connect the same to the layer thickness at any time and the corresponding void ratio, assuming that the total volume of solids in the clay layer is unity. If 'e_0' is the initial void ratio, and 'e' is the void ratio at any time $t>0$,

$$da = 1 + e_0 \tag{3.6}$$

$$d\xi = 1 + e \tag{3.7}$$

$$dz = 1 \tag{3.8}$$

In order to transfer from one coordinate system to the other, the following relations can be used.

$$\frac{da}{d\xi} = \frac{1 + e_0}{1 + e} \tag{3.9}$$

$$\frac{d\xi}{dz} = 1 + e \tag{3.10}$$

$$\frac{dz}{da} = \frac{1}{1 + e_0} \tag{3.11}$$

TH-3534_186104002

$$\xi = \int_0^z \big(1 + e(z, t)\big) dz \tag{3.12}$$

Thus, the coordinate systems can be converted to one another through a simple integration.

2.5 Settling column test

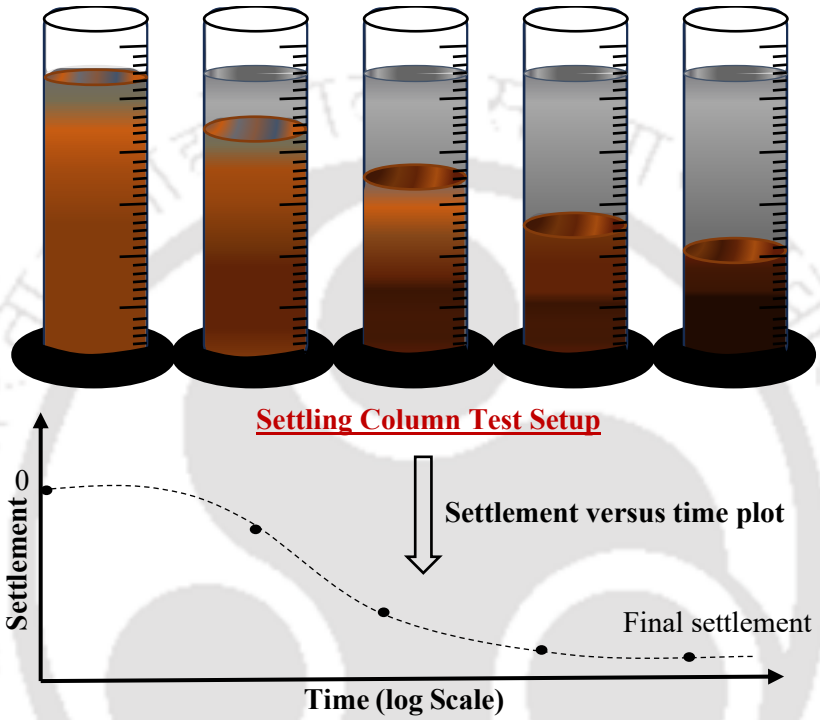


Figure 3.5 Illustration of simple settling column test

The simple settling column test is often customised to study the solids' density profile and base pore pressure (Been, 1980; Been & Sills, 1981). The slurry sample is thoroughly mixed with no chance of segregation under self-weight and poured into long cylindrical columns, as shown in Figure 3.5. Initially, the void ratio profile of the sample is generally assumed to be uniform. Generally, this setup simulates a single drainage condition with an impermeable boundary at the bottom and free drainage at the top unless customised otherwise. Even though the sample can initially undergo sedimentation in some cases, eventually, the particles come in contact with each other, triggering effective stress development, and the solid-liquid boundary is observed to move downwards with time. Under the influence of self-weight, the slurry slowly drains and settles, resulting in excess pore pressure reduction at different locations, which can be monitored using pore pressure transducers.

TH-3534_186104002

3.6 Centrifuge modelling

Centrifuge modelling is an advanced experimental method employed in geotechnical engineering to investigate the performance of soils and soil-structure systems under simulated gravity conditions. This technique involves placing a reduced-scale physical replica of a geotechnical structure inside a centrifuge and subsequently rotating it at high velocities. The resultant centrifugal force acting outwards simulates an artificial gravitational field, allowing the scaled model to experience stresses comparable to that a full-scale prototype would be subjected to in the field (Taylor, 2005).

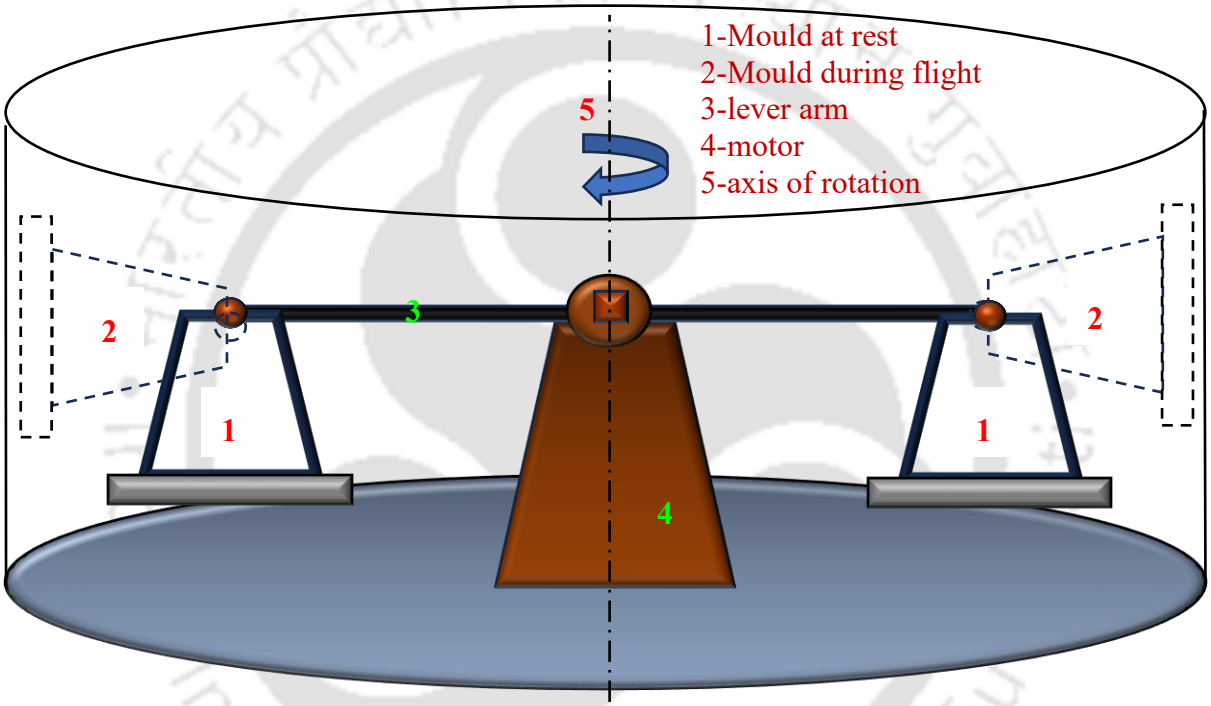


Figure 3.6 Illustration of a geotechnical centrifuge and its important parts

Centrifuge testing is most suited for geotechnical projects where gravity plays a significant role, such as retaining structures, natural and man-made slopes, underground excavation, buried structures, groundwater contaminant migration, and self-weight consolidation. The mechanical characteristics of soil are non-linear and depend on both effective stress and stress history. Therefore, it is crucial to maintain consistent stress levels in model testing and prototypes. The unit weight and thickness of a soil deposit determine the self-weight stress in the soil. In a centrifuge model test, the equivalent stress in a prototype and a model is attained by reducing the thickness of the deposit and increasing the unit weight of the specimen. In model experiments, the unit weight of soil can be enhanced by either increasing the density of

TH-3534_186104002

the soil or the gravitational acceleration level. So as to accurately replicate the behaviour of a real-field scenario, objective model tests employ materials with similar properties to those found in the field. This includes using materials with the same density in both the models and prototypes. To reach the same unit weight in the model, the gravitational acceleration is increased. Gravitational acceleration can be augmented by inducing the rotation of the sample in a horizontal plane using a centrifuge. The purpose of using a centrifuge is to artificially amplify the gravitational force in the model by rotating the sample on a nearly horizontal plane. The general setup of a drum centrifuge is illustrated in Figure 3.6.

3.6.1 Scaling laws in centrifuge modelling

For a centrifuge, the basic scaling law is supposed to ensure the stress similarity between the prototype and the corresponding model. Vertical stress at depth h_m in the model measured from the top of the model and h_p in prototype, if an acceleration *N* times g is applied on a material of density ρ is given for the model as:

$$\sigma_{vm} = \rho h_m N g \tag{3.13}$$

For prototype:

$$\sigma_{vp} = \rho h_p g \tag{3.14}$$

Therefore, for the stress to be equal $\sigma_{vp} = \sigma_{vm}$ which means $h_m = \frac{h_p}{N}$, making the scale factor for linear dimensions *1: N*. The other important scaling relationships are given in Table 3.1.

Table 3.1 Scaling of various parameters in centrifuge models (Sorta, 2015)

Quantity	Model	Prototype
Length	1	N
Acceleration	N	1
Stress	1	1
Strain	1	1
Mass density	1	1
Consolidation time	1	N^2
Mass	1	N^3
Velocity	N	1

TH-3534_186104002

3.6.2 Concept of effective radius

The experiments in a centrifuge complete faster than other methods but the observations from the same cannot be directly applied in the field. The appropriate scale factor scales the centrifuge observations to represent the field observation. However, the sample in a centrifuge field is observed to undergo linear variation in the acceleration scale factor from top to bottom of the sample, as shown in Figure 3.7. This variation is disregarded for simplicity in most cases by assuming a constant scale factor value. However, this neglect can cause a mismatch in field observations and scaled centrifuge observations.

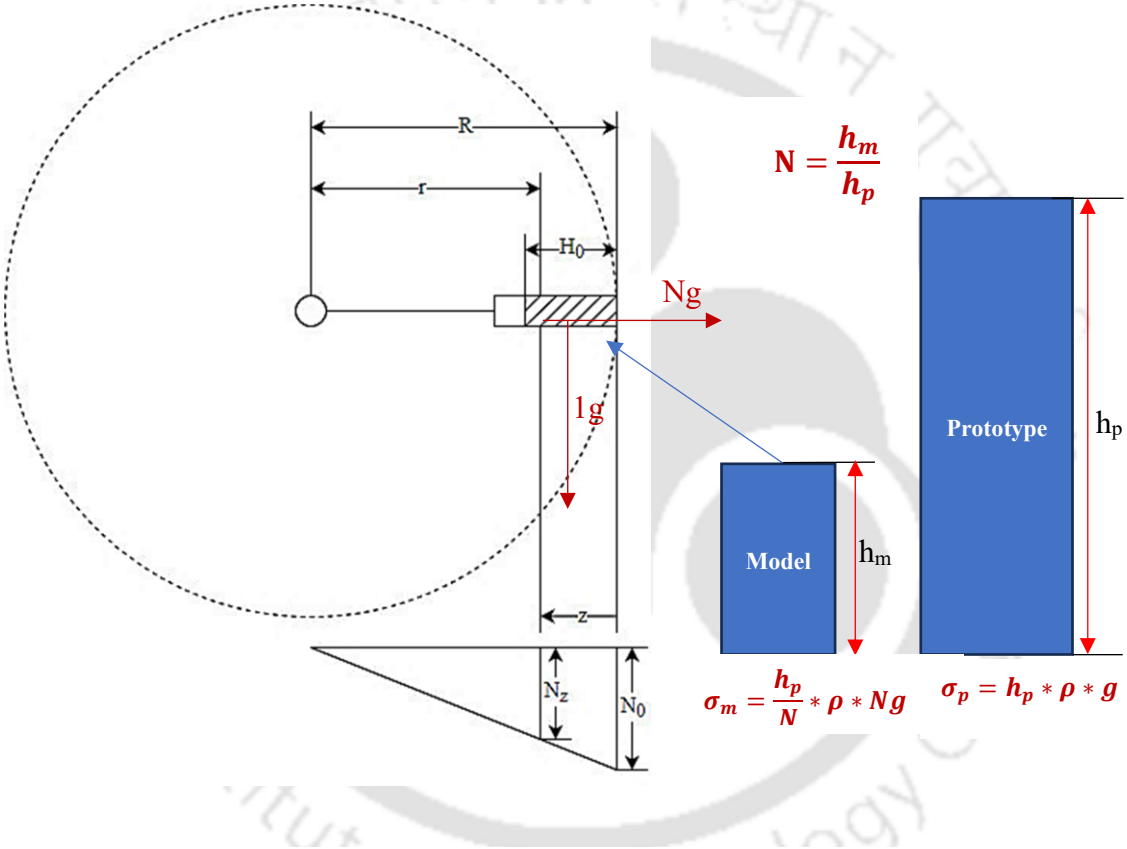


Figure 3.7 Variation of acceleration scale factor with depth on centrifuge model and the stress at the base of the sample

A small error in the prediction of settlement in the model can lead to a difference of a huge volume of material in the mine tailings storage facilities due to the large area of land these facilities cover.

Another reason for the discrepancies is that the acceleration field produced in the centrifuge results in a non-linear stress distribution in the sample, unlike the field condition, where the same is linear. The value of the Earth's gravity 'g' is constant throughout the depth of the

TH-3534_186104002

prototype. However, the centrifugal acceleration that appears on the model is a function of the radius of rotation, as shown in Figure 3.7.

$$inertial\ acceleration\ field = \omega^2 r \tag{3.15}$$

The stress variation caused in the model due to this in comparison to the stress experienced by the prototype is shown in Figure 3.8. (non-linear variation in stress in the model is given exaggerated for clarity) According to Taylor (1995), this variation can be overcome by selecting a radius called an effective centrifuge radius at which the *N* value can be calculated such that it can be kept constant for the entire depth.

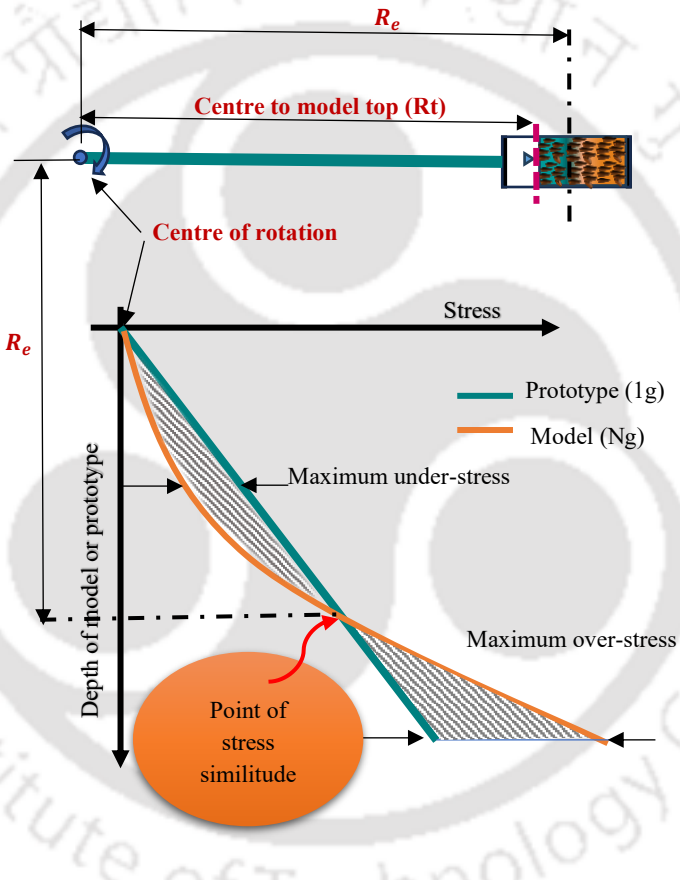


Figure 3.8 Comparison of stress distribution in the field and in a centrifuge

Vertical stress at depth h_p in a prototype which is equal to 'Nh_m *'is* given as:

$$\sigma_{vp} = \rho h_p g = \rho(Nh_m)g \tag{3.16}$$

The effective centrifuge radius 'R_e' for the model is defined as

$$Ng = \omega^2 R_e \tag{3.17}$$

TH-3534_186104002

Vertical stress, a depth' z' from the top in the model, if 'R_t' is the radius from the centre of the centrifuge to the top of the sample, is given as

$$\sigma_{vm} = \int_0^z \rho\omega^2(z + R_t)dz = \rho\omega^2 z\left(R_t + \frac{z}{2}\right) \quad (3.18)$$

Let the vertical stress at z=hi become equal in the model and prototype, then from the above equations. $$R_e = R_t + 0.5h_i \quad (3.19)$$

The relative magnitude of under and overstress is considered to minimise the error in stress. The under stress at any depth 'h' is given as

$$\sigma_{vp} - \sigma_{vm} = \rho gNh - \rho\omega^2 h\left(R_t + \frac{h}{2}\right) \quad (3.20)$$

Maximum under stress occurs at a depth $h_i/2$ according to equation 3.20.

$$r_u = \frac{maximum\ understress}{prototype\ stress\ at\ that\ height} = \frac{0.5h_i\rho gN - 0.5h_i\rho\omega^2\left(R_t + \frac{0.5h_i}{2}\right)}{0.5h_i\rho gN} = \frac{h_i}{4R_e} \quad (3.21)$$

Similarly for overstress $r_o = \frac{h_m - h_i}{2Re}$ (3.22)

The over-stress must eventually balance the under-stress. Therefore, $r_0 = r_u$.. Therefore,

$$h_i = \left(\frac{2}{3}\right)h_m \ and\ r_u = r_o = \frac{h_m}{6R_e} \quad (3.23)$$

Connecting to equation 2.20, we get

$$R_e = R_t + \frac{h_m}{3} \quad (3.24)$$

Equation 3.24 suggests that there is exact correspondence in the vertical stress between the prototype and the model at two-thirds of the model depth. The effective centrifuge radius R_e has to be measured at a depth of one-third of the sample from the central axis. Equation 3.23 gives the maximum error in stress. These factors need to be given due consideration to ensure appropriate scaling of stress values while comparing the prototype and centrifuge behaviour.

The effective radius values have been defined by other researchers as given in Table 3.2. Consolidation operations are usually modelled numerically using a single acceleration value for the whole soil profile. Although it is not possible to achieve such a scenario in every centrifuge, it is regarded as acceptable to assume a single acceleration value as long as the variance in acceleration across the model is less than 22% (Celorie et al., 1989). This limitation

TH-3534_186104002

can easily be satisfied on beam centrifuges. However, the acceleration variation across the sample in desk-top centrifuges is beyond the appropriate range.

Table 3.2 Definitions of effective radius values

Base	$R_e = R$
Mid-Height (Fox et al., 2005)	$R_e = R - H_m + \frac{H_m}{2}$
Cooke (1991)	$R_e = R - H_m + 0.41 * H_m$
Schofield (1982) and Taylor (1995)	$R_e = R - H_m + \frac{H_m}{3}$
$\boldsymbol{Effective\ Scale\ Factor\ N_e = R_e * \frac{\omega^2}{g}}$	

3.6.3 Finite Strain Consolidation Theory for Centrifuge Environment

Bharat and Ubaid (2019) introduced an analytical model for the one-dimensional settlement behaviour of soft soils in a finite strain framework. The soil self-weight, relative velocities of the solid and liquid phases, varying soil compressibility and hydraulic conductivity, and acceleration factor variation along the length of the specimen were all incorporated into the model. The analytical model assumed the validity of Darcy's law and followed the mass and momentum conservation laws. The governing equation given below forms the *Ng* equivalent to Gibson's model (1981) for 1g FSC

$$\left(\frac{\gamma_s}{\gamma_w} - 1\right)\left[N_z^2 \lambda(e)\ \frac{\partial e}{\partial z} - 2\alpha N_z k(e)\right] + \frac{\partial}{\partial z}\left[\frac{N_z}{\gamma_w}\phi(e)\frac{\partial e}{\partial z}\right] + N_z \frac{\partial e}{\partial t} = 0 \qquad (3.25)$$

where γ_w is the unit weight of water (9.81 kN/m^3) and γ_s is the unit weight (kN/m^3) of the solids, z is the space coordinate in the material coordinate system. The N_z is the scale factor at any point in the sample, which is given as

$$N_z = N_0 - \alpha \int_0^z [e(z,t) + 1]dz \qquad (3.26)$$

where N_0 is the scale factor value at the base of the sample as given by $N_0 = R\omega^2/g$, and $\alpha = \omega^2/g$. In these expressions R is the centrifuge radius and ω is the angular velocity. The $\lambda(e)$ and $\phi(e)$ in equation 3.27 and 3.28 are given by

TH-3534_186104002

$$\lambda(e) = \frac{d}{de}\left[\frac{k(e)}{1+e}\right] \tag{3.27}$$

$$\phi(e) = \frac{k(e)}{1+e}\frac{d\sigma'}{de} \tag{3.28}$$

The *k(e)* represents the permeability function and *σ'(e)* is the compressibility function.

In the next chapter, the theoretical concepts introduced here, such as consolidation theories and centrifuge modeling, are applied to the slurry materials studied. It will provide a detailed overview of the material properties, experimental methodologies, and numerical approaches used to investigate the FSC behavior of these materials.

TH-3534_186104002

4. Materials and Methodology

4.1 General

This chapter offers a comprehensive overview of the relevant properties of the slurry materials used in the experimental analysis described in this study. The FSC behaviour of a few sediments and tailings slurries sourced from various literature were incorporated in this study. The material properties of these slurries were discussed in detail. Furthermore, this chapter elaborates on the various experimental, numerical, and graphical methodologies adopted in this study.

4.2 Materials

4.2.1 General

In this section, the materials considered for the present study were elaborated. Broadly, the present study can be divided into four sections. The first section involves an experimental study on slurry materials, and the second is a numerical study on slurries in 1g condition based on settlement data. The third section is a numerical study on slurries using *Ng* condition settlement data. In the fourth section, pore pressure data from 1g and *N*g conditions from the literature were used. The important properties of these materials are explained in this section.

4.2.2 Materials Used for Experimental Study

In **Chapter 5**, four different soils, namely, black cotton soil from Jamnagar, Gujarat (BCS), locally sourced Laterite soil (RS), black cotton soil from Jabalpur, Madhya Pradesh (MBC), and commercially procured Kaolin (Kao-I) without any pretreatment, were used (shown in Figure 4.1(a-d)).

Table 4.1 Characteristics of slurries used for experimental study

S.no	Material	Name	Specific Gravity (G_s)	Liquid Limit (LL%)	Plastic Limit (PL%) *
1	Black Cotton Soil-1	BCS	2.67	106	48
2	Red Soil	RS	2.67	42	20
3	Black Cotton Soil-2	MBC	2.65	84	38
4	Kaolinite	Kao-I	2.62	40	32

***** Das (2022)

The BCS was darker in colour than MBC and differed in the liquid and plastic limits. A brownish-red hue distinguished laterite red soil, while the kaolinite sample was white. The soil

TH-3534_186104002

particles passing the 425-micron sieve were taken for all the tests. The specific gravity (G_s) was determined using the pycnometer method (IS 2720-Part 3-1980) for the soils. An average of three tests for each soil was reported. The Liquid Limit (LL) of the soils was determined manually using the Casagrande apparatus, using the standard procedure (IS 2720-5-1985). The relevant properties of these soils are reported in Table 4.1.

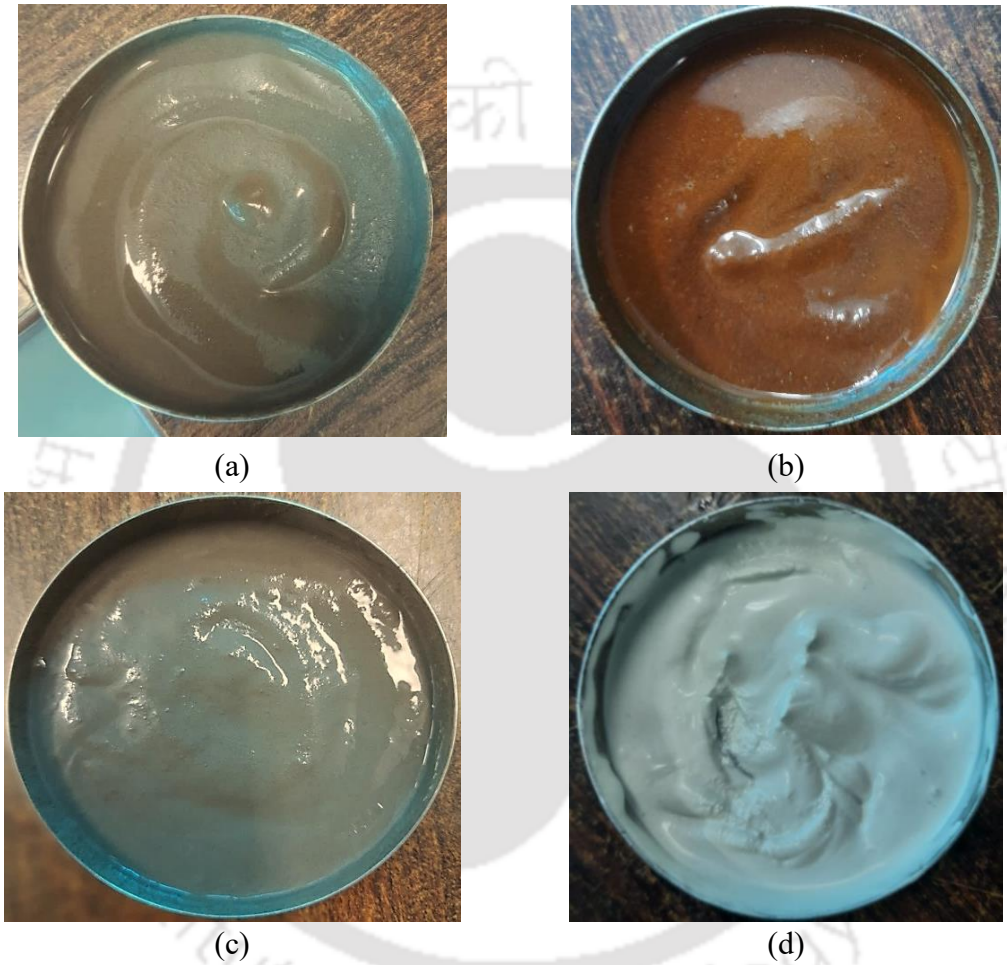


*Figure 4.1. Samples used in the oedometer test in **Chapter 5** (a) BCS (b) RS (c) MBC (d) Kao-I*

4.2.3 Materials considered from past studies

The slurry materials considered in this study differ by their sources, mineralogy, and the process involved in their production. Consequently, their compressibility, hydraulic characteristics and specific gravity are observed to vary for these materials, leading to their unique finite strain consolidation behaviour. The FSC behaviour of eight mine tailings and seven dredged slurries

TH-3534_186104002

reported in various literature were considered for the development and validation of the inverse analysis models discussed in this study.

The study considers the FSC behaviour of slurries under standard *1g* and centrifuge (*Ng*) gravity conditions. Properties of certain materials were used to generate synthetic FSC behaviour to test various procedures proposed in this study. These approaches were further validated using literature data. The compressibility and hydraulic conductivity function for power form and modified power form were fitted to experimental data from various literature studies and are presented below in Tables 4.2 and 4.3.

4.2.3.1 Literature Data used for 1g condition

The settlement data from 1g FSC tests were used in **Chapter 8** of this study. The constitutive relations were used in **Chapter 6** for numerical simulations. The experimental pore pressure dissipation data were used in **Chapter 10**.

The settlement behaviour from the tank test described in McVey et al. (1986), under a small surcharge load of 0.224 kPa, was taken as input along with the properties in Table 4.2. McVey et al. (1986) studied the settlement of phosphatic clay from the International Minerals and Chemicals Co. Kingsford Mine, Florida (Phosphatic Clay). Somogyi et al. (1984) derived the constitutive functions of the Phosphatic clay by conducting field and laboratory experiments. Somogyi et al. (1984) conducted the constant rate of deformation test (CRD) and incremental loading or stress-controlled slurry consolidometer test to obtain the effective stress versus void ratio relationship. Constant head permeability tests were conducted after each load increment in the stress-controlled slurry consolidometer test to measure the hydraulic conductivity. The hydraulic conductivity function was estimated after the CRD test using an analytical method proposed by Znidarcic and Schiffman (1981). The field test for compressibility function involved the determination of solid contents and the excess pore fluid pressure at various depths within the consolidating slurry. The field permeability was measured by conducting rising head tests using a permeability probe. The engineering approximations for the best-fit functions, given by Somogyi et al. (1984), were used in the current study for simulation and comparison.

The second experimental data for the 1g condition considered in this study was taken from the work of Soleimani et al. (2014) on polymer-amended mature fine tailings (PA-MFT). Settlement versus time data from the settling column test with top-drainage was taken as input, along with the compressibility function obtained from the multi-step loading test and other relevant properties in Table 4.2.

TH-3534_186104002

Bartholomuseen et al. (2002) conducted an elaborate prediction exercise on dredged slurry from the river Scheldt in the Antwerp province of Belgium (Antwerpen Slurry). They used four calibration test data to predict the self-weight consolidation observations of a fifth experiment. Top-drained settling column test data from one of the calibration tests (Sidc2) and the pore data measured using ports connected to pressure transducers for another calibration test (Sidc6) (named in this study as AS-2) were used in the present study as input. The compressibility function was estimated from the density profiles and pore pressure profiles. The predicted hydraulic conductivity function was compared with the same estimated indirectly by Bartholomuseen et al. (2002) using Darcy-Garsevanov's Equation from the density profiles and excess pore pressure data.

The excess pore pressure data for thickened gold tailings (Gold Tailings) were taken from the work of Bonin et al. (2014). Gold Tailings slurry consisted mainly of silt-sized particles with less than 11% clay-sized particles. Bonin et al. (2014) conducted the settling column test, draining at the top, on Gold Tailings. The total pore pressure dissipation monitoring at three locations, including the bottom of the column, was carried out using LMP 331 BD Sensors attached to the settling column wall. The excess pore pressure was estimated from this pore pressure transmitter data by subtracting the hydrostatic pressure. The optimized hydraulic conductivity function retained for the simulations used in Bonin et al. (2013) was used for comparison in the present work.

4.2.3.2 Literature Data used for Ng condition

The settlement data from centrifuge tests were used in **Chapter 6, Chapter 7**, and **Chapter 9** of this study. The experimental pore pressure dissipation data were used in **Chapter 10**. Various literature-derived constitutive function coefficients were used for comparison and validation purposes in this study. The temporal settlement data from self-weight consolidation tests conducted in a centrifuge environment were available for the cases of Singapore Marine Clay (SMC) (Robinson et al., 2003), Albian flocculated oil sand tailings (AL15), Edgar Plastic Kaolin clay (Kaolinite) slurry and flocculated thickened tailings with 50% fines (TT50) (Sorta et al., 2015). The hydraulic conductivity versus void ratio relationship of SMC was derived by conducting a falling head test at various stress increments, while its compressibility relationship was obtained from oedometer consolidation test data. For Kaolinite slurry and TT50, the effective stress versus void ratio relations were derived based on the water content profile at the end of self-weight consolidation, using a modified Large Strain Consolidation Test (LSCT) setup. For AL15, this relation was derived from the centrifuge test data. Hydraulic conductivity

TH-3534_186104002

relations for AL15, TT50, and Kaolinite were derived using beam centrifuge tests modified to monitor the inflight pore pressure, density, and solids content profile. Sorta (2015) estimated the permeability values for Kaolinite, TT50, and AL15 using observations from beam centrifuge tests. The models were divided into five equal sections. At the material nodes of these sections, the void ratio values were estimated from the solids content profiles monitored at the sections using a Time Domain Reflectometer (TDR). The pore pressure profiles at different times were recorded using pore pressure transducers. By applying generalized Darcy's law, materials system of coordinates, and the continuity principle, hydraulic conductivities at various nodal points were estimated using the equation $k = v/i$, where k is the hydraulic conductivity, v is assumed as the velocity of settling solids, and i is the hydraulic gradient. While computing the hydraulic conductivity using the aforementioned equation, the individual solid particle velocity was approximated as the shift in the placement of material nodes divided by the time taken for the shift. The hydraulic gradient was estimated from the pore pressure data for a point near the mid-depth of the model, as the pore pressure transducers are fixed in the model, and the material nodes are continuously shifting. The hydraulic conductivity at various material nodes for various void ratios was plotted.

Experimental data from the base pore pressure dissipation measured at various times steps in a Clements Orbital-420 benchtop centrifuge was available for a sample of Kaolinite slurry (Kao-III) (Reid et al., 2012). The compressibility function of this material reported in the literature was determined by using Rowe cells, and the hydraulic conductivity function was derived using a constant head test conducted at each load increment in Rowe cells.

The relevant material properties of the slurries studied under the centrifuge environment are given in Table 4.3.

4.2.3.3 Generation of Synthetic Data

For a set of slurries for which experimental data in 1g or Ng condition is not available, the FSC behaviour data were generated from the numerical analysis of the corresponding FSC governing differential equation. These are continuous plots with closely spaced discrete points. To use these data for representing experimentally measured data, a maximum of 5 per cent white noise was added to the simulated data, and some data points were arbitrarily selected from it to represent corresponding curves, that, i.e. either pore pressure dissipation curve or settlement versus time curve.

TH-3534_186104002

Table 4.2. Properties of various slurries considered in the present study used for testing and validation in 1g environment

Material	Specific Gravity	Liquid Limit (%)	Plastic Limit (%)	Hydraulic Conductivity Function Parameters		Compressibility Function Parameters			Initial Void Ratio	Initial Height (m)	Reference
				M (m/s)	P	A (1/kPa)	B (kPa)	C			
MFT 5*	2.65	-	-	2.50E-11	3.39	3.27	0.074	-0.195	6	0.2	Znidarcic et al. (2011)
MFT 6*	2.65	-	-	1.60E-11	3.71	3.2	0.007	-0.169	4	0.2	Znidarcic et al. (2011)
Rutgers*	2.58	120	87	2.00E-11	6	2.859	0.135	-0.209	4.89	0.5	Janbaz and Maher (2017)
Phosphatic clay**	2.71	230	155	1.40E-11	4.11	12.19	0	-0.29	18.81	6.33	McVey et al.(1986)
PA-MFT	2.12	80	45	5.36E-10	8.233	1.99	0.111	-0.318	4	0.5	Soleimani et al. (2014)
Antwerpen slurry**	2.72	39	28	1.68E-09	8.257	1.41	0.006	-0.085	2.17	0.215	Barthelomuseen et al. (2002)
Gold Tailings	2.76	29	25	3.50E-07	3.3	1.03	0	-0.047	1.3	0.3	Bonin et al.(2014)
AS-2	2.72	39	28	5.07E-08	4.5	1.69	0.046	-0.12	2.53	0.592	Barthelomuseen et al. (2002)

* Synthetic Data Cases for settlement and ** Experimental case for settlement, Synthetic Case for pore pressure Note: The compressibility and hydraulic conductivity function coefficients given in Table 4.2 and 4.3 are either available as such in the literature or based on fitting of curves to the experimental data points available

TH-3534_186104002

Table 4.3 Properties of various slurries considered in the present study used for testing and validation in centrifuge environment

Material	Specific Gravity (G_s)	Liquid Limit (%)	Plastic Limit (%)	Compressibility Function Parameters*			Hydraulic Conductivity Function Parameters*		Initial Void Raito (e_o)	Initial Height (m)	Radius (m)	Omega (rad/s)	N_0	Reference
				A (1/kPa)	B (kPa)	C	M (m/s)	P						
Rutgers*	2.58	120	87	2.89	0.135	-0.209	2.00E-11	6	4.89	0.15	1.8	23.874	104.6	Janbaz & Maher (2017)
MFT 5*	2.65	-	-	3.2	0.007	-0.169	1.60E-11	3.7	6	0.02	0.15	104.76	167.8	Znidarcic et al (2011)
MFT 6*	2.65	-	-	3.27	0.074	-0.195	2.40E-11	3.4	6	0.019	0.1274	99.98	129.8	Znidarcic et al (2011)
OFT*	2.73	27	19	1.67	0.006	-0.127	4.62E-08	3.06	3.21	0.1	1.8	23.874	104.6	Agapito & Bareither (2018)
TT 60**	2.65	30	17	1.198	0.101	-0.25	2.24E-09	3.42	1.66	0.1219	1.95	21.278	90	Sorta (2015)
Kaolinite**	2.65	52	31	3.165	0	-0.21	1.70E-09	4.01	3.41	0.125	1.95	20.061	80	Sorta (2015)
TT 50	2.65	26	16	1.534	0	-0.162	2.00E-09	3.55	1.7	0.119	1.95	22.429	100	Sorta (2015)
AL15	2.6	40	22	3.091	0	-0.255	6.00E-10	3.35	2.91	0.135	1.95	17.373	60	Sorta (2015)
SMC	2.65	83	32	3.187	0.642	-0.178	8.83E-12	5.99	3.26	0.26	1.8	23.87	104.5	Robinson et al., (2003)
Kao-III	2.58	61	27	2.61	1	-0.15	5.00E-10	4.61	2.58	0.083	0.1696	146.67	371.89	Reid et al (2012)

* Synthetic Data Cases for settlement and ** Experimental case for settlement, Synthetic Case for pore pressure

TH-3534_186104002

The data were generated using MATLAB codes for the numerical solution of the governing differential equations for FSC in *1g* and *Ng* conditions. The values of initial void ratio, specific gravity, and initial depth, which are not available in the literature, were assumed appropriately to ensure the fast running of the MATLAB codes.

Matured fine tailings of oil sands (MFT 5 and MFT 6) were studied by Znidarˇci'c et al. (2011), and Janbaz and Maher, 2017 worked on the sediment from Newark Bay (Rutgers).

The hydraulic conductivity and compressibility functions of these materials were established using the seepage-induced consolidation tests (SICT) in the corresponding literature. These functions were used to simulate the settlement data for **Chapter 7, Chapter 8,** and **Chapter 9**. The constitutive function parameters provided by Agapito and Bareither (2018) were used for the simulation of the FSC behaviour of finer fractions of copper mine tailings called overflow tailings (OFT) in **Chapter 7**. The relevant properties of these materials given in Table 4.2 and Table 4.3 were used to generate synthetic settlement data used in this study. Two sets of synthetic data points were generated by adding white noise to the excess pore pressure dissipation data simulated for Antwerpen Slurry and Phosphatic Clay samples in **Chapter 10**. The properties of AL15 and TT50, given in Table 4.3, were used to simulate synthetic pore pressure data from centrifuge tests used in **Chapter 10.**

4.3 Experimental Methods

4.3.1 General

The FSC behaviour of four slurries shown in section 4.2.2 was explored using a conventional oedometer and a benchtop centrifuge. This section describes the procedure involved in the sample preparation and undertaking of experiments in detail. The challenges and limitations are also discussed.

4.3.2 Oedometer Test

Four samples of soil slurry were subjected to conventional one-way drainage oedometer experiments in one dimension, as specified in IS-2720 part 15-1986, in order to ascertain the rate of settlement. The set up used was as shown in Figure 4.2. The oedometer experiment data were utilized to estimate additional properties, including the coefficient of compressibility (a_v), compression index (c_c), volumetric compressibility (m_v), coefficient of consolidation (c_v), and hydraulic conductivity (k) at each load level. As a result of the high moisture content of the soil sample that was placed into the consolidation ring, it was susceptible to finite strains during

TH-3534_186104002

settlement. The porous stones were positioned horizontally above the soil specimen to enable a consistent distribution of load over it. The oven-dry technique was used to determine the water content. Distilled water was used to fill the consolidation cell over the whole duration of the test. Although a small sample size is used, this study is time-consuming, taking around 35 to 40 days to conduct a single experiment.



Figure 4.2 Oedometer set up at IIT Guwahati

4.3.2.1 Sample Preparation

The sample preparation was done such that the materials behaved like a slurry and yet were relatively convenient to handle and load. Oven-dried soil sieved through 425 microns was used since the process of consolidation is affected mainly by the fine particles. Sufficient distilled water was added to attain a moisture content equivalent to the liquid limit value. It is to be noted that this was the approximate moisture content at which the sample in centrifuge mould existed after the sedimentation phase was completed. This moisture content results in the initial void ratio of the oedometer samples being within the range of the centrifuge samples. The slurry sample was mixed thoroughly and stored in a desiccator for 48 hours to ensure a uniform distribution of water. After 48 hours the sample was ready to be tested. The consolidation ring had a diameter of 60 mm and a height of 20 mm. Silicone grease was used to lubricate the inside of the rings in order to reduce side friction between the clay specimen and the rings. At the top and bottom of the ring, saturated porous stones were positioned, along with filter papers, to prevent the fine particles from blocking the pores of the stone. The ring was filled with the slurry sample, reaching a height of roughly 10mm in each case.

TH-3534_186104002

4.3.2.2 Loading

In order to avoid the expulsion of samples under sudden loading, the loads were applied as gradually as possible. The test started at a load of 5 kilopascals (kPa). The deflection in the dial gauge was recorded throughout. The process was repeated with heavier loads, and at each load, the material was allowed to settle completely. The load rising pattern was as follows: 5 kPa, 10 kPa, 20 kPa, 50 kPa, 100 kPa, 200 kPa, and 400 kPa. Further, the loads were released progressively. The consolidation parameters were estimated by determining the final water content, void ratio, and solid mass.

4.3.2.3 Estimation of Consolidation Parameters

The oedometer test follows the conventional theory of consolidation. Various parameters were computed based on Terzaghi's theory after the completion of the test. The following relation was used to estimate the void ratio from the final moisture content.

$$e = \frac{wGs}{s} \tag{4.1}$$

Where w is the moisture content, e is the void ratio, s is the degree of saturation, which is 1 for consolidation, and Gs is the specific gravity of the material. At each loading step, the variation in void ratio (Δe) corresponding to the compression (Δh) was back-calculated by the equation

$$\Delta e = \Delta h \frac{(1 + e_0)}{h_f} \tag{4.2}$$

In the above equation h_f is the final sample height. The effective stress-void ratio relationship was plotted based on the void ratio values at each load step. At the final stage of consolidation, the excess pore pressure is fully dissipated, which results in effective stress equal to applied stress. The coefficient of compressibility (a_v), which is the decrease in the void ratio of slurry per unit increment in the effective stress, was determined using equation 4.3

$$a_v = \frac{\Delta e}{\Delta \sigma} \tag{4.3}$$

The compression index (c_c) was calculated from the semi-log scale plot of the effective stress-void ratio relation using equation 4.4 and the volumetric compressibility (m_v), using equation 4.5.

$$c_c = \frac{\Delta e}{\log(\Delta \sigma)} \tag{4.4}$$

TH-3534_186104002

$$m_v = \frac{a_v}{(1 + e_o)} \tag{4.5}$$

The coefficient of consolidation (c_v) representing the soil sample's settlement rate is determined using the square root of time approach and log-t method, and an average was reported. The equation to determine c_v is given as:

$$c_v = \frac{T_v d^2}{t} \tag{4.6}$$

Where T_v is the time factor, d is the drainage path length, and t is the time. Theoretically, the hydraulic conductivity (k) was determined at each load step using equation (4.7).

$$k = c_v * m_v * \Upsilon_w \tag{4.7}$$

where, Υ_w is the unit weight of water.

4.3.3 Benchtop Centrifuge Test

Conventional FSC testing is slow and tedious and takes multiple weeks to complete. The presence of plastic fines further increases the time required. The availability of the conventional FSC apparatus such as Rowe cell, slurry consolidometer, seepage induced consolidation test set up, etc, are limited. The limited availability of appropriate devices, in conjunction with the growing demand for consolidation testing of slurries, can lead to substantial delays in project schedules. The consequence of this is that consolidation testing frequently becomes a component of the critical path for a design project. In comparison to the prototype, the model within the centrifuge exhibits significantly shorter drainage path lengths and a greater pore pressure gradient. Thus, the model's consolidation proceeds at a significantly faster pace than that of the equivalent prototype (Schofield, 1980; Wood, 2004).

4.3.3.1 Sample Preparation

A known weight of oven-dried samples passing through the 425 micros sieve was mixed thoroughly with appropriate moisture content (to result in a final moisture content approximately equal to the liquid limit which is 106% for BCS, 42% for RS, 84% for MBC, around 80% for Kao-I due to difficulty in sample preparation at liquid limit) so that the slurry concentration could be handled in odometer test conditions as well (for all cases except Kao-I). This moisture content was arrived at through a number of trials. An equal amount of dry sample with distilled water was prepared in two conical flasks (Figure 4.3 (a)), placed in a shaker, and thoroughly mixed for thirty minutes to one hour. Once the samples are mixed well,

TH-3534_186104002

the slurry is transferred to two transparent acrylic centrifuge moulds. The sample is transferred carefully so that there is no loss of material and that the weight of solids used in preparing the sample remains a known quantity. These slurries were then allowed to undergo sedimentation for a fixed time, depending on the material. The moulds have to be of equal weight to ensure the centrifuge balances while rotating

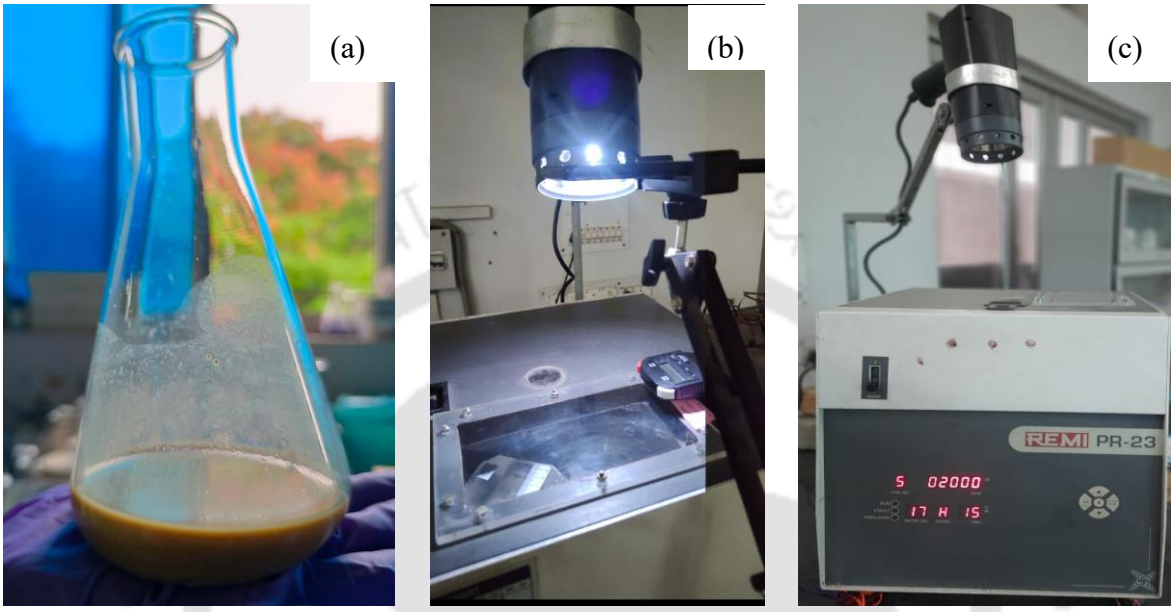


Figure 4.3: (a) conical flask of slurry prepared for mixing in the shaker (b) top-view of the centrifuge set up (c) the centrifuge experimental set up.

4.3.3.2 Preliminary testing

In order to compare the test results from centrifuge tests with the oedometer test results, the initial void ratio for the samples needs to be fixed. A number of trial tests were conducted at different initial solid and water contents, and the post-sedimentation void ratio in the centrifuge moulds was noted. At the threshold void ratio, the self-weight consolidation starts. The oedometer samples were prepared at the moisture content corresponding to this void ratio, such that the initial void ratio for the slurries in the oedometer can be brought within the range of the initial void ratios of samples tested in the centrifuge.

4.3.3.3 Centrifuge test:

The experiment utilised a REMI-PR 23 benchtop centrifuge (Figure 4.3 (b and c))) along with two transparent acrylic moulds. These moulds had an inner diameter of 35 mm and a height of 90 mm. A scale was inscribed on the moulds to record the vertical measurement of the sample during the test. Moulds were positioned at the ends of the revolving arm. The distance from the

TH-3534_186104002

centre of the rotation axis to the base of the moulds was 150 mm (centrifuge radius). The moulds were of equal weight and positioned directly across from one other. The centrifuge was operated at three different speeds, 1000 RPM, 1500 RPM, and 2000 RPM, for each of the slurries. The speeds were selected to ensure that a difference in final settlement values observed at these RPMs were discernible, with a magnitude greater than 1 mm.

Each test involved running the centrifuge for at least 20 minutes. A glass plate was placed on the top of the benchtop centrifuge to allow for observation of the moulds during operation. A stroboscope set at the same frequency as the angular velocity of the centrifuge was employed to see the moulds. During the rotation of the centrifuge, the moulds were positioned in a horizontal orientation. The temporal settlement data was recorded. Following the examination, the final height was recorded, and the final void ratio was calculated, which is assumed to be the average void ratio of the sample.

In order to plot the effective stress versus void ratio relation, the effective stress at the bottom of the sample was computed using Equation (4.8) given by Robinson et al. (2003).

$$\sigma'_b = N_0 * L_s\,(Gs - 1) * \Upsilon_w \qquad (4.8)$$

Where L_s is the height of solids present in the slurry sample, N_0 is the value of N at the base of the sample, as shown in the Figure 3.7.

4.4 Methodology for Numerical Analyses

4.4.1 General

In this section, the detailed procedure for various numerical and graphical approaches adopted in this study is discussed.

4.4.2. Numerical solution of FSC equation using Explicit Finite Difference Method (EFDM)

4.4.2.1 FSC in 1g Condition

The finite difference method is a numerical technique that writes differentials in terms of small finite differences for easier numerical computability. Discussed here is the explicit finite difference method (EFDM). The entire soil depth is divided into small layers of thickness δ each. Also, the time taken for consolidation is divided into smaller time steps of τ each. A mesh, as shown in Figure 4.4. (a), can be imagined. Now, the derivative of the void ratio with respect to time can be expressed as:

TH-3534_186104002

$$\frac{\partial e_{i,j}}{\partial t} = \frac{e_{i,j+1} - e_{i,j}}{\tau} \tag{4.9}$$

And the space derivative of the void ratio can be expressed as:

$$\frac{\partial e_{i,j}}{\partial z} = \frac{e_{i+1,j} - e_{i-1,j}}{2\,\delta} \tag{4.10}$$

The EFDM solution to Gibson's FSC equation given by Cargill (1982) is below.

$$e_{i,j} = e_{i,j-1} - \frac{\tau}{\gamma_w}\left[\left\{(\gamma_s - \gamma_w)\,\beta(e_{i,j-1}) + \frac{\alpha(e_{i+1,j-1}) - \alpha(e_{i-1,j-1})}{2\,\delta}\right\}\frac{e_{i+1,j-1} - e_{i-1,j-1}}{2\,\delta} + \alpha(e_{i,j-1})\left\{\frac{e_{i+1,j-1} - 2\,e_{i,j-1} + e_{i-1,j-1}}{\delta^2}\right\}\right] \tag{4.11}$$

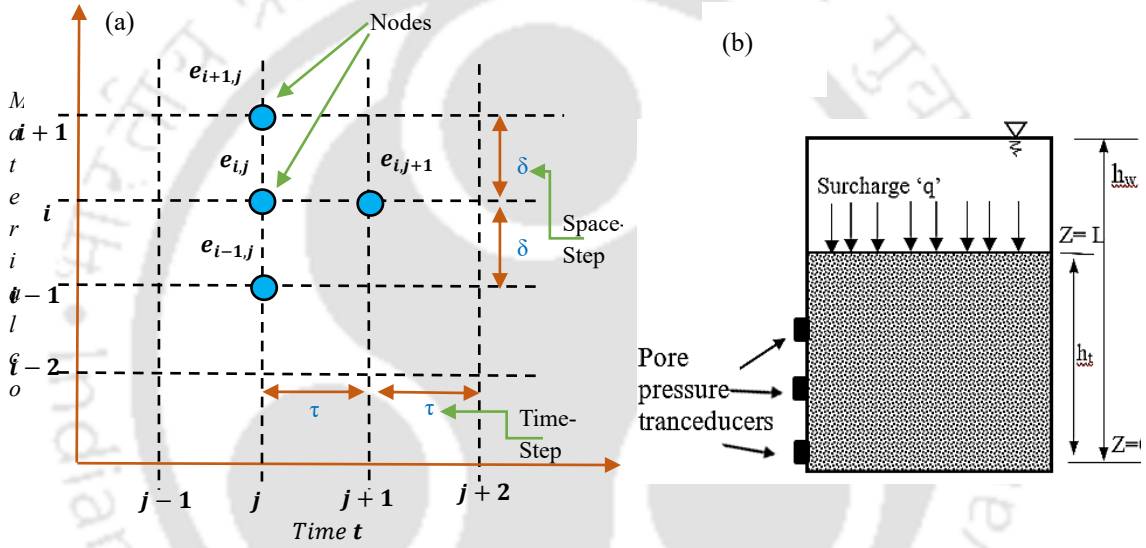


Figure 4.4: (a) finite difference mesh used for the EFDM solution of the FSC governing equation. (b) Sample under 1g FSC

The terms α and β are short-forms expanded as $\alpha(e) = \left(\frac{k(e)}{1+e}\right)\left(\frac{d\sigma'}{de}\right)$ and $\beta(e) = \frac{d}{de}\left(\frac{k(e)}{1+e}\right)$ where $k(e)$ is the hydraulic conductivity function and $\sigma'(e)$ is the compressibility function.

In the present study, the conductivity data of all the studied materials were represented in power functional form, as shown below.

$$k = Me^P \tag{4.12}$$

where k is the hydraulic conductivity, e is the void ratio, and M and P are the multiplier and power, respectively. The compressibility function used in this study was expressed in the power form (Equation (4.13a)) or the extended power (Equation (4.13b)) form as given below.

TH-3534_186104002

$$e = A(\sigma')^c \tag{4.13a}$$

$$e = A(\sigma' + B)^c \tag{4.13b}$$

where $\sigma'$is the effective stress, and A, B and C are constants coefficients. The settlement of any point in the sample at each time step was calculated from the void ratio profile (Equation 4.14). From this, the settlement versus time curves can also be plotted.

$$S(z,t) = \int_0^z [1 + e(z,0)]dz - \int_0^z [1 + e(z,t)]dz \tag{4.14}$$

where S is the settlement, z is the depth of location in the material coordinate system, and t is the time of settlement (Figure 4.4 (b)). The effective stress at all points was calculated from the compressibility relationship after the void ratio profile was determined. Total pore pressure at any point is the sum of static and excess pore water pressure values. The static pore pressure at all mesh points at any given time was computed using equation 3.17

$$u_S(z,t) = \gamma_w[h_w - \xi(z,t)] \tag{4.15}$$

where u_S is the static pore water pressure. As shown in Figure 4.4(b), h_w is the height of water above the datum, z=0, and, ξ is the convective coordinate (Equation (4.15)) of the mesh point under consideration at a given time.

$$\xi = \int_0^z [1 + e(z,t)]dz \tag{4.16}$$

The total stress at any point in the sample is the weight per unit area of the material overlaying the point considered. This is the sum of the weight of solids and the weight of water above the considered point, and a surcharge load, if any, is present, given as

$$\sigma(z,t) = \gamma_w[(h_w - L) + \int_z^L e(z,t)dz] + \gamma_s \int_z^L dz + q \tag{4.17}$$

After computing the effective stress, static pore water pressure, and effective stress, the excess pore water pressure profile was simulated using the effective stress principle. Total pore water pressure at any point was given by Equation (4.18). The excess pore water pressure profile was obtained using Equation (4.19).

$$u_t(z,t) = \sigma(z,t) - \sigma'(z,t) \tag{4.18}$$

$$u_e(z,t) = u_t(z,t) - u_s(z,t) \tag{4.19}$$

4.4.2.2 FSC in Centrifuge Environment

TH-3534_186104002

Bharat and Ubaid (2020) proposed the material coordinate-based analytical model for nonlinear finite strain consolidation in a centrifuge environment, accounting for the variation in the acceleration factor (*N*) within the model given by Equation (2.25), given below as:

$$\left(\frac{\gamma_s}{\gamma_w}-1\right)\left[N_z^2\lambda(e)\,\frac{\partial e}{\partial z}-2\alpha N_z k(e)\right]+\frac{\partial}{\partial z}\left[\frac{N_z}{\gamma_w}\phi(e)\frac{\partial e}{\partial z}\right]+N_z\frac{\partial e}{\partial t}=0 \tag{4.20}$$

The explicit finite difference solution for the governing equation was also derived, as given by Equation (4.21)

$$e_i^{n+1}=e_i^n-\frac{\tau}{\gamma_w}\left(\frac{e_{i+1}^n-e_{i-1}^n}{2\Delta}\right)\left\{(N_z(i)\lambda(e_i^n)(\gamma_s-\gamma_w)+\left(\frac{\phi(e_{i+1}^n)-\phi\left(e_{i_1-1}^n\right)}{2\Delta}\right)\right\}-\frac{\phi(e_i^n)\tau}{\gamma_w\Delta^2}(e_{i+1}^n-2e_i^n+e_{i-1}^n)+\frac{\tau\,\alpha}{\gamma_w}\left[2(\gamma_s-\gamma_w)k(e_i^n)+\frac{(1+e_i^n)\phi(e_i^n)(e_{i+1}^n-e_{i-1}^n)}{2N_z(i)\Delta}\right] \tag{4.21}$$

The term τ stands for the time-step adopted, while Δ is the space-step in material coordinates. The acceleration factor at any point in the model N_z is estimated as

$$N_z=N_0-\alpha\Sigma_{j=1}^{i}(1+e_j)\Delta \tag{4.22}$$

where, N_0 is the acceleration factor at the base of the model as given by $N_0=R\omega^2/g$. The settlement at any point of time is obtained for the entire sample of initial height *H* from the void ratio profile obtained for the model at that time using Equation (4.21) by Equation (4.14).

In this study, the top boundary of the model was taken as being free-draining and the bottom as impermeable. At the top boundary, since the effective stress is zero, the void ratio was taken as constant throughout the process. The value of the base void ratio (e_0^n) at each time step was calculated by considering a fictitious point beyond the impermeable boundary imaginary boundary, using the central difference scheme given by the equation

$$e_0^n=e_2^n+2\Delta z\left(\frac{de}{d\sigma'}\right)_{e_1^n}(\gamma_s-\gamma_w) \tag{4.23}$$

The term $\frac{de}{d\sigma'}$ was calculated at the point e_1^n using the compressibility relation of the sample and the void ratio for that mesh point obtained using Equation (4.16). The value of e_2^n was computed using the Equation (4.16).

The convergence and stability of this EFDM solution was ensured by adopting space and time step values that satisfy the following equations throughout the numerical simulation process.

TH-3534_186104002

$$Space\ step\ \Delta_i \leq -\frac{2\phi(e_i)}{(\gamma_s - \gamma_w - 1)N_z(i)\lambda(e_i) + \frac{\partial\phi(e_i)}{\partial z} - \frac{\alpha\phi(e_i)}{N_z(i)}(1 + e_i)} \quad (4.24)$$

$$time\ step\ \tau_i \leq -\frac{(\Delta z_i)^2\gamma_w}{2\phi(e_i)} \quad (4.25)$$

The error in choosing the appropriate space and time steps will result in absurd results, which get compounded over iterations. In some cases, the appropriate time step and space step values can be very small, resulting in increased computation cost and time.

A MATLAB code was written to estimate the void ratio profiles, settlement curves, and pore pressure dissipation curves. The flow chart for the same is given in Figure (4.5)

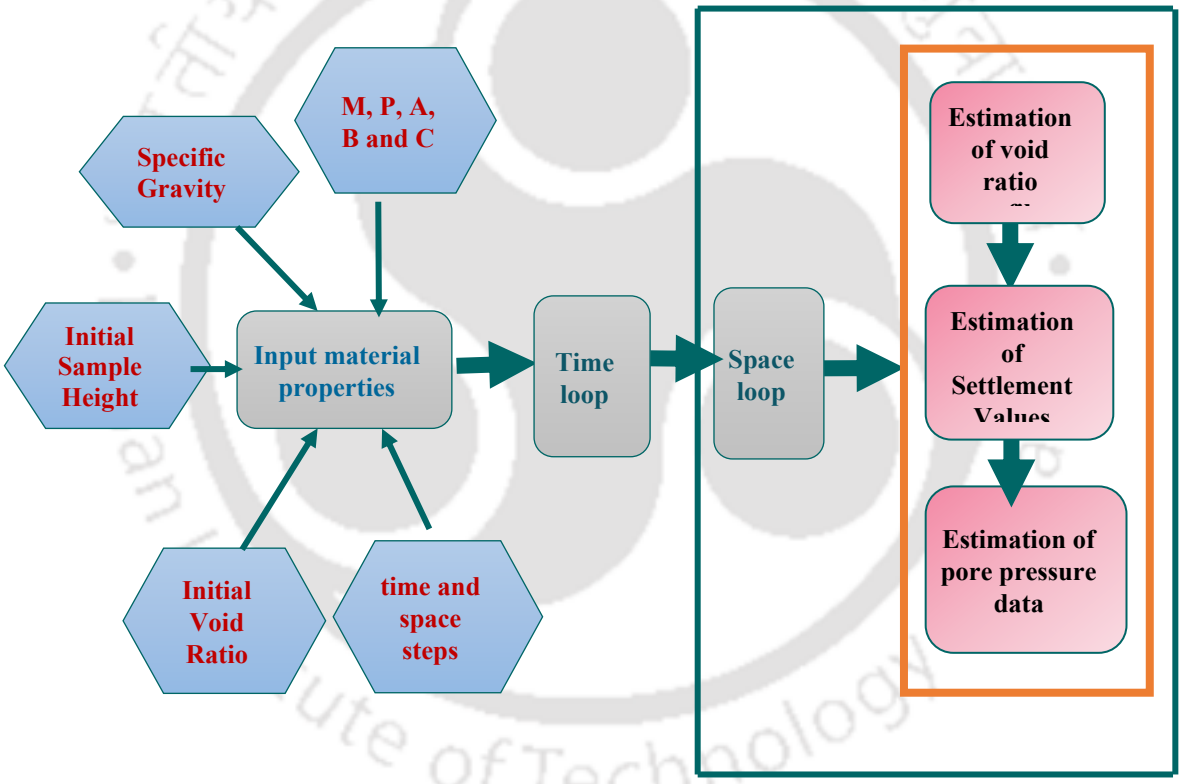


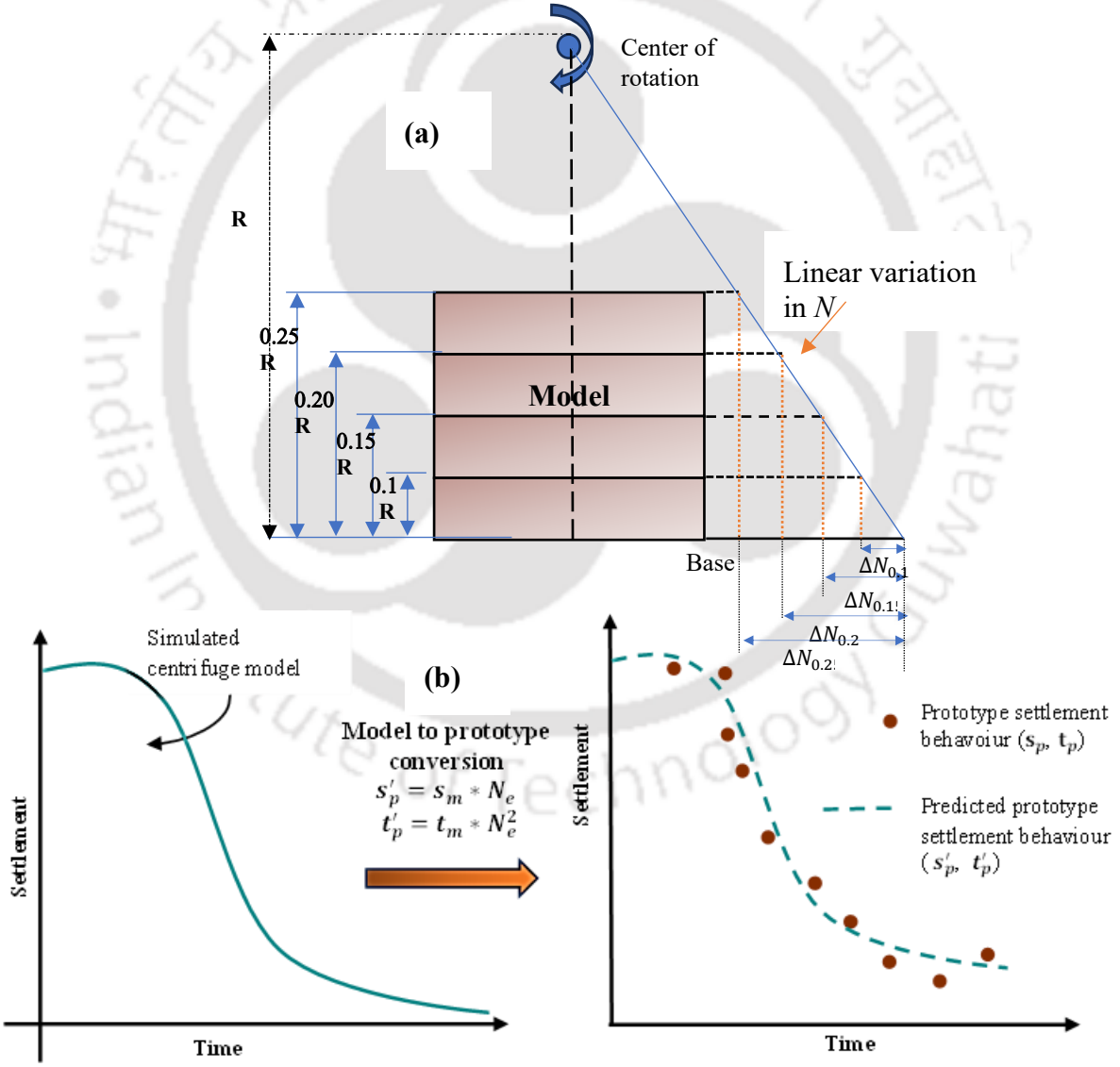
Figure 4.5: Flow chart of numerical analysis of FSC equation using MATLAB code.

4.4.3 Concept and implementation of effective scale factor

The scale factor *N,* defined as the height of the prototype to the model height, is also generally taken as the acceleration factor for the centrifuge $N=R\omega^2/g$. Where R is the radius of the centrifuge, ω is the speed of rotation of the centrifuge in radians/second, and g is the earth's acceleration due to gravity, i.e., 9.8 1kN/m^2. The various observations obtained from the centrifuge model need to be scaled up using this factor *N* and applying appropriate scaling laws. However, this acceleration factor is a function of distance from the centre of rotation. In

TH-3534_186104002

a time-dependent process like consolidation, the model depth is a function of time. This causes the *N* value to become a function of space and time. Therefore, it is a challenge to understand how to use this factor to ensure proper scaling of model observations to the field/prototype level. The effective radius defines the exact point of stress similitude between the model and the field within the model. Centrifuge modelling often assumes that centrifugal acceleration remains constant. Then, the speed of rotation of the sample is determined based on the effective radius values at the beginning of the test. However, these scale factors are time-dependent in the case of FSC studies due to the continuous deformation of the sample, which is not accounted for when they are defined based on the initial sample height. It is a general practice to scale the data using the *N* value corresponding to the base of the sample (N_o).



TH-3534_186104002

Figure 4.6: Illustration of the impact of model heights on the variation in acceleration scale factor value (N) from top to bottom, (b) illustration of conversion of model data to prototype data

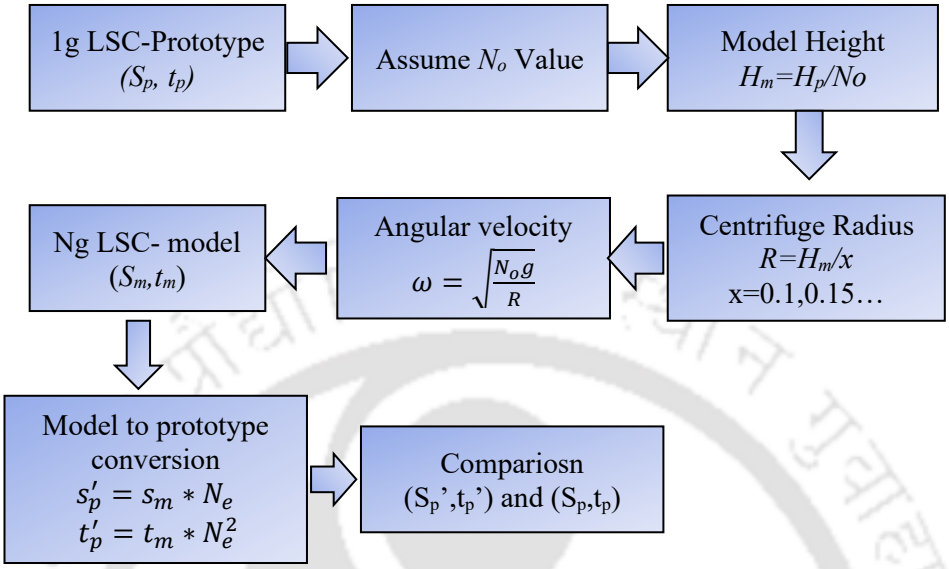


Figure 4.7: Flow chart for the steps for the numerical study on the influence of effective scale factor on scaling of centrifuge FSC data to prototype data

The advantage of this choice is that throughout the process of consolidation, the base of the sample will be under the same acceleration level, and therefore, this definition offers a level of consistency and, more importantly, convenience. Therefore, the impact of using effective acceleration scale factors defined based on the effective radius values for converting model data to prototype data when the angular velocity is fixed based on *N* at the base of the sample (N_0) was explored.

The geometric scale factor (Height of prototype /Height of model) was taken as N_0. The model height H_m is therefore calculated as H_p/N. Fox et al. (2005) suggested that the effect of scale factor *N* on the settlement behaviour of soft clays is influenced mainly by the ratio of model depth to the radius of the centrifuge (H_m/R) (Figure 4.6(a)). Fox et al. (2005) suggest that maintaining this ratio to be less than 0.2 can reduce the error during conversion. To understand how this ratio affects the accuracy of conversion of centrifuge settlement curve to prototype curve, it was varied from 0.1 to 0.25 while the values N_0 and H_m were kept fixed. Thus, the radius of centrifuge *R* was computed as $H_m/0.1$, $H_m/0.15$, etc. After the radius was calculated, the centrifuge rotation speed was calculated as $\omega = \sqrt{N_0 g/R}$. Based on the ratio of H_m/R, the values of *R* and ω were changed. From the known initial height of the model, effective radius

TH-3534_186104002

values *Re* can be obtained. For a model rotated at the angular velocity ω (rad/s), as computed before, the effective scale factor N_e corresponding to each R_e can be computed as $\omega\ N_e = \omega^2 R_e/g$. For the prototype in the 1g environment settling under self-weight, the complete consolidation curve was generated using the FSC curve for N=1 and rotation speed (ω) of zero. Numerical simulations for the FSC behaviour of the model were carried out using various Hm/R ratios. The value of the acceleration scale factor was N_0 at the base, and its linear variation across the sample is also accounted for. These simulations were then converted to prototype settlement curves by multiplying their time coordinates with the square of N_e and the settlement values with N_e. The procedure is elaborated using Figure 4.6(b) and the flow chart given (Figure 4.7).

4.4.4 Numerical analysis of time-scale factor exponent

Literature reports that the consolidation time value from the centrifuge is multiplied with N^2 to get the corresponding prototype time for any given degree of consolidation. However, certain studies show that the time-scaling exponent varies with the degree of consolidation in the FSC framework, but the average is close to the theoretical time-scaling exponent of 2. A preliminary numerical study was conducted to avail insights into these aspects. For this, the centrifuge settlement curves simulated for various H_m/R ratios were used. These settlement plots were converted into the degree of consolidation versus time graphs. The time values corresponding to degrees of consolidations at 10-degree intervals were considered (T_{model}). The prototype time ($T_{prototype}$) corresponding to the same degrees of consolidation was noted. The relation between the model time and the prototype time is given below.

$$T_{prototype} = T_{model} * N^x \tag{4.26}$$

Where 'x' is the time scale factor exponent, which can be computed as

$$x = \left(\frac{1}{N}\right) * ln\left(\frac{T_{prototype}}{T_{model}}\right) \tag{4.27}$$

The scale factor N considered in the literature is the N at base value, so the same is adopted here as well. The average time scale factor exponent for various H_m/R ratios and a number of N values were computed and reported.

4.4.5 Graphical Inverse Analysis from *N*g Settlement Data

4.4.5.1 Method 1 -Using Settlement Data

TH-3534_186104002

Recently evolved techniques (Qi and Simms 2020, Qi et al. 2020) for predicting the multiplier and power values of the hydraulic conductivity function from the 1g settlement versus time curves were adopted for the centrifuge test analysis for a known and time-invariant compressibility function in this study. A unique set of *M* and *P* values can represent a set of settlement versus time data measured from the settling column tests. The iteration histories during optimization consistently showed a linear or straight-line behaviour in the *P-ln M* space in these cases. For a given self-weight consolidation test in a centrifuge environment, the shape of the curve in settlement versus the logarithm of the time plane was dependent on the *P* value, while the position on the curve with respect to *log t* space was dependent on the *M* value as seen in the numerically simulated settlement curves shown in Figures 4.8(a-b). Substituting the Equations (2.28) and (2.27) in Equation (2.25) resulted in Equation (4.28)

$$\left(\frac{\gamma_s}{\gamma_w}-1\right)\left[N_z\frac{\partial}{\partial z}\left(\frac{k}{1+e}\right)+\frac{k}{1+e}\frac{dN_z}{dz}\right]+\frac{\partial}{\partial z}\left[\frac{1}{\gamma_w}\left(\frac{k}{1+e}\right)\frac{\partial\sigma'}{\partial z}\right]+\frac{\partial e}{\partial t}=0 \qquad (4.28)$$

Substituting $k=Me^P$ in Equation (4.28) and shifting the term *M* to the right-hand side in the resulting equation, Equation (4.29) was obtained.

$$(1-G_S)\left[N_z\frac{\partial}{\partial z}\left(\frac{e^P}{1+e}\right)+\frac{e^P}{1+e}\frac{dN_z}{dz}\right]-\frac{\partial}{\partial z}\left[\frac{1}{\gamma_w}\left(\frac{e^P}{1+e}\right)\frac{\partial\sigma'}{\partial z}\right]=\frac{\partial e}{\partial(Mt)} \qquad (4.29)$$

The differential Equation (4.29) has solutions of the form *f (Mt, z),* where the term *Mt* and the spatial coordinate *z* are independent variables. Therefore, identical solutions are obtained by keeping the product *Mt* constant for different *M* and *t* values. This implies:

$$M_1 * t_1 = M_2 * t_2 = M_3 * t_3 \qquad (4.30)$$

Where M_1, M_2, and M_3 are three different *M* values and t_1, t_2, and t_3 time values at different data points in the settlement curves corresponding to M_1, M_2, *and* M_3. Taking the natural logarithm of the product of the multiplier *M* and time *t* gives the following equation:

$$\ln(Mt) = \ln M + \ln t \qquad (4.31)$$

It is evident from Equation (4.31) that when time *t* is scaled by a value *M*, in a natural logarithm space, it is equivalent to the translation by a distance *ln M.* Therefore, the settlement versus time curves of a centrifuge test simulated using the same *P* value but different *M* values are geometrically congruent (Figure 4.8(a)). This suggests that if the *P* value is known, then simple translation using this observation can help to reach the original settlement versus time curve from an initially assumed curve as they differ by the *M* factor. These observations were found

TH-3534_186104002

to match with the recent findings (Qi and Simms, 2020) on the settlement data from 1g settling column tests. The following two methods were explored in this study to predict the hydraulic conductivity function from the centrifuge settlement data.

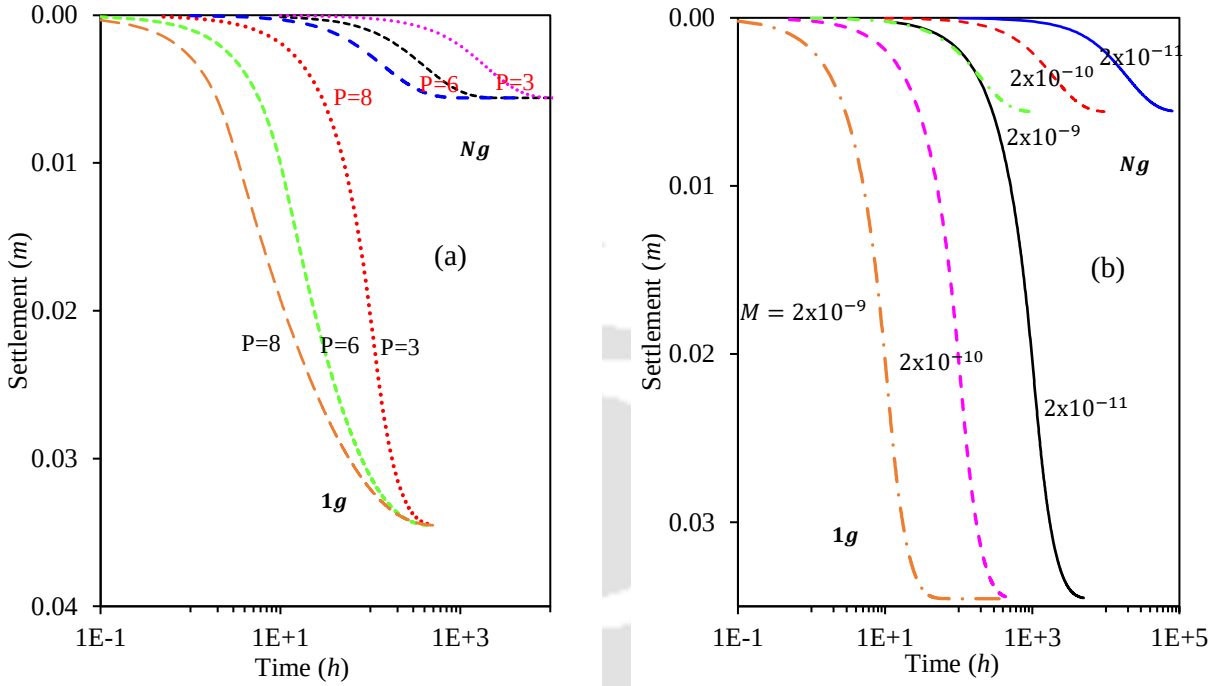


Figure 4.8. Comparison of Ng and 1g settlement versus time curves, numerically generated using the material properties of Rutgers, for (a) different P values (b) different M values

Method 1 requires a minimum of two numerically simulated FSC curves using two pairs of M and P were arbitrarily chosen as (M_1, P_1) and (M_2, P_2). The method can be applied when more data sets are available as well. The values P_1 and P_2 were selected to represent the extreme boundaries of the expected P value. If the original settlement versus time curve had n data points, for each of the corresponding points in settlement curves of (M_1, P_1) and (M_2, P_2), the M values were shifted. Equations (4.32) and (4.33) were used to estimate the shift for the j^{th} point (S_j, T_j) on the original curve.

$$M_{1j} = \frac{M_1 * t_{1j}}{t_j} \tag{4.32}$$

$$M_{2j} = \frac{M_2 * t_{2j}}{t_j} \tag{4.33}$$

Where t_{1j} and t_{2j} are the time coordinates for the corresponding points in the settlement curves simulated using (M_1, P_1) and (M_2, P_2), respectively. This shift produced a set of pairs of M and P, (M_{1j}, P_1) and (M_{2j}, P_2), where j takes values 1,2,3…n. As illustrated in Figure 4.9(a-d), these

TH-3534_186104002

pairs of parameters all generated points that led to optimal *M* and *P* values that replicated settlement curves passing through each of the observed or original data points.

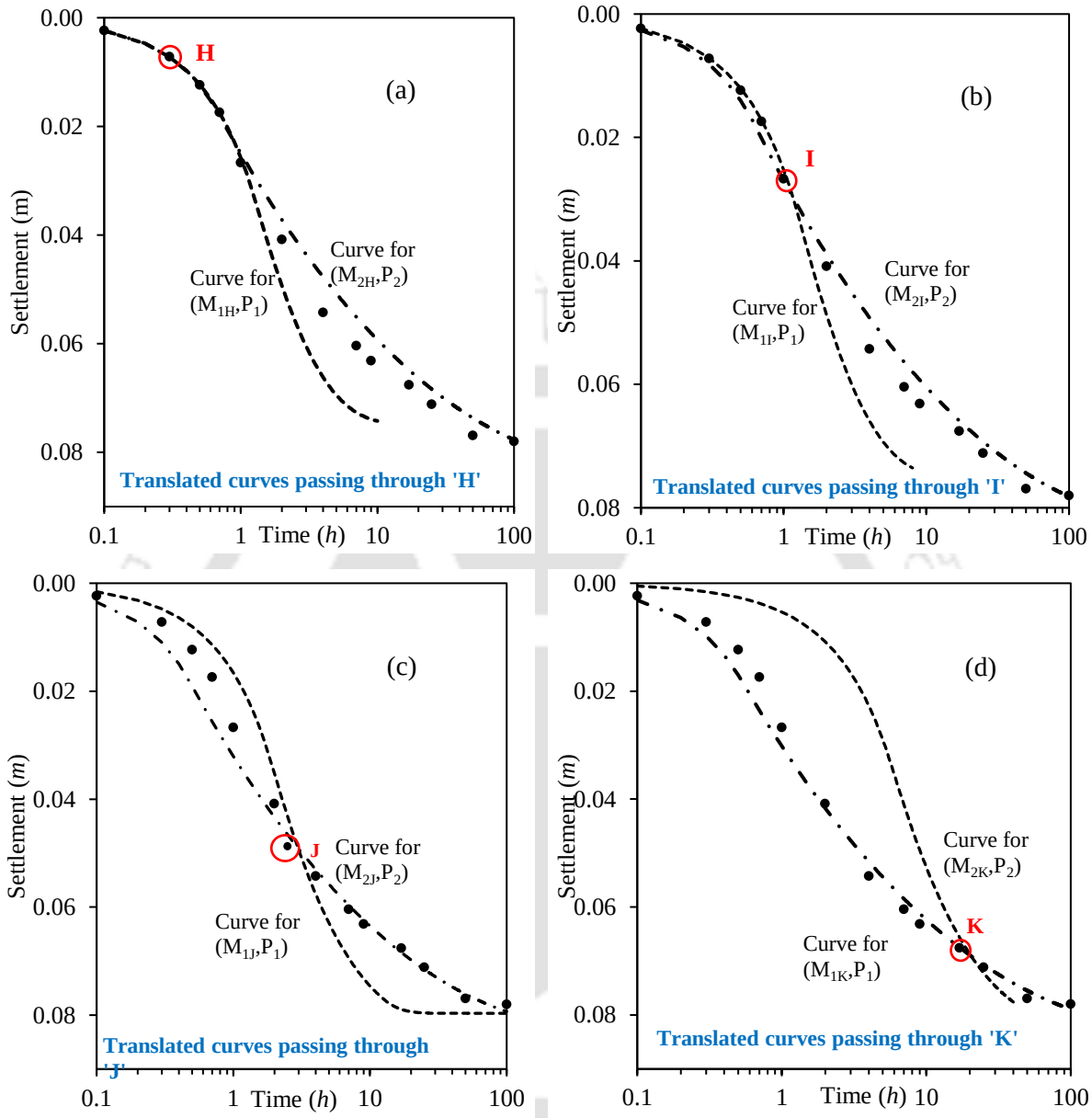


Figure 4.9. Translation of the arbitrary settlement versus time curves, using two pairs of initial guesses, (M_1, P_1) and (M_2, P_2), through four points (H, I, J, and K) on a synthetic settlement versus time curve (a) translation of (M_1, P_1) and (M_2, P_2) through H (b) (M_1, P_1) and (M_2, P_2) through I (c) (M_1, P_1) and (M_2, P_2) through J (d) (M_1, P_1) and (M_2, P_2) through K

When a back-analysis was carried out from the centrifuge self-weight consolidation test data using a swarm-based stochastic optimization algorithm, the various trial values leading to the optimal *M* and *P* values were observed to form a straight line in the *P-ln M* space, as shown in Figure 4.10(a). If three initial guess curves were considered (*(M_1, P_1), (M_2, P_2) and (M_3, P_3)*),

TH-3534_186104002

after translation along the *log t* axis, three translated curves would pass through each of the points in the synthetic curve. It was observed that, for each point of the synthetic curve, the hydraulic conductivity parameters of the three translated curves ((M_{1j}, P_1), (M_{2j}, P_2) and (M_{3j}, P_3)) formed a straight line in the *P-ln M* space and the straight lines for all the points intersected at a common point. This point gives the optimal *P* and *M* values since it means that the corresponding translated curve passes through all the points in the synthetic curve. As shown in Figure 4.10(b), two initial guess values are sufficient to obtain the point of intersection. However, it is important to select the values P_1 and P_2 such that the point of intersection falls within this range considered.

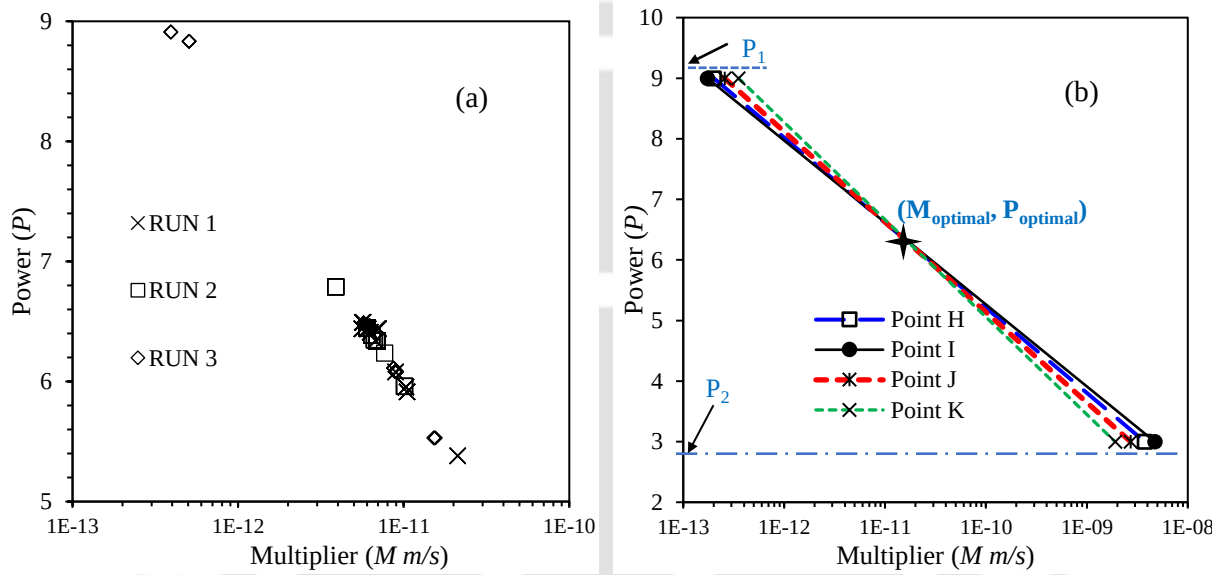


Figure 4.10. Illustration of Method 1 (a) Iteration history for three runs of a swarm based stochastic optimisation algorithm for back analysis on centrifuge settlement data of SMC.(b) Linear relationships in the P-lnM space obtained for various data points (H, I, J, and K) on the synthetic curve

The straight lines formed by (M_{1j}, P_1) and (M_{2j}, P_2) in *P-ln M* space can be represented by the general Equation (4.34).

$$P = \omega_j + \lambda_j \ln M \tag{4.34}$$

Where *j* ranges from 1 to *n*, therefore, *n* such straight lines were formed, one each for each point in the measured settlement curve. For an ideal case of initial settlement versus time curve, these lines meet at a single point ($ln\ M_{optimum}$, $P_{optimum}$) where $P_{optimum}$ is the optimal value of parameter *P*. The optimal value of *M* can be calculated from $ln\ M_{optimum}$. However, in reality, these lines do not intersect at a single point but at *(n-1)!* points within a narrow range. Hence, the arithmetic average of *lnM* and *P* values obtained as points of intersection was taken to get

TH-3534_186104002

the optimal parameters. Cases, where the lines have nearly identical equations were ignored while determining the points of intersection. In such conditions, they meet at infinity or give infinite value for *ln M* and *P.* Solutions with *P* values exceeding the limit *[P_1, P_2]* were also excluded.

4.4.5.2 Method 1 -Using Pore Pressure Dissipation Data

Using the forward analysis MATLAB code, the excess pore pressure dissipation curves were simulated for various *M* values, keeping the *P* value constant and vice versa. It was observed that changing the value of *M* for a constant *P* value translates the curve along the log-t axis without changing the shape of the curve (Figure 4.11(a)). However, for a given *M*, changing the *P* value slightly shifts the curves and influences the shape of the curves (Figure 4.11(b)).

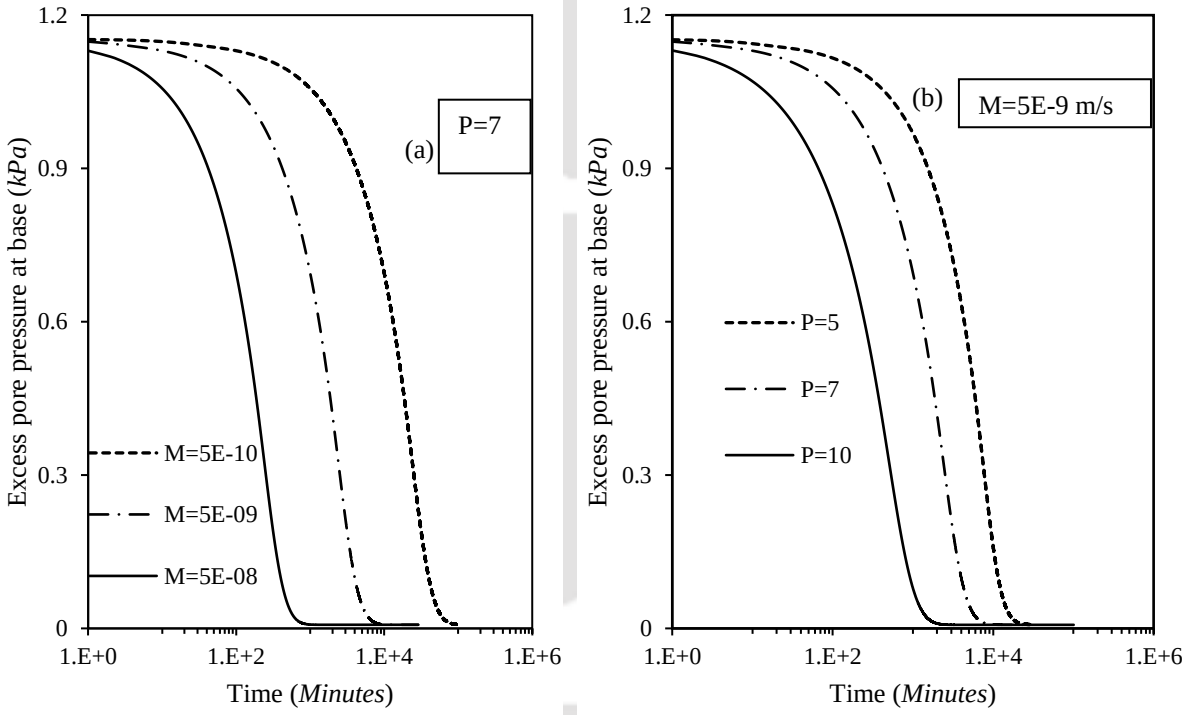


Figure 4.11: Simulated excess pore pressure at base dissipation curves simulated for Antwerpen Soil (a) Effect of M-value (M in m/s) on the curve, for a constant P-value (b) Effect of P-value on the curve, for a constant M-value

Equation 4.35 is the LSC equation (Somogyi, 1980) for a quiescent state in terms of excess pore pressure.

$$\frac{\partial u}{\partial t}+\left(\frac{d\sigma'}{de}\right)\left(\frac{k(e)}{1+e}\right)\frac{\partial^2 u}{\partial z^2}+\left(\frac{1}{\gamma_W}\right)\left(\frac{d\sigma'}{de}\right)\left(\frac{\partial}{\partial z}\left(\frac{k}{1+e}\right)\right)\frac{\partial u}{\partial z}=0 \qquad (4.35)$$

TH-3534_186104002

Where z is the material coordinate , and u is the excess pore pressure. Substituting $k=Me^P$ in Equation (4.35) and rearranging gave Equation (4.36).

$$\left(\frac{e^P}{1+e}\right)\left(\frac{d\sigma'}{de}\right)\frac{\partial^2 u}{\partial z^2}+\left(\frac{1}{\gamma_W}\right)\left(\frac{d\sigma'}{de}\right)\left(\frac{\partial}{\partial z}\left(\frac{e^P}{1+e}\right)\right)\frac{\partial u}{\partial z}=-\frac{\partial u}{\partial(Mt)} \tag{4.36}$$

The solutions to the differential Equation (4.36) take the form *f (Mt, z)*, where *Mt* and *z* are independent variables. Therefore, for various values of *M* and *t*, similar solutions are found by maintaining the product *Mt* constant. This observation is the same for the settlement data-based inverse analysis, which makes the Equations (4.30) - (4.35) true or the base excess pore pressure as well. Therefore, for a particular settling column test, keeping the *P* value constant and varying the *M* value will produce geometrically congruent base excess pore pressure curves (i.e., curves of the same shape and size) at various positions along the log-t axis.

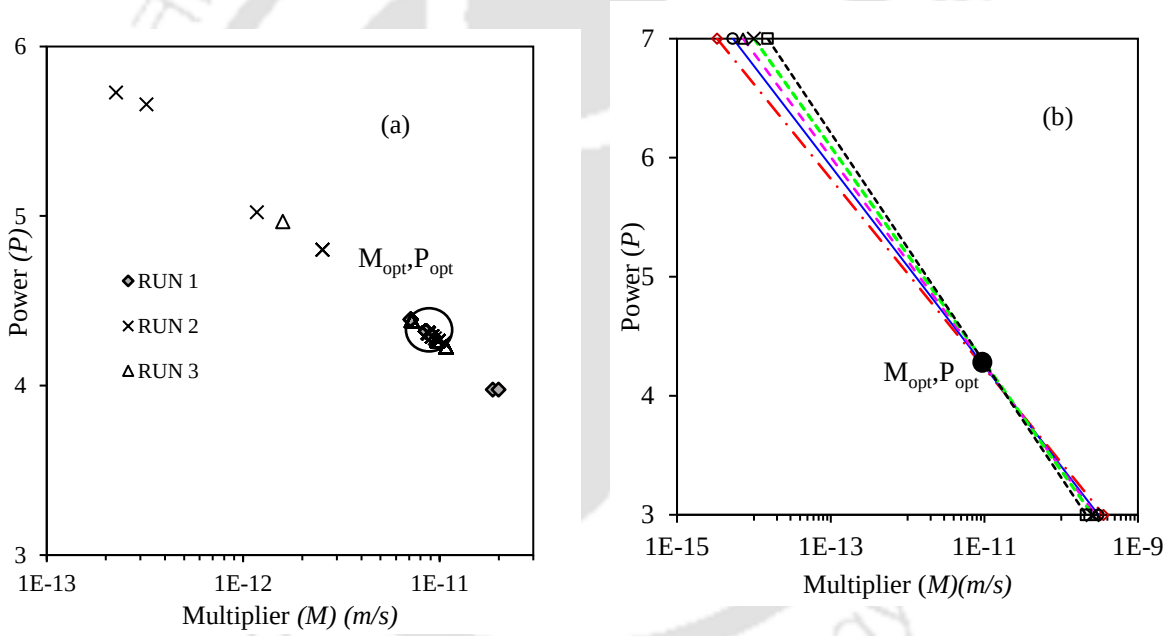


Figure 4.12. For Phosphatic Clay (a) Iteration history for three runs of a swarm-based stochastic optimization algorithm for back analysis on simulated base excess pore pressure dissipation data(b) Linear relationships in the P-lnM space obtained for various data points on the synthetic base excess pore pressure dissipation curve.

This suggests that if the *P* value is known, then simple translation using this observation can help to reach the original dissipation curve from an initially assumed curve, as they differ by only the *M* factor. Back-analysis from the simulated base excess pore pressure dissipation data using a swarm-intelligence-based optimization algorithm showed that the various trial values leading to the optimal *M* and *P* values formed a straight line in the *P-ln M* space (Figure 4.12

TH-3534_186104002

(a-b)). All these observations are in excellent agreement with the findings of Qi and Simms (2020). Therefore, it is appropriate to adopt the same methodology of analysis in the current study as well.

The graphical technique needs at least two simulated excess pore pressure dissipation curves comprising two combinations of *M* and *P* that were randomly selected as *(M_1, P_1)* and *(M_2, P_2)*. The values P_1 and P_2 were taken as the upper and lower bounds of the expected optimum *P* value. The reset of the procedure is the same as that proposed for the settlement data.

4.4.5.3 Graphical Method -2

This approach varies from the previous method in the prediction of *P* value. The variance of time coordinates was used to establish a relation between the *P* value and the shape of the settlement curves. For a simulated centrifuge self-weight consolidation settlement behaviour, as shown in Figure 1(b), the spread of the settlement versus time curve along the *log t*-axis increased with an increase in the *P* value. This spread was quantified mathematically using the variance of the *log t* coordinates of a few random heights or settlement values selected from the measured/original/simulated settlement versus time curve. The variance *V* from the available data set of *n* data points was estimated as:

$$V = \frac{\left[\sum_{j=1}^{n}\left(\log t_j - \frac{\sum_{i=1}^{n} log t_i}{n}\right)^2\right]}{n} \tag{4.37}$$

Where t_i and t_j are the time coordinates for the data points in question. At least three pairs of *(M, P)* were used to simulate FSC settlement curves in the *Ng* condition. Groups of points from each of these curves were used to compute variance values, which were related to power *P* as follows:

$$V = aP^b + \Psi \tag{4.38}$$

Where *a, b,* and Ψ are the fitting parameters obtained by fitting Equation (4.38) to the variance and power values computed for settlement versus time curves simulated using at least three arbitrary pairs of *M* and *P*. These steps are illustrated in Figures 4.13(a) and 4.13(b). Similarly, the variance of the measured settlement versus time curve was computed by considering the group of data points corresponding to the ones selected from the simulated settlement curves. This variance value was substituted in Equation (4.38) to predict the *P* value. From the available set of data points, multiple groups were made, and each group yielded different *a, b*, and Ψ values in Equation (4.38). The *P* values for each of these cases were back-predicted

TH-3534_186104002

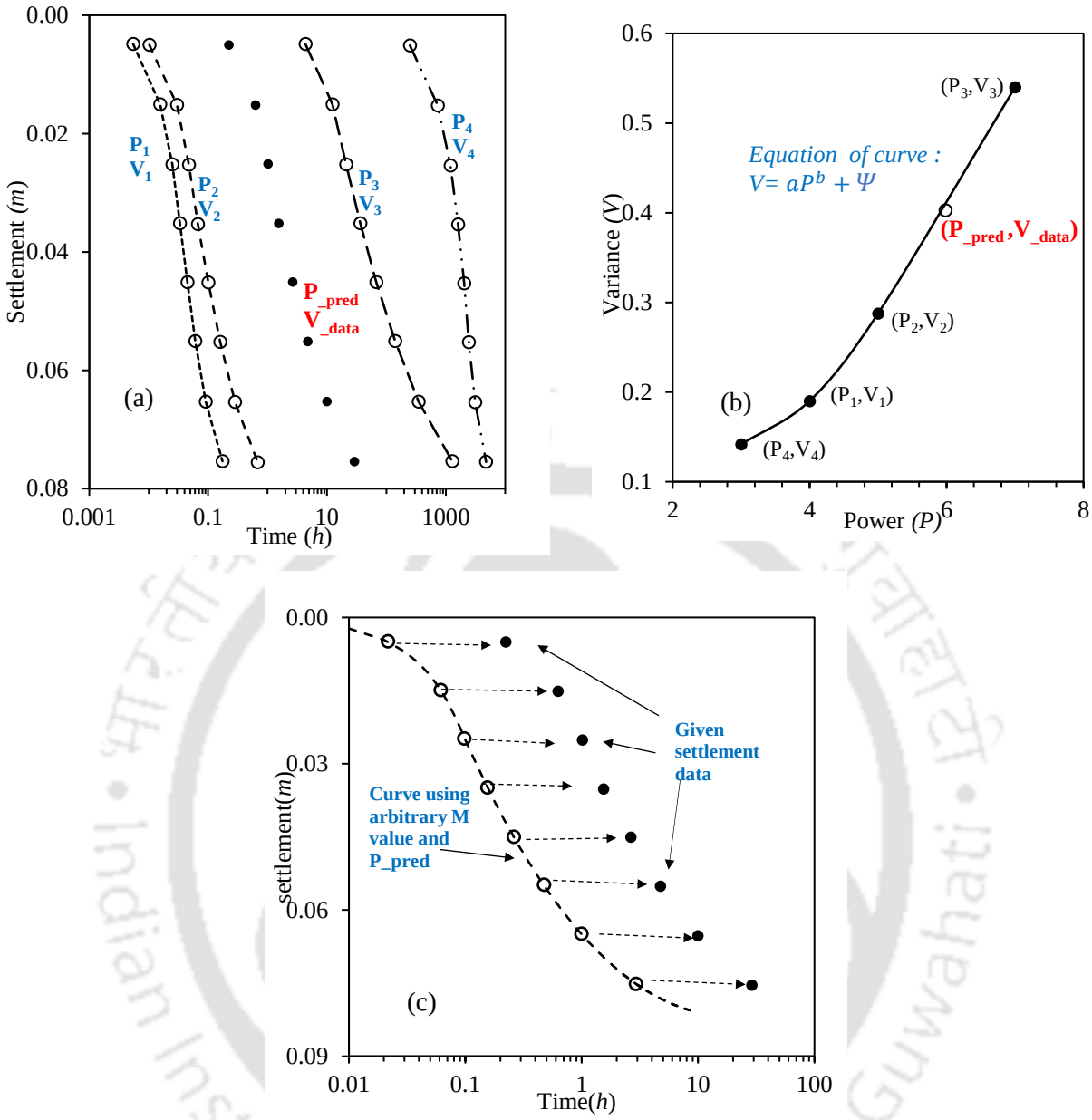


Figure 4.13: Illustrating Method 2 (a) Points considered from the simulated settlement curves and the measured settlement curve used for the calculation of variance b) proposed correlation fitted to power versus variance data, c) showing the shifting of settlement curve generated using arbitrary M value and predicted power value (P_pred).

using the Equation (4.38) and was found to be almost identical. Using an arbitrary M value (say M_{arb}) and each of these predicted P values, Ng FSC settlement versus time curves were numerically simulated. Distances between the corresponding points in the simulated curve and the measured/original curve were graphically measured along the *log* t-axis. The average of these distances was computed as $\bar{X}$. The optimal value of M (say M_{pred}) was found by

TH-3534_186104002

translating each point on the simulated curve to the original curve's corresponding point (figure 3(c)), as shown in Equations (4.39) and (4.40).

$$\log M_{pred} = \log M_{Arb} - \bar{X} \tag{4.39}$$

$$M_{pred} = M_{Arb}\left(10^{\bar{X}}\right) \tag{4.40}$$

The average of M_{pred} values and precited P values gives the optimum values of M and P.

Inverse analysis by Method 1 required two forward FSC simulations, and Method 2 required at least three simulations for predicting the optimal pair of M and P values. Method 1 involved shifting settlement curves to the original settlement curve and determining the intersection points of straight lines in P-ln M space by taking a combination of two lines at a time, followed by taking the arithmetic average of the coordinates of these points. A MATLAB code was written to carry out this analysis. Method 2 predicted the P value from the variance of measured and simulated settlement versus *log t* curves followed by shifting of a simulated curve to the measured curve for predicting the M value.

4.5 Optimisation-Based Inverse Analysis

4.5.1 General

In this section, the concept of inverse analysis for the constitutive function parameters (i.e., hydraulic conductivity function coefficients and compressibility function coefficients) using various optimization algorithms is discussed. Deterministic algorithms- *fmincon and fminsearch* are discussed. Detailed descriptions of the conventional PSO and ABC algorithms are given, along with advanced algorithms like QPSO. The study proposed three novel algorithms: HABC, MABC, and HPSO. An in-depth understanding of these algorithms are provided in this section.

4.5.2 Inverse Analysis Procedure

Qi and Simms (2020) reported that the power P from the hydraulic conductivity function controls the slope and spread of the settlement curve and excess pore pressure dissipation curves, while the multiplier M influences the position of the FSC settlement curve with respect to the log-time axis. These observations are demonstrated using the properties of Rutgers and Antwerpen Slurry in Figures 4.8(a-b) and 4.11(a-b), respectively. The compressibility function parameters A and C were observed to influence the final settlement values, as shown in Figures 4.14(a-b) for Rutgers. Therefore, these parameters are observed to influence the settlement and pore dissipation process during FSC significantly and can hence be back-predicted from these

TH-3534_186104002

data through inverse analysis. The proposed inverse analysis approach for the simultaneous estimation of compressibility and hydraulic conductivity function coefficients is basically a forward analysis algorithm embedded inside an appropriate optimization algorithm that performs a parameter search operation. The settlement data points or the base pore pressure dissipation data points and relevant material properties are given as input values. The optimization algorithm strives to match the available observed FSC data points of a material with the forward analysis data points simulated using various combinations of the decision variable values. This is achieved by minimizing the objective function value, defined by Equation (4.41), over a number of iterations of the inverse analysis algorithm.

$$RMSE = \sqrt{\left(\frac{1}{n}\right)\sum_{i=1}^{n}\left(O_o^i - O_p^i\right)^2} \tag{4.41}$$

In the above equation, *RMSE* is the root mean square error value, *n* is the number of data points available, O_o^i is the i^{th} observed settlement data or pore pressure value, while O_p^i is the corresponding simulated settlement value from the forward analysis curve as Figure 4.15(a)

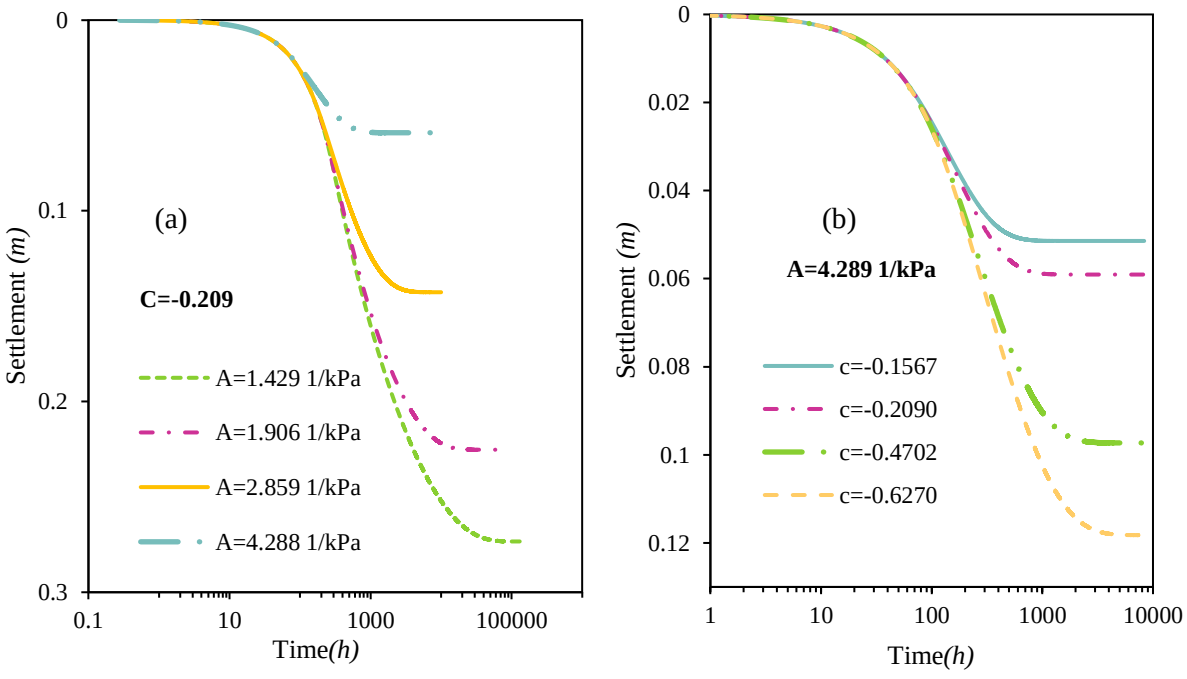


Figure 4.14. FSC Settlement curves simulated for Rutgers by varying the (a) value of coefficient A and (b) value of coefficient C from the compressibility function

TH-3534_186104002

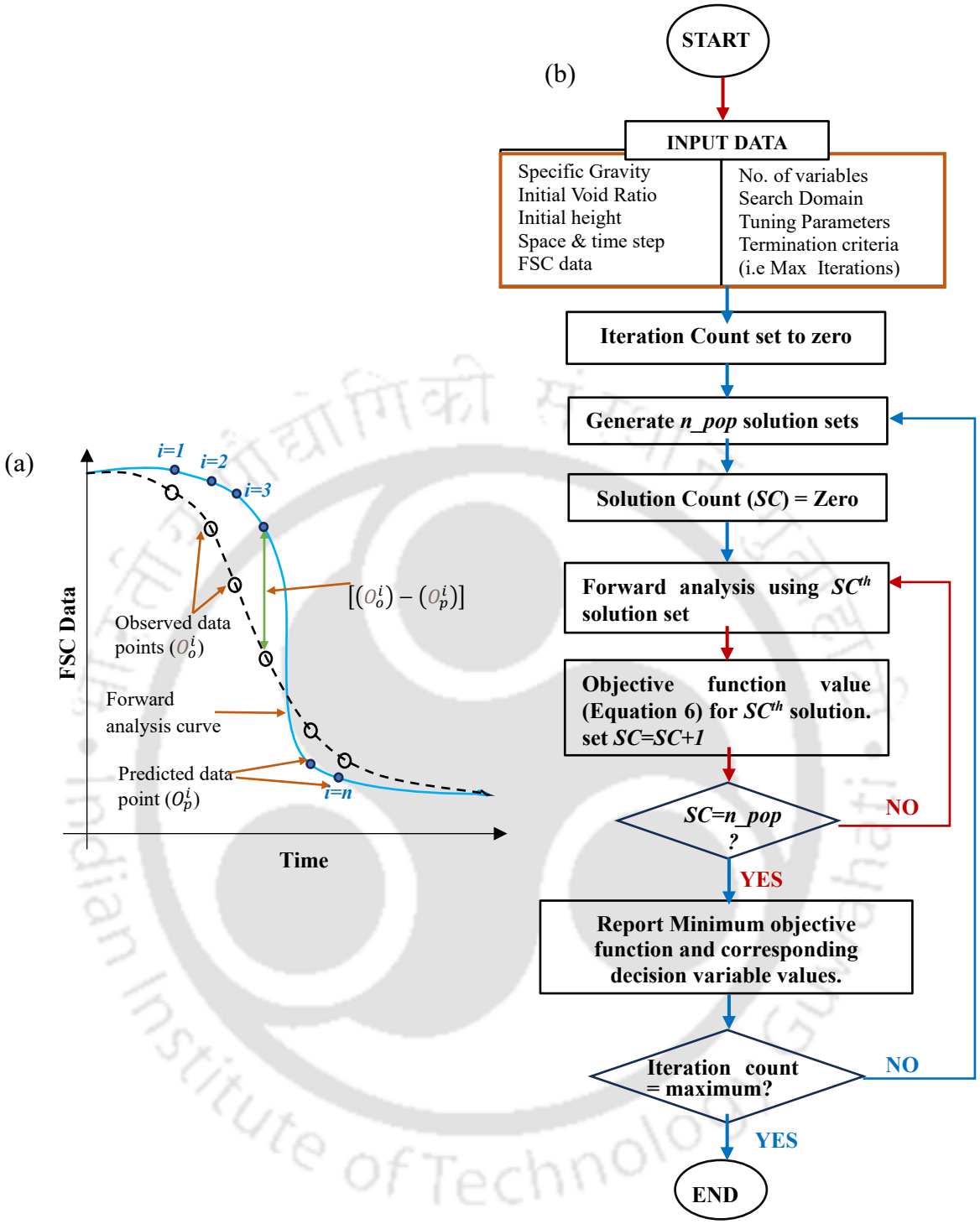


Figure 4.15: (a) illustration of the objective function used for the optimization (b) flow chart for the inverse analysis procedure for the simultaneous estimation of hydraulic conductivity and compressibility function coefficients

explains. The detailed process of inverse analysis is provided as a flow chart in Figure 4.15(b). Metaheuristic optimization techniques are recommended for inverse analysis when the problem exhibits intricate, nonlinear inter-variable relationships and possesses a complicated analytical

TH-3534_186104002

solution. These algorithms are well-suited for navigating extensive search spaces with multiple dimensions. This study considers PSO, QPSO, and HPSO for comparative performance analysis. They are especially beneficial when the computational expense for evaluating the objective function is significant or when conventional gradient-based approaches are unable to achieve appropriate results. The considered algorithms are efficient due to the population-based approach strategy and the ease of implementation. While QPSO is an improved version of PSO, considering a probabilistic approach throughout the optimization process, HPSO is a hybridised version with a semi-deterministic nature.

4.5.3 Fmincon

The *fmincon* function is a powerful optimization tool provided by MATLAB Optimization Toolbox. It is designed to effectively handle a wide range of constrained optimization problems. In contrast to its counterpart, *fminsearch*, which is mainly intended for unconstrained optimization, *fmincon* provides a flexible and efficient approach to optimizing scalar functions while satisfying both linear and nonlinear constraints, irrespective of whether these are equalities or inequalities.

Fmincon employs a variety of optimization techniques, including interior-point methods, active-set methods, and sequential quadratic programming (SQP), making it highly adaptable and applicable to a variety of optimization problems. *fmincon* allows the incorporation of derivatives, which can enhance the speed of convergence, rendering it especially advantageous in cases where analytical derivatives are easily obtainable. However, in cases where the objective and constraint functions lack analytical derivatives, obtaining these gradients can be computationally expensive and challenging. The success of the optimization process is dependent upon the quality of the starting point chosen to initiate the algorithmic search. Insufficient or poorly selected initial points may result in suboptimal solutions or convergence towards local optima. *fmincon* may encounter difficulties when dealing with non-convex and multi-modal problems characterized by the presence of multiple local optima. In instances of this kind, it is possible for the algorithm to settle on a local minimum instead of the global minimum. Further details and examples of the application of fmincon are available in the Mathwork Documentation.

4.5.4 Fminsearch

The *fminsearch* algorithm is a very effective optimization tool included in MATLAB's Optimization Toolbox. The tool is specifically developed for unconstrained nonlinear

TH-3534_186104002

optimization, rendering it very advantageous for scenarios involving the determination of the minimum or maximum value of a scalar function with numerous variables without any restrictions imposed by boundaries or other limitations.

It is appropriate for functions that are not readily differentiable or for cases where obtaining derivatives is computationally expensive or impractical, as it doesn't need any gradient information. The optimization methodology used by *fminsearch* is the Nelder-Mead method, which is sometimes referred to as the simplex search or pattern search. The strategy used in this method can be characterized as a trial-and-error process. It involves iteratively refining the search in the parameter space through the contraction, expansion, and reflection of the simplex.

Although *fminsearch* is a simple method, it is a reliable tool for many optimization situations. The effectiveness of the method is enhanced when the objective function exhibits a smooth and well-behaved nature, leading to convergence towards a local minimum in most cases. *fminsearch* function does not provide a guarantee of finding a global minimum. The selection of initial points may influence the final result, and in the case of functions that are highly non-convex and possess several local optima, the algorithm may get trapped in a poor solution.

In order to use the *fminsearch* function, it is necessary to provide a starting estimate for the solution, while the optimization function is given as a parameter. The constraints, such as the bounds for the optimised variables, can be handled separately in the objective function formulation. The output corresponds to the optimal values of the parameters considered, which minimizes the objective function. The Mathwork Documentation can be referred to for more information about *fminsearch.*

4.5.5 Particle Swarm Optimization (PSO)

Functionally, for an optimization problem with N decision variables, the PSO algorithm generates a population of particles within an N-dimensional search space. Each of these particles has two characteristics, namely position and velocity. Each particle, the position of which is determined by a combination of N coordinates (corresponding to the N decision variables), is accelerated continuously towards the global optima using the velocity vector. Ideally, the particles explore the search space through recurring iterations and finally arrive at the position of the global optimal solution. Throughout the successive iterations, each particle keeps track of its previous position coordinates and best position so far, corresponding to the one simulating the best objective function value (personal best position value). Meanwhile, the

TH-3534_186104002

population, as a whole, tracks the overall best position attained globally so far in the search operation (global best position value).

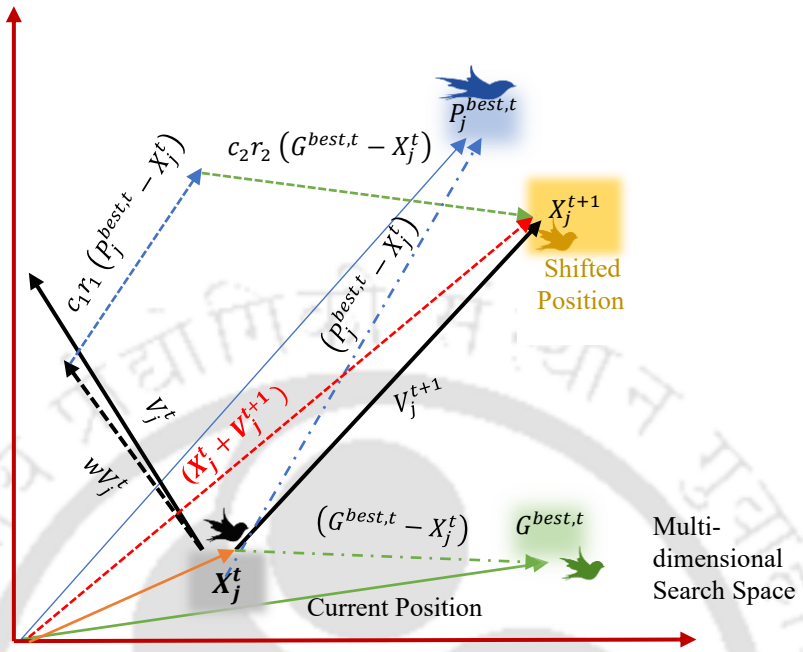


Figure 4.16. Illustration of the updation of the position of a particle in the PSO algorithm

A proper balance of exploitation in the areas near the best positions and exploration within the search domain is necessary to ensure convergence to the actual global optima. Equations (4.42) and (4.43), as given below, explain the iterative calculations involved in updating the velocity of each particle to accelerate the position in each iteration.

$$Velocity\ Update:\ V_{i,j}^{t+1} = wV_{i,j}^t + c_1r_1\left(P_{i,j}^{best,t} - X_i^t\right) + c_2r_2\left(G_i^{best,t} - X_{i,j}^t\right) \quad (4.42)$$

$$Position\ Update:\ X_{i,j}^{t+1} = X_{i,j}^t + V_{i,j}^{t+1} \quad (4.43)$$

The polygon method of vector addition can effectively demonstrate the process involved in shifting a particle's position, as shown in Figure (4.16). In the above equations, *i* stands for the decision variable number (*i=1 to N*), *j* stands for the particle number in the population *(j=1 to swarm size),* and *t* stands for the iteration value. Therefore, the update-equations above are for the i^{th} decision variable of j^{th} particle for the t^{th} iteration, *V* is the velocity, and *X* is the position. The value $P_{i,j}^{best,t}$ is the personal best value of the i^{th} coordinate of the j^{th} particle, based on the tracking up to the t^{th} iteration. Similarly, $G_i^{best,t}$ is the value of i^{th} coordinate of the global best position, determined by considering the whole population, based on the position of particles till the present iteration (t^{th} iteration). The objective function values are computed using the

TH-3534_186104002

updated position values of the particles, and the personal best and global best position values are reinitialized based on this. The inertia weight *w* exerts control over the effect of the velocity from the preceding iteration on the updated value. In order to stochastically modify the relative influence of the personal and global best values, the coefficients r_1 and r_2 varied randomly within the range of [0, 1], are used. The cognitive (c_1) and social acceleration (c_2) coefficients are user-defined and manage the movement of particles toward the personal best and global best positions. These tuning parameters impact the equilibrium between exploration and exploitation throughout the search process. A progressive depreciation in the value of *w* was maintained in this study to encourage effective exploration at the initial iterations and enhanced exploitation towards the final iteration values. The pseudocode for the PSO algorithm is given in the Appendix

4.5.6 Quantum Particle Swarm Optimization (QPSO)

Integrating the principles of quantum mechanics and PSO, Sun et al. (2004) devised the probabilistic optimization algorithm called quantum-behaved particle swarm optimization (QPSO). The trajectory of a particle in standard PSO is determined by its position and velocity; the particle proceeds in accordance with the predetermined trajectory as described by Newtonian mechanics. The uncertainty principle proposes that the position and velocity of a particle cannot be determined concurrently. Based on this idea, the QPSO algorithm uses the Schrödinger wave function $\Psi(x, t)$ to define a particle instead of exact position and velocity. QPSO assumes that each particle is subject to the effects of a quantum potential field. (Sun et al., 2004; Sun et al., 2012). The quantum potential field corresponds to the fundamental forces exerted on the particle, similar to the functioning of potential energy fields. This helps define a domain that maps out the probability of locating a particle at different locations within the search space. Potential wells are formed within this field, where the probability values are high, signifying a possible local or global optimal location. The square of the wave function is used as the probability density function for the potential field. The global best value of the swarm and the personal best values of each particle are adjusted after each iteration, like PSO.

The "local accelerator" defines the probability value that a particle will be present at a particular position, and the "mean best" value for the swarm is the mean value of the personal best values of each variable till the current iteration. These parameters guide the particles toward the global optimum position.

TH-3534_186104002

The QPSO algorithm for an optimization problem with *N* decision variables and a swarm having a population of *Npop* number of particles, set to run for a maximum iteration value of *Iter_Max,* defines various factors as explained below. The j^{th} particle in the population in t^{th} iteration is represented as $X_j^t = \left(x_{1,j}^t, x_{2,j}^t, x_{3,j}^t, \ldots . x_{N,j}^t\right)$. The personal best position value for this particle can be defined as $P_j^{best,t} = \left(p_{1,j}^t, p_{2,j}^t, p, \ldots . p_{N,j}^t\right)$, while the global best particle for the swarm is given as $G^{best,t} = (g_1^t, g_2^t, g_3^t \ldots . g_N^t)$. The mean of the personal best values for the swarm is defined as $M^{best,t} = (m_1^t, m_2^t, m_3^t \ldots . m_N^t)$, where each variable is calculated as

$$m_i^t = \left(\frac{1}{Npop}\right) \sum_{j=1}^{Npop} p_{i,j} \tag{4.44}$$

The local attractor for the j^{th} particle in the population for the t^{th} iteration is $LA_j^t = (L_{1,j}^t, L_{2,j}^t, L_{3,j}^t \ldots . L_{N,j}^t)$. The local attractor value for each of the variables of a particle is calculated using the following equation incorporating the weighted influence of the personal and global best values.

$$L_{i,j}^t = p_{i,j}^t * \phi_{i,j}^t + \left(1 - \phi_{i,j}^t\right) g_i^t \tag{4.45}$$

Where

$$\phi_{i,j}^t = \frac{c_1 r_{i,j}^t}{(c_1 r_{i,j}^t + c_2 R_{i,j}^t)} \tag{4.46}$$

In the above expression, acceleration coefficients c_1 and c_2 are typically assigned the same values. The values $r_{i,j}^t$ and $R_{i,j}^t$ are random numbers distributed uniformly between (0,1). In order to translate the probabilistic locations of particles into concrete positions, which can be updated within the search space, Monte Carlo inverse transformation is applied to the probability density function. This results in the transformation of the quantum state into a classical state, which is used to define the new position of the particle as given in the equations below

$$x_{i,j}^{t+1} = \begin{cases} L_{i,j}^t + \left(\frac{\beta_{i,j}^t}{2}\right) \ln\left(\frac{1}{u_{i,j}^{t+1}}\right) \; when \; k_{i,j}^t \geq 0.5 \\ L_{i,j}^t + \left(\frac{\beta_{i,j}^t}{2}\right) \ln\left(\frac{1}{u_{i,j}^{t+1}}\right) when \; k_{i,j}^t < 0.5 \end{cases} \tag{4.47}$$

$$\text{Where } \beta_{i,j}^t = 2\alpha^t |x_{i,j}^t - m_i^t| \tag{4.48}$$

TH-3534_186104002

$$\alpha^t = \frac{(\alpha_1 - \alpha_2)(Max_Iter - t)}{Max_Iter} + \alpha_2 \tag{4.49}$$

The values $u_{i,j}^{t+1}$ and $k_{i,j}^{t}$ are random numbers uniformly distributed on (0, 1). *α1* and *α2* are user-defined positive real numerical values corresponding to the beginning and end values of *α*, respectively.

Overemphasis on global search in QPSO leads to slow convergence, while the same on local search results in premature convergence to local minima. This aspect can be controlled by establishing a balance between exploration and exploitation. For clarity, the pseudocode for QPSO is provided in the Appendix.

4.5.7 Hybrid Particle Swarm Optimization Algorithm (HPSO)

Stochastic optimization algorithms apply weighted random searching to explore the domain. These methods can explore areas with low gradients by employing random search tactics. However, it is crucial to acknowledge that these approaches involve substantial computational costs and show slow convergence speed. Deterministic algorithms that depend on gradients demonstrate accelerated convergence speeds by using derivative information to choose the most efficient search path. However, a prevalent limitation of these algorithms is their vulnerability to local minimum entrapment, leading to premature convergence. Deterministic methods have difficulties when attempting to minimize functions that have flat regions with low gradients around the global minimum. The ultimate convergence of deterministic, gradient-based algorithms relies significantly on the initial starting point.

Hybrid Particle Swarm Optimization (HPSO) is an innovative approach that merges the rapid convergence and exploitation capabilities of *fmincon,* a gradient-based optimization tool offered by MATLAB Optimization Toolbox, with the exploration possibilities of PSO. *Fmincon* is engineered to efficiently address a diverse set of constrained optimization problems when the starting values for the decision variables are initialized appropriately. The suggested technique involves alternating sequential execution of the PSO and *fmincon* algorithms. The initial values for the decision variables required for executing the *fmincon* function are the global minimum position coordinates to which PSO converged after a specific number of iterations. The global minimum was recalibrated using the converged outcomes after a specified number of iterations of the *fmincon* algorithm. This optimization strategy reduces the computational expense of the PSO, allowing it to converge more rapidly to the optimal region,

TH-3534_186104002

where further enhancement can be done. The pseudocode for HPSO is provided in the Appendix.

4.5.8 Artificial Bee Colony Algorithm (ABC)

This metaheuristic algorithm, mimicking the foraging behaviour of honey bees, was introduced by Dervis Karaboga (2005). Karaboga and Basturk (2007) compared the performance of ABC with other swarm-based algorithms, such as PSO and genetic algorithm, in optimising multivariate optimisation and showed that ABC is capable of getting out of local optima in most cases. ABC considers a colony of artificial bees with employed bees, scout bees and onlooker bees as components. A collective of simulated bees navigates the search space or the domain in a stochastic manner. The algorithm is controlled by the factors-colony size and number of repeated iterations (maximum number of cycles). In each successive iteration, the food quality is improved, eventually leading to the best solution for optimised parameters. The number of food sources is equal to the number of employed bees, which is also equal to the number of onlooker bees. Therefore, the colony size is twice the number of food sources. The algorithm initially generates a set of potential solution sets (food sources) randomly within the domain. The i^{th} food source can be represented as $x_i = (x_i^1, x_i^2 \ldots x_i^N)$ for an N-dimensional search space. The values $x_i^1, x_i^2 \ldots x_i^N$ are randomly generated potential optimal values for the parameters to be optimised. The amount of nectar is the measure of quality or fitness of the chosen set of parameter values represented by the food source considered. The fitness values for minimisation problems are generally taken as the inverse of the objective function values. During the initialisation step, employed bees randomly choose food source locations and determine the solution fitness of these sources. The fitness information of these food sources are then conveyed to the onlooker bees. In the second step, after sharing the fitness information, each employed bee visits the food source region based on its memory from the previous cycle and picks a new food source in the vicinity. During the third stage, the onlooker bees choose a food source based on the fitness information. Upon reaching the chosen food source, she selects a nearby food (candidate food source) source based on the fitness value of the nearby source compared to the previously chosen food source. The location of the best of the two food sources is maintained in the memory of the onlooker bee. The vicinity of each food source is thoroughly searched in this manner by improving it a number of times to find the source with the best quality nectar, i.e., the best fitness value. If a food source is not improving even after a limited number of trials, the source is abandoned. The scout will randomly move around in the domain, searching for a probable food source, and will be responsible for exploration. The abandoned

TH-3534_186104002

food source is replaced by a better source chosen by the scout bees. In the original model of ABC, the number of scout bees was maintained as one. The probability of selection ($prob(x_i)$) of i^{th} food source (x_i) by the onlooker bees is based on Equation (4.50)

$$prob(x_i) = 0.9 * \frac{fit(x_i)}{\max(fit(x_i))} + 0.1 \tag{4.50}$$

The modification of the food source chosen based on information from the employed bee to produce a candidate source v_i^j in the vicinity uses the following equation.

$$v_i^j = x_i^j + \phi_i^j (x_i^j - x_k^j) \tag{4.51}$$

$$fitness(v_i) = \begin{cases} 1 + obj(v_i), & if obj(v_i) > 0 \\ 1/(1 + |obj(v_i)|), & otherwise \end{cases} \tag{4.52}$$

In this equation, $obj(v_i)$ is the objective function value at the updated food source v_i , the value of *j* varies from 1 to *N*, the number of dimensions, *i* varies from 1 to *M*, and *k* is a number not equal to *i*, chosen randomly and varies from 1 to *M*. The factor ϕ_i^j is a random number in [-1,1]. The term $(x_i^j - x_k^j)$ decreases in value as the optima approach, showing adaptive reduction of step length. Once all the v_i values are obtained a comparison of performance-based on the fitness values based on Equation (4.52) is done with the current solution set x_i^j. Then, a greedy selection operation is performed wherein the sources with the best fitness values replace the less fit ones.

4.5.9 Modified Artificial Bee Colony Algorithm (MABC)

Several modifications were incorporated into the original ABC to formulate the MABC. One of these was the opposition-based learning (Tizhoosh, 2005). The stochastic algorithms initialise the population randomly within the domain. Rapid convergence may result if the randomly selected values are close to the optimal solution. However, if the random initialization is extremely far from the optimal values, or in the worst-case scenario, if these estimates are located in the opposite direction of the optimal values, then the optimization will take significantly longer to resolve. Therefore, a corresponding food source from the opposite direction in the domain is chosen for each food source, thereby eliminating the possibility of a worst-case scenario occurring due to arbitrary assignment. If x_i is a food source in the random initialisation, then a food source in the opposite direction $\tilde{x_i}$ is computed as given by Equation (4.53)

TH-3534_186104002

$$\widetilde{x_i} = a_i + b_i - x_i \tag{4.53}$$

Here a_i and b_i is upper and lower bound values, respectively. Either $\widetilde{x_i}$ or x_i is chosen further by analyzing the fitness values for both cases.

Improving upon the position update rule proposed by Chung et al. (2014), MABC incorporates the following position update rule.

$$v_i^j = \lambda * g_{best}^j + (1 - \lambda) * \left(x_i^j + \phi_i^j\left(x_i^j - x_k^j\right)\right) \tag{4.54}$$

Where v_i^j is the updated value of the j^{th} parameter of the i^{th} food source. g_{best}^j is the global best value till the current iteration, other parameters hold the same definition as in the case of the original ABC. The term λ is defined as

$$\lambda = \frac{iter - c}{maxcycle - c + 1} \tag{4.55}$$

The value of the term λ is set to zero until the number of iterations reaches one-tenth of the maximum number of iterations. This approach is employed in order to maintain the randomness and prevent any potential misdirection caused by pseudo-global optima in the beginning steps. Subsequently, the value of λ is determined in accordance with Equation (4.55). In case the global best (g_{best}) fails to exhibit improvement within a certain number of iterations (in this study, this limit was set as $1/15^{th}$ of the maximum number of iterations), the parameter c is set equal to the present iteration number. In this scenario, the global best position is discarded and replaced with a randomly selected food source location. Variable c has been integrated into the algorithm to mitigate the issue of becoming trapped at a local minimum and increase diversity. The new position update equation helps in guiding the search towards the global optimum. The probability calculation equation is modified so that the probability of the food source estimated for the previous iteration is also given due consideration. This is done so that if a particular food source had a good probability value previously, then it will contribute to the probability value of the new food source chosen from the vicinity of that food source. The modified probability equation is given below.

$$prob(x_i) = 0.95 * 0.5 * \frac{fitness(x_i)}{\max\left(fitness(x_i)\right)} + 0.95 * 0.5 * prob(x_i) + 0.05 \tag{4.56}$$

The equation is a combination of information about the fitness of the current food source ($fitness(x_i)$), the fitness of the best food source in the colony (max($fitness(x_i)$), the previous probability $prob(x_i)$, and a degree of randomness (0.05) to update the probability

TH-3534_186104002

value. Factor 0.5 is used in addition to 0.95 as a balancing scale factor to prevent over-domination of the influence of either the fitness values or the previous probability. The weighting factors (0.95 and 0.05) control the trade-off between exploiting the known best solutions (i.e., the solutions with high fitness and high previous probability) and exploring new solutions (i.e., low previous probability or by introducing randomness).

The last modification included in the MABC algorithm is the integration of Euclidean distance-based computing to determine the neighbourhood during the onlooker bee phase. Instead of randomly picking neighbours or using probabilistic methods, the selection process involves choosing neighbours that are located within a certain Euclidean distance threshold from the present food source (x_i),. This method of selection of neighbourhood (Equation (4.57)) was proposed by Karaboga and Gokremli (2012). The optimal neighbour within this neighbourhood replaces the existing food sources (x_i).

$$x_i \leq mean(d_i) \tag{4.57}$$

Where d_i is the sum of Euclidean distance of i^{th} food source from all the other points. The pseudocode of MABC is provided in the Appendix

4.5.10 Hybrid Artificial Bee Colony Algorithm (HABC)

The hybrid ABC proposed in this study is a simple combination of the ABC algorithm and *fminsearch* function. The *fminsearch,* a tool from the MATLAB Optimization Toolbox, excels at unconstrained nonlinear optimization and is ideal for functions with no gradient information. It employs the Nelder-Mead method, a trial-and-error procedure that is most effective for smooth functions. While dependable, it may not converge to the global minimums when an appropriate starting point for the search is not defined, particularly in non-convex landscapes. The advantage of *fminsearch* over *fmincon* is its simplicity and applicability to non-differentiable functions, which eliminates the computational expense of obtaining derivatives. Further insights on *fminsearch* can be found in the Mathwork documentation.

HABC involves repeating the ABC algorithm iteratively for a preset number of iterations, followed by the *fminsearch* algorithm for a number of iterations. This cycle continues till the maximum number of iterations set for the problem is reached. The implementation of the ABC algorithm facilitates a comprehensive exploration of the search space. This approach guarantees the consideration of a wide range of alternative solutions during the initial stages, allowing the algorithm to avoid being trapped in suboptimal solutions. Combining this with the *fminsearch* algorithm, which specializes in local refinement, provides the algorithm with a

TH-3534_186104002

balanced approach that increases the convergence rate and accuracy of the final solution. ABC is well-suited for complex, multi-modal problems, while *fminsearch* is notably effective for fine-tuning solutions around a local minimum. The ABC can provide an appropriate initial point for *fminsearch* to start optimising. HABC is particularly useful in cases where the optimisation landscape is characterised by multiple local minima, making it challenging for a global optimisation strategy to converge to the actual global minima. The integration of both algorithms takes advantage of their mutually beneficial features, presenting a robust and flexible optimization methodology that can effectively address complex problems. Furthermore, the HABC is highly adaptable as the iteration numbers allocated for the two algorithms can be varied according to the problem requirements. The pseudocode of HABC is given in the Appendix

4.6 FEM Formulation of Centrifuge FSC

4.6.1 General

The pore pressure-based inverse analysis further increased the computational expense of the objective function. The time and space step constraints restrict the existing EFDM model. Therefore, the recently developed FEM model for the *N*g FSC settlement (Srinivasulu, 2023), which is free from such limitations, was used for pore pressure-based inverse analysis for the centrifuge case. The settlement and void ratio profiles were derived using the FEM model, and the pore pressure values were computed based on these data. A brief description of the formulation is given below

4.6.2 FEM model for centrifuge FSC

The governing equation of FSC under centrifugal action proposed by Bharat and Ubaid (2019) can be written in the form:

$$\frac{\partial}{\partial z}\left\{\frac{k(e)}{1+e}\left(N_z(\gamma_s-\gamma_w)+\frac{\mathrm{d}\sigma'}{\mathrm{d}e}\frac{\partial e}{\partial z}\right)\right\}+\gamma_w\frac{\partial e}{\partial t}=0 \tag{4.58}$$

Using a weighted residual approach, the variational statement of Equation (4.58) was derived as

$$\left[\frac{k(e)}{1+e}\left(N_z\gamma_c+\frac{\mathrm{d}\sigma'}{\mathrm{d}e}\frac{\partial e}{\partial z}\right)\right]_0^L-\int_0^L\frac{k(e)}{1+e}\left(N_z\gamma_c+\frac{\mathrm{d}\sigma'}{\mathrm{d}e}\frac{\partial e}{\partial z}\right)\frac{\mathrm{d}v}{\mathrm{d}z}\mathrm{d}z+\int_0^L\gamma_w\frac{\partial e}{\partial t}v\mathrm{d}z=0, \tag{4.59}$$

TH-3534_186104002

where v is the variation in the void ratio. γ_c is the difference between solid and water unit weight. Application of the free draining boundary condition at the top and impermeable boundary condition at the base results in the boundary term (1st term) in Equation (4.59) equal to zero. The resulting equation is the variational statement applied with the described boundary conditions, given as

$$\int_0^L \gamma_w \frac{\partial e}{\partial t} v \mathrm{d}z - \int_0^L \frac{k(e)}{1+e}\left(N_z\gamma_c + \frac{\mathrm{d}\sigma'}{\mathrm{d}e}\frac{\partial e}{\partial z}\right)\frac{\mathrm{d}v}{\mathrm{d}z}\mathrm{d}z = 0. \tag{4.60}$$

Then, the spatial domain was discretized into small elements, and each element was mapped to a master element. The coordinate (η) of the master element ranges from -1 to 1. Next, the material space, void ratio and its variation, and temporal rate of void ratio were discretized using the quadratic Lagrange shape functions. The discretized equations were substituted in Equation (4.60), and using the arbitrariness of the variation, the FEM equation was obtained as

$$\mathbf{M}\dot{\hat{\boldsymbol{e}}} - \mathbf{K}\hat{\boldsymbol{e}} = \mathbf{0} \tag{4.61}$$

where **M** and **K** are global mass and stiffness matrices given by

$$\mathbf{M} = \sum \gamma_w \mathbf{N}^{\mathrm{T}}\mathbf{N} J \mathrm{d}\eta, \tag{4.62}$$

$$\mathbf{K} = \sum \frac{k(e)}{1+e}\left(N_z\gamma_c e^{-1}\mathbf{B}^{\mathrm{T}}\mathbf{N} + \frac{\mathrm{d}\sigma'}{\mathrm{d}e}\mathbf{B}^{\mathrm{T}}\mathbf{B}\right) J \mathrm{d}\eta. \tag{4.63}$$

Here,

$$\mathbf{N} = \left[\frac{\eta(\eta-1)}{2}, \quad (1-\eta^2), \quad \frac{\eta(1+\eta)}{2}\right], \tag{4.64}$$

J is half of the elemental material height (L_e) i.e., $J = \frac{L_e}{2}$, $\mathbf{B} = \frac{1}{J}\frac{\mathrm{d}\mathbf{N}}{\mathrm{d}\eta}$. Next, the temporal domain was discretized using θ-method (Reddy, 2019), which resulted in

$$(\mathbf{M} - \theta\Delta t\mathbf{K}^{n+1})\hat{\boldsymbol{e}}^{n+1} - (\mathbf{M} + (1-\theta)\Delta t\mathbf{K}^{n})\hat{\boldsymbol{e}}^{n} = \mathbf{0} \tag{4.65}$$

Equation (4.65) is a nonlinear equation that was solved using the Newton-Raphson method. The Newton-Raphson method was set using the Taylor series expansion as

$$(\mathbf{M} - \theta\Delta t\mathbf{K}_{\boldsymbol{m}}^{n+1})\hat{\boldsymbol{e}}_{\boldsymbol{m}}^{\boldsymbol{n+1}} - (\mathbf{M} + (1-\theta)\Delta t\mathbf{K}^{n})\hat{\boldsymbol{e}}^{n} + \mathbf{K_T}\left(\hat{\boldsymbol{e}}_{\boldsymbol{m+1}}^{\boldsymbol{n+1}} - \hat{\boldsymbol{e}}_{\boldsymbol{m}}^{\boldsymbol{n+1}}\right) = \mathbf{0} \tag{4.66}$$

TH-3534_186104002

Here, $\mathbf{K_T}$ is the tangent-stiffness matrix, the derivative of $(\mathbf{M} - \theta\Delta t\mathbf{K}^{n+1})\hat{\boldsymbol{e}}^{n+1}$ with respect to $\hat{\boldsymbol{e}}^{n+1}$. Previously converged solution $(\hat{\boldsymbol{e}}^{n})$ was considered the initial guess of the Newton-Raphson scheme. In this study, θ was set to one. The Newton-Raphson was stopped when the error $E = \frac{\|\hat{e}_{m+1}^{n+1} - \hat{e}_{m}^{n+1}\|}{\hat{e}^{n}}$ was less than 10^{-6}.

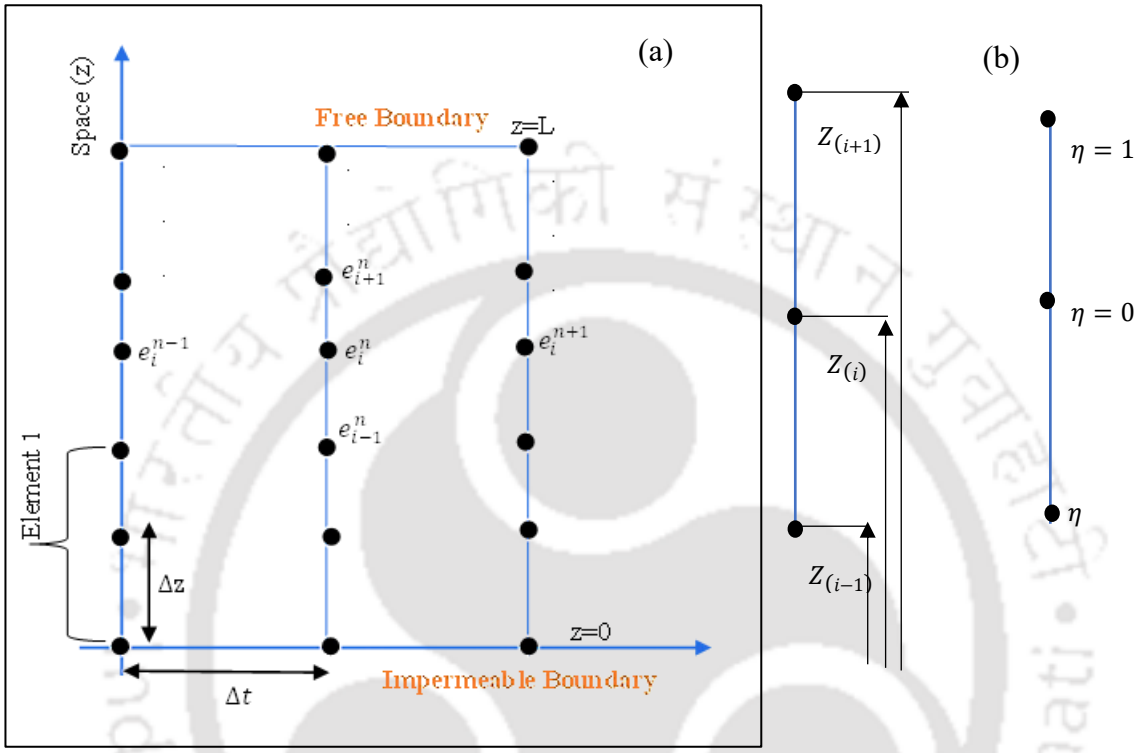


Figure 4.17: Numerical grid for FEM formulation (a) details of the mesh with nodes (b) mapping the physical element (element (i)) to one-dimensional quadratic master element.

For a sample with no free water above, when the consolidation progresses, a water column is formed on the top of the settling boundary. The hydrostatic pressure due to this water column on the settling boundary at any time $(\sigma_{H_{top}}(t))$is given as

$$\sigma_{H_{top}}(t) = S(t) * \gamma_w * \left(R - h_0 + S(t)\right) * \frac{\omega^2}{g} \tag{4.67}$$

Where *S(t)* is the settlement at any time, *R* is the centrifuge radius, h_0 is the initial height of the sample, *ω* is the angular velocity of the centrifuge. The total stress at the base of the sample at any time is the sum of the stress due to the weight of the water in the voids and the self-weight of the solid particles.

$$\sigma_{Total_{base}}(t) = \left[\int_{z=0}^{z=L} N_z(e\gamma_w + N_z\gamma_S * 1)\, dz\right] + \sigma_{H_{top}}(t) \tag{4.68}$$

TH-3534_186104002

Effective stress at the bottom can be computed by using the compressibility correlation and the void ratio at the bottom of the sample at a given time. $\sigma'(e_b)$. The total pore pressure at the base of the sample at any time is computed using the equation

$$\sigma_{P_{base}}(t) = \sigma_{Total_{base}}(t) - \sigma'(e_b) \tag{4.69}$$

4.7. Summary

This chapter detailed the experimental and numerical methods adopted in the study, along with the significant properties of the materials analyzed. It covered the procedures for oedometer and benchtop centrifuge tests conducted on four soil slurries, including detailed explanations of the sample preparation process. The EFDM-based numerical solution for the 1g and *N*g FSC governing equations were presented, emphasizing the importance of selecting appropriate time and space step values to ensure stable and consistent solutions. The MATLAB code used for simulating settlement behavior under 1g and *N*g conditions were outlined through a flowchart, providing clarity on the numerical implementation.

The effective radius concept was explained and the estimation of the time scale exponent was discussed. These aspects are essential for interconverting centrifuge and field-scale observations. Two graphical methods were also explained for back-predicting hydraulic conductivity function parameters from centrifuge settlement curves. The first method relies on the shape and translation of the settlement curve on a log-time scale, while the second uses variance calculations based on the curve's spread for back prediction.

Additionally, the chapter explored the development of inverse analysis approaches using optimization algorithms for back-estimating constitutive function parameters. It employed conventional algorithms like PSO and ABC, along with three proposed methods: HABC (a hybrid version of ABC), HPSO (a hybrid version of PSO), and MABC (a modified ABC). The advanced QPSO algorithm, based on quantum mechanics principles, was also explained.

Lastly, an FEM-based numerical model for simulating settlement and pore pressure dissipation was presented, highlighting its advantage over the EFDM approach due to its ability to use larger time steps without compromising solution accuracy.

The next chapter presents the experimental results from oedometer and centrifuge consolidation tests conducted on these slurries, comparing the effectiveness of centrifuge tests as an alternative method for studying compressibility.

TH-3534_186104002

5. Experimental Analysis of Soft-Soil Consolidation Behavior

5.1 General

This chapter presents the results of the oedometer and centrifuge consolidation tests on four soil slurries. Carefully prepared slurries of RS, BCS, JBC and Kao-I were used in the tests. In the first section, the results of oedometer consolidation tests conducted on each sample was presented. In the second section, the outcomes from bench-top centrifuge consolidation tests were presented. A comparison was made to elaborate on the effectiveness of centrifuge tests as a viable alternative for compressibility studies of these materials

5.2 Oedometer Test Results

5.2.1 General

The standard oedometer was used to conduct the tests. The settlement behaviour and compressibility of the RS, BCS, JBC and Kao-I are discussed in the section. The relevant properties of these materials were presented in Table 4.1. The initial void ratio and moisture content of the oedometer samples were attempted to be maintained within the range of the observed initial void ratio of centrifuge samples. The samples were loaded at a slow rate to prevent the slurry from flushing out of the mould.

5.2.2 Conventional consolidation test on soil slurries

The initial conditions of the samples were presented in Table 5.1.

Table 5.1 Initial properties of the slurries used to conduct the oedometer tests

Material	BCS	RS	MBC	Kao-I
Initial Height (*m*)	0.0072	00093	0.0094	0.0083
Initial Void Ratio	3.48	1.258	4.54	2.37

The oedometer test on BCS was conducted at a moisture content of 106% to match the centrifuge model's initial moisture conditions. The oven-dried sample passing through a 425-micron sieve was thoroughly mixed with distilled water and placed overnight in a desiccator to allow proper moisture distribution within the sample. The slurry was placed in the oedometer mould and loaded slowly, starting with 5kPa. The test was terminated at 400 kPa. The final water content, final void ratio, and void ratio corresponding to different loads were computed. The experiment was time-consuming as it took 37 days to complete the settlement at each load step (Figure 5.1(a)). The settlement data under each load were presented in Figure 5.1(b). The

TH-3534_186104002

sample settled by 44% of its initial height at the end of the test. Various consolidation parameters for BCS were evaluated using expressions based on Terzhagi's theory. These parameters were presented in Table 5.2. The estimated hydraulic conductivity was computed using the coefficient of consolidation and coefficient of volume compressibility under each loading. These values were plotted against the corresponding final void ratios under each of the loads, as shown in Figure 5.2 (b). Here, it is assumed that the entire sample has a uniform void ratio.

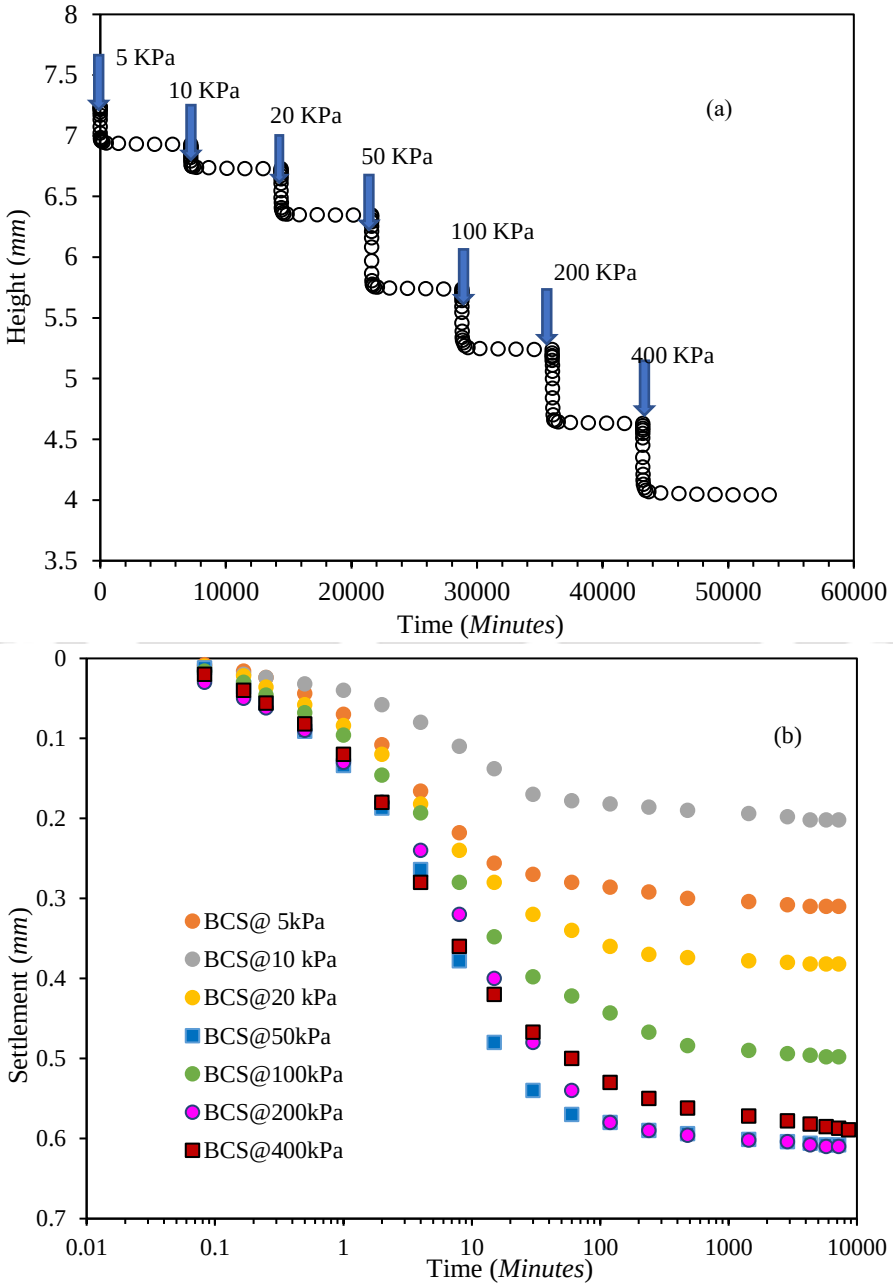


Figure 5.1: Oedometer test conducted on BCS (a) Change in height with time at different load steps (b) settlement plots under various loads

TH-3534_186104002

Table 5.2: Consolidation parameters estimated from oedometer tests on BCS

Load (kPa)	Coefficient of compressibility a_v (m^2/kN)	Compression Index c_c	Volumetric Compressibility m_v (m^2/kN)	Coefficient of consolidation c_v (m^2/s)	Hydraulic Conductivity k(m/s)
5	3.89E-02		9.06E-03	2.83E-08	2.51E-09
10	2.33E-02	0.354	5.09E-03	7.17E-08	3.58E-09
20	2.16E-02	0.785	4.99E-03	2.84E-08	1.39E-09
50	1.45E-02	1.095	4.14E-03	1.82E-08	7.38E-10
100	5.77E-03	0.958	1.79E-03	1.27E-08	2.22E-10
200	3.22E-03	1.069	1.11E-03	2.20E-08	2.40E-10
400	1.99E-03	1.324	8.00E-04	1.44E-08	1.13E-10

The hydraulic conductivity was observed to reduce by 93% at the end of consolidation under 400 kPa. The effective stress versus void ratio relationship was plotted as shown in Figure 5.2 (a). The non-linear relation between the effective stress and void ratio and the same between the hydraulic conductivity and void ratio was clearly noticeable.

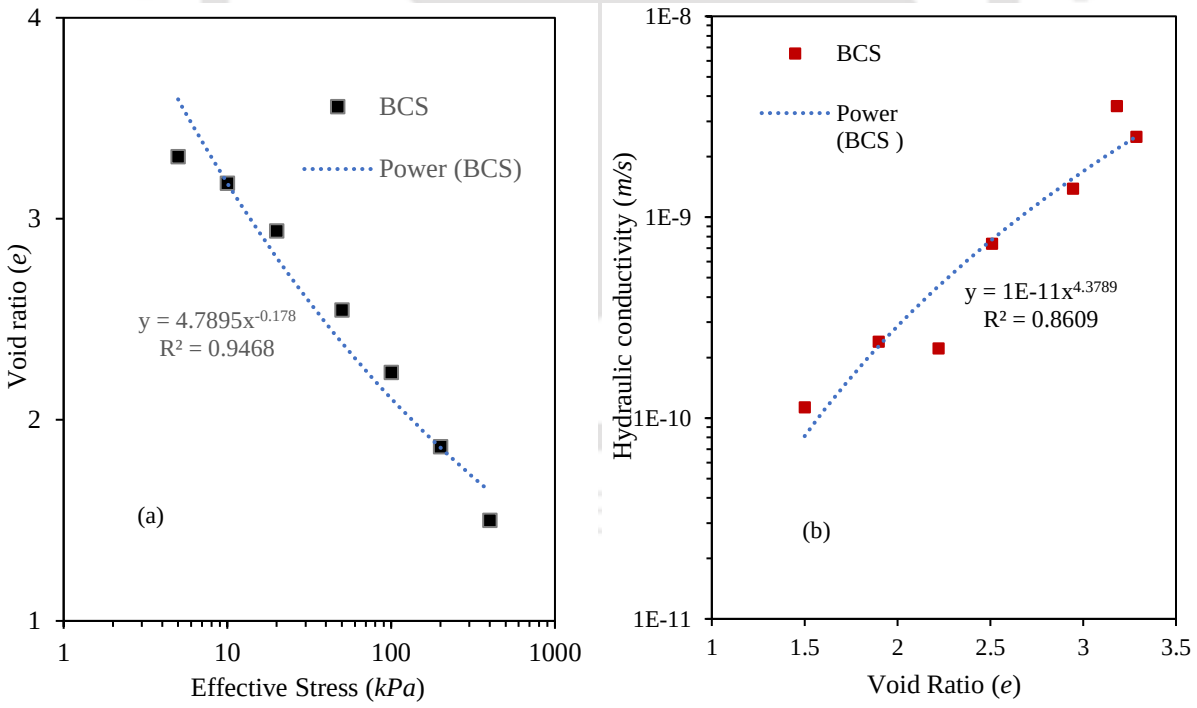


Figure 5.2: Constitutive relationships from the oedometer observations (a) Effective stress versus void ratio relationship for BCS (b) Hydraulic Conductivity versus void ratio relationship for BCS

TH-3534_186104002

The oedometer test for red soil was conducted at an initial water content of 40%, which corresponds to the liquid limit of the soil. Loading was done step by step from 5kpa to 400 kPa. Care was taken to prevent abrupt loading, which can result in the formation of internal channels or seepage of samples out of the mould due to sudden pore pressure build-up.

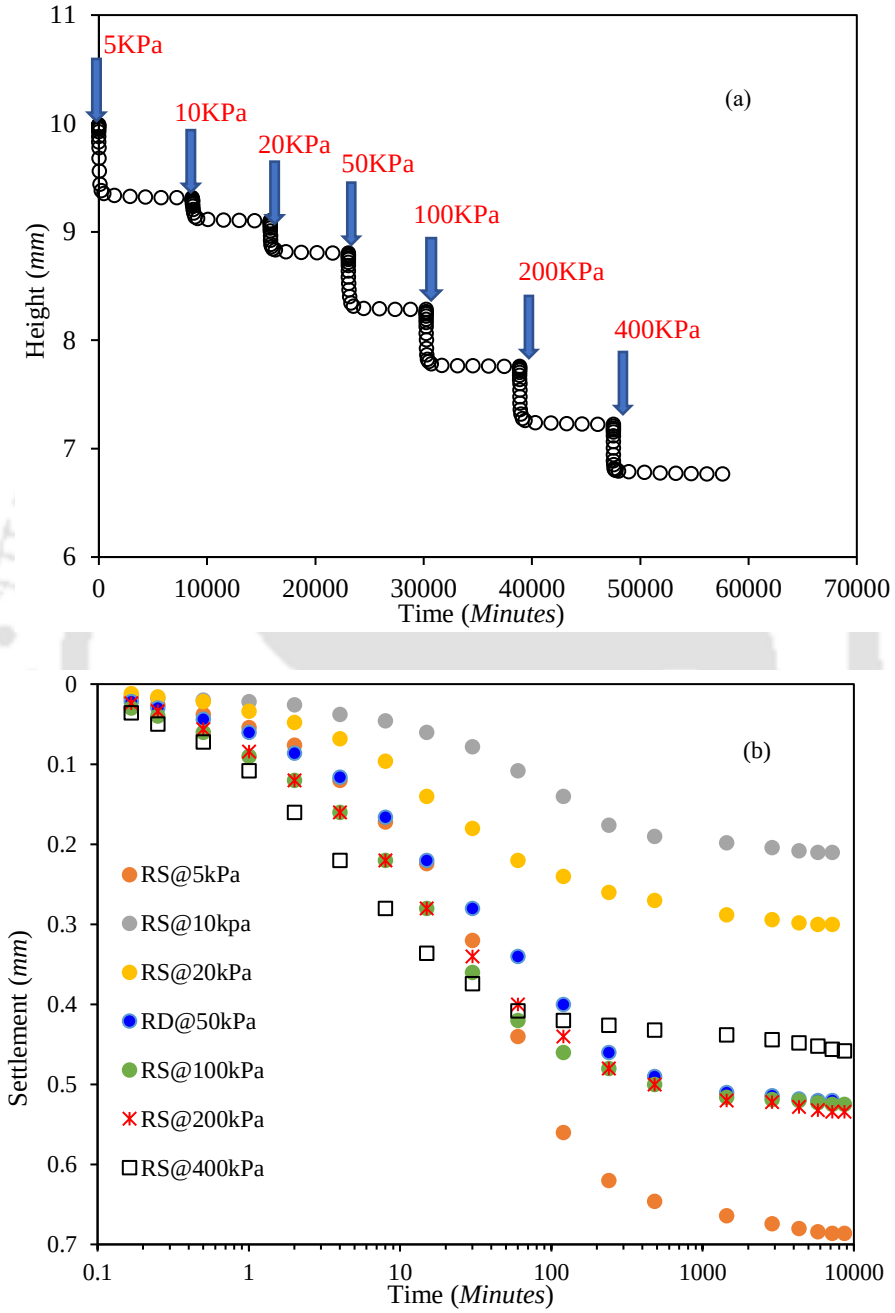


Figure 5.3: Oedometer test conducted on RS (a) Change in height with time at different load steps (b) settlement plots under various loads

TH-3534_186104002

Table 5.3: Consolidation parameters estimated from oedometer tests on RS

Load (kPa)	Coefficient of compressibility a_v (m^2/kN)	Compression Index (c_c)	Volumetric Compressibility m_v (m^2/kN)	Coefficient of consolidation c_v (m^2/s)	Hydraulic Conductivity k(m/s)
5	3.32E-02		1.47E-02	7.36E-08	1.06E-08
10	1.02E-02	0.169	4.61E-03	1.30E-07	5.89E-09
20	7.28E-03	0.242	3.42E-03	5.41E-08	1.82E-09
40	4.24E-03	0.320	2.12E-03	3.87E-08	8.05E-10
80	2.56E-03	0.426	1.37E-03	2.80E-08	3.76E-10
200	1.31E-03	0.434	7.50E-04	3.67E-08	2.70E-10
400	5.70E-04	0.378	3.50E-04	4.01E-08	1.38E-10

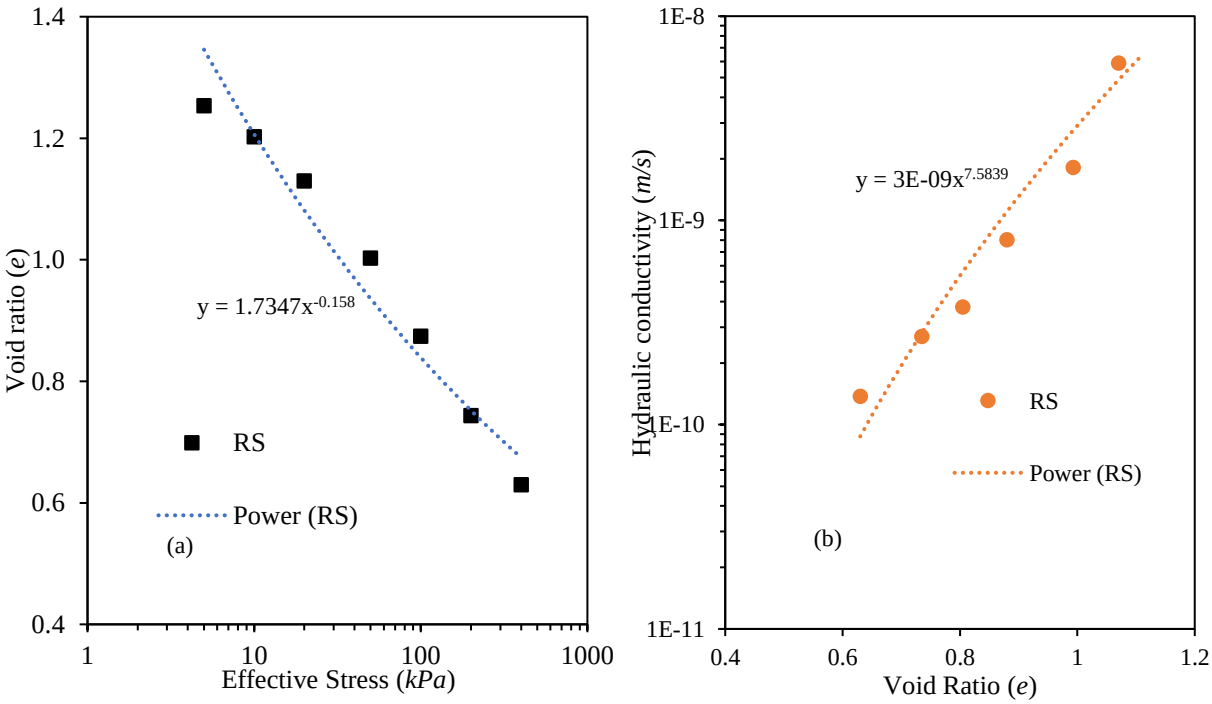


Figure 5.4: Constitutive relationships from the oedometer observations (a) Effective stress versus void ratio relationship for RS (b) Hydraulic Conductivity versus void ratio relationship for RS

The sample was allowed to consolidate fully under each load, which lasted for a total of 38 days (Figure 5.3(a)). An overall settlement of 32.6% was observed in case of RS. The settlement of the sample under various loads was given in Figure 5.3(b). The initial sample height was reduced by 27% at the end of all loading steps. The reduction in height due to the settlement was caused by the particles coming closer to each other.

TH-3534_186104002

Consequently, the void ratio reduced, and thus the reduction in the estimated hydraulic conductivity values. The estimated hydraulic conductivity function and the effective stress versus void ratio relations for RS were presented in Figures 5.4 (a and b). The hydraulic conductivity was observed to reduce considerably under each loading, resulting in an overall reduction of 98% at the end of the test.

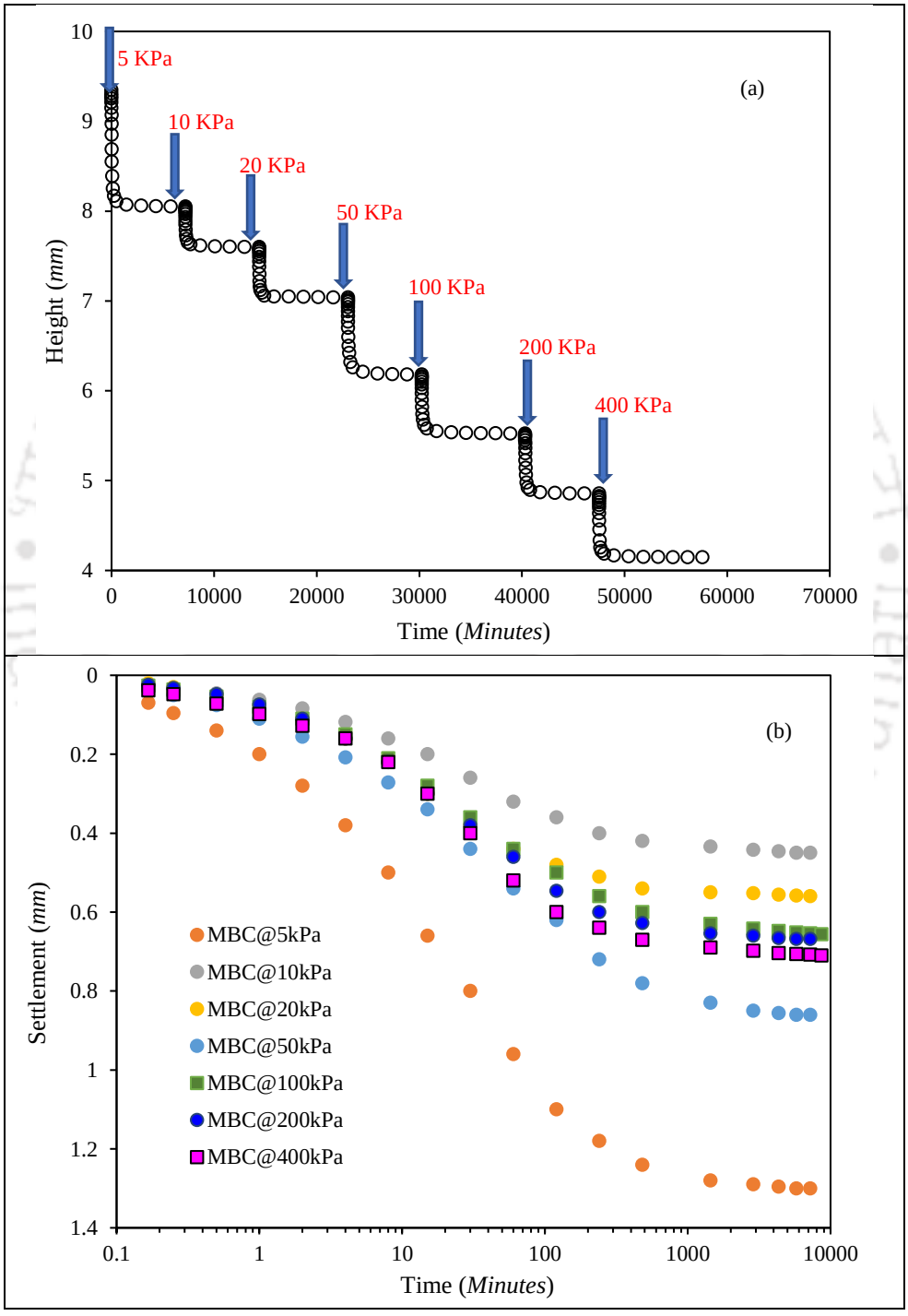


Figure 5.5: Oedometer test conducted on MBC (a) Change in height with time at different load steps (b) settlement plots under various loads

TH-3534_186104002

Table 5.4: Consolidation parameters estimated from oedometer tests on MBC

Load (kPa)	Coefficient of compressibility a_v (m^2/kN)	Compression Index (c_c)	Volumetric Compressibility m_v (m^2/kN)	Coefficient of consolidation c_v (m^2/s)	Hydraulic Conductivity k(m/s)
5	1.54E-01		3.22E-02	6.25E-08	1.98E-08
10	5.34E-02	0.886	1.18E-02	9.08E-08	1.05E-08
20	3.29E-02	1.093	7.88E-03	5.54E-08	4.28E-09
40	1.72E-02	1.296	4.69E-03	3.41E-08	1.57E-09
80	7.23E-03	1.202	2.19E-03	3.50E-08	7.53E-10
200	3.96E-03	1.316	1.36E-03	2.41E-08	3.22E-10
400	2.11E-03	1.399	8.50E-04	1.77E-08	1.48E-10

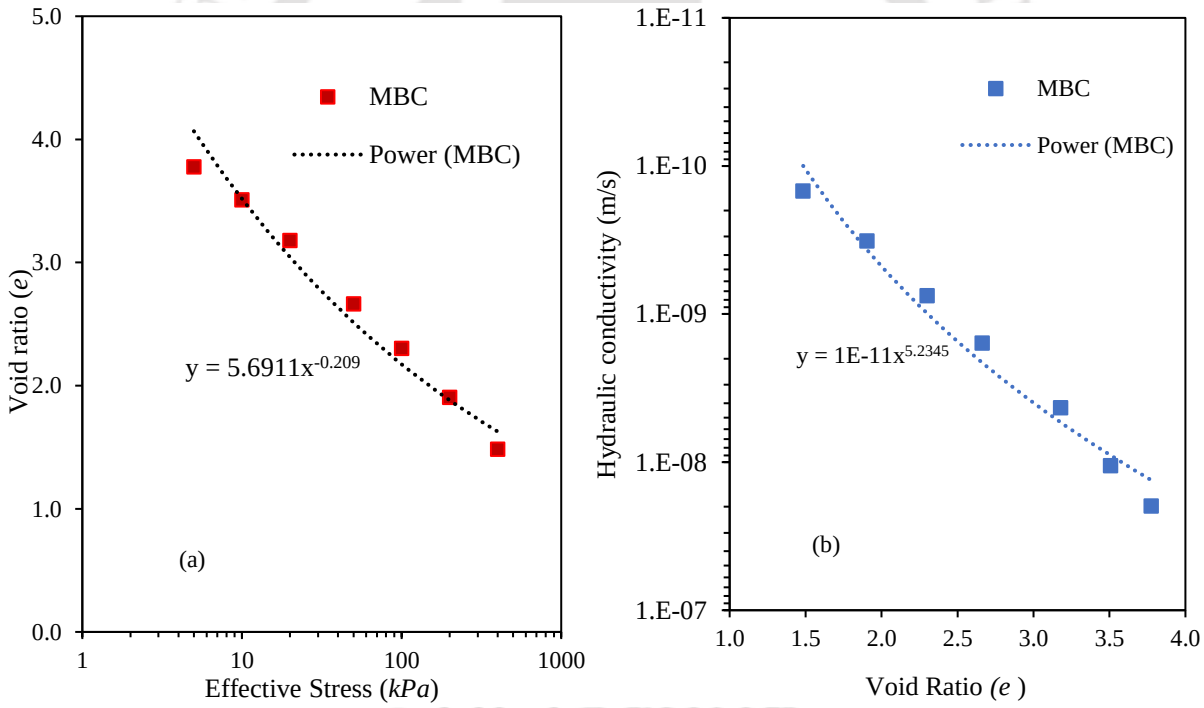


Figure 5.6: Constitutive relationships from the oedometer observations (a) Effective stress versus void ratio relationship for MBC (b) Hydraulic Conductivity versus void ratio relationship for MBC

The sample was dried, and the void ratio values and other parameters were determined, as presented in Table 5.3.

The MBC sample was prepared at a moisture content of 84%. Under careful loading from 5kPa to 400kPa, the sample was stage-wise consolidated. Under each loading step, sufficient time was provided to ensure at least 90% consolidation. The timeline for the process was presented

TH-3534_186104002

in Figure 5.5 (a). The test took 40 days to complete, including the unloading. The sample was then dried to obtain the solids content and void ratio values. Relevant consolidation properties were presented in Table 5.4. All the parameters were observed to reduce continuously under successive step-by-step loading.

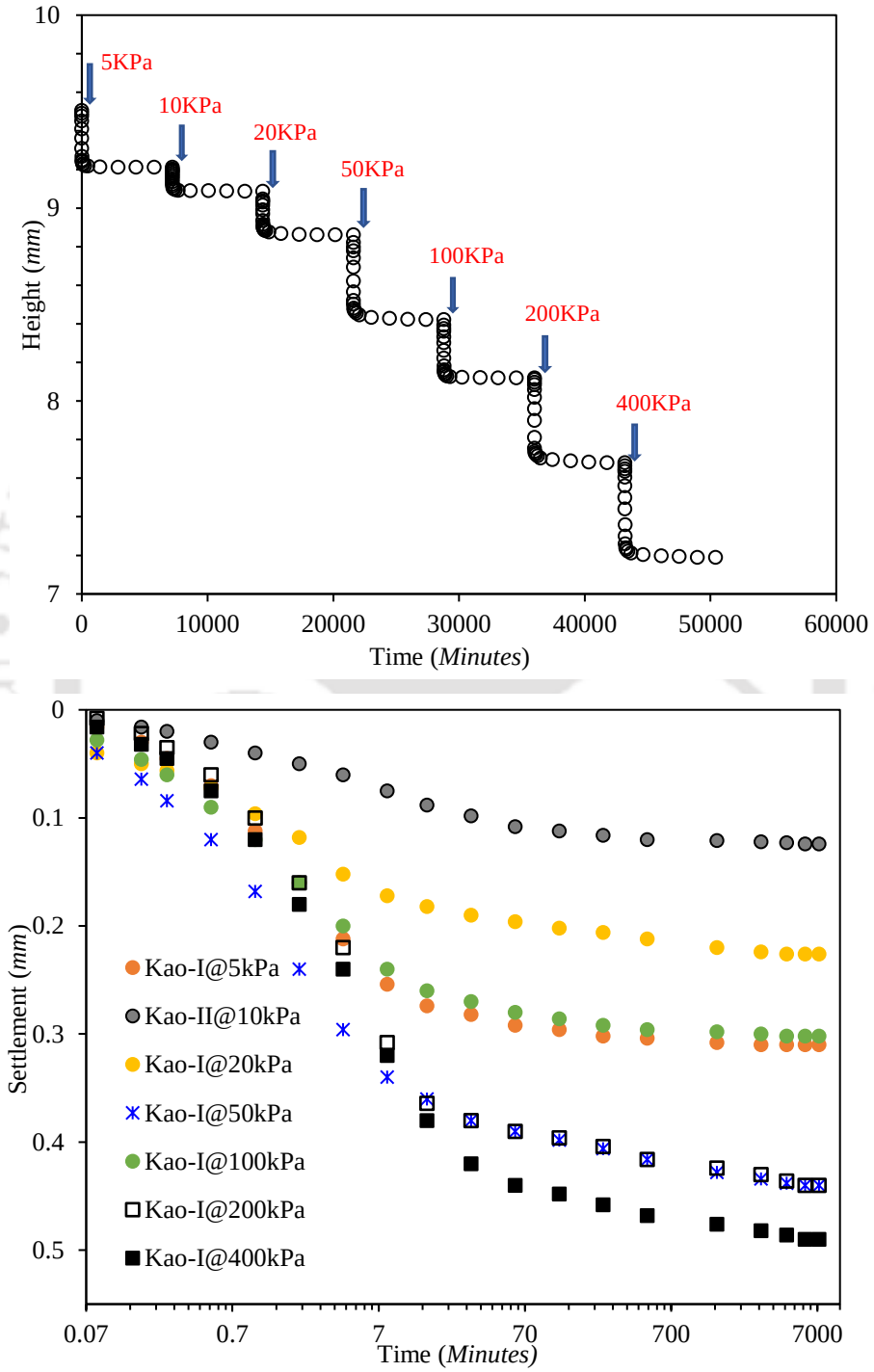


Figure 5.7: Oedometer test conducted on Kao-I (a) Change in height with time at different load steps (b) settlement plots under various loads

TH-3534_186104002

Table 5.5 Consolidation parameters estimated from oedometer tests on Kao-I

Load (kPa)	Coefficient of compressibility a_v (m^2/kN)	Compression Index (c_c)	Volumetric Compressibility m_v (m^2/kN)	Coefficient of consolidation c_v (m^2/s)	Hydraulic Conductivity k(m/s)
5	1.88E-02		6.73E-03	3.20E-07	2.11E-08
10	7.40E-03	1.23E-01	2.68E-03	2.31E-07	6.06E-09
20	6.85E-03	2.28E-01	2.55E-03	7.90E-08	1.98E-09
40	5.66E-03	4.27E-01	2.25E-03	1.18E-07	2.60E-09
80	1.83E-03	3.04E-01	7.50E-04	1.79E-07	1.31E-09
200	1.25E-03	4.15E-01	5.40E-04	1.92E-07	1.01E-09
400	7.40E-04	4.93E-01	3.50E-04	3.72E-07	1.28E-09

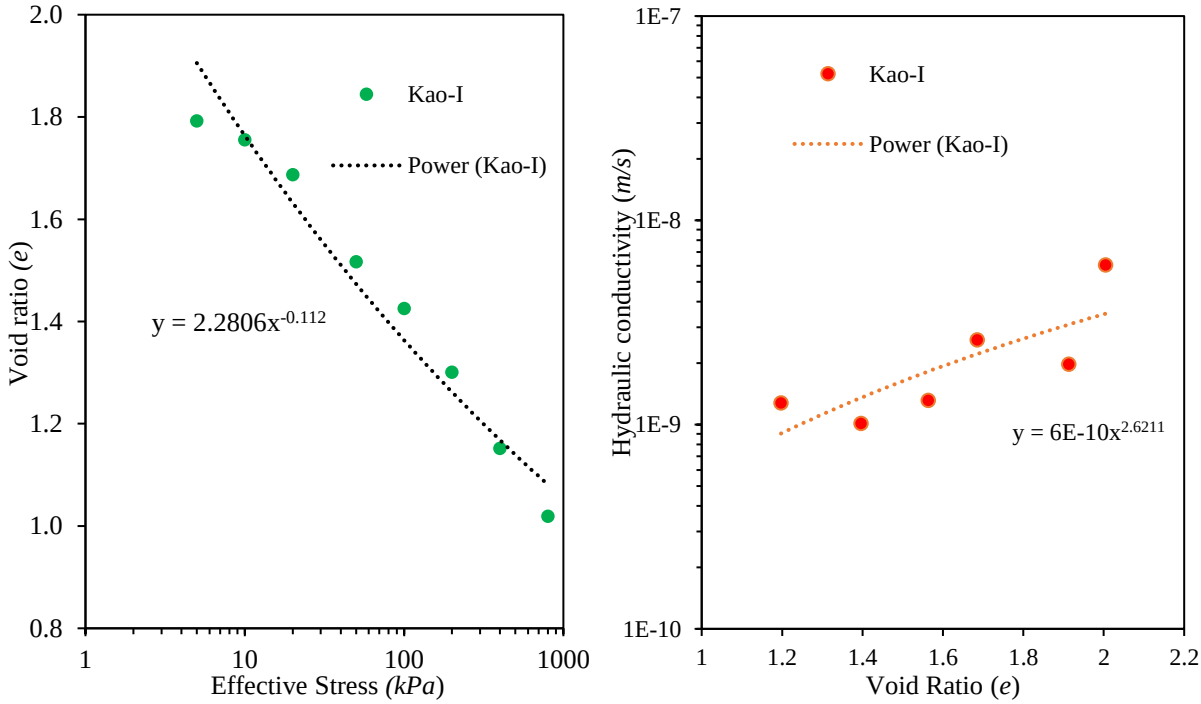


Figure 5.8: Constitutive relationships from the oedometer observations (a) Effective stress versus void ratio relationship for Kao-I (b) Hydraulic Conductivity versus void ratio relationship for Kao-I

The consolidated height of the sample was only 55% of the initial height. Settlement under individual loads was presented in Figure 5.5(b). The estimated hydraulic conductivity function and the compressibility functions were presented in Figure 5.6 (a-b). It was observed that the estimated hydraulic conductivity value was reduced by 99% at the end of the last loading step at 400 kPa.

TH-3534_186104002

The kaolinite (Kao-I) sample was difficult to handle in slurry form due to its extremely fine nature. The major issue was the tendency of material loss while preparing the slurry and transferring it to the consolidation mould. The initial void ratio to match with the centrifuge test was not possible to maintain as the slurry possessed high moisture content, which resulted in seepage of the sample from the mould under loading. The test was conducted at 60% moisture content, which was 1.5 times the liquid limit. Loading at each step was challenging. The sample was loaded with care from 5 kPa to 400 kPa. The test took 35 days. The loading phases of the oedometer test are shown in Figure 5.7(a). The sample height was reduced by 34.8% at the end of the test. The settlement behaviour of the Kao-I slurry under each load step was presented in Figure 5.7(b). The hydraulic conductivity function was plotted using the estimated hydraulic conductivity values corresponding to each load step. The estimated hydraulic conductivity value was observed to reduce by 94% after the final loading stage. The effective stress versus void ratio and hydraulic conductivity functions are plotted in Figures 5.8 (a-b). The consolidation properties for the samples were presented in Table 5.5.

The final consolidated stage of all samples was presented in Table 5.6.

Table 5.6 Properties of slurry samples after complete consolidation

Sample	**BCS**	**RS**	**MBC**	**Kao-I**
Final void ratio (e_f)	1.5	0.63	1.48	1.1524
Final height (mm)	4.04	6.737	4.189	7.19

5.3 Bench-top Centrifuge Test Results

5.3.1 General

In this section, the results of bench-top consolidation tests conducted on RS, BCS, MBC and Kao-I were presented. A bench-top centrifuge was explored for efficiency and speed in FSC testing. When the conventional experimental approaches take weeks to complete, this method concludes with results within a few hours. The effectiveness of bench-top centrifuge in the determination of compressibility of slurries was studied in comparison with the oedometer results. The resulting insights were presented in various subsections in this part of the chapter.

5.3.2 FSC testing of slurries in Bench-top Centrifuge

Three set of slurry samples were prepared for each material. These samples were tested independently at 1000 RPM, 1500 RPM and 2000 RPM.

TH-3534_186104002

The initial conditions, after the sedimentation process, were maintained to be the same for all three RPMS, as given in Table 5.7.

Table 5.7 Initial properties of the slurries used to conduct the centrifuge tests

Material	**BCS**	**RS**	**MBC**	**Kao-I**
Initial Height (*m*)	0.06	0.039	0.059	0.075
Initial Void Ratio	5.16	2.04	5.02	8.45

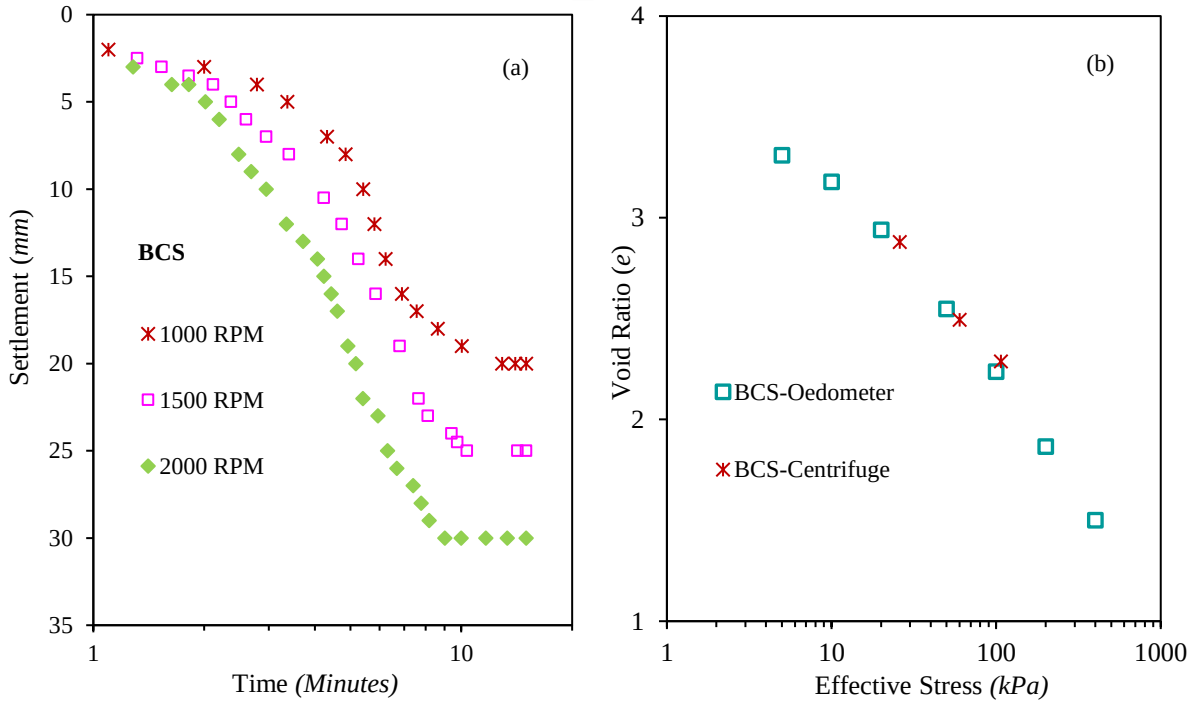


Figure 5.9: Based on bench-top centrifuge FSC test on BCS (a) Measured settlement versus time curves for various RPMs (b) Comparison of effective stress relationships from oedometer and bench-top centrifuge

In all the cases, the settlement values were observed to increase with the increase in RPM. The settlement versus time plot for the BCS sample is shown in Figure 5.9(a). The stress at the base of the sample at various RPMs was presented in Table 5.8. At 1000 RPM, the BCS sample settled by 33%, while the settlement observed in the case of 1500 RPM was 41%. At 2000 RPM, a 50% reduction in initial height was observed. The effective stress relationship obtained was compared with the oedometer result in Figure 5.9(b). A good correspondence was observed for the stress values considered.

The centrifuge settlement behaviour of RS was presented in Table 5.10(a). Due to high specific gravity and higher hydraulic conductivity (based on the estimated values from the

TH-3534_186104002

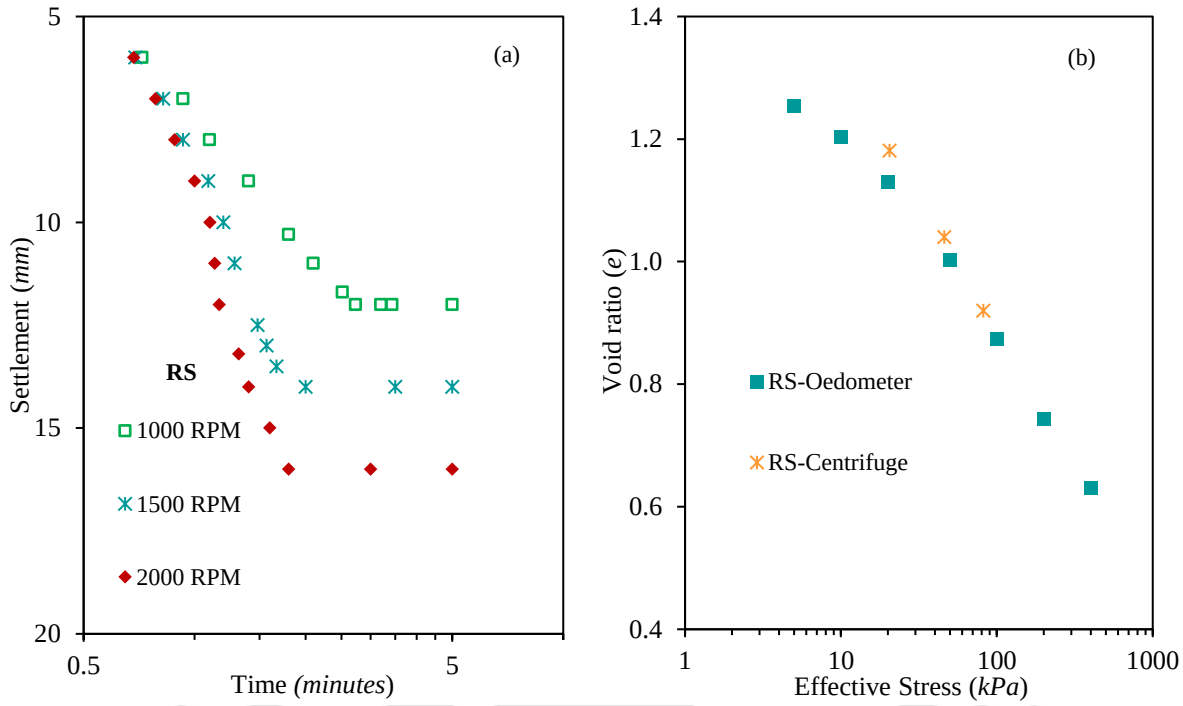


Figure 5.10: Based on bench-top centrifuge FSC test on RS (a) Measured settlement versus time curves for various RPMs (b) Comparison of effective stress relationships from oedometer and bench-top centrifuge

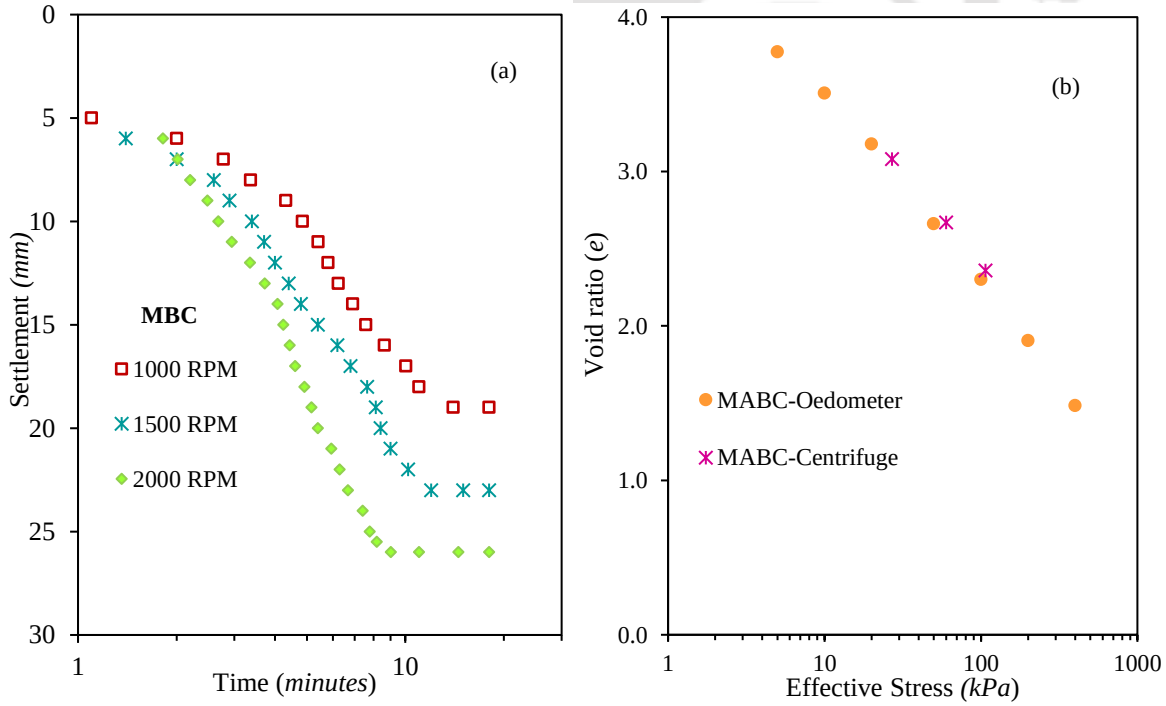


Figure 5.11: Based on bench-top centrifuge FSC test on MBC (a) Measured settlement versus time curves for various RPMs (b) Comparison of effective stress relationships from oedometer and bench-top centrifuge

TH-3534_186104002

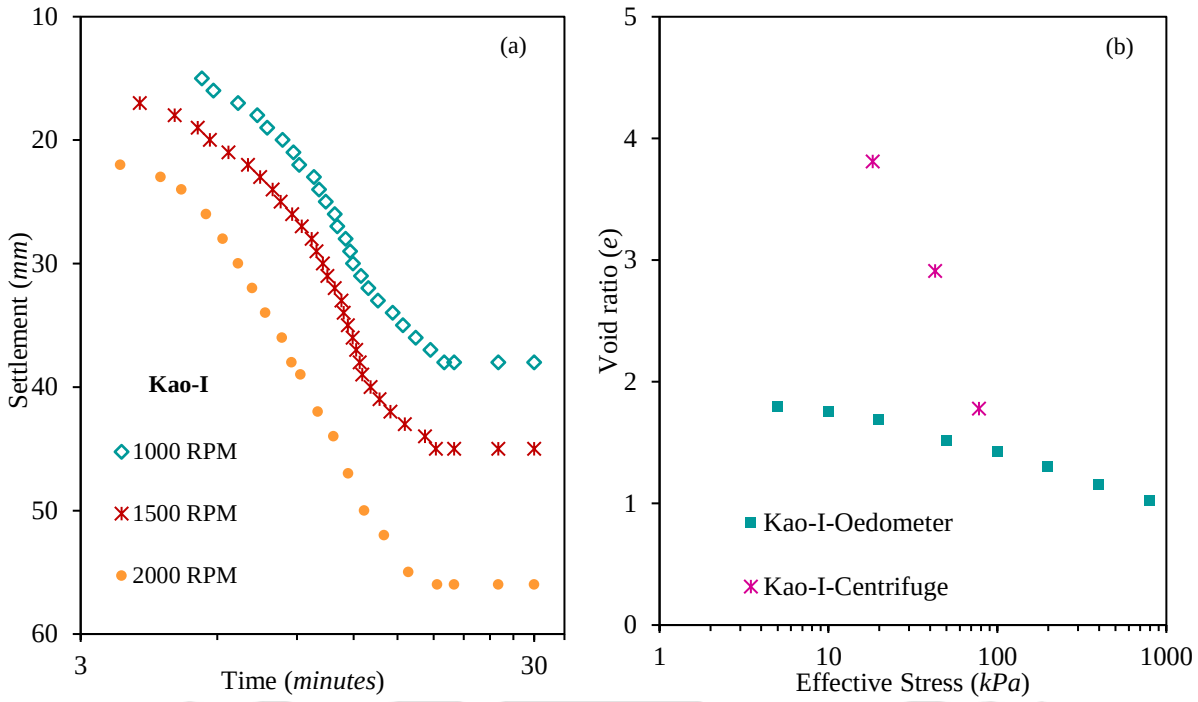


Figure 5.12: Based on bench-top centrifuge FSC test on Kao-I (a) Measured settlement versus time curves for various RPMs (b) Comparison of effective stress relationships from oedometer and bench-top centrifuge

oedometer), the rate of settlement was faster. As a result, a significant number of data points were lost in the initial phase of consolidation because of the time taken to stabilize the instrument. The RS sample settled by 31% under 1000 RPM, 36% under 1500 RPM and 41% under 2000 RPM. The effective stress relationship derived using the centrifuge observations is compared with the corresponding oedometer data in Figure 5.10(b). A good correspondence was observed between the two tests.

The MBC sample showed 35% settlement under 1000 RPM, while the settlement was 39% at 1500 RPM. At 2000 RPM, the MBC sample settled by 44%, based on Figure 5.11(a). These are within the range of BCS observations. The effective stress-void ratio correlation from the centrifuge was observed to match well with the oedometer data as per Figure 5.11(b)

The Kao-I was a challenging sample compared to all other cases. This is discussed in the next section for clarity. The sample was tested without sedimentation. The settlement plots are shown in Figure 5.12(a). The Kao-I sample was observed to settle by 50.67% at 1000 RPM, 60% at 1500 RPM and 74.6% at 2000 RPM. However, due to the inherent challenges in the preparation of identical samples for centrifuge and oedometer in this case, the initial void ratios in both cases varied by a large margin. The initial void ratio has been reported to control the compression under applied stress. While other samples of the oedometer and centrifuge

TH-3534_186104002

differed by a small offset, in the case of Kao-I, the initial void ratio in the centrifuge was 4.5 times higher than the same in the oedometer. This could be the reason for the observed mismatch between the compressibility functions presented in Figure 5.12(b).

5.4 Challenges and Limitations

Conventional oedometer tests are challenging for FSC studies due to a number of reasons. Unless customized, the sample size is generally too small to accurately measure the excessive deformations. The computations involved follow the principles of Terzaghi's theory of consolidation, which has many limitations, as discussed before. At each loading, the sample is assumed to have a uniform void ratio profile. This assumption can reduce the accuracy as large deformations tend to result in non-uniform void ratio distribution. The time taken for consolidation is long. The samples are in a slurry state, which makes the loading process challenging. If the loading is not carried out at a sufficiently slow pace, the sample will get expelled from the mould, as shown in Figure 5.13(a). Another limitation is that the primary driving force of consolidation is not self-weight. The settlements resulting from consolidation under surcharge can be more abrupt in comparison, and therefore, the rate of settlement might be higher in the initial phase.

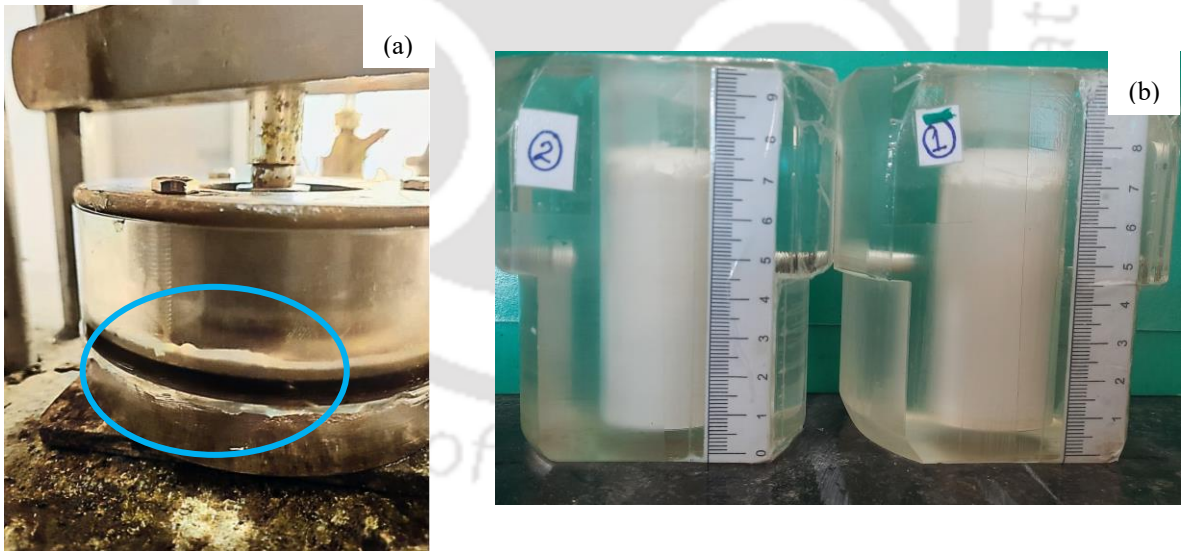


Figure 5.13 (a) Kaolinite sample leaking from the mould due to sudden loading (b) Kaolinite slurry sample undergoing slow sedimentation- without properly visible settling boundary

Handling the slurry of Kao-I was challenging. In the case of centrifuge tests, it was not possible to transfer the sample from the conical flask to the mould without loss of materials. It was

TH-3534_186104002

difficult to ensure uniform moisture distribution within the sample in this case as well. Therefore, the solids contents in the slurry samples in the centrifuge moulds were not known initially. The moulds were placed in an oven and regularly weighed till the balance showed constant weight for the consequent days to measure the mass of the solids. The initial void ratio was calculated from this value.

All samples except Kao-I were tested after sedimentation. In the case of Kao-I, the sedimentation resulted in an opaque interface due to smearing effect, which made it difficult to read the movement of the settling boundary (Figure 5.13(b)). A turbid mass exited above the moving boundary. However, as soon as the sample is rotated in the centrifuge, the stress causes the forced completion of the sedimentation process, and a discernable boundary of settlement is observed. The reduction in the height of Kao-I due to sedimentation was studied separately and noted. The centrifuge settlement data points beyond the sedimentation height were considered as the self-weight consolidation part.

The balancing of the centrifuge after the spinning started took two to three minutes. As a result, the settlement values for this duration were not recorded.

Though the centrifuge allows the testing of large water content slurries, it is difficult to place materials of thicker, paste-like consistency within the moulds for the testing. At the same time, the oedometer cannot work with watery slurries. As a result, an initial sedimentation phase was necessary for the centrifuge so that the watery slurry could undergo sedimentation and arrive at the initial void ratio condition that matched the oedometer.

A trial test was conducted on an iron tailings sample. The sample was observed to settle instantly within the time of setting up the instrument. It did not show much settlement inside the centrifuge during rotation. Slurries of large specific gravity make it difficult to get meaningful observations from small centrifuge models.

5.5 Summary

In this chapter, the compressibility and consolidation settlement behaviour of four soil slurries were experimentally analyzed using a conventional Oedometer and a bench-top centrifuge. The consolidation under step-wise loading in the oedometer was observed to be laborious and time-consuming, lasting for more than 30 days per sample. The samples were prepared at appropriate initial void ratios to match the centrifuge tests. Loading had to be done in a careful manner to avoid a sudden uprise in pore pressure resulting in spillage. The hydraulic conductivity functions were derived using the hydraulic conductivity estimated after consolidation under

TH-3534_186104002

each load step using Terzhagi's theory-based relations. It was observed that the hydraulic conductivity value was reduced by at least 90% at the end of the loading phases.

The centrifuge consolidation tests were conducted at 1000 RPM, 1500 RPM and 2000 RPM. It was observed that the settlement value was proportional to the RPM. The time taken for centrifuge samples to consolidate fully under each load (each RPM) was observed to be less than 30 minutes. The comparison of effective stress relations derived from centrifuge data and oedometer data showed appreciable correspondence for the stress values considered, provided the initial void ratio values for both tests are within the same range.

A bench-top centrifuge offers the convenience of testing slurries having a larger moisture content. Besides, larger stress values can be attained in a centrifuge using increased RPMs. A bench-top centrifuge is a viable and more efficient alternative to a conventional oedometer for deriving the the effective stress-void ratio correlations of slurry materials.

Building on the experimental approach using centrifuge presented in the present chapter, next chapter presents a numerical analysis of the scaling effects in centrifuge modeling. It investigates how variations in the effective centrifuge radius and scaling exponents impact the accuracy of replicating settlement and consolidation behavior within the FSC framework

TH-3534_186104002

6. Scaling Effects in Centrifuge

6.1 General

This chapter provides a quantitative analysis of the impact of scaling in replicating the actual behaviour of a centrifuge model based on the FSC framework. The chapter is partitioned into two segments. The initial section investigates the impact of different definitions of effective centrifuge radius on the scaled settlement value. The error in the final settlement values was analysed by comparing the results obtained when different scale factors, based on varying effective radii, were employed to scale the settlement and time values for replicating the prototype behaviour. The second section presents a quantitative analysis of how the exponent value for the scale factor, which is used to scale the model settlement time, is influenced by the degree of consolidation.

6.2 Influence of Effective Centrifuge Radius on Scaling

6.2.1 General

In the present study, the effect defining the scale factor based on the effective radius values suggested by Schofield (1980), Cooke (1991), and Fox et al. (2005) as the model to prototype conversion factor, in comparison to N at the base (N_0) was studied numerically. Free drainage was considered at the top, and the void ratio was initially assumed to be uniform throughout the depth. The stage of sedimentation was assumed to be over, and the material settled under the self-weight. The influence of these factors was observed to be mostly pronounced in the final phase of settlement. Therefore, a comparison was made based on the error in ultimate settlement values predicted for various scale factor cases. The influence of the model height to centrifuge ratio on the errors was studied, along with the impact of speed of rotation for three cases. A synthetic prototype data set was simulated using the properties of SMC, and the aforementioned factors were tested. Further, the column test data of PA-MFT and the tank test data for Phosphatic Clay were considered prototype data, and the ultimate settlement errors were compared.

6.2.2 Numerical study using synthetic prototype data

The settlement behaviour of Singapore Marine Clay (SMC) was studied in 1g and Ng conditions through numerical simulations.

TH-3534_186104002

Table 6.1. Influence of Hm/R ratio on the error in ultimate settlement when different factors are used to convert model settlement data to prototype data

***N* at base**	**Model Height H_m (m)**	**Height to radius Ratio *Hm/R***	**Radius R (m)**	**Angular velocity ω (rad/s)**	**Percentage error in ultimate settlement**			
					Base	**Fox**	**Cooke**	**Schofield**
60.0	0.450	0.10	4.500	11.437	1.075	6.021	6.911	7.670
		0.15	3.000	14.007	1.514	8.900	10.230	11.362
		0.20	2.250	16.174	1.967	11.770	13.535	15.038
		0.25	1.800	18.083	2.437	14.632	16.827	18.697
90.0	0.300	0.10	3.000	17.155	1.959	6.861	7.743	8.495
		0.15	2.000	21.011	2.400	9.720	11.037	12.160
		0.20	1.500	24.261	2.858	12.572	14.321	15.810
		0.25	1.200	27.125	3.331	15.415	17.590	19.443
104.6	0.258	0.10	2.581	19.938	2.373	7.255	8.133	8.882
		0.15	1.721	24.419	2.830	10.118	11.430	12.547
		0.20	1.291	28.193	3.283	12.952	14.692	16.175
		0.25	1.033	31.525	3.741	15.774	17.940	19.784

In order to expedite the numerical computations and facilitate the graphical presentation of error values, the study adopted an arbitrary prototype height of 27 meters. Figure 6.1 (a-d) to Figure 6.3 (a-d) compares the scaled settlement plots with the numerically simulated arbitrary prototype behaviour for various values of *Hm/R* from 0.1 to 0.25

It was observed that using the value N_0 as the conversion scale factor, the settlement behaviour is not simulated correctly in the initial stages of settlement, while the ultimate settlement value is predicted close to the simulated prototype value. If any of the other scale factors are used, the final settlement value is lower than the field simulated value, causing an assumption that the field settlement has achieved its maximum value earlier than the observed time. From Table 6.1, it can be seen that the percentage error in the ultimate settlement is smallest when the conversion factor corresponds to the N_0. For different N_0 values, the effect of H_m/R was studied. It was indicated that the N_0 value does not influence the error as much as the *Hm/R* ratio. The error was observed to increase slightly for all cases with an increase in N_0. Further, the effect of the *Hm/R* ratio is greater when conversion factors other than the N_0 were used.

The increase in error values with an increase in N_0 was compared. It was observed that for an *Hm/R* ratio of 0.1, the ultimate settlement error increased by 1.29 % when N_0 was changed-

TH-3534_186104002

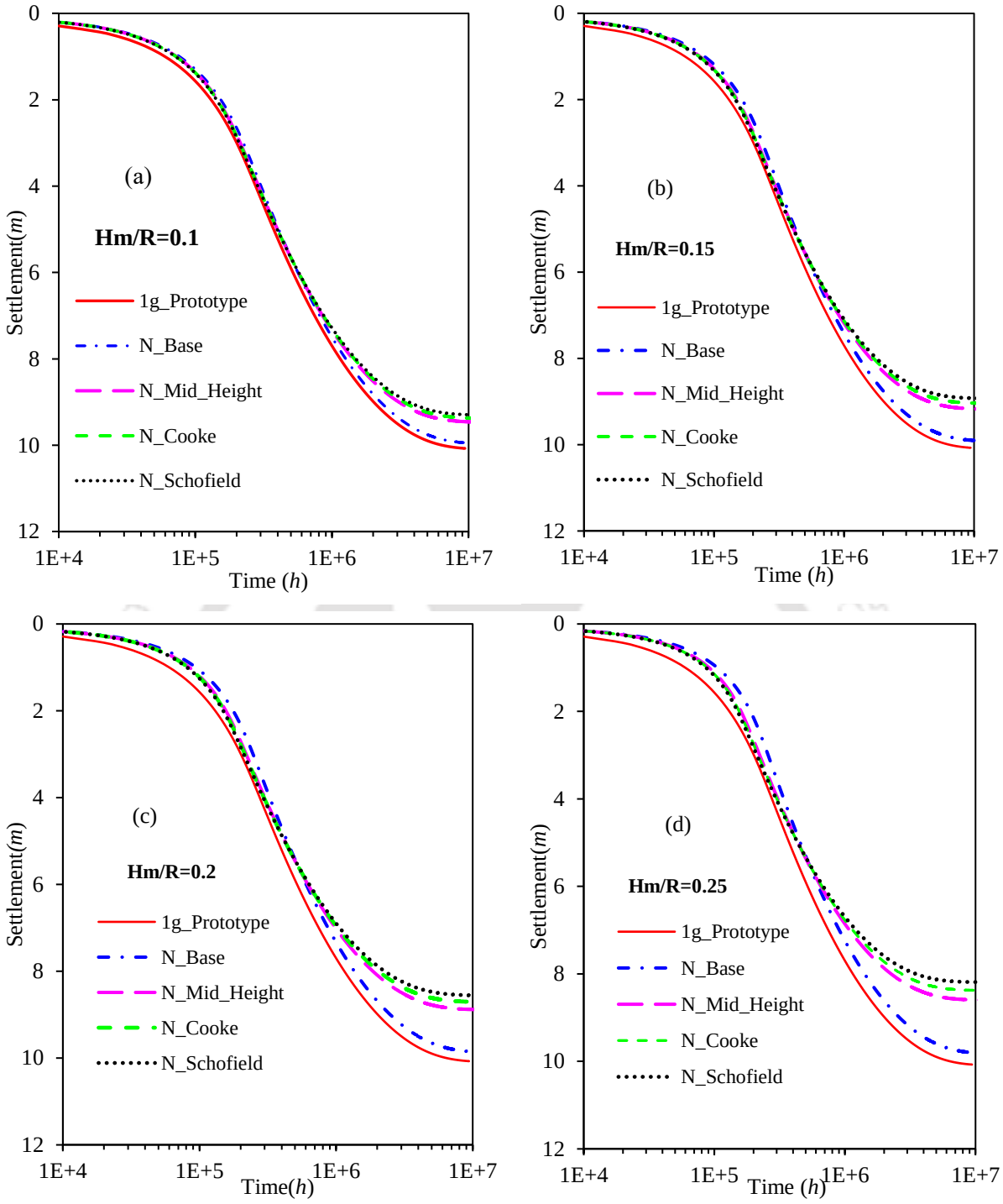


Figure 6.1 Comparison of the scaled settlement curves of SMC, with the prototype behaviour for N_o=60 when (a) Hm/R=0.1, (b) Hm/R=0.15, (c) Hm/R=0.2, and (d) Hm/R=0.25

from 60g to 104.6 g. The value of error increments for Fox, Cooke and Schofield were observed to be 1.23 %, 1.22 % and 1.21 %, respectively. At *Hm/R*=0.25, the error increments were 1.3 %, 1.14 %.1.08 % respectively, for N_0, Fox, Cooke and Schofield. The significant influence of *Hm/R* values on the error was understood by comparison of increments in errors for various

TH-3534_186104002

Hm/R values. At 60g, the error was observed to increase by 1.66 % when *Hm/R* was increased from 0.1 to 0.25 for the base case. The error increments for Fox, Cooke and Schofield were 8.6 %, 9.9 % and 11 % respectively.

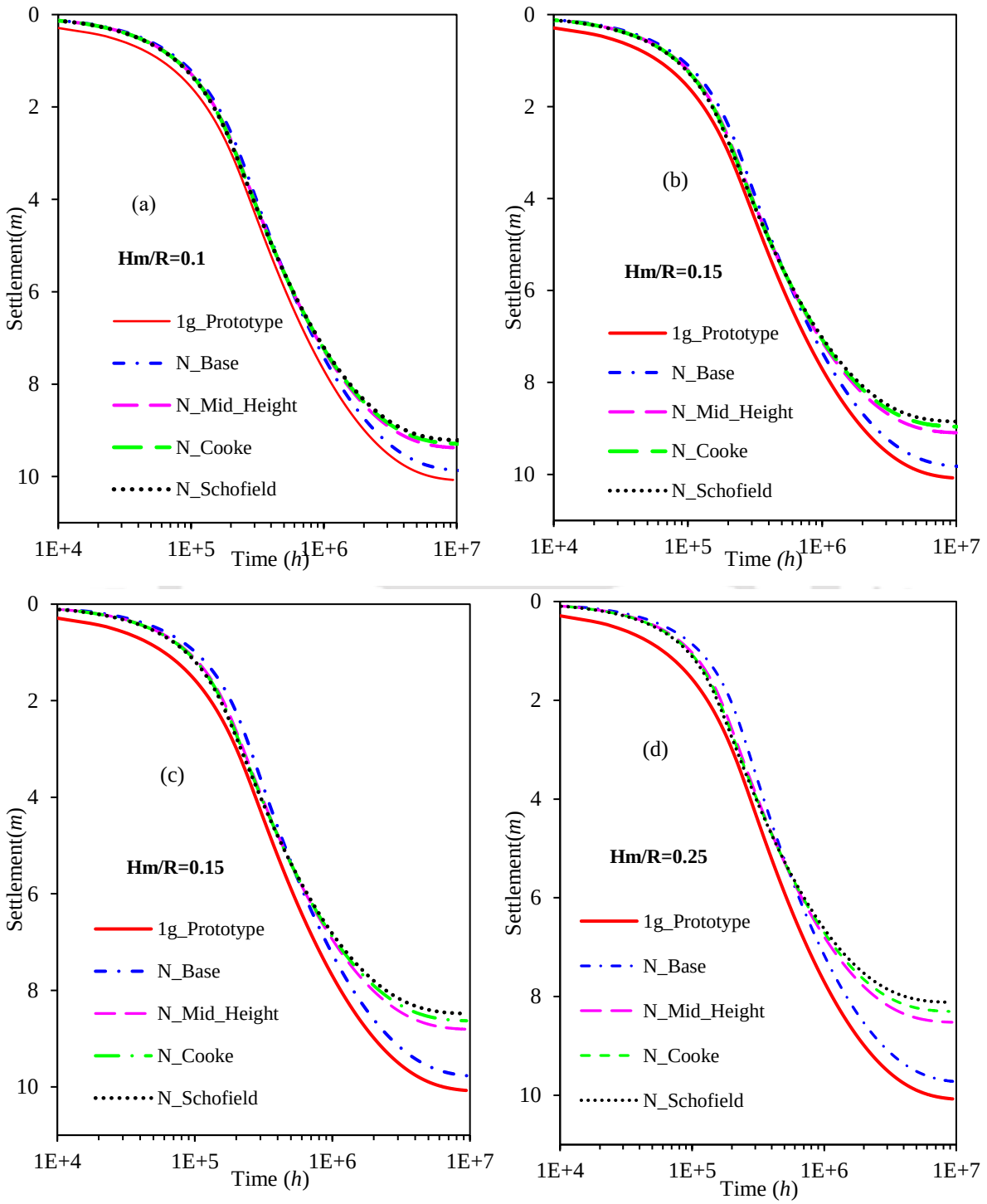


Figure 6.2 Comparison of the scaled settlement curves of SMC, with the prototype behaviour for N_o=90 when (a) Hm/R=0.1, (b) Hm/R=0.15, (c) Hm/R=0.2, and (d) Hm/R=0.25

TH-3534_186104002

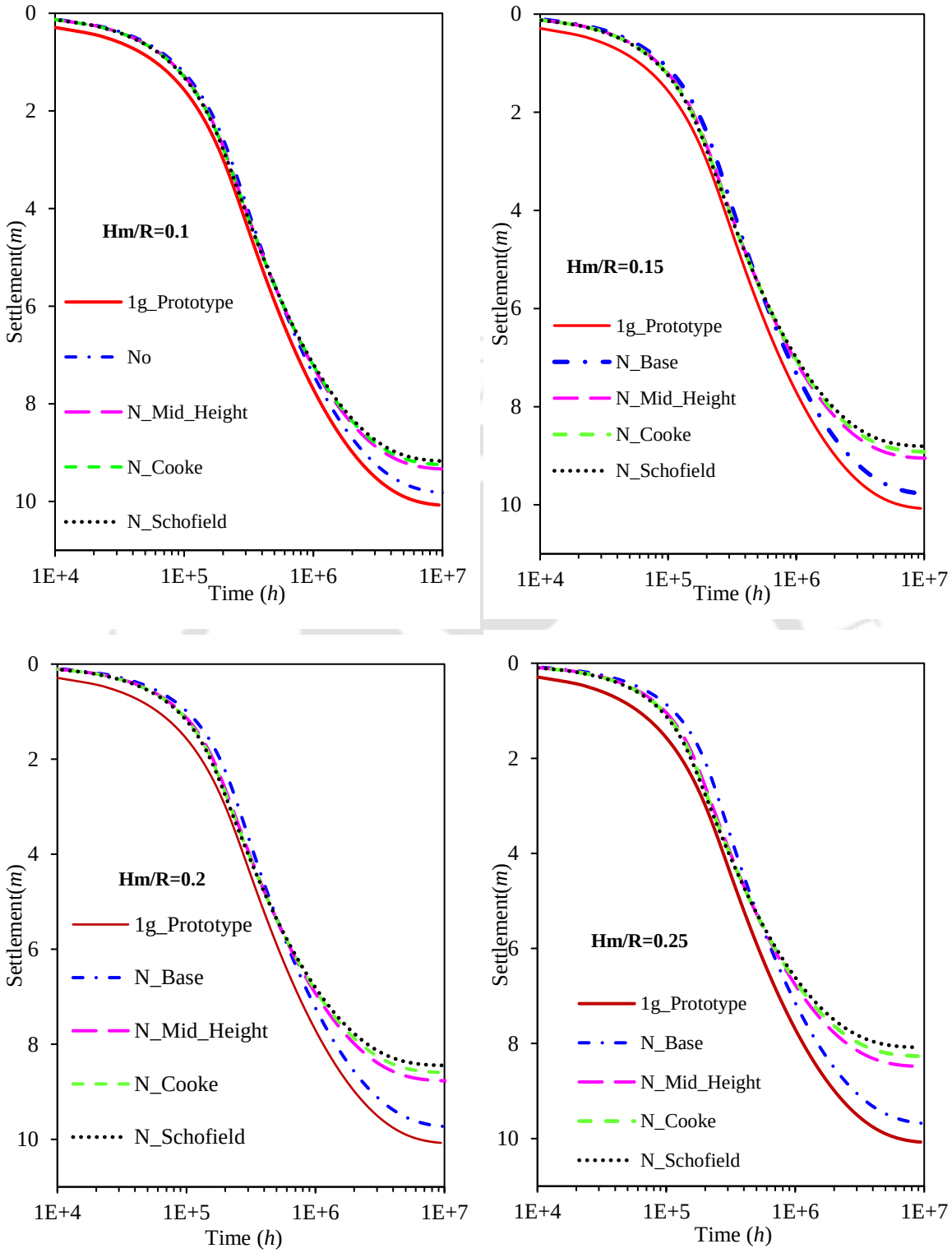


Figure 6.3 Comparison of the scaled settlement curves of SMC, with the prototype behaviour for No=104.6 when (a) Hm/R=0.1, (b) Hm/R=0.15, (c) Hm/R=0.2, and (d) Hm/R=0.25

At 104.6g, these increments were reported as 1.37 %, 8.5 %, 9.8 % and 10.9 % respectively. Scaling using N at the base was observed to be least affected by the *Hm/R* ratio and N_0 values

TH-3534_186104002

compared to other cases. Figure 6.3(d) shows that the maximum error in the ultimate settlement was observed when the effective scale factor corresponding to the Schofield radius was used, 19.784%, when N_0=104.6.

6.2.3 Numerical study using experimental prototype data

In this section, the settling column experiment data PA-MFT and the tank test data of Phosphatic Clay were considered prototype data. In order to include the final phase of consolidation, the data points of which were unavailable in these cases, the FSC behaviour of the prototypes was numerically simulated so that ultimate settlements could be compared. These data sets were used to understand the effect of choosing various N values corresponding to the effective radius values suggested by Schofield (1980), Cooke (1991), and Fox et al. (2005) as the model to prototype conversion factor in comparison to N_0.

Table 6.2 Influence of Hm/R ratio on the error in ultimate settlement when different factors are used to convert model settlement data to prototype data for PA-MFT

***N* at base**	**Model Height Hm (m)**	**Height to radius Ratio *Hm/R***	**Radius R (m)**	**Angular velocity ω (rad/s)**	**Percentage error in ultimate settlement**			
					Base	**Fox**	**Cooke**	**Schofield**
60	0.0083	0.1	0.083	84.043	0.893	5.849	6.741	7.500
		0.15	0.056	102.931	1.092	8.511	9.846	10.983
		0.2	0.042	118.855	1.289	11.16	12.937	14.451
		0.25	0.033	132.883	1.567	13.871	16.086	17.772
100	0.005	0.1	0.05	140.071	1.131	6.074	6.964	7.722
		0.15	0.033	171.552	1.34	8.739	10.071	11.206
		0.2	0.025	198.091	1.578	11.42	13.191	14.701
		0.25	0.02	221.472	1.809	14.083	16.292	18.174
150	0.0033	0.1	0.033	210.107	1.704	6.619	7.503	8.257
		0.15	0.022	257.328	2.008	9.357	10.68	11.807
		0.2	0.017	297.136	2.161	11.945	13.706	15.206
		0.25	0.013	332.209	2.36	14.565	16.762	18.633

TH-3534_186104002

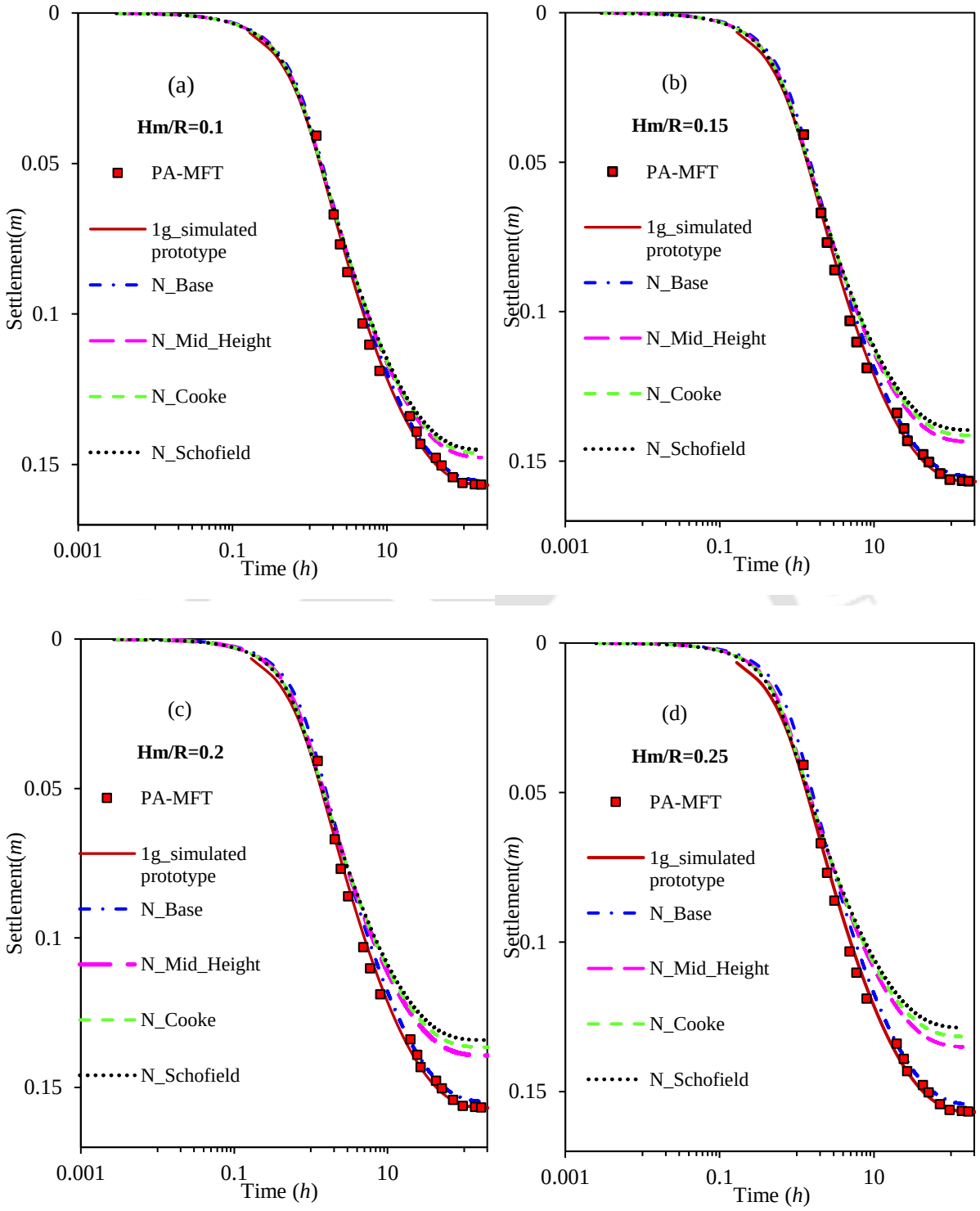


Figure 6.4 Comparison of the scaled settlement curves of PA-MFT, with the prototype behaviour for N=60g when (a) Hm/R=0.1, (b) Hm/R=0.15, (c) Hm/R=0.2, and (d) Hm/R=0.25

It was observed that using the value N_0 as the conversion scale factor, the settlement behaviour is not simulated correctly in the initial stages of settlement for larger values of N_0, while the

TH-3534_186104002

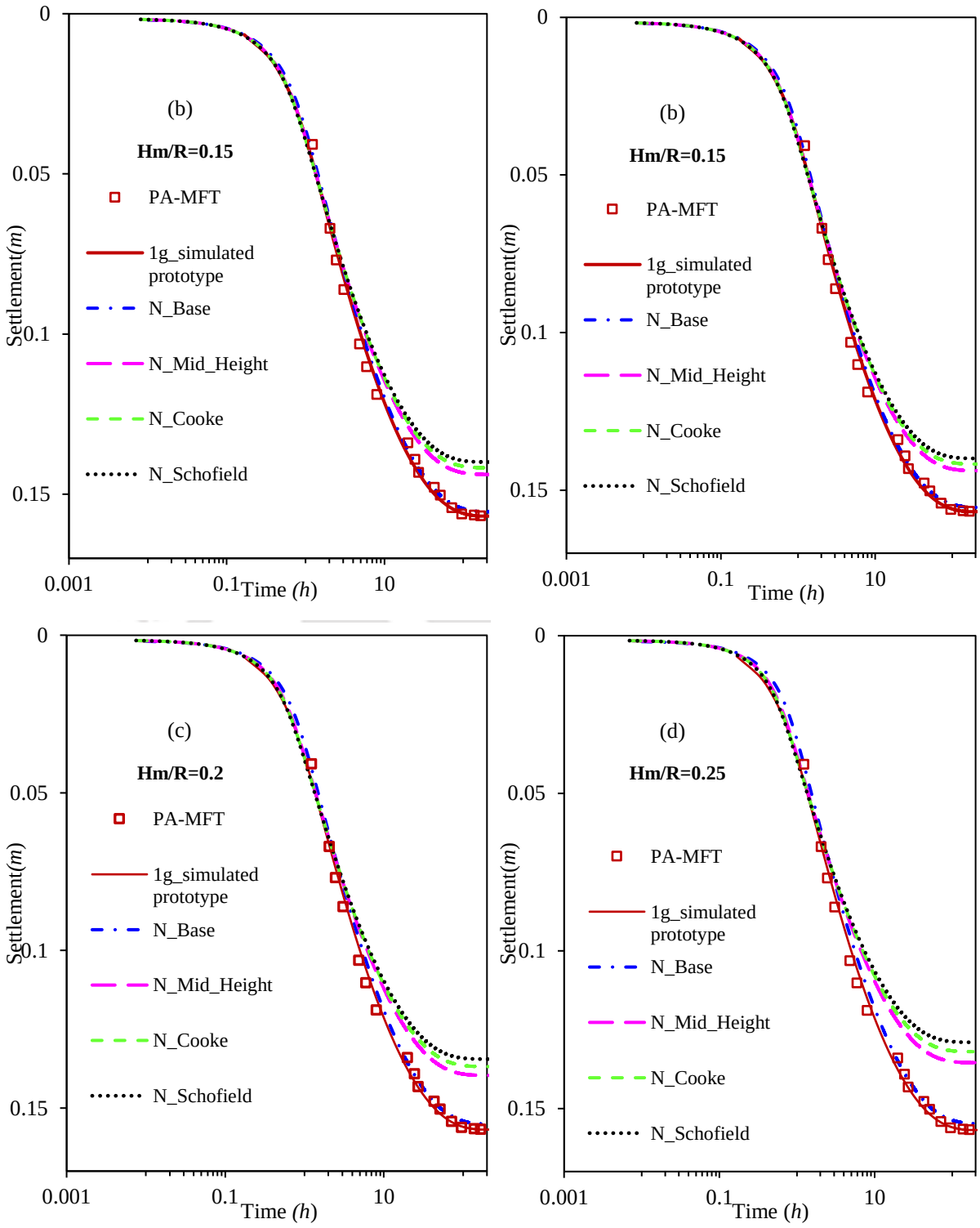


Figure 6.5. Comparison of the scaled settlement curves of PA-MFT, with the prototype behaviour for N=100 when (a) Hm/R=0.1, (b) Hm/R=0.15, (c) Hm/R=0.2, and (d) Hm/R=0.25

TH-3534_186104002

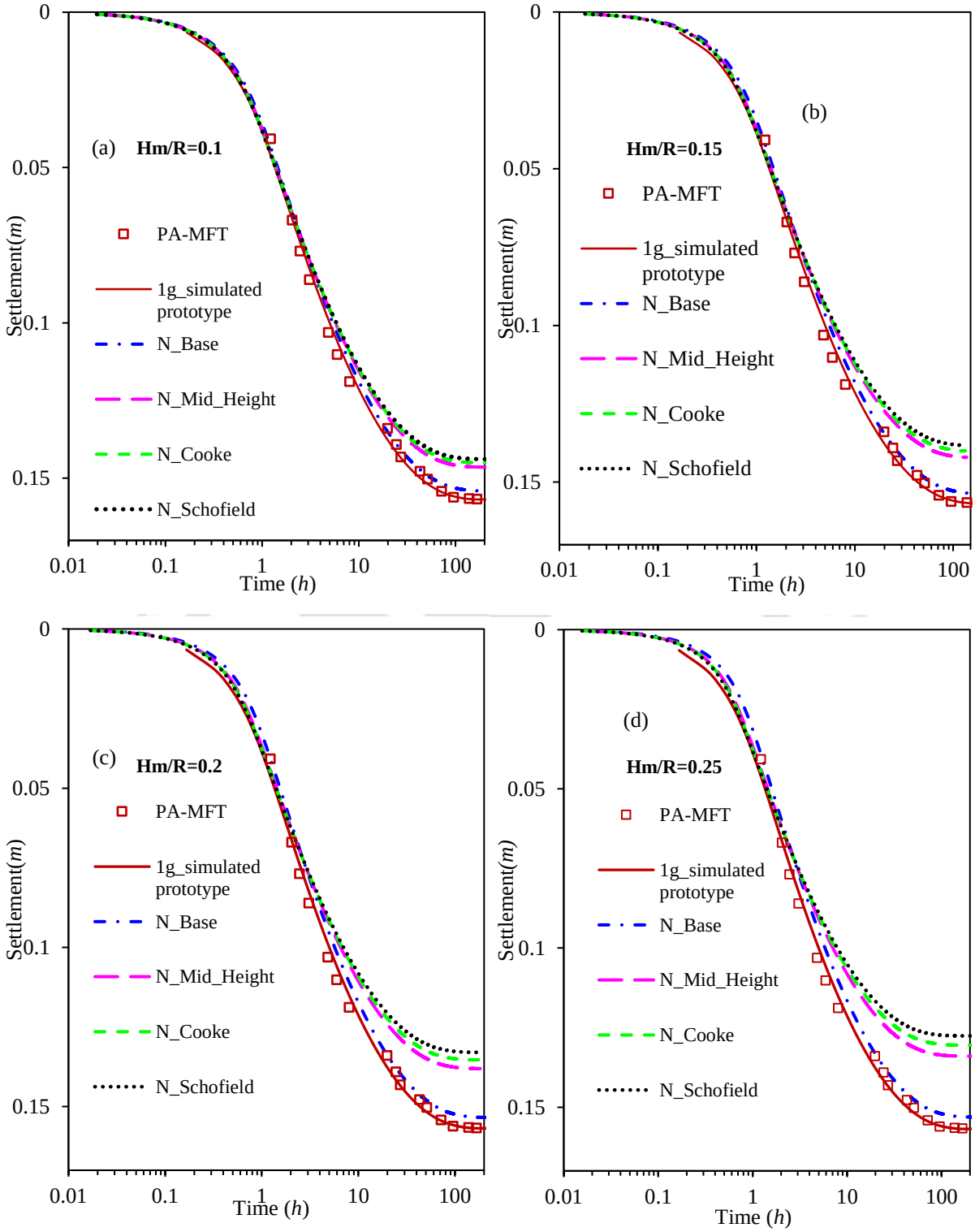


Figure 6.6. Comparison of the scaled settlement curves of PA-MFT, with the prototype behaviour for N=150 when (a) Hm/R=0.1, (b) Hm/R=0.15, (c) Hm/R=0.2, and, (d) Hm/R=0.25

the ultimate settlement value is predicted close to the simulated prototype value. If any of the other scale factors are used, the final settlement value is much lower than the field simulated

TH-3534_186104002

value, causing an assumption that the field settlement has achieved its maximum value earlier than the observed time.

From Tables 6.2 and 6.3, it can be seen that the percentage error in the ultimate settlement is the smallest when the conversion factor corresponds to the N_0.

Table 6.3 Influence of Hm/R ratio on the error in ultimate settlement when different factors are used to convert model settlement data to prototype data for Phosphatic Clay

***N* at base**	**Model Height Hm(m)**	**Height to radius Ratio *Hm/R***	**Radius R (m)**	**Angular velocity ω (rad/s)**	**Percentage error in ultimate settlement**			
					Base	**Fox**	**Cooke**	**Schofield**
80	0.079	0.1	0.791	31.494	2.286	7.171	8.051	8.8
		0.15	0.528	38.572	2.866	10.151	11.463	12.58
		0.2	0.396	44.539	3.376	13.038	14.777	16.259
		0.25	0.317	49.796	3.894	15.907	18.07	19.912
100	0.063	0.1	0.633	39.367	2.687	7.553	8.229	9.075
		0.15	0.422	48.215	3.181	10.443	11.75	12.863
		0.2	0.317	55.673	3.649	13.284	15.018	16.496
		0.25	0.253	62.245	4.242	16.212	18.367	20.202
120	0.053	0.1	0.528	47.24	3.377	7.659	8.255	9.519
		0.15	0.352	57.857	4.501	11.663	12.952	14.051
		0.2	0.264	66.808	5.018	14.517	16.226	17.683
		0.25	0.211	74.694	5.581	17.383	19.508	21.317

The maximum error value for the value of the ultimate settlement is 5.6% for *Hm/R*= 0.25 and N_o =120g. It can be noted that for all cases maintained at an *Hm/R* ratio less than 0.2, it is safe to use N_o as the conversion factor.

In order to understand the influence of the *N* values at the base on the increment in the error values, were compared for various values of *N*. When the *N* at the base was increased from 60 to 150 at *Hm/R*=0.1, the error in the ultimate settlement was observed to increase by 0.81 %, 0.77 %, 0.76 % and 0.75 %, respectively for N_0, Fox, Cooke and Schofield. The increment values corresponding to an *Hm/R* value of 0.25 were 0.8 %, 0.68 %, 0.67 % and 0.86 % for N_0, Fox, Cooke and Schofield, respectively.

TH-3534_186104002

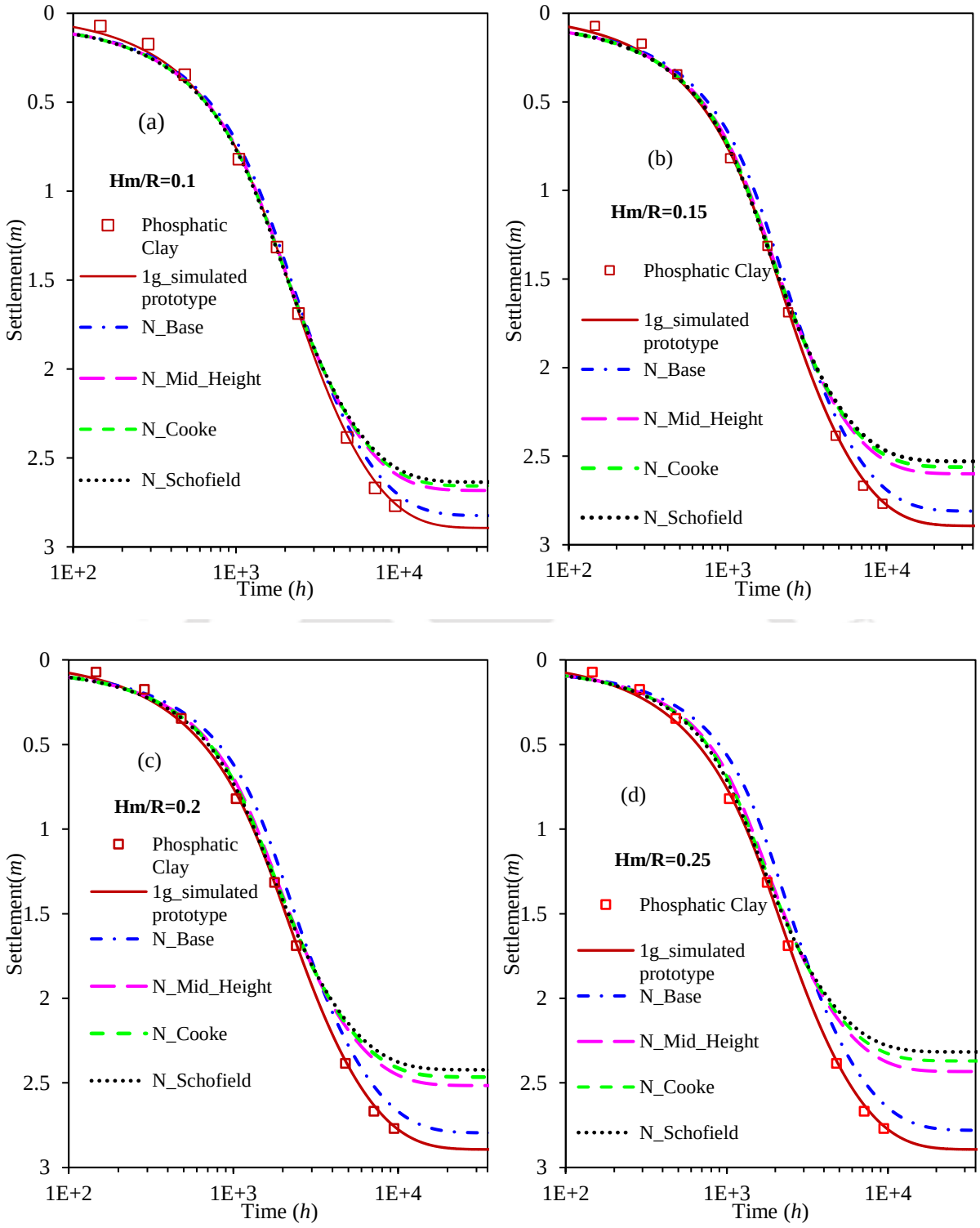


Figure 6.7. Comparison of the scaled settlement curves of Phosphatic Clay, with the prototype behaviour for N=80 when (a) Hm/R=0.1, (b) Hm/R=0.15, (c) Hm/R=0.2, and, (d) Hm/R=0.25

TH-3534_186104002

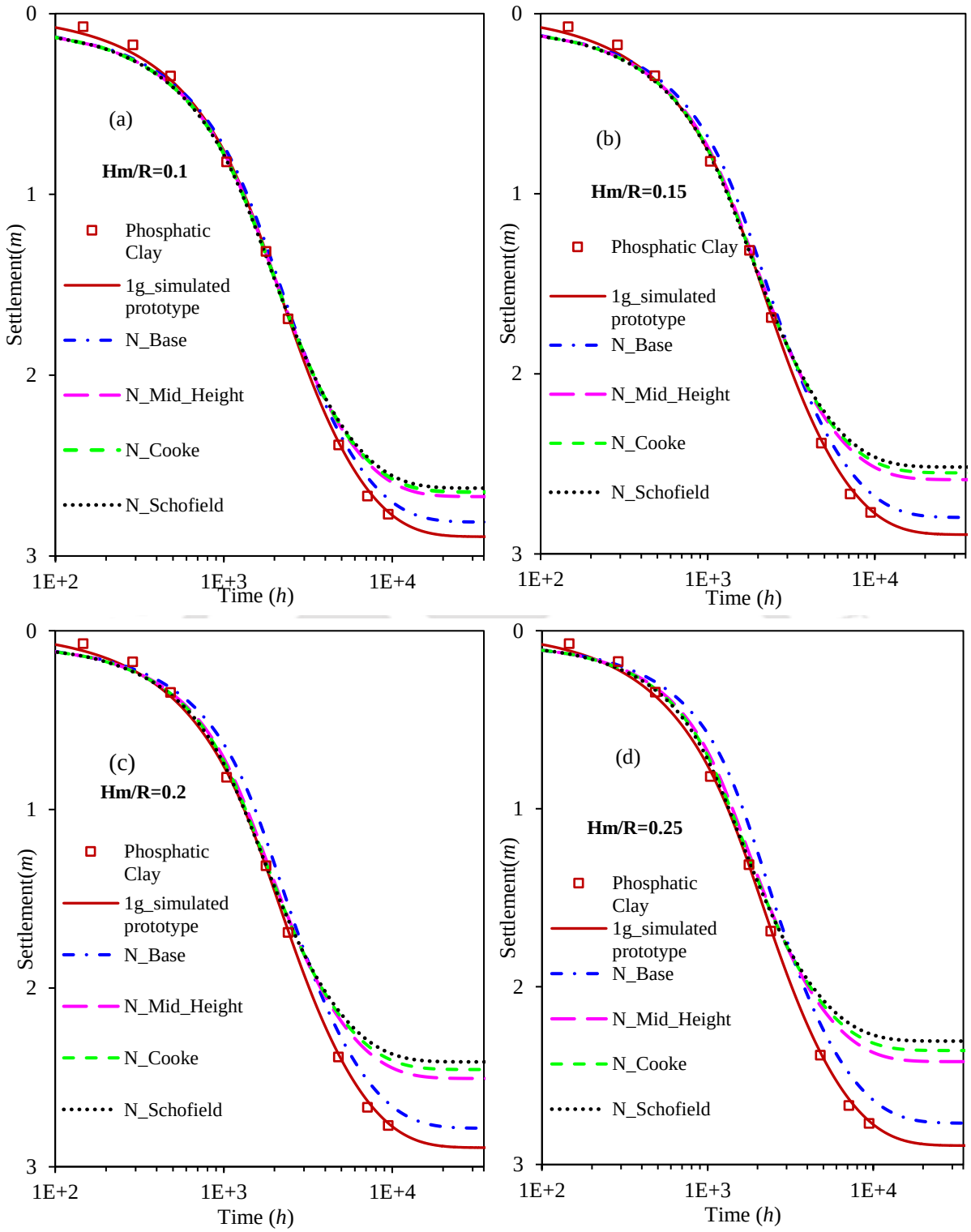


Figure 6.8. Comparison of the scaled settlement curves of Phosphatic Clay, with the prototype behaviour for N=100 when (a) Hm/R=0.1, (b) Hm/R=0.15, (c) Hm/R=0.2, and, (d) Hm/R=0.25

The increment in error observed with an increase in *Hm/R* value were more pronounced than the influence of *N* at the base. At N_0=60g, the increase of *Hm/R* from 0.1 to 0.25 resulted in the increase in the prediction error in the ultimate settlement by 0.67 %, 8.02 %, 9.34 %,

TH-3534_186104002

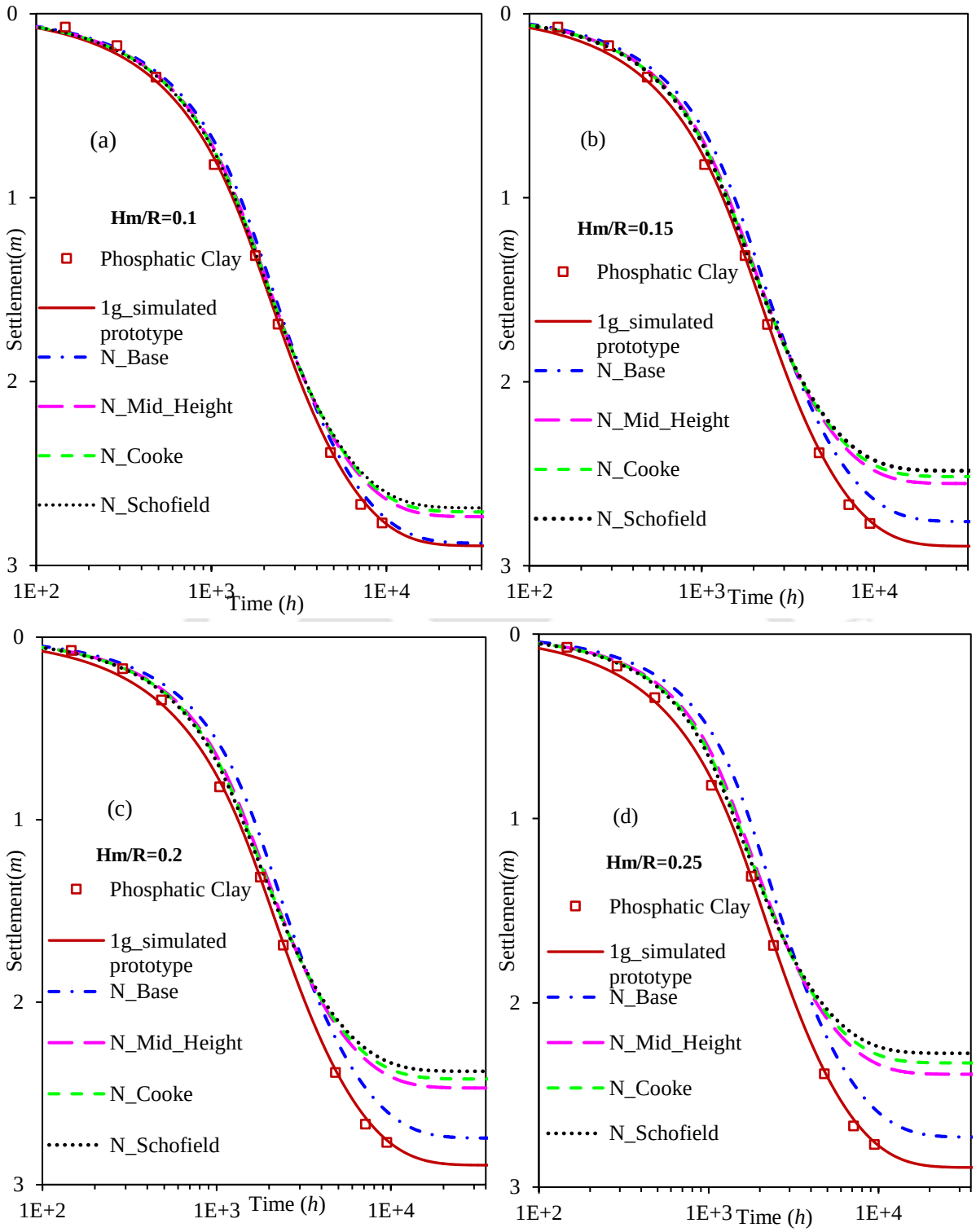


Figure 6.9 Comparison of the scaled settlement curves of Phosphatic Clay, with the prototype behaviour for N=120 when (a) Hm/R=0.1, (b) Hm/R=0.15, (c) Hm/R=0.2, and, (d) Hm/R=0.25

and 10.27 % respectively for N_0, Fox, Cooke and Schofield. At N_0=150g, the increased *Hm/R* values result in the increment of error by 0.65 %, 7.94 %, 9.26 % and 10.37 %, respectively,

TH-3534_186104002

for N_0, Fox, Cooke and Schofield. The percentage error in predicted ultimate settlement values was observed to increase by 1.1 %, 0.49 %, 0.20 % and 0.72 %, respectively, for N_0, Fox, Cooke and Schofield-based conversion factors, at an *Hm/R*-value of 0.1 when the *N* value was increased from 80g to 120g. Physically, this change was made by reducing the initial model height and rotating the sample at a higher angular velocity in a smaller centrifuge, as described in Table 6.3. For an *Hm/R* value of 0.25, this error increment was 1.69 %, 1.48 %, 1.44 % and 1.40 %, respectively, for N_0, Fox, Cooke and Schofield. In the case of variation of *Hm/R*, for a given *N* value, the error increments for 80g were 1.61 %, 8.74 %, 10.0 % and 11.1 %, respectively, for *N*=80g. When *N*=120, these increments were 2.2 %, 9.7 %, 11.25 %, and 11.79 %, respectively, for N_0, Fox, Cooke and Schofield.

6.3 Numerical Study on the Exponent of Time Scale Factor

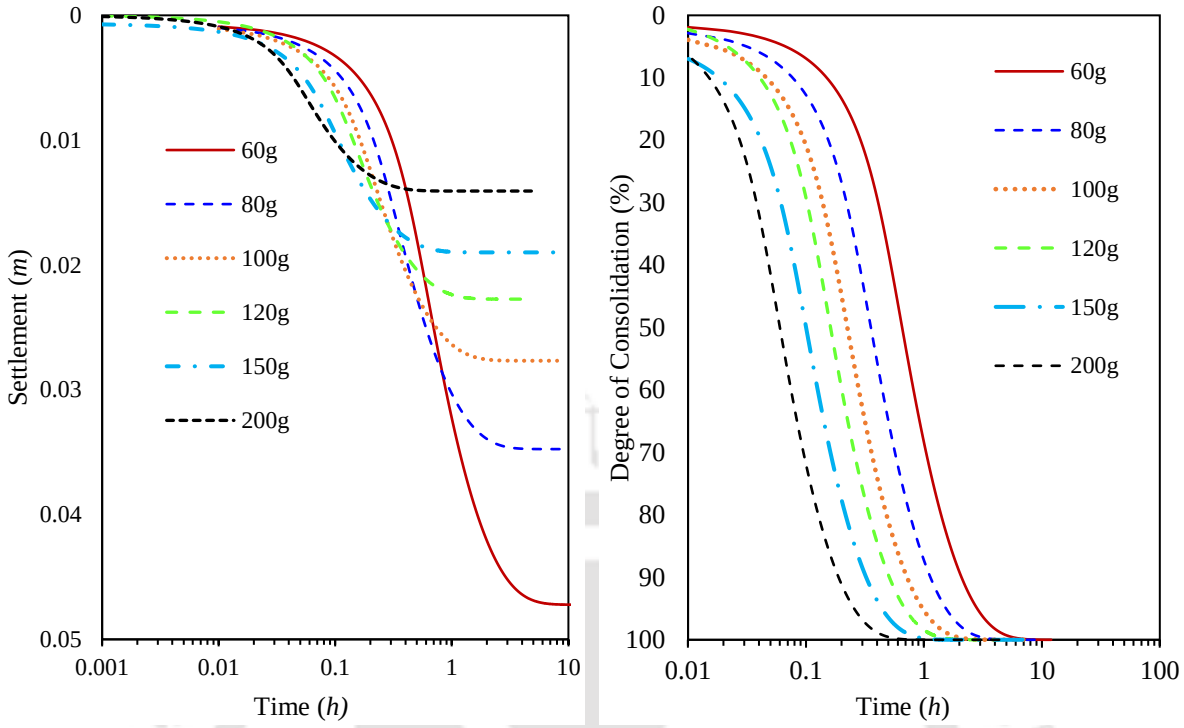
6.3.1 General

It is a general practice to multiply the square of the scale factor by the model-time value to scale it to the corresponding field time value. Studies reveal that the power of the scale factor is not exactly a constant but rather changes with the degree of consolidation. This indicates that the relationship between the time in the centrifuge model and the actual time varies at different phases of the consolidation process. The behaviour of the soil changes with time; therefore, the early phases of consolidation may need a scaling factor different from the later stages. Therefore, it is crucial to take into consideration this fluctuation in the time scaling factor during the centrifuge test in order to produce reliable estimations for the prototype behaviour and better mimic real-world conditions. In this section, this concept is explored numerically using two prototype data sets. The influence of model height to centrifuge radius ratio and the scale factor values is also presented in this section.

6.3.2 Time Scale Exponent Versus Degree of Consolidation

The centrifuge consolidation curves simulated by varying the *Hm/R* ratio for different N_0 values for PA-MFT and Phosphatic Clay were considered for this study. The relevant properties are given in the Table 4.2. The simulated *Ng* settlement curves for various N_0 values for a given *Hm/R* are illustrated in Figure 6.10 (a) for a sample of Phosphatic Clay. The degrees of consolidation plots were derived from the settlement plots for *Hm/R*=0.1, 0.15, 0.2 and 0.25, and the N_0 values of 60g, 80g, 100g, 90g, 150g and 200g. The prototype and model consolidation time corresponding to degrees of consolidation at 10-degree intervals were taken

TH-3534_186104002



(a) (b)

Figure 6.10. For a given prototype, (a) the effect of varying the scale factor N on the settlement versus time plot, (b) Settlement versus time plots or various N values converted into the degree of consolidation versus time plots (illustrated using data from Phosphatic Clay, at Hm/R=0.25)

from these curves. The numerically simulated curves for the prototypes were used instead of the experimental data points, as those points did not include a full consolidation process. The time scale exponent values were computed for these cases using the model and prototype time values. In order to show the range of variation, these values are reported in Table 6.4 and Table 6.5, respectively, for Phosphatic Clay and PA-MFT. It can be seen that the value of the time scaling exponent is not exactly two but varies with the degree of consolidation and the *N* value used. The general trend shows that with an increase in the *Hm/R* ratio, more variation is observed.

Table 6.6 shows the average value of the exponent of the time scale factor for the entire process of consolidation for various *Hm/R* values at different *N* values. The influence of the factor on the time calculated is larger towards the end of consolidation. The *N* value at the base was used for the centrifuge to prototype conversion, corresponding to the least error based on ultimate settlement prediction.

TH-3534_186104002

Table 6.4 Time scale exponent values for different degrees of consolidation for Phosphatic Clay at different Hm/R values

Degree	Time Scale Exponent for *Hm/R*=0.1					Time Scale Exponent for *Hm/R*=0.15				
	60g	90g	100g	150g	200g	60g	90g	100g	150g	200g
10	1.994	2.016	2.033	2.044	1.977	1.967	1.992	2.009	2.034	1.956
20	1.987	1.996	2.008	2.015	1.982	1.959	1.976	1.987	1.997	1.965
30	1.987	1.996	2.001	2.003	1.982	1.975	1.992	1.998	1.997	1.981
40	1.987	1.996	1.995	2.003	1.985	1.979	1.992	2.001	1.997	1.984
50	1.994	1.996	2.004	2.000	1.993	1.983	1.992	1.998	1.991	1.978
60	1.990	1.996	2.001	2.003	1.988	1.988	1.988	1.994	2.001	1.984
70	1.994	2.000	2.001	2.003	1.993	1.988	1.995	2.001	2.001	1.991
80	1.990	2.000	2.004	2.000	1.993	2.000	1.999	2.009	2.001	1.997
90	1.990	2.000	2.004	2.000	1.993	1.988	1.992	1.994	1.997	1.984
Degree	**Time Scale Exponent for *Hm/R*=0.2**					**Time Scale Exponent for *Hm/R*=0.25**				
	60g	90g	100g	150g	200g	60g	90g	100g	150g	200g
10	1.944	1.970	1.984	2.011	1.937	1.915	1.938	1.957	1.981	1.914
20	1.940	1.955	1.967	1.973	1.945	1.924	1.942	1.954	1.961	1.935
30	1.960	1.970	1.977	1.981	1.962	1.947	1.959	1.963	1.970	1.953
40	1.965	1.975	1.980	1.982	1.969	1.953	1.967	1.971	1.973	1.960
50	1.966	1.972	1.979	1.978	1.970	1.956	1.969	1.969	1.971	1.962
60	1.969	1.977	1.982	1.982	1.972	1.961	1.975	1.974	1.979	1.970
70	1.974	1.983	1.986	1.985	1.978	1.966	1.974	1.982	1.979	1.974
80	1.984	1.990	1.991	1.993	1.985	1.973	1.981	1.984	1.985	1.979
90	1.973	1.982	1.982	1.982	1.977	1.962	1.975	1.979	1.976	1.970

TH-3534_186104002

Table 6.5 Time scale exponent values for different degrees of consolidation for PA-MFT at different Hm/R values

Degree	Time Scale Exponent for *Hm/R*=0.1					Time Scale Exponent for *Hm/R*=0.15				
	60g	90g	100g	150g	200g	60g	90g	100g	150g	200g
10	1.969	1.986	1.969	1.979	2.022	1.956	1.976	1.987	1.962	2.009
20	1.982	1.992	1.977	1.984	2.003	1.971	1.979	1.983	1.977	2.000
30	1.991	1.995	1.994	1.992	2.005	1.978	1.985	1.990	1.987	2.000
40	1.988	1.998	1.991	1.994	2.008	1.985	1.991	1.996	1.990	2.003
50	1.982	1.986	1.985	1.989	2.003	1.977	1.984	1.989	1.984	1.999
60	1.982	1.989	1.988	1.992	2.000	1.978	1.985	1.989	1.986	1.998
70	1.985	1.992	1.988	1.994	2.003	1.982	1.983	1.990	1.989	2.000
80	1.994	1.995	1.994	1.994	2.003	1.985	1.989	1.996	1.994	2.003
90	1.997	2.000	2.002	2.000	2.010	1.999	1.993	1.995	1.998	2.003
100	1.962	2.011	1.919	1.897	1.924	1.940	1.928	1.897	2.001	1.959
Degree	**Time Scale Exponent for *Hm/R*=0.2**					**Time Scale Exponent for *Hm/R*=0.25**				
	60g	**90g**	**100g**	**150g**	**200g**	**60g**	**90g**	**100g**	**150g**	**200g**
10	1.920	1.942	1.953	1.935	1.982	1.906	1.931	1.939	1.927	1.968
20	1.955	1.965	1.970	1.961	1.981	1.947	1.955	1.960	1.958	1.977
30	1.964	1.975	1.974	1.970	1.990	1.965	1.970	1.973	1.970	1.987
40	1.969	1.980	1.985	1.974	1.994	1.971	1.975	1.978	1.976	1.991
50	1.968	1.979	1.978	1.974	1.986	1.961	1.972	1.975	1.972	1.984
60	1.970	1.978	1.980	1.978	1.985	1.967	1.972	1.975	1.977	1.987
70	1.975	1.976	1.984	1.979	1.991	1.973	1.977	1.982	1.978	1.990
80	1.985	1.983	1.990	1.987	1.999	1.976	1.980	1.983	1.982	1.992
90	1.987	1.990	1.994	1.989	2.000	1.981	1.981	1.989	1.983	1.995
100	1.808	1.821	1.845	1.933	1.946	1.964	1.927	1.918	1.910	1.965

TH-3534_186104002

Table 6.6 The average value of exponent for full consolidation at different Hm/R values for various scale factors

Prototype	*Hm/R*	Time Scale Factor Exponent Value				
		60g	**90g**	**100g**	**150g**	**200g**
Phosphatic Clay	0.1	1.988	1.988	1.994	1.996	1.978
	0.15	1.978	1.984	1.987	1.99	1.971
	0.2	1.963	1.964	1.971	1.975	1.958
	0.25	1.951	1.956	1.961	1.966	1.95
PA-MFT	0.1	1.983	1.994	1.981	1.982	1.998
	0.15	1.975	1.979	1.981	1.987	1.997
	0.2	1.95	1.959	1.965	1.968	1.986
	0.25	1.961	1.964	1.967	1.963	1.984

6.4 Summary

The acceleration factor is a variable within the depth of the model. Nevertheless, the acceleration factor value at the base remains unchanged throughout the process of consolidation. Conversion scale factors can be obtained using the various effective radius values suggested in the literature to convert the centrifuge model settlement versus time curve into a 1g prototype/field settlement curve. The accuracy of these effective scale factors and the *N* value at the base were compared using numerically simulated settlement curves for the model in a centrifuge environment and the prototype in the 1g condition. It was observed that using the N_0 as the conversion factor produces the least error in the ultimate settlement, followed by the scale factor considering effective radius to initial mid-height suggested by Fox et al. (2005). The maximum error was observed in the case of Schoefiled's scale factor. The *Hm/R* ratio influences the difference in ultimate settlement from the simulated prototype curve more than the N_0 value. The influence was greater when the effective scale factors were used. The error in predicted ultimate settlement values was observed to be influenced by the *Hm/R* ratio more than the geometric scale factor *N*. Scaling using N at the base was observed to be least affected by the Hm/R ratio and N_0 values compared to other cases. The 1g curves obtained using effective radius-based conversion factors match the simulated prototype settlement curve more during the initial phase of consolidation. The difference between these converted curves and the simulated prototype curve increases and comes to the maximum at the ultimate settlement.

TH-3534_186104002

The initial phase of consolidation was observed to vary from prototype behaviour when the N_0 is used as the conversion factor. This variation was observed to increase with the increase in *Hm/R* value. This error continues to decrease with consolidation.

The exponent of the time scaling factor is not exactly equal to the theoretical value of 2. It varies with the *Hm/R*, *N* value and the degree of consolidation. The exact relation between the time scaling factor exponent needs a more elaborate study.

Obtaining ultimate settlement values from full-scale prototype testing is a time-intensive and costly process, often hampered by long testing durations and high operational expenses. By conducting centrifuge tests under optimized conditions, as outlined in this study, the ultimate settlement can be rapidly obtained and reliably scaled to field/prototype conditions, significantly reducing both time and costs associated with full-scale testing.

The present chapter concludes by emphasizing the need to incorporate the variation in acceleration scale factor with depth when simulating the settlement behavior of slurries in centrifuge. The next chapter builds on this by simulating the settlement behavior with the depth-dependent variation in the acceleration scale factor, and using the simulated behaviour to conduct the graphical analysis and estimation of hydraulic conductivity parameters.

TH-3534_186104002

7. Graphical Estimation of Hydraulic Characteristics

7.1 General

In this work, inverse analyses using the temporal settlement from centrifuge tests were carried out to predict the model parameters of the conductivity function using the available time-invariant compressibility data. Two recent methods (Qi and Simms 2020; Qi et al. 2020) for the estimation of hydraulic conductivity parameters of 1g settlement versus time data were explored for the parameter estimation in the centrifuge environment. The centrifuge FSC analysis was carried out using the finite-difference solution of the analytical model (Bharat & Ubaid 2019). The proposed approaches were first tested on the synthetic settlement versus time data of four different samples and then validated on four measured centrifuge test data sets from the literature. The proposed methods were found to be robust and applicable for a quick estimation of the conductivity function parameters of a given slurry material.

The geotechnical properties and constitutive relationships governing the FSC behavior of eight different samples were used in this study to back-predict their hydraulic conductivity function parameters. Material properties and relationships, as given in Table 4.3, were used to test the inverse analysis for Matured fine tailings of oil sands (MFT 5 and MFT 6), finer fractions of copper mine tailings called overflow tailings (OFT), and dredged clay sediment (Rutgers). The temporal settlement data from self-weight consolidation tests conducted in a centrifuge environment are available for the cases of Singapore Marine Clay (SMC) (Robinson et al. 2003), Albian oil sand tailings (AL15), Edgar Plastic Kaolin clay (Kaolinite) slurry, and thickened flocculated tailings with 50% fines (TT50) (Sorta 2015, Sorta et al. 2016). The Ng-FSC behaviour of these materials were used for the validation of these methods

7.2 Prediction of Hydraulic Conductivity Characteristics

7.2.1 Prediction Using Synthetic Settlement Data

Method 1 requires a minimum of two initially assumed pairs of M and P values and their corresponding simulated FSC settlement versus time curves for each slurry. In this study, four initial guesses were assumed to simulate settlement curves, as given in Table 7.1. Synthetic settlement versus time curves to represent experimental data for Rutgers, OFT, MFT 5 and MFT 6 were generated using consolidation and centrifuge parameters presented in Table 4.3.

TH-3534_186104002

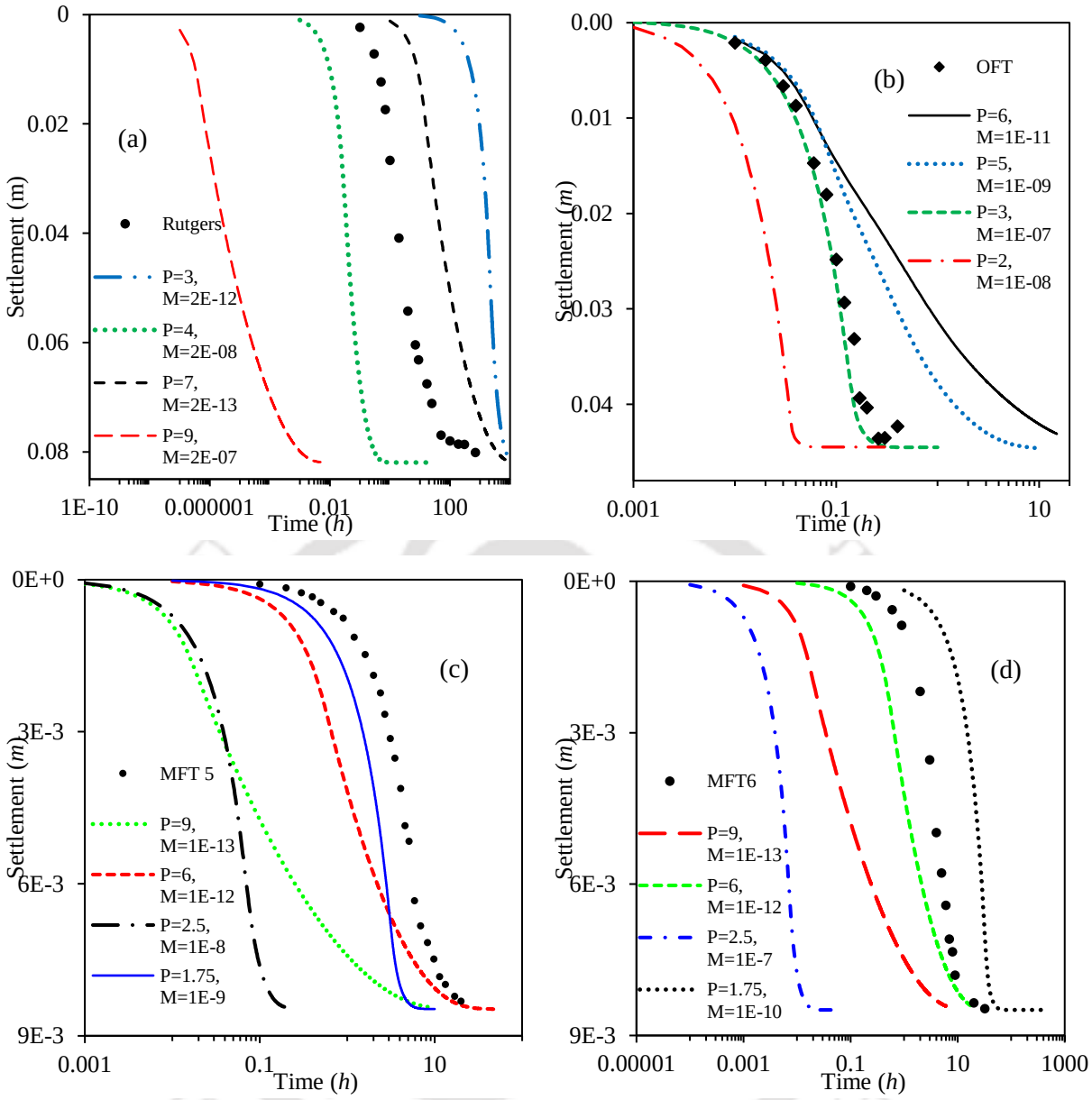


Figure 7.1. Settlement versus time behaviour simulated numerically for (a) Rutgers, (b) OFT, (c) MFT 5, and (d) MFT 6, using initial guess values of M and P given in Table 7.1 and the synthetic data points simulated using hydraulic conductivity function parameters from Table 4.3 for Method 1 (Qi and Simms, 2020)

The centrifuge radius values were assumed such that it simulated a beam centrifuge for Rutgers and OFT and a small benchtop centrifuge for MFT 5 and MFT 6. The centrifuge rotation speeds (ω rad/s) were calculated from the assumed centrifuge radius values and scale factors. The settlement vs time curves were generated numerically using the initial guess values of *M* and *P*, given in Table 7.1, for each slurry as given in Figure 7.1 (a-d). The positions of some of the curves, with respect to the synthetic data points, were far apart, while some were close to each other based on their *M* values. They also possessed different spreads along the *log-t* axis

TH-3534_186104002

according to their *P* values. The optimal *M* and *P* values were predicted using combinations of four pairs of initial guesses for each sample type. While considering the combination, the pair having a larger *P* value was considered as the first set, i.e., (M_1, P_1), and the other as the second set (M_2, P_2), and the predicted *P* value will be lying within the bounds $[P_1, P_2]$. The FSC settlement versus time curves for Rutgers (Figure 7.1(a)) were simulated using four pairs of initial guess values for *(M, P)* in Table 7.1, along with the input properties and centrifuge parameters in Table 4.3. Four different combinations of these simulated curves were considered as (M_1, P_1) and $(M_2.P_2)$ to check the robustness of the prediction. The first combination considered used the pair ($2x10^{-7}$, 9) as (M_1, P_1) and ($2x10^{-12}$, 3) as (M_2, P_2). The corresponding settlement versus time curves were shifted to pass through the points in the synthetic settlement versus time curve by computing the *M* value related to those curves while maintaining the *P* values.

Table 7.1 Initial guess values used for simulating arbitrary settlement curves for applying the graphical methods

Materials	Method 1		Method 2		Materials	Method 1		Method 2	
	M	P	M	P		M	P	M	P
Rutgers	$2x10^{-12}$	3	$2x10^{-12}$	3	**SMC**	$2x10^{-10}$	8	$3x10^{-11}$	4
	$2x10^{-8}$	4	$2x10^{-9}$	5		$3x10^{-11}$	4	$4x10^{-12}$	6
	$2x10^{-13}$	7	$2x10^{-13}$	7		$2x10^{-9}$	3	$4x10^{-10}$	7
	$2x10^{-7}$	9				$3x10^{-8}$	7		
						$4x10^{-12}$	6		
OFT	$1x10^{-11}$	6	$1x10^{-6}$	2	**TT50**	$2x10^{-11}$	2	$2x10^{-9}$	3
	$1x10^{-9}$	5	$1x10^{-7}$	3		$2x10^{-7}$	8	$2x10^{-8}$	4
	$1x10^{-7}$	3	$1x10^{-7}$	4		$2x10^{-8}$	7	$2x10^{-10}$	5
	$1x10^{-6}$	2				$2x10^{-12}$	3		
						$2x10^{-6}$	9		
MFT5	$1x10^{-13}$	9	$1x10^{-8}$	3	**Kaolinite**	$1x10^{-12}$	8	$1x10^{-9}$	4
	$1x10^{-12}$	6	$1x10^{-10}$	4		$1x10^{-8}$	3	$1x10^{-8}$	6
	$1x10^{-8}$	2.5	$1x10^{-11}$	5		$1x10^{-7}$	2.5	$1x10^{-12}$	8
	$1x10^{-9}$	1.75				$1x10^{-11}$	9		
						$1x10^{-9}$	4		
MFT6	$1x10^{-13}$	9	$1x10^{-9}$	3	**AL15**	$1x10^{-7}$	2	$1x10^{-9}$	4
	$1x10^{-12}$	6	$1x10^{-11}$	5		$1x10^{-6}$	1.5	$1x10^{-10}$	5
	$1x10^{-7}$	2.5	$1x10^{-12}$	6		$1x10^{-8}$	6	$1x10^{-8}$	6
	$1x10^{-10}$	1.75				$1x10^{-12}$	9		
						$1x10^{-11}$	7		

TH-3534_186104002

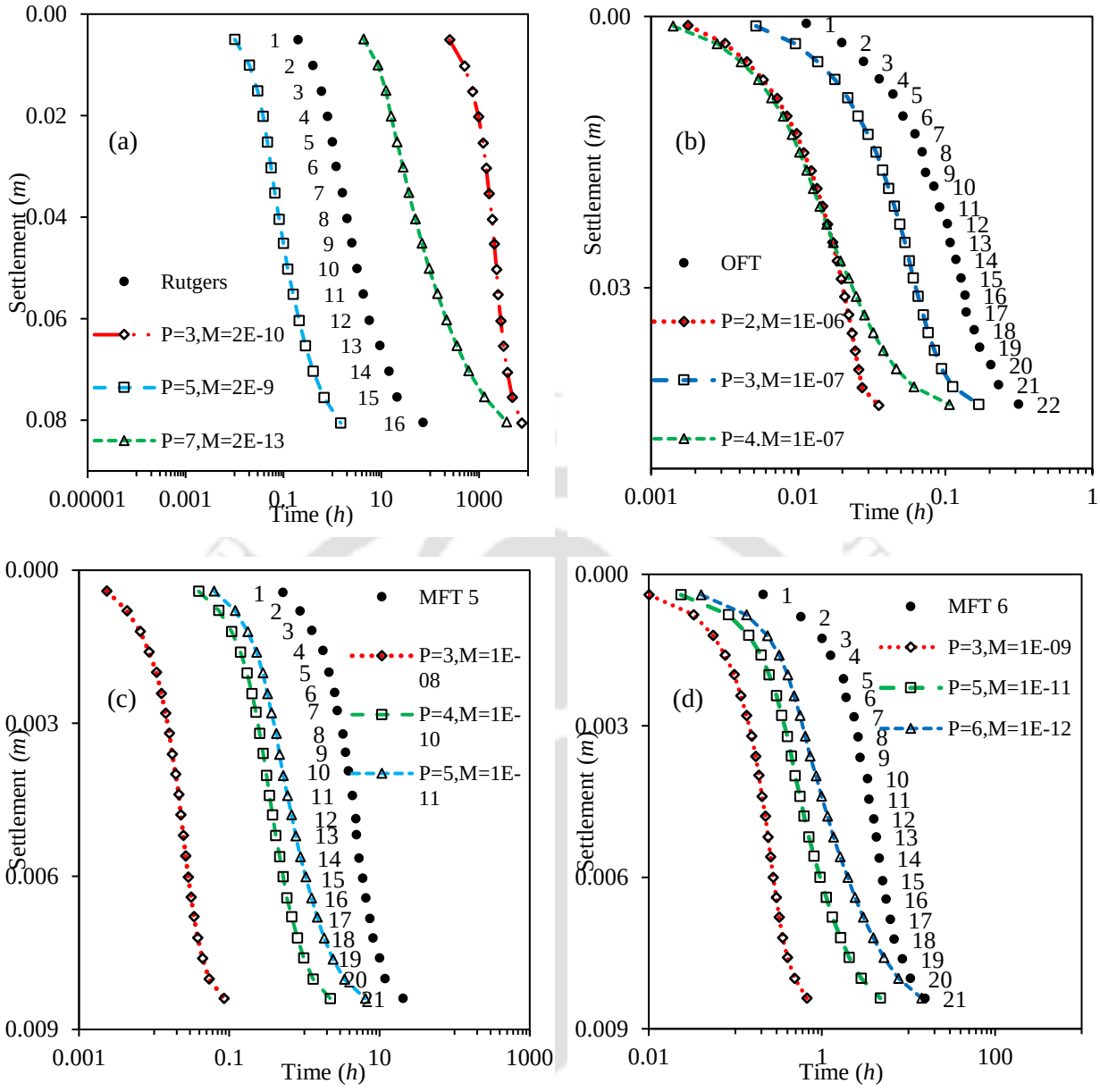


Figure 7.2 Settlement versus time curves showing the synthetic data points and corresponding points from the simulated curves for initial guesses considered in group 1 for predicting the power P using Method 2 (Qi et al.2020) for (a) Rutgers (b) OFT (c) MFT5 and (d) MFT6

The pairs of *M* and *P* values thus obtained were plotted in *P vs ln-M* space. In this space, there were two points corresponding to each point in the synthetic settlement curve. These points were connected with straight lines, and the points of intersection of these lines were estimated using the MATLAB code. The arithmetic average of the coordinates of points of intersection, which were obtained as 2.699 $x10^{-11}$ m/s and 5.952, was the optimal *M* and *P* values, respectively, as given in Table 7.2. The procedure was performed again using three more such combinations to predict values of parameters as given in Table 7.2. All four combinations resulted in predicted values in close proximity, showing that the graphical method is robust.

TH-3534_186104002

The average of these four sets of predicted *M* and *P* values were computed to be 2.312×10^{-11} m/s and 6.011, respectively. The average predicted *M* and *P* values were observed to be almost equal to the parametric values of the synthetic cases given in Table 4.3.

Table 7.2 M and P values predicted for synthetic data cases using Method 1

Cases	M_1	P_1	M_2	P_2	Predicted Values	
					M	P
Rutgers	2×10^{-7}	9	2×10^{-12}	3	2.699×10^{-11}	5.952
	2×10^{-7}	9	2×10^{-8}	4	1.625×10^{-11}	6.257
	2×10^{-13}	7	2×10^{-12}	3	2.903×10^{-11}	5.805
	2×10^{-13}	7	2×10^{-8}	4	2.020×10^{-11}	6.031
	Average of predicted values				**2.312×10^{-11}**	**6.011**
OFT	1×10^{-11}	6	1×10^{-7}	3	3.92×10^{-8}	3.208
	1×10^{-11}	6	1×10^{-6}	2	3.939×10^{-8}	3.197
	1×10^{-9}	5	1×10^{-7}	3	3.990×10^{-8}	3.192
	1×10^{-9}	5	1×10^{-6}	2	7.969×10^{-8}	2.597
	Average of predicted values				**4.954×10^{-8}**	**3.048**
MFT 5	1×10^{-13}	9	1×10^{-8}	2.50	4.245×10^{-11}	3.135
	1×10^{-13}	9	1×10^{-9}	1.75	1.15×10^{-10}	2.599
	1×10^{-12}	6	1×10^{-8}	2.50	3.37×10^{-11}	3.348
	1×10^{-12}	6	1×10^{-9}	1.75	7.66×10^{-11}	2.806
	Average of predicted values				**6.693×10^{-11}**	**2.972**
MFT 6	1×10^{-13}	9	1×10^{-7}	2.50	1.722×10^{-11}	3.696
	1×10^{-13}	9	1×10^{-10}	1.75	2.064×10^{-11}	3.573
	1×10^{-12}	6	1×10^{-7}	2.50	2.017×10^{-11}	3.581
	1×10^{-12}	6	1×10^{-10}	1.75	2.071×10^{-11}	3.555
	Average of predicted values				**1.968×10^{-11}**	**3.600**

The values of *M* and *P* predicted by applying Method 1 for Rutgers, MFT 6, MFT 5, and OFT using different combinations of initial guesses are given in Table 7.1. Figure 7.3 (a-d) shows the comparison of the average value of the predicted hydraulic conductivity functions with the actual functions for the synthetic data cases for Method 1. All the parameters were observed to match well with the actual function, except for MFT 5. The variation observed in this case can be attributed to the white noise added to the settlement data. In order to further clarify the efficiency of this method, settlement curves were generated using the predicted hydraulic -

TH-3534_186104002

Table 7.3. Values of M (m/s) and P predicted using Method 2, using the equations connecting the power and variance of settlement versus log time curves, formed for different groups, each containing different numbers of points considered from the synthetic settlement versus time data and the corresponding points from the curves of initial guesses given in Table 7.1.

Cases	Groups	Points considered	No. of points	a	b	Ψ	Variance	Predicted values	
								P	M
	1	1-16	16	4.50E-03	2.485	0.062	0.428	5.872	2.449E-11
	2	1,2,4,5,7,8,10,11,13,14,16	11	5.08E-03	2.456	0.079	0.489	5.978	2.126E-11
Rutgers	3	1,3,5,7,9,11,13,15	8	3.08E-03	2.590	0.089	0.373	5.736	2.946E-11
	4	1,2,6,8,12,14,16	7	8.81E-03	2.332	0.108	0.681	5.991	2.098E-11
						Average of predicted values		**5.894**	**2.405E-11**
	1	1-22	22	2.82E-04	4.172	0.098	0.122	2.899	5.492E-08
	2	1-3,5,6,8,9,11-22	19	3.34E-04	4.115	0.106	0.132	2.885	5.569E-08
OFT	3	1-3,5,6,8,9,11,13-15,17-19	16	4.56E-04	3.986	0.117	0.148	2.877	5.592E-08
	4	1,2,4,6,8,10,12,14,16,19,21,22	12	6.87E-04	3.808	0.131	0.168	2.852	5.761E-08
						Average of predicted values		**2.878**	**5.603E-08**
	1	1-21	21	9.67E-04	3.009	0.103	0.139	3.306	2.638E-11
	2	1-3,5-8,10,11,13,14,16-21	17	1.30E-03	2.930	0.119	0.162	3.305	2.662E-11
MFT 5	3	1-3,5,6,8,11,13,14,16,17,19-21	14	1.43E-03	2.938	0.139	0.187	3.303	2.656E-11
	4	1-3,5,8,11,14,17,19-21	11	2.12E-03	2.827	0.167	0.229	3.303	2.656E-11
						Average of predicted values		**3.304**	**2.653E-11**
	1	1-21	21	3.29E-03	2.346	0.124	0.179	3.331	3.092E-11
	2	1-4.6-10.12-15,17-21	18	3.86E-03	2.319	0.139	0.202	3.346	2.991E-11
MFT 6	3	1-4,6,7,9,10,12,14,15,17-21	16	4.80E-03	2.264	0.152	0.226	3.347	2.948E-11
	4	1,2,4,6,8,10,12,14,16,18-21	13	6.31E-03	2.179	0.166	0.254	3.337	3.051E-11
						Average of predicted values		**3.340**	**3.020E-11**

TH-3534_186104002

-conductivity functions along with other known properties. Figure 7.4(a-d) shows the comparison between the synthetic settlement curves and the settlement curves obtained based on the average predicted *M* and *P* values using Method 1 for all the slurry studied. In Figure 7.4(a), a maximum difference of 0.95 mm was observed between the synthetic settlement versus time curve and the settlement versus time curve obtained using the average of predicted. *M* and *P* values for the Rutgers slurry. In the case of OFT, according to Figure 7.4(b), a maximum variation of 2.14 mm was observed, whereas for MFT 5, as shown in Figure 7.4(c), this difference has a maximum value of 0.39 mm. For MFT 6, the variation goes to a maximum of 0.17mm, as can be seen in Figure 7.4(d). These variations were negligible and had a maximum value of 8% from the synthetic curve when the predicted *M* and *P* values were used for generating the settlement versus time curves. Therefore, the predicted hydraulic conductivity parameters for the power function form, that is, $k=Me^{P,}$ can be considered to represent the settlement behavior in a centrifuge environment.

Method 2 required at least three arbitrarily simulated settlement versus time curves for the prediction of hydraulic conductivity parameters. Using the *M* and *P* values given in Table 7.1, settlement versus time curves were generated for each type of slurry. For Rutgers clay, the pairs of ($2x10^{-12}$, 3), ($2x10^{-9}$, 5), and ($2x10^{-13}$, 7) were used as *M* and *P* values to generate the arbitrary settlement versus time curves, as shown in Figure 7.2(a). From the synthetic settlement versus time curve, sixteen points were considered arbitrarily, as group 1. Corresponding points in the simulated settlement versus time curves were considered to compute the variance of these curves. A correlation of the form given in equation (18) was obtained using the variance and power values of these curves. The coefficients of this equation *a, b* and Ψ were obtained as $4.50x10^{-3}$, 2.485, and 0.062, respectively. The variance of the synthetic settlement curve for group 1 was obtained as 0.428. The value of *P* was predicted as 5.872 by substituting the variance value of synthetic settlement versus time curve in the fitted correlation. A settlement curve was then simulated using the predicted *P* value of the group and an arbitrary *M* value of $2x10^{-10}$ m/s chosen suitably for the fast simulation of the FSC settlement curve. This simulated curve was further shifted to the synthetic curve using the equation (19) which resulted in the predicted *M* value as 2.449×10^{-11} m/s. Three more groups were made using data points arbitrarily selected from the synthetic data set and the corresponding data points of the simulated curves. The same process that was applied to group 1 was repeated for these three groups as well. For all the groups, the arbitrary M value used for the prediction of the M value was maintained at $2x10^{-10}$ m/s. The values of variance-power correlation

TH-3534_186104002

coefficients and the variance values for the synthetic settlement versus time curve for all the groups are given in Table 7.3, along with the predicted value of parameters *M* and *P*. The predicted *M* and *P* values were nearly the same, showing the robustness of the method. The average of the predicted values of *M* and *P* were obtained as 5.894 and 2.405×10^{-11} m/s, which was very close to the input value used to generate the synthetic settlement versus time curve.

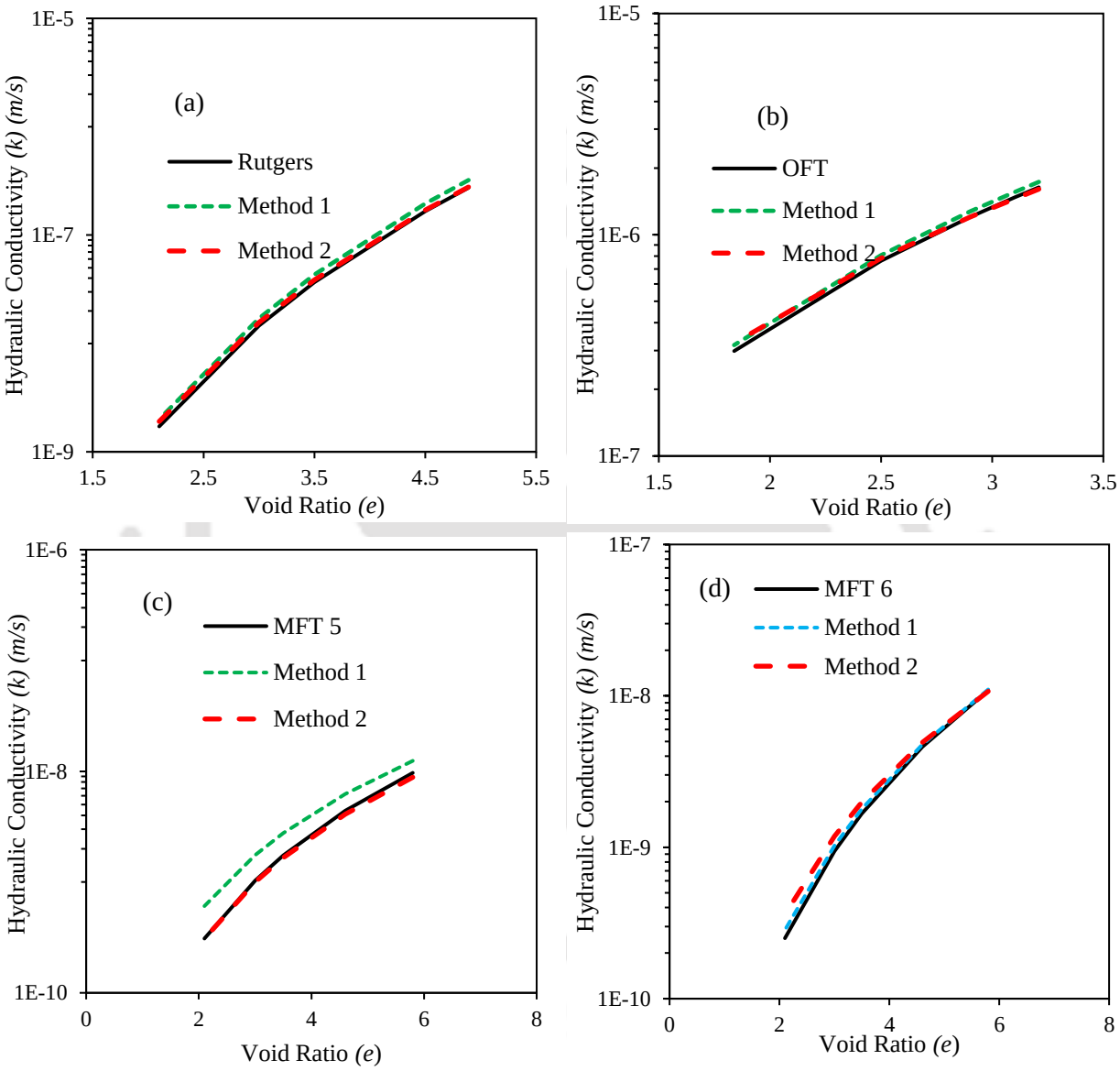


Figure 7.3. Comparison of the average of predicted hydraulic conductivity functions with functions used for generating synthetic settlement data for (a) Rutgers (b) OFT (c) MFT 5 (d) MFT 6

The procedure was repeated for other slurries, grouping data points ensuring that each data set can effectively represent the spread of the entire settlement curve. Group 1 of all the tailings/soils are shown in Figure 7.2(a-d). The arbitrary *M* value considered for translation for OFT was 1×10^{-9} m/s, while the same was 1×10^{-8} m/s for MFT 6 as well as MFT 5. Table 7.3

TH-3534_186104002

shows the *M* and *P* values predicted using Method 2. It was observed that, for each of the cases, the predicted parameter values from different groups were comparable. The arithmetic average of the predicted *M* and *P* values was calculated for each material, which, when compared to actual functions, as shown in Figure 7.3 (a-d), depicted good congruence.

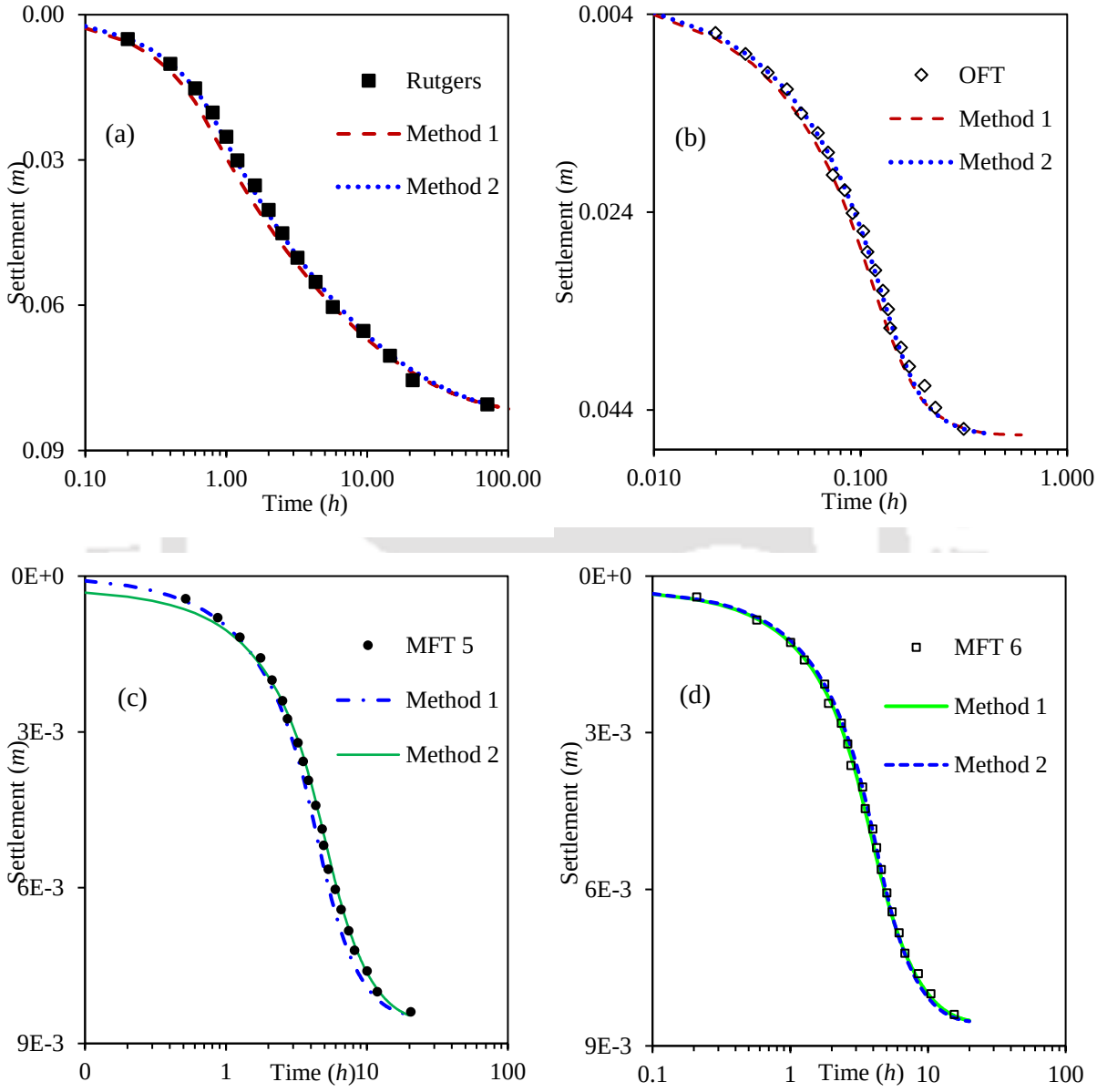


Figure 7.4. Synthetic settlement versus time curve data points and the curves generated using the average predicted values of hydraulic conductivity parameters using Method 1 and Method 2 for (a) Rutgers, (b) OFT, (c) MFT5, (d) MFT6

The average predicted parameter values were further used to simulate the FSC settlement curve for comparison with the corresponding synthetic data set, as shown in Figure 7.4(a-d).

TH-3534_186104002

Figure 7.4(a) shows that the predicted curve for Rutgers has a maximum deviation of 1.2 mm from the synthetic data considered. Figure 7.4(b) suggests that OFT has a maximum deviation of 1.37 mm from the original curve. For MFT 6 and MFT 5, the deviation is 0.16 mm and 0.21 mm, respectively, as can be seen in Figures 7.4(d) and 7.4(c). The maximum percentage deviation was 3.7% observed for the case of MFT 5. Therefore, Method 2 can predict conductivity function parameters in *Ng*case such that the predicted parameters form a function that can simulate the settlement behavior accurately.

Method 1 predicted higher settlement values than the corresponding synthetic settlements at some time instances for both Rutgers and OFT, as shown in Figure 7.4(a-d). In the case of MFT 5, in Method 1, a slight over-predicting nature was observed during the initial few hours of run, while Method 2 started marginally overestimating the settlement value after a certain time. The simulated settlement versus time curves using predicted parameters from both Method 1 and Method 2 were found to perfectly match the synthetic settlement behavior for MFT 6. Only two FSC plots using properly selected initial pairs of M and P were necessary to arrive at a good prediction for the hydraulic conductivity parameters in the case of Method 1, while only three FSC simulations were necessary in the case of Method 2. The requirement of continuous generation of multiple simulated settlements versus time plots was eliminated in these two graphical approaches, unlike the methods using optimization techniques.

7.2.2. Prediction Using Centrifuge Settlement Data from Literature

Method 1 was used for predicting the hydraulic conductivity parameters from settlement versus time curves obtained from centrifuge experiments conducted by Robinson et al. (2003) and Sorta (2015) on beam centrifuges. Four types of samples were considered, the properties of which are provided in Table 4.3.

The settlement versus time curves obtained from different centrifuge tests were used in the graphical computations involved in Method 1, along with the curves generated numerically. The initial assumptions for M and P used are given in Table 7.1. Five initial guesses were considered for each slurry such that the settlement versus time curves generated numerically with these are spaced apart and have visibly different slopes, as shown in Figure 7.5(a-d). Four combinations of these initial guesses were considered, resulting in four sets of predicted parameter values for each of the sample types, which are presented in Table 7.4.

The average of predicted hydraulic conductivity parameters are compared with the experimental data from the literature in Figures 7.7(a-d). The predicted function was observed

TH-3534_186104002

to be in the range of the reported literature values. The settlement versus time curves generated numerically using the average of predicted parameters were compared with data from centrifuge tests, as shown in Figure 7.8(a-d). The maximum difference between the settlement curve obtained using the average value of the parameters predicted for each sample using Method 1 and the measured settlement value from centrifuge was observed to be 4.6 mm for SMC (Figure 7.8(a)), 1.2 mm for Kaolinite (Figure 7.8(b)), 1.73 mm for TT50 (Figure 7.8(c)), and 2.83 mm for AL15 (Figure 7.8(d)). The percentage error corresponding to the maximum deviation from the measured settlement curve was 9.8%, observed in the case of AL15.

Table. 7.4 M and P values predicted for synthetic data cases using Method 1

Cases	M_1	P_1	M_2	P_2	Predicted Values	
					M	P
SMC	$2x10^{-10}$	8	$3x10^{-11}$	4	$9.590x10^{-12}$	6.068
	$2x10^{-10}$	8	$2x10^{-9}$	3	$1.297x10^{-11}$	5.823
	$4x10^{-8}$	7	$3x10^{-11}$	4	$1.260x10^{-11}$	5.761
	$3x10^{-8}$	7	$4x10^{-12}$	6	$6.160x10^{-12}$	6.431
	Average of predicted values				**$1.033x10^{-11}$**	**6.02**
Kaolinite	$1x10^{-12}$	8	$1x10^{-7}$	2.5	$2.886x10^{-10}$	6.214
	$1x10^{-11}$	9	$1x10^{-7}$	2.5	$1.717x10^{-10}$	6.611
	$1x10^{-11}$	9	$1x10^{-8}$	3	$4.816x10^{-10}$	5.817
	$1x10^{-12}$	8	$1x10^{-9}$	4	$2.680x10^{-10}$	6.244
	Average of predicted values				**$3.020x10^{-10}$**	**6.221**
TT50	$2x10^{-6}$	9	$2x10^{-11}$	2	$3.008x10^{-9}$	4.371
	$2x10^{-6}$	9	$2x10^{-12}$	3	$2.282x10^{-9}$	4.849
	$2x10^{-7}$	8	$2x10^{-12}$	3	$2.345x10^{-9}$	4.765
	$2x10^{-8}$	7	$2x10^{-11}$	2	$2.902x10^{-9}$	4.338
	Average of predicted values				**$2.634x10^{-9}$**	**4.581**
AL15	$1x10^{-11}$	7	$1x10^{-6}$	1.5	$3.949x10^{-10}$	4.189
	$1x10^{-8}$	6	$1x10^{-6}$	1.5	$4.002x10^{-10}$	4.147
	$1x10^{-12}$	9	$1x10^{-7}$	2	$3.039x10^{-10}$	4.455
	$1x10^{-8}$	6	$1x10^{-2}$	2	$3.593x10^{-10}$	4.236
	Average of predicted values				**$3.646x10^{-10}$**	**4.256**

TH-3534_186104002

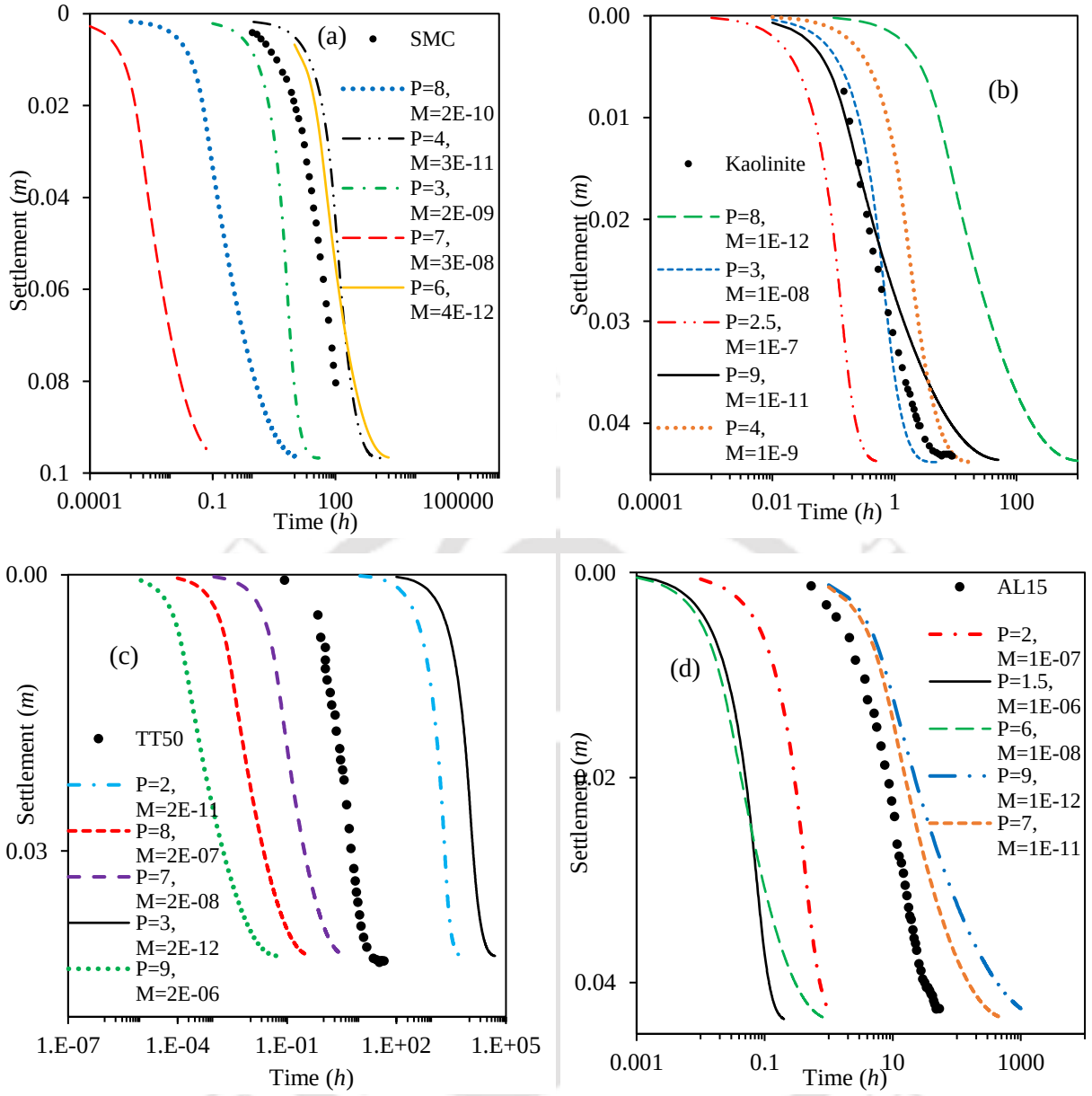


Figure 7.5. Settlement versus time plots generated for different initial guess values of M and P given in Table 7.1, and the data points measured from centrifuge for (a) SMC (b) Kaolinite (c) TT50 and (d) AL15 for Method 1

The application of Method 2 on synthetic data cases showed promising results. Therefore, Method 2 was tested on four sets of settlement versus time data obtained from self-weight consolidation tests conducted in a centrifuge environment, taken from the literature. The input properties given in Table 4.3 were used along with the initial guess values given in Table 7.1 to simulate settlement versus time curves for each of the experimental data cases. For each of these cases, by considering the appropriate set of data points from the measured and simulated settlement curves, four groups were made and corresponding variance-power relationships were established. The variance value of the measured data points for each of these groups was

TH-3534_186104002

substituted in the corresponding correlation to predict the respective *P* values. Figure 7.6(a-d) shows the group 1 data set for different sample types from which, by removing a few points, more groups were formed. The *M* and *P* values predicted using Method 2 for various groups for each of the experimental data cases are given in Table 7.5.

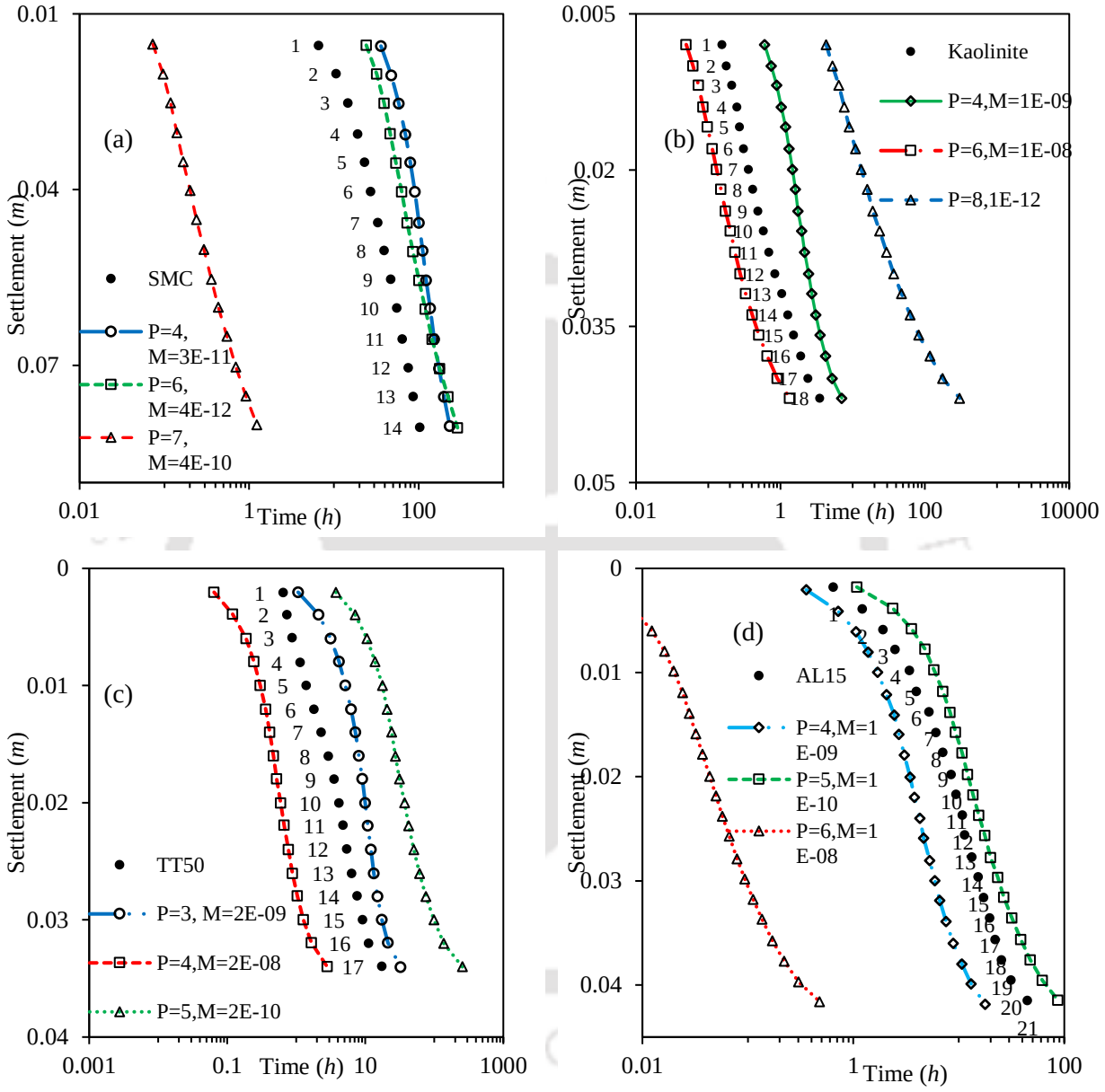


Figure 7.6. Settlement versus time curves showing the data points measured from the centrifuge consolidation test and corresponding points from the simulated curves for initial guesses considered in group 1 for predicting the power P value using Method 2 for (a) SMC (b) Kaolinite (c) TT50 (d) AL15

The average predicted values of hydraulic conductivity function parameters were compared to the corresponding literature data in Figures 7.7 (a-d), which showed good matching. Using the

TH-3534_186104002

average values of predicted parameters, settlement versus time curves were simulated to compare them with the original/measured settlement curve. The comparison plots are given in Figure 7.8(a-d). Figure 7.8(a) suggests that for the SMC, a maximum deviation of 3.48 mm was observed from the original settlement curve, assuming that the measured data points form a continuous curve. For TT50, Figure 7.8(c) suggests that the maximum deviation value is 1.84 mm. For AL15 (Figure 7.8(d)), a 1.95mm deviation was seen, while for Kaolinite, the maximum deviation is 1.18 mm, according to Figure 7.8(b).

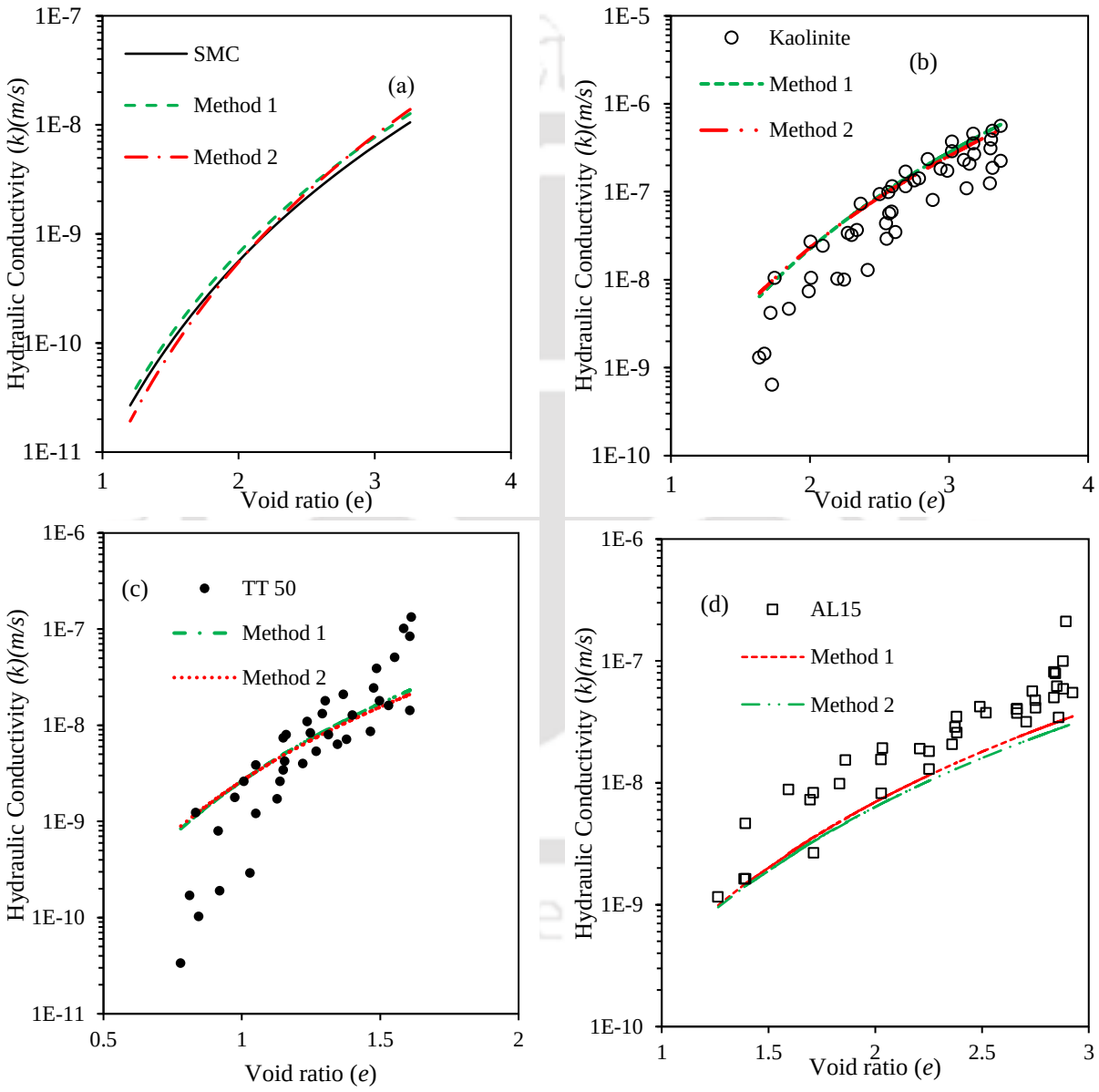


Figure 7.7. Comparison of the average of predicted permeability functions with data from the literature for (a) SMC, (b) Kaolinite, (c) TT50, (d) AL15

TH-3534_186104002

Table 7.5. Values of M (m/s) and P predicted using Method 2, using the equations connecting the power and variance of settlement versus log time curves, formed for different groups, each containing different numbers of points considered from the experimental settlement versus time data and the corresponding points from the curves using the initial guesses given in Table 7.1

Cases	Groups	Points considered	No. of points	a	b	Ψ	Variance	Predicted values	
								P	M
SMC	1	1-14	14	5.23E-04	2.701	0.031	0.119	6.668	5.322E-12
	2	1,3-7,9-14	12	5.89E-04	2.665	0.028	0.117	6.553	6.022E-12
	3	1,3,4,6,7,9,10,12,13,14	10	6.69E-04	2.644	0.032	0.130	6.585	5.733E-12
	4	1,3,5,7,9,11,13,14	8	7.54E-04	2.631	0.037	0.146	6.620	5.539E-12
						Average of predicted values		**6.606**	**5.654E-12**
Kaolinite	1	1-18	18	2.24E-03	2.262	0.030	0.156	5.938	3.766E-10
	2	1-3,5-8,10,11,13-18	15	2.55E-03	2.254	0.034	0.176	5.933	3.748E-10
	3	1-3,5,6,9,10,12,14,16-18	12	2.83E-03	2.264	0.042	0.197	5.864	4.043E-10
	4	1,3,5,7,9,11,13,15,17	9	2.18E-03	2.222	0.030	0.145	5.936	3.765E-10
						Average of predicted values		**5.918**	**3.830E-10**
TT50	1	1-17	17	1.61E-03	2.571	0.105	0.176	4.370	2.624E-09
	2	1-4,7,8,10-12,14-16	12	8.11E-04	2.847	0.126	0.178	4.322	2.720E-09
	3	1,3-6,9,10,12,15,16	10	3.62E-04	3.300	0.120	0.167	4.367	2.645E-09
	4	1,3-5,9,10,12,15	8	4.59E-05	4.266	0.127	0.152	4.364	2.639E-09
						Average of predicted values		**4.356**	**2.657E-09**
AL15	1	1-21	21	2.15E-02	1.309	0.079	0.218	4.145	3.612E-10
	2	1-5,7-9,11-14,16,17,19-21	17	2.55E-02	1.281	0.090	0.247	4.127	3.629E-10
	3	1-4,6,7,9,11,14,17,19-21	14	3.09E-02	1.275	0.103	0.291	4.109	3.648E-10
	4	1,2,4,6,9,11,14,17,19,21	10	5.12E-02	1.076	0.078	0.316	4.156	3.578E-10
						Average of predicted values		**4.134**	**3.617E-10**

TH-3534_186104002

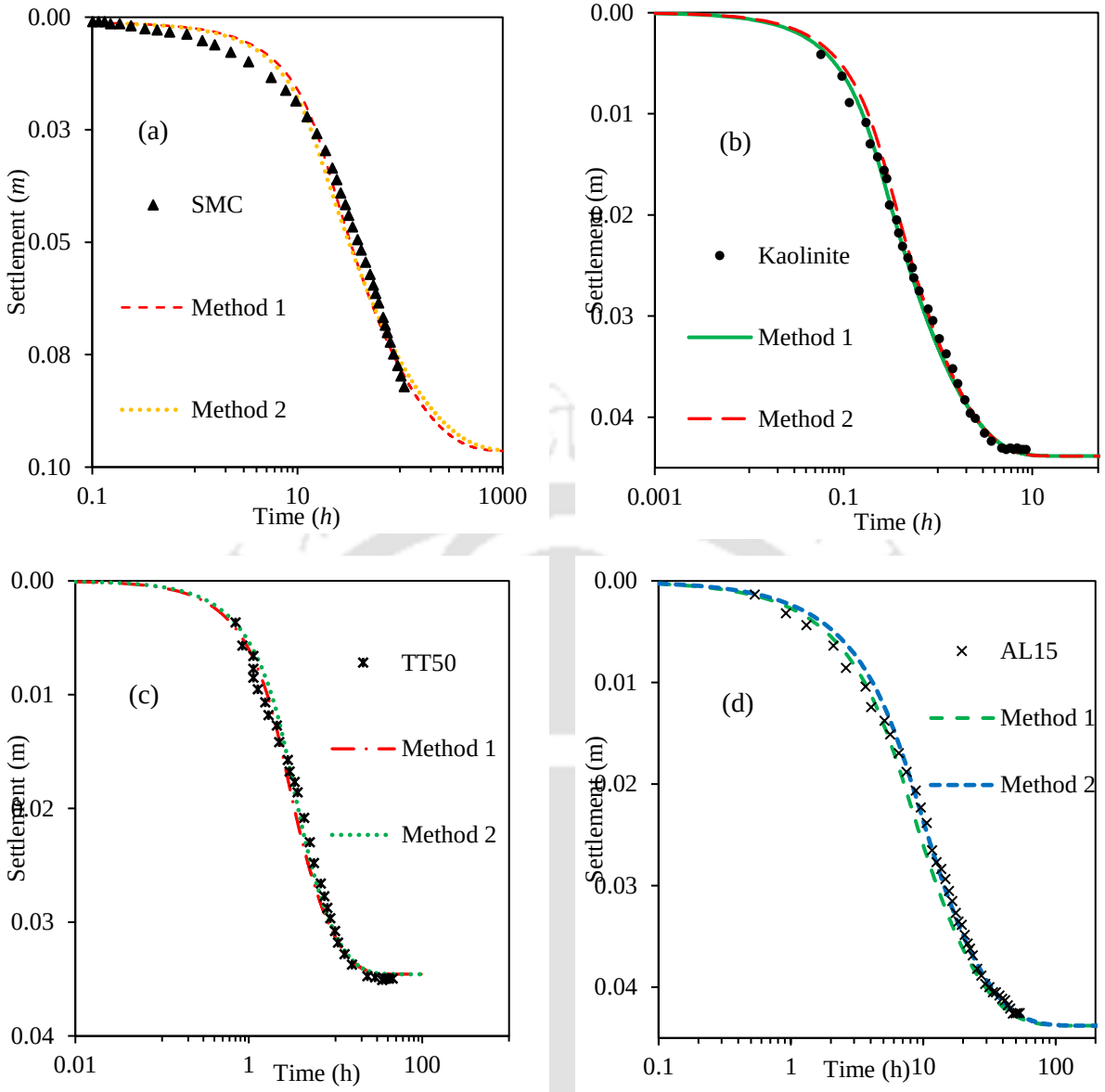


Figure 7.8. Measured settlement versus time curve data points and the curves generated using the average predicted values of hydraulic conductivity parameters using Method 1 and Method 2 for (a) SMC, (b) Kaolinite, (c) TT50, (d) AL15

The maximum percentage deviation observed is in the case of AL15, with a value of 8.5%. Minor overestimation in settlement value was observed for certain time intervals when Method 1 was used in the cases of Kaolinite and TT50, as shown in Figures 7.8(b) and 7.8(c), respectively. Slight under-prediction was also observed for both methods in the case of TT50 at around 1 hour.

Method 2 underestimates the settlement value more than Method 1 does in this case. For SMC (Figure 7.8(a)), up to around 10 hours, both methods underestimate the settlement value. After 10 hours, a negligible over-estimation nature is observed for Method 1 as well as Method 2. In

TH-3534_186104002

the case of AL15 (Figure 7.8(d)), a relatively good match was seen between the simulated curves and the measured data points up to 2.5 hours, beyond which both methods slightly overestimate settlement. As the consolidation progressed, Method 2 was observed to be able to predict the settlement behavior better than Method 1.

7.2.3. Inverse analysis using 50% of the measured data

In practice, centrifuge runs may not be long enough to produce data to the end of self-weight consolidation. To simulate such a condition, the methods were tested for a subset of data points for the cases of Rutgers and OFT. Points from 1 to 8 were considered for Rutgers, while points from 1 to 11 were considered for OFT. Method 1 was applied with three initial guess values for *M* and *P* each for OFT and Rutgers (Table 7.6). Since the number of points considered is lesser, we have considered only one group each for both the slurries for Method 2. It was observed that the optimal *M* and *P* parameters predicted using Method 1 have values closer to the average predicted optimal values (Table 7.2) than Method 2 (Table 7.3).

Table 7.6. M (m/s) and P values predicted using Method 1 and Method 2, considering only 50% of the data points for the analysis

Method	Cases	M_1	P_1	M_2	P_2	Predicted Values	
						P	M
Method 1	**Rutgers**	2.00E-07	9	2.00E-08	4	5.501	4.76E-11
		2.00E-13	7	2.00E-08	4	5.742	3.11E-11
				Average of predicted values		**5.622**	**3.94E-11**
	OFT	1.00E-11	6	1.00E-07	3	3.774	2.05E-08
		1.00E-11	6	1.00E-06	2	3.1804	4.07E-08
				Average of predicted values		**3.4772**	**3.06E-08**

	Cases	Points	a	b	c	Variance	Predicted Values	
							P	M
Method 2	**Rutgers**	1 to 8	3.22E-07	5.898	0.0741	0.0947	6.526	1.08E-11
	OFT	1 to 11	0.0533	0.292	0.005	0.0736	2.371	9.66E-08

The settlement versus time curves simulated using the predicted parameters are compared with the synthetic temporal settlement data for OFT and Rutgers in Figure 7.9(a-b). It was observed that the simulated curve for Method 1 is closer to the synthetic data points than the simulated curve for Method 2. The maximum variation of the simulated curves was observed to be 11.165% and 12.12% of the corresponding synthetic settlement value for Rutgers and OFT, respectively, by Method 1. These values were 28.05% and 16% of the corresponding synthetic

TH-3534_186104002

settlement value for Rutgers and OFT, respectively, when Method 2 was used. The larger variation with Method 2 can be attributed to the fact that the points considered for analysis were located at the upper part of the curve and were not dispersed enough along the log-time axis. Therefore, the corresponding variance values cannot represent the spread of the entire settlement versus time curve correctly. Therefore, it is recommended to use Method 1 for analysis when a lesser number of settlement data points are available.

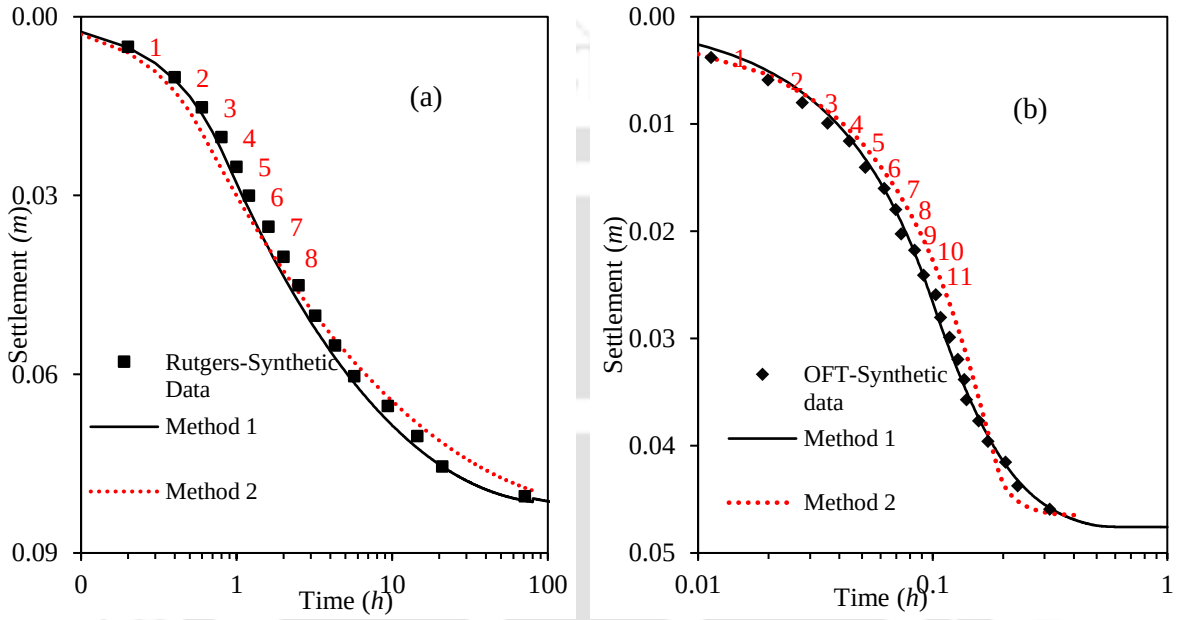


Figure 7.9. Testing the Method 1 and Method 2 using 50% of the settlement versus time data points for (a) Rutgers (b) OFT

7.3. Summary

This work used two established graphical techniques of inverse analysis to predict the hydraulic conductivity parameters based on settlement-time data obtained from centrifuge testing. The approaches were previously used in 1g column testing but were implemented for centrifuge tests in the present study. The numerical simulation of FSC behaviour was conducted by using the explicit finite difference method solution of the governing equation for the self-weight FSC in centrifuge conditions. The change in the scale factor of acceleration over the depth of the sample was taken into account. Four slurry materials were used for generating synthetic settlement-time curves, and the hydraulic conductivity parameters were estimated using graphical techniques. The techniques were then validated using settlement-time data obtained from four centrifuge consolidation experiments reported in the literature. As observed in 1g

TH-3534_186104002

self-weight consolidation, the study discovered that the variation in the position of the settlement-time curve along the log t-axis in response to a change in the multiplier of the hydraulic conductivity function is also relevant to centrifuge consolidation tests and can be applied for predicting the optimal multiplier value. The shape and spread of settlement-time curves in centrifuge tests showed a dependency on the power value, similar to consolidation in the 1g environment, which helped in predicting the optimal power value. The settlement curves, determined using predicted multiplier and power values, exhibited strong concordance with actual settlement data. The methods were applicable to both beam and benchtop centrifuges, various initial void ratios, and compressibility functions. The graphical approaches were observed to be robust and quick methods of inverse analysis.

The present chapter established the effectiveness of the graphical approaches in predicting the hydraulic conductivity function parameters. The next chapter develops a refined approach towards inverse analysis, using metaheuristic optimisation algorithms for the back prediction. Simultaneous back-prediction of hydraulic conductivity function and compressibility function is carried out using 1g settlement data.

TH-3534_186104002

8. Inverse Analysis Using 1g Settlement Data

8.1 General

This chapter explores the implementation of six optimisation algorithms for the back-estimation of constitutive function parameters, that is, the coefficients of compressibility and hydraulic conductivity functions from conventional FSC tests such as settling column test or tank test, conducted in 1g condition. Three novel optimisation algorithms based on conventional PSO and ABC, namely, MABC, HABC and HPSO, are presented in this chapter. QPSO, an advanced version of the conventional PSO algorithm, was also explored. The efficiencies of these algorithms were compared in terms of the quality of estimated parameters and the robustness of convergence, based on three runs each per slurry material. The algorithms were first tested using the synthetic settlement data generated for MFT 5, MFT 6 and Rutgers samples. The experimental settlement data for Antwerpen Slurry, Phosphatic Clay and PA-MFT were used for validation. The EFDM solution to the governing equation of 1g FSC were used for the numerical simulation of settlement data in the forward analysis part. The best runs out of the three runs for each algorithm were compared in terms of speed of convergence. The characteristics of novel optimisation algorithms were explored to optimise their use in further applications. In Section 8.2, the optimisation problem of estimating hydraulic conductivity coefficients when the compressibility function is known and time-invariant is analysed. In Section 8.3, simultaneous back-estimation of coefficients of the compressibility function and hydraulic conductivity function are presented.

8.2 Inverse analysis for hydraulic conductivity parameters

The power (P) and multiplier (M) values of the hydraulic conductivity function for slurries were observed to regulate the slope and location of the settlement curve with respect to the *log t*-axis, respectively. The back-prediction of M and P parameters from these data can be achieved using optimization algorithms with material properties given in Table 4.2 and observed FSC settlement values at different times as input.

8.2.1 Independent performance of initial value-based algorithms

The *fmincon* and *fminsearch* algorithms are deterministic optimisation methods that can extract the global minimum provided the exact nearby area is defined. This is done by providing the

TH-3534_186104002

initial point values for the parameters being optimised at the onset of the optimisation process. The sensitivity to initial values results in a lack of robustness and a lower degree of convergence to appropriate solutions when the optimisation landscape has multiple peaks. The heavy dependency of the *fmincon and fminsearch* on the initial guess values was explored as a part of this study. Inverse analysis was run in *fmincon* using settlement data from Phosphatic Clay and Rutgers, while *fminsearch* was used for inverse analysis from the settlement data of Antwerpen Slurry and Phosphatic Clay. The initial guess values for the parameters to be predicted (*M* and *P*) were chosen randomly and given as input, along with other relevant properties from Table 4.2.

Table 8.1. Hydraulic conductivity parameters -power (P) and multiplier (M), predicted using fmincon and fminsearch

Method	Material	Initial guess		Number of iterations	RMSE	Predicted Values	
		P	M *(m/s)*			P	M *(m/s)*
fmincon	**Phosphatic Clay**	4.11	1.41E-11	23	2.41E+00	4.02	1.87E-11
		3.33	**2.12E-09**	**26**	**1.15E+07**	**4.22**	**9.59E-07**
		5.50	5.00E-11	30	1.17E+07	4.22	1.00E-06
	Rutgers	6.67	2.50E-12	25	7.41E-01	6.41	1.51E-13
		10.00	1.02E-17	32	9.44E-01	7.29	3.61E-14
		6.25	**1.20E-11**	**10**	**1.40E+07**	**2.97**	**7.03E-06**
fminsearch	**Antwerpen Slurry**	**4.00**	**1.00E-07**	**271**	**1.17E+07**	**3.56**	**2.14E-11**
		9.00	1.00E-11	66	2.90E-02	8.03	1.92E-09
		5.00	1.00E-12	250	2.15E+00	3.87	6.78E-09
	Phosphatic Clay	7.00	1.00E-07	263	1.140E+07	4.22	9.82E-10
		3.00	1.00E-09	94	2.414E+00	4.02	1.87E-11
		8.00	**1.00E-08**	**250**	**8.043E+07**	**4.22**	**6.83E-09**

The objective function values and the *M* and *P* values back-predicted using *fmincon* and *fminsearch* were observed to vary based on the initial guess values used, as shown in Table 8.1. The algorithm converged at different final optimal values after varying numbers of iterations based on the initial guess values provided. These algorithms converged to the local minima if local minima were present near the initial guess values. The significant advantages were that fast convergence was observed to the global optima in cases initialised with appropriate initial values and for multiple runs using the same initial guess values of *M* and *P*,

TH-3534_186104002

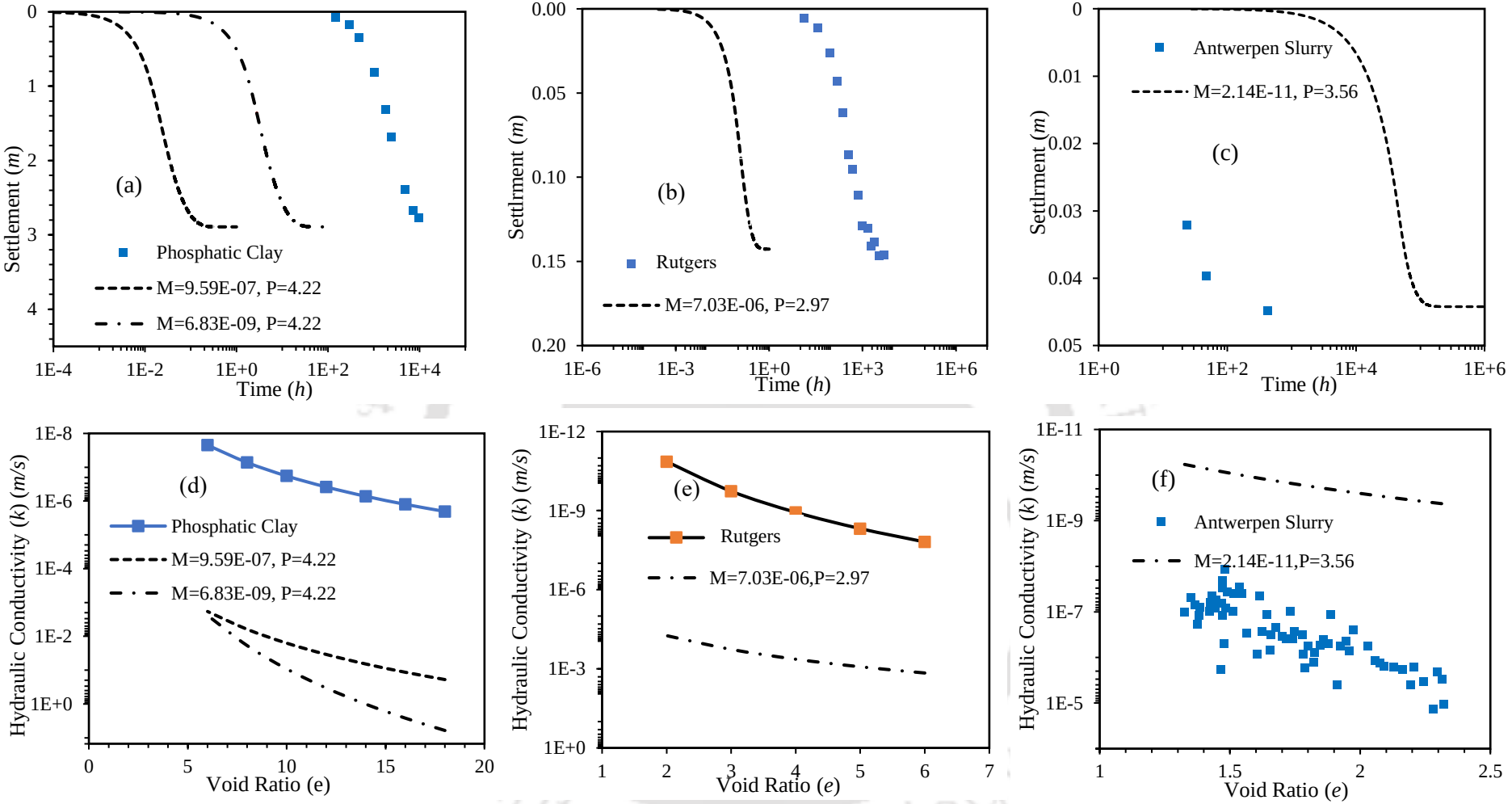


Figure 8.1. Comparison of worst-case predictions obtained using fmincon and fminsearch with settlement versus time data for (a) Phosphatic Clay (b) Rutgers (c) Antwerpen Slurry, and in terms of hydraulic conductivity function for (d) Phosphatic Clay (e) Rutgers (f) Antwerpen Slurry

TH-3534_186104002

these algorithms converged to the same optimal values, showing the robustness and repeatability of these methods. The worst values of predicted *M* and *P* based on the RMSE, as given in Table 8.1, were used to simulate the settlement versus time curves for the corresponding cases, as shown in Figures 8.1(a-c). The hydraulic conductivity functions plotted using these *M* and *P* values were also compared with the corresponding actual hydraulic conductivity function in Figures 8.1(d-f). It was observed that the worst-case predictions significantly varied from the original behaviour. The dependency of optimal values on the initial guesses necessitates the knowledge of the actual value of the predicted parameters. This obstructs the primary purpose of inverse analysis, which is the estimation of unknown parameters. The ability of these algorithms to consistently converge to the same parameters, given appropriate initialization, can be harnessed by employing swarm-based optimization approaches to explore the search space and determine the initial values for these algorithms.

8.2.2 Swarm-based algorithms and tuning parameters

Swarm intelligence-based algorithms do not rely on initial guesses or gradients for inverse analysis. These algorithms, however, move more slowly than gradient-based ones or simplex methods. The capacity of swarm-based algorithms to tackle complicated, dynamic problems through parallel exploration and exploitation of solution spaces, along with the predictability, assurance of optimality, and efficiency of deterministic algorithms, is much sought after. Consequently, hybrid algorithms emerged. This study proposes two novel hybrid algorithms, HPSO and HABC, incorporating deterministic methods, *fmincon* and *fminsearch*, respectively, for inverse analysis. The classic PSO and ABC algorithms and the modified variants, QPSO and MABC, are also discussed. The hybrid algorithms have two more tuning parameters in comparison, which are the number of iterations designated for the swarm-based algorithm and the same for the initial point-based algorithm.

The forward analysis function used to compute the objective function values is computationally expensive. Therefore, robust convergence within the least number of iterations possible, using smaller populations, is desired in the optimization algorithms. Performances of six algorithms were studied based on the objective function values and the convergence. The algorithms were run three times for each of the material cases. Appropriate upper and lower bounds were maintained to define the search space. The personal learning and social learning coefficients for all the PSO cases were maintained as 1.5 and 2, respectively. The value of inertia weight was initialized as 0.9, which was damped to 0.99 times at the end of each iteration. The swarm

TH-3534_186104002

population size was maintained at 40 for all the cases. The ABC algorithm for all cases utilized a colony size of 80, consisting of the employed and onlooker bees. The food number, therefore, becomes equal to 40, which in turn defines the number of employed and onlooker bees as 40 each. The improvement limit for each solution was maintained at 50. The performance-related, user-defined parameters for QPSO include the size of the swarm and contraction expansion factor. The swarm size considered was 40. The computation of the contraction expansion factor was based on Equation (4.49). The values of α_1 and α_2 for this computation were taken as 0.01 and 0.1, respectively. As a result, the contraction expansion factor was observed to vary from 0.9901 to 0.01 for a maximum of 100 iterations. The values used for learning coefficients and inertia weight for HPSO were the same as those of PSO, mentioned above. The swarm size was maintained at 40.

The sensitivity of optimal values obtained and convergence speed on these tuning parameters can be further understood by trial and error. The parameters can be fixed through hyperparameter estimation to fine-tune the performance. These aspects were not explored in the present study. The objective function values for inverse analysis were calculated using Equation (4.41). The errors were calculated using the settlement values in meters. The best run was defined as the one that converged to the least RMSE value among the three runs when the converged RMSE values for the runs differed. In a scenario where all three runs achieved the same converged value for the objective function, the run that attained the lowest RMSE within the fewest number of iterations was regarded as the most efficient. The performance of various algorithms were compared based on the best, worst, and mean RMSE values and the speed of convergence of the best run.

8.2.3 Back-estimation using Synthetic Settlement Data

The observations from the inverse analysis using synthetic settlement data are presented in Table 8.3. The best objective function values of all the algorithms were almost equal to each other within the considered number of iterations. It was observed that the hybrid algorithms produced the most robust solutions as the difference between mean and best values of objective function values were the least in these cases. The independent runs failed to converge to the same objective function values for QPSO and PSO for all the cases, while ABC showed this issue in the case of MFT5. The iterations versus RMSE value of the best runs of all the algorithms for these materials are shown in Figures 8.2(a-c). QPSO converged to near-optimal values faster and continued to improve over the rest of the iterations to reach the lowest value.

TH-3534_186104002

Table 8.2: Performance of different inverse analysis algorithms using synthetic settlement data as the input for predicting the power (P) and multiplier (M)

Material	Algorithm	RMSE Values			Iteration	Best predicted values	
		Best	Mean	Worst	Number	P	M (m/s)
MFT 5	**PSO**	5.19E-03	7.51E-03	9.21E-03	66	3.62	1.65E-11
	HPSO	5.34E-03	5.31E-03	5.32E-03	48	3.437	2.99E-11
	QPSO	5.27E-03	2.68E-02	4.29E-02	8	3.313	2.45E-11
	ABC	5.03E-03	8.20E-03	1.39E-02	36	3.409	2.42E-11
	MABC	5.56E-03	6.05E-03	8.25E-03	51	3.447	2.27E-11
	HABC	4.22E-03	4.22E-03	4.22E-03	58	3.447	2.27E-11
MFT 6	**PSO**	2.08E-03	2.19E-03	2.40E-03	57	3.912	1.21E-11
	HPSO	2.08E-03	2.14E-03	2.22E-03	45	3.898	1.24E-11
	QPSO	2.16E-03	4.73E-03	6.95E-03	11	3.87	1.28E-11
	ABC	2.08E-03	2.09E-03	2.13E-03	11	3.898	1.24E-11
	MABC	2.13E-03	2.10E-03	2.13E-03	52	3.879	1.27E-11
	HABC	2.08E-03	2.08E-03	2.08E-03	51	3.898	1.24E-11
Rutgers	**PSO**	0.2673	0.3789	0.5915	56	5.968	2.10E-11
	HPSO	0.2029	0.2029	0.2029	50	6.217	1.40E-11
	QPSO	0.2603	0.2959	0.3668	14	6.193	1.50E-11
	ABC	0.2623	0.2779	0.2897	52	6.129	1.63E-11
	MABC	0.2598	0.272	0.2962	65	6.232	1.41E-11
	HABC	0.2598	0.2598	0.2598	51	6.212	1.39E-11

TH-3534_186104002

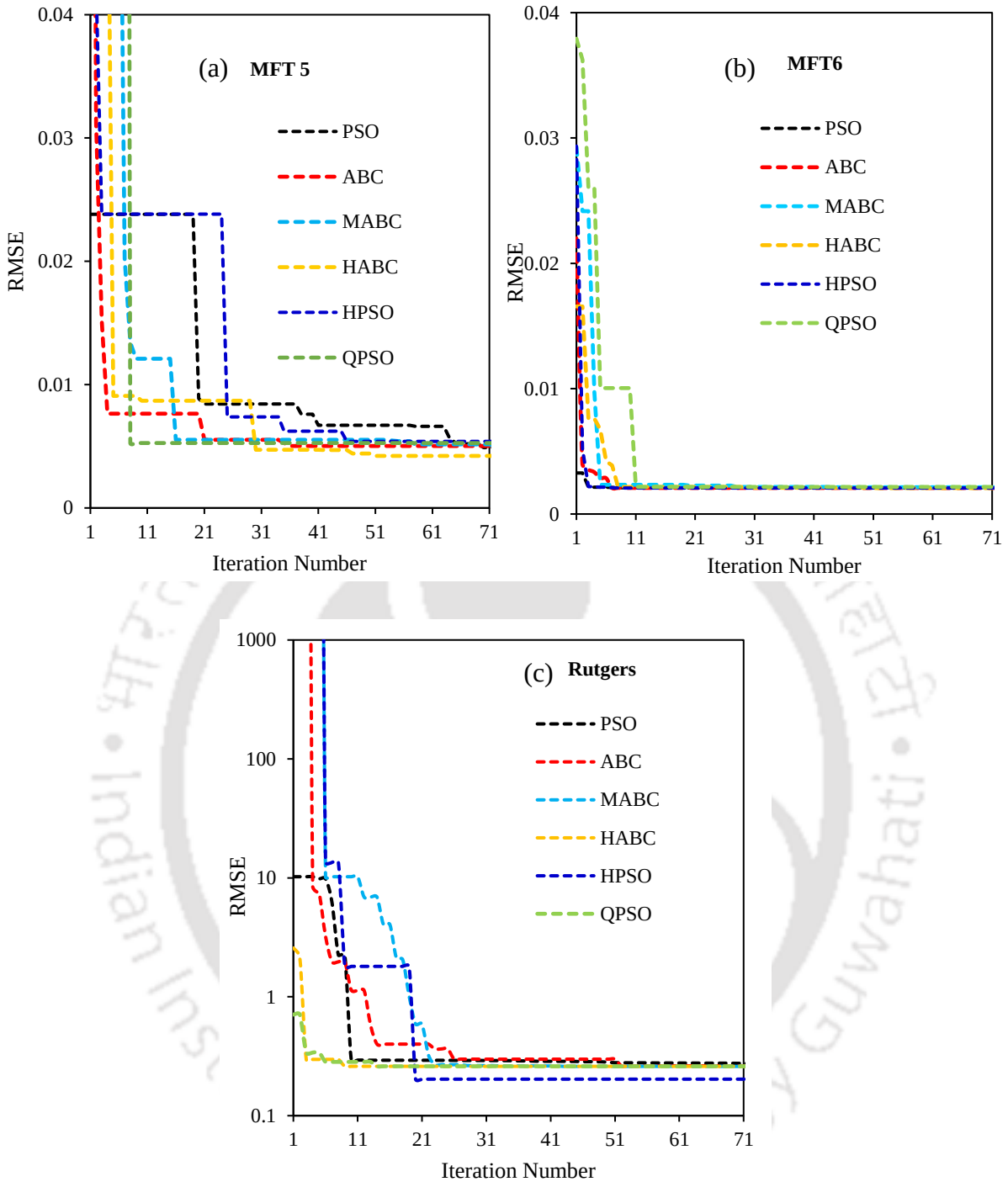


Figure 8.2. The objective function value (RMSE) versus the number of iterations plotted for the best run of each of the algorithms employed for inverse analysis using synthetic settlement data of (a) MFT5, (b) MFT6 and (c) Rutgers

The optimised power and multiplier values for these cases, as given in Table 8.2, are compared with the actual values in the form of the hydraulic conductivity function in Figure 8.3(a-c). It was observed that the optimised values for *M* and *P* from all the algorithms were in good

TH-3534_186104002

agreement with the original functions used to generate the synthetic data, irrespective of the minor

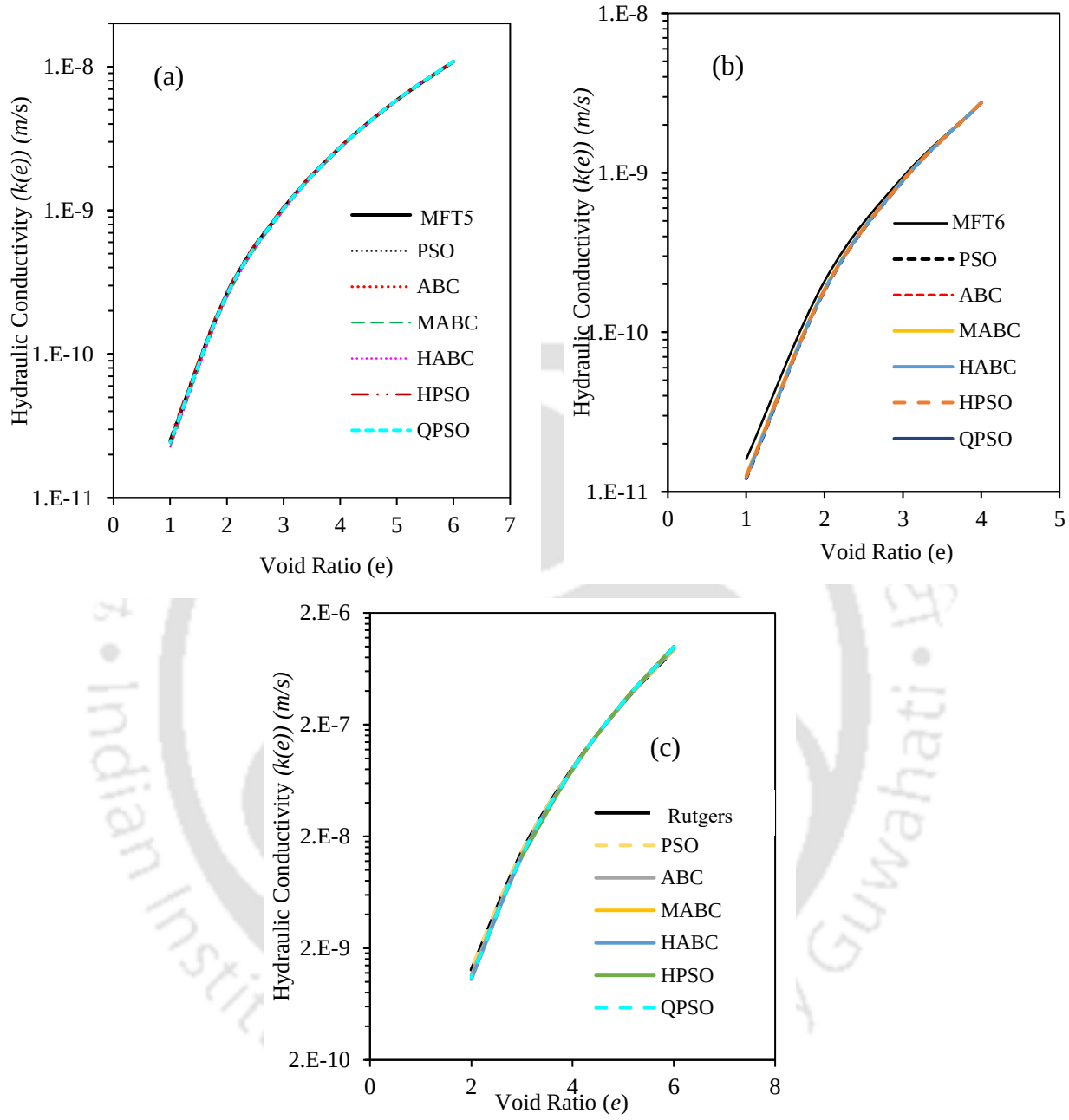


Figure 8.3. Comparison of optimised power (P) and Multiplier (M) values from various algorithms with the actual values in the form of hydraulic conductivity function for (a) MFT5, (b) MFT6, and (c) Rutgers

differences in the best objective function values. The settlement behaviour of synthetic data cases, simulated using back predicted parameters as inputs, are shown in Figures 8.4(a-c). In each of the cases, the settlement curves simulated for all six algorithms were found to overlap

TH-3534_186104002

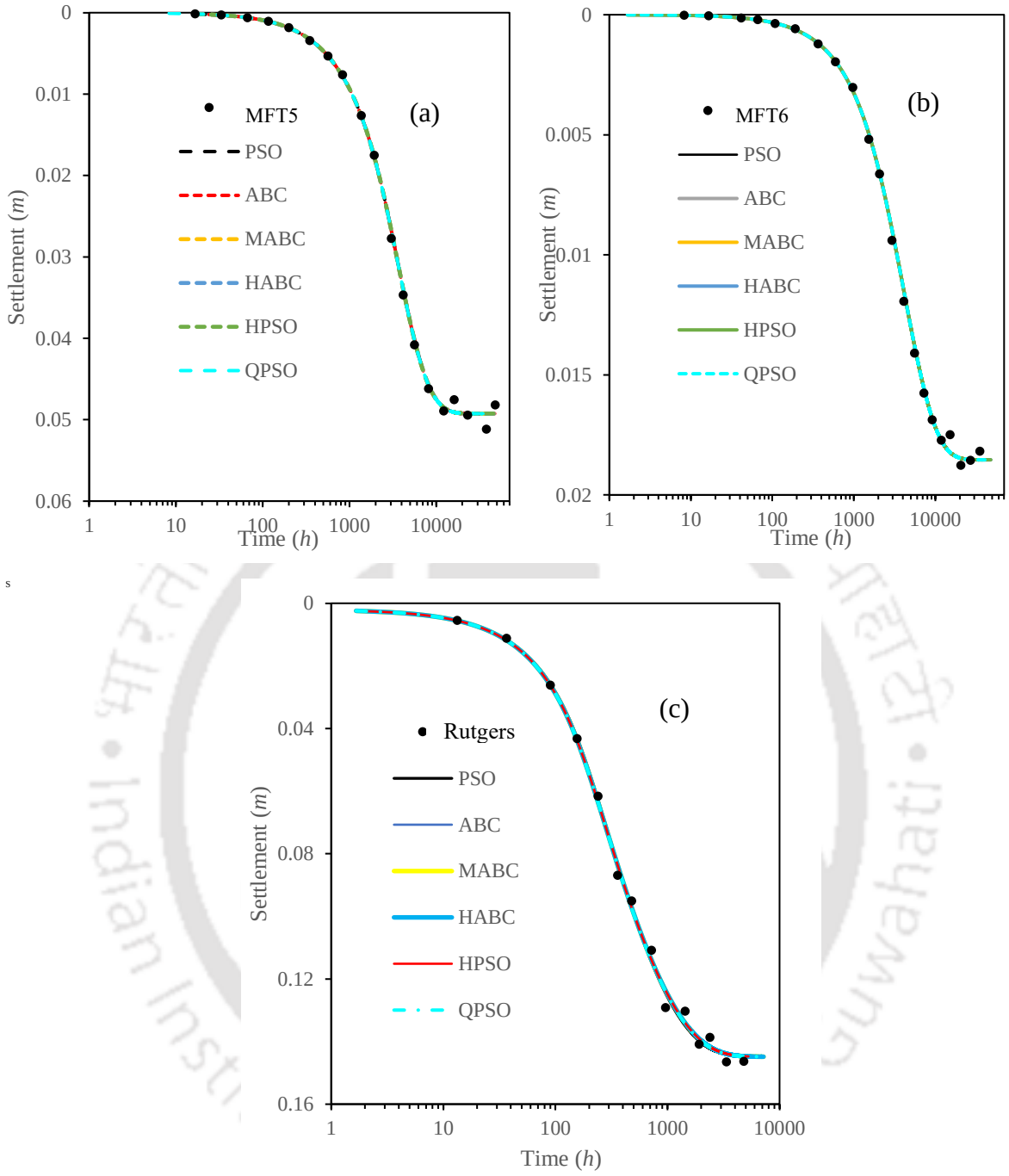


Figure 8.4. Comparison of synthetically generated settlement data points given as input for inverse analysis using the algorithms considered and settlement curves simulated using the hydraulic conductivity function parameters predicted by inverse analysis for (a) MFT5, (b) MFT6, and (c) Rutgers

and closely model the synthetic data used for optimization. The under-prediction of settlement values meant the simulated or predicted settlement value at a given time point was lesser than the corresponding synthetic data point, while the over-prediction meant that the predicted

TH-3534_186104002

settlement value was larger than the corresponding synthetic settlement data. The maximum percentage error when the overlapping simulated settlement curves from all the algorithms were compared with the synthetic data points was 3.9% under-prediction at 3795 hours for MFT5 for MABC. PSO outcomes over-predicted the settlement values for MFT6 by 4.2%, while other algorithms simulated 4 % over-prediction at 15200 hours. For Rutgers, PSO over-predicted the settlement value at 1440 hours by 3.6%. The maximum percentage error in settlement predicted by optimal parameters from QPSO was 4.1% (under-prediction) at 960 hours. Other algorithms under-predicted the settlement value by 4.2% at the same time point.

8.2.4 Back-estimation using experimental settlement data

Table 8.3 compares objective function values and converging iteration numbers for the three experimental cases considered, i.e., Phosphatic Clay, Antwerpen Slurry, and PA-MFT. The mean, worst, and best objective function values for HABC and HPSO were nearly equal in these cases. The maximum variation was observed in the case of PSO for the Phosphatic Clay. In this case, the mean RMSE value was four times the best run value, while the worst case converged to an RMSE value 11 times the best RMSE value, clearly showing a convergence to local optima. Figures 8.5(a-c) illustrate the iterations versus RMSE values of the best runs of all the algorithms for these materials. The predicted M and P values from Table 8.3 were used to simulate the hydraulic conductivity function for the materials. These functions were compared with the corresponding experimental results from the literature, as shown in Figure 8.6(a-c) in the literature in the case of PA-MFT and Phosphatic Clay. The comparison is made with all the data points available in the literature in the case of Antwerpen Slurry. All the predicted hydraulic conductivity functions showed appreciable matching with the measured data. The settlement curves simulated using the best parameters from the algorithms were compared, as shown in Figures 8.7(a-c). It was shown that when parameters predicted by ABC were employed for the simulation, the simulated curves for PA-MFT overpredicted settlement values by a maximum of 7.8% at the time point of 25 hours. The maximum error value was 7.2 % over-prediction for the same time point for all the other algorithms.

The suggested methods worked well in both synthetic and experimental cases studied. These methods are a feasible substitute for laboratory testing for the hydraulic conductivity of slurries, as demonstrated by the effective prediction of hydraulic conductivity function parameters using settlement data. The predicted functions were compared with the reported fitted hydraulic conductivity functions.

TH-3534_186104002

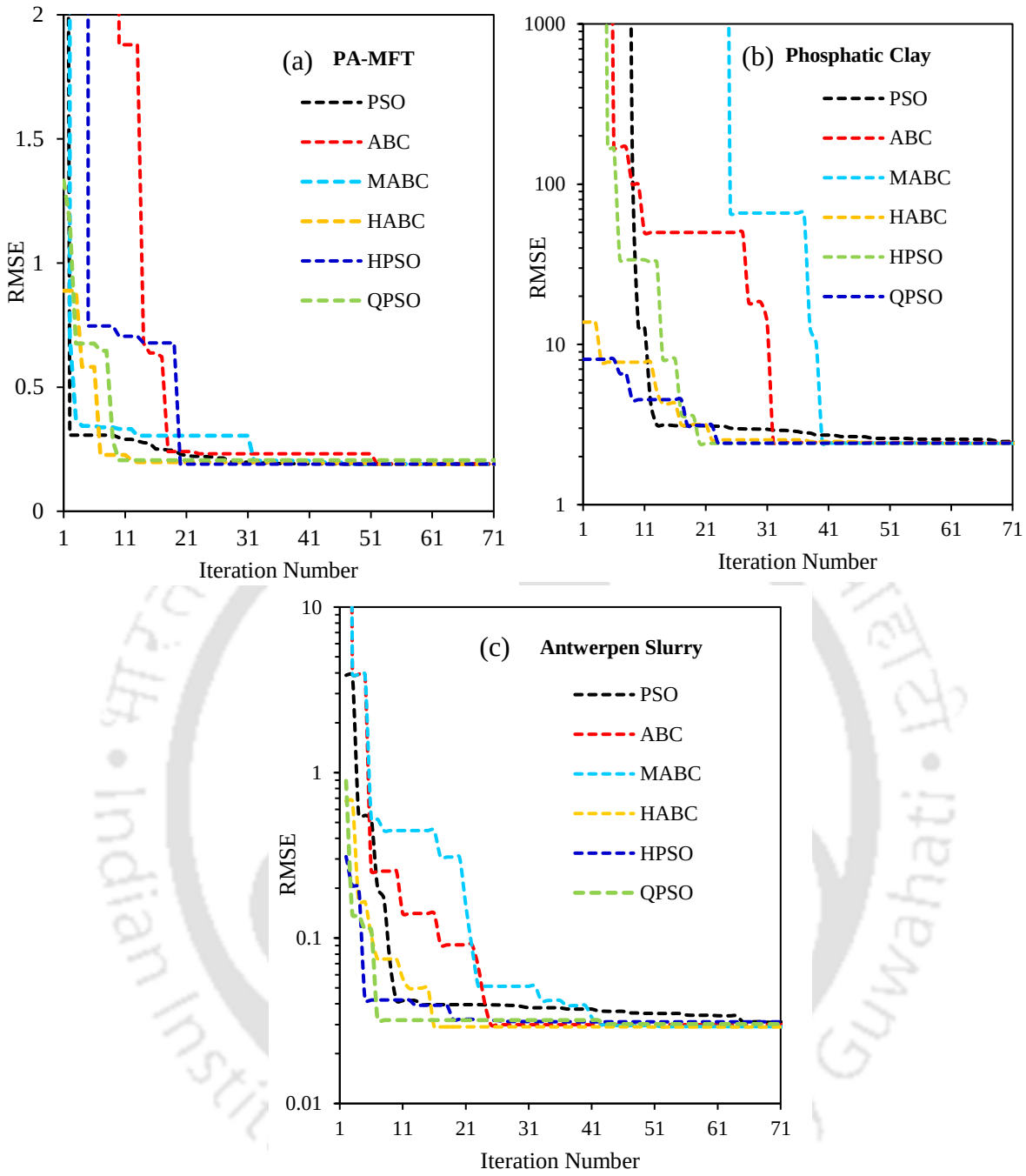


Figure 8.5 Comparison of the objective function value (RMSE) with progressing iterations of the best of three runs of the inverse analysis algorithms using experimental settlement data cases (a) PA-MFT (b) Phosphatic Clay and (c) Antwerpen Slurry

TH-3534_186104002

Table 8.3 Performance of different inverse analysis algorithms using experimental settlement data as the input for predicting the power (P) and Multiplier (M) parameters

Experimental Data	Algorithm	RMSE Values			Iteration Number	Best predicted values	
		Best	Mean	Worst		P	M (m/s)
PA-MFT	**PSO**	0.1898	0.2631	0.4097	59	8.659	3.43E-10
	HPSO	0.1898	0.1898	0.1898	20	8.66	3.43E-10
	QPSO	0.1952	0.2238	0.2688	40	8.656	3.49E-10
	ABC	0.1907	0.3298	0.4374	53	8.728	3.16E-10
	MABC	0.1898	0.1949	0.2033	49	8.566	3.85E-10
	HABC	0.1898	0.1898	0.1898	51	8.66	3.43E-10
Phosphatic Clay	**PSO**	2.4805	12.136	30.467	69	4.032	2.00E-11
	HPSO	3.4138	2.4138	2.4138	59	4.015	1.87E-11
	QPSO	2.42	2.913	3.7663	23	4.019	1.86E-11
	ABC	2.4417	7.258	11.015	32	3.992	1.86E-11
	MABC	2.4139	2.4279	2.4555	60	4.017	1.87E-11
	HABC	2.4138	2.4138	2.4138	51	4.015	1.87E-11
Antwerpen Slurry	**PSO**	0.0312	0.0373	0.0438	64	8.17	1.76E-09
	HPSO	0.0312	0.0312	0.0312	51	8.393	1.66E-09
	QPSO	0.0302	0.0325	0.0343	42	8.225	1.70E-09
	ABC	0.0299	0.0482	0.0839	38	8.382	1.55E-09
	MABC	0.0309	0.0314	0.0351	52	8.34	1.58E-09
	HABC	0.029	0.029	0.029	51	8.033	1.92E-09

TH-3534_186104002

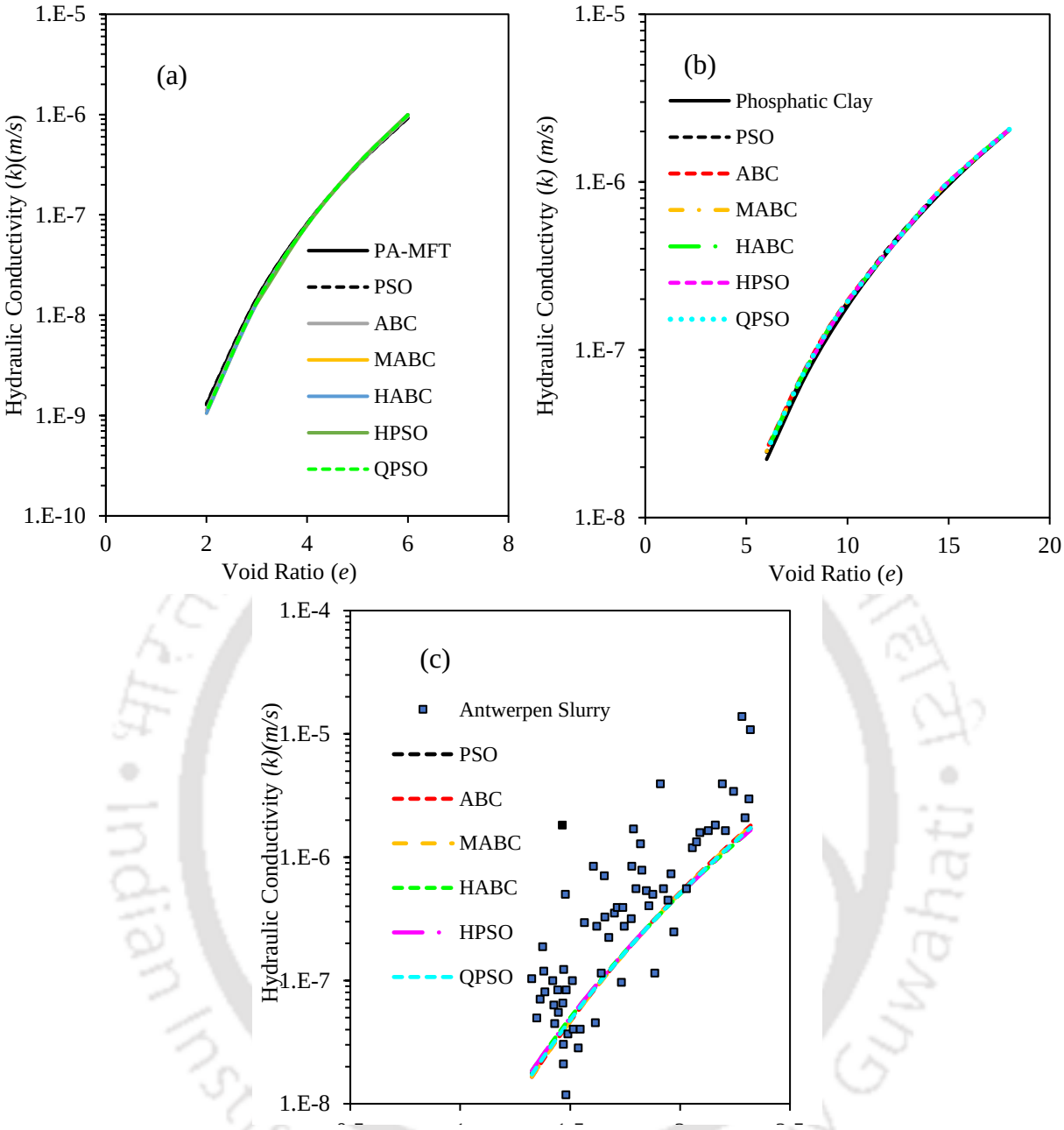


Figure 8.6. Comparison of hydraulic conductivity functions reported in the literature for the experimental data cases and the same predicted using inverse analysis from the algorithms considered for (a) PA-MFT, (b) Phosphatic Clay, (c) Antwerpen Slurry

TH-3534_186104002

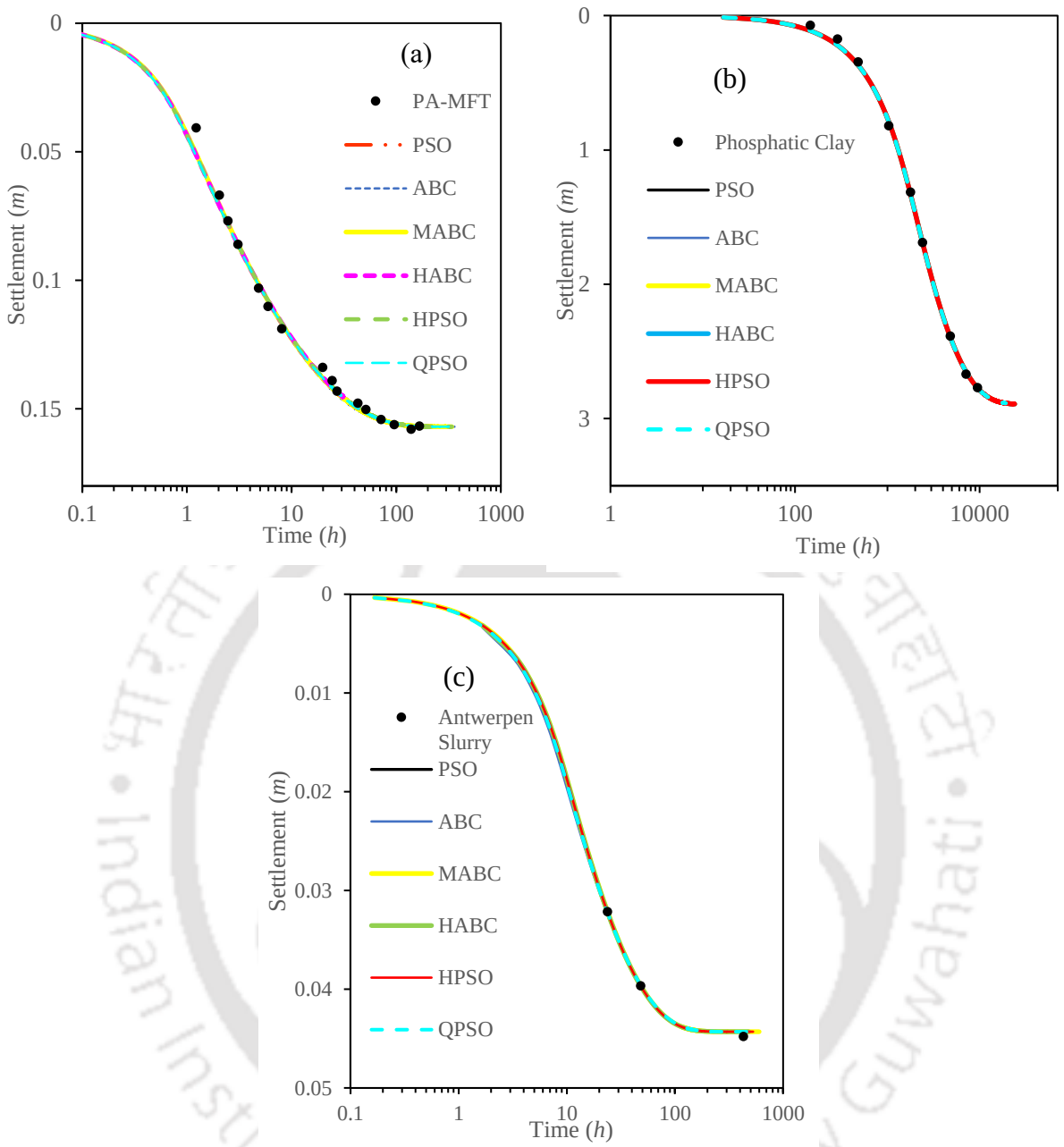


Figure 8.7. Comparison of experimental data points given as input for inverse analyses using the algorithms considered and settlement curves simulated using the hydraulic conductivity function parameters predicted by inverse analysis for (a) PA-MFT, (b) Phosphatic clay and (c) Antwerpen Slurry

8.2.5 Discussion on Significant Observations

8.2.5.1 The linear relationship between power (P) and natural logarithm of multiplier (ln M)

The hydraulic conductivity function parameters get optimised after several forward analysis steps at each iteration. The iteration history of *M* and *P* values obtained from the stochastic

TH-3534_186104002

algorithms, when plotted, aligned to form a straight line in the *ln M* versus *P* space. This peculiar behaviour was observed by Qi and Simms (2020) when the optimization was carried out using the Nelder Mead Simplex algorithm, using settlement data as input. Therefore, regardless of the type of optimization algorithm adopted, it can be concluded that the optimal pair of (*M, P*) is situated on a straight line created by the *M* and *P* values of subsequent iterations in the *P* - *lnM* plane. The demonstration of these observations for the Phosphatic Clay is shown in Figure 8.8(a). Each algorithm begins at different sets of random initial populations of *M* and *P* values within the search area and eventually travels along the same straight line in the *ln M* versus *P* space, leading to the perfect pair of *M* and *P*. The settlement data were used to generate three-dimensional error surfaces for the inverse analysis problems (Figure 8.8(b)), which demonstrated a valley formation with different pairs of *M* and *P* in the iteration history forming straight lines in the *ln M -P* space.

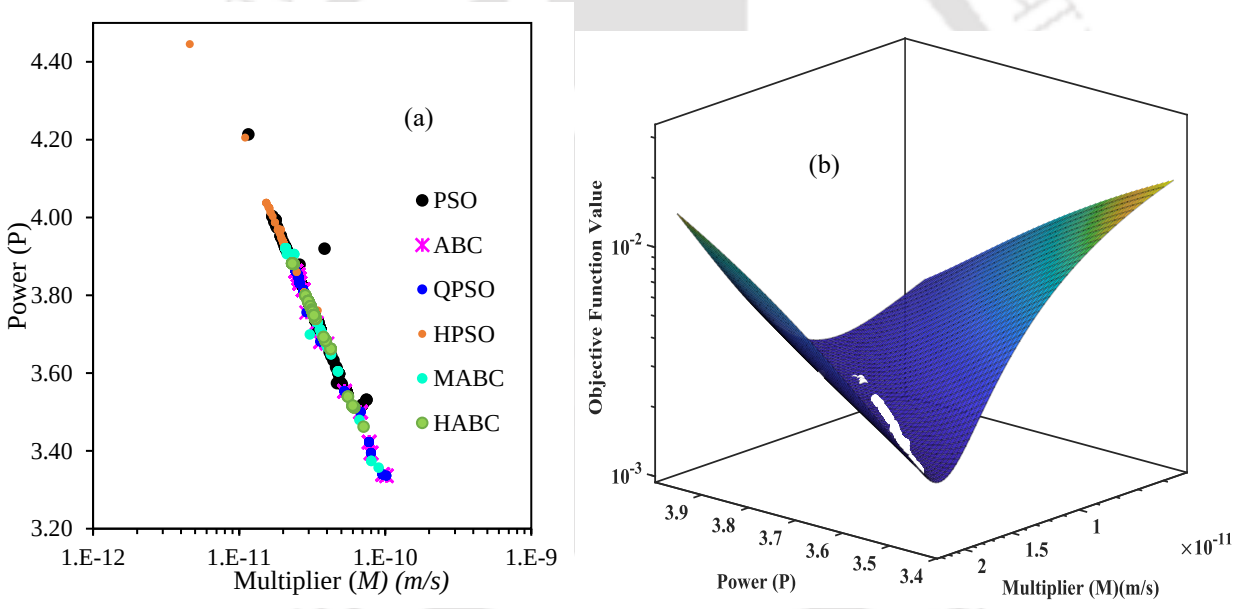


Figure 8.8. (a) M and P values from successive iterations converging to a straight line leading to the optimal pair of values when settlement data for Phosphatic clay was used for inverse analysis (b) Three-dimensional error surface for the optimisation problem derived for the Phosphatic Clay sample

8.2.5.2. Consequences of inaccurate estimation of optimal parameters.

The optimal parameters obtained using probabilistic algorithms are heavily influenced by the inherent randomness involved in the swarm or population of particles generated in the search space. The efficiency of the algorithms is determined not only by the capability to converge to

TH-3534_186104002

the optimal solution within the least number of iterations but also by the ability to converge to near-optimal solutions in all the runs. An over-sensitivity to initial populations or conditions can result in inconsistent values of predicted optimal parameters, rendering the algorithm less reliable. The observations discussed in Table 8.2 and Table 8.3 show the comparison of consistency of the parameters predicted using the algorithms through the best, worst, and mean objective function values. PSO and QPSO were observed to show less reliability in terms of repeatability of results. The observations from the case of inverse analysis using settlement data of Phosphatic Clay employing PSO were considered to illustrate this. Figure 8.9(a-b) shows the three runs of PSO for this case and the variation of the worst-case predicted parameters from the best and actual parameters. The second (best run) and third runs converged to nearly the same objective function values, 3.221 and 3.226, respectively. However, the first run converged to an objective function value of 30.467 after the limit of iterations considered.

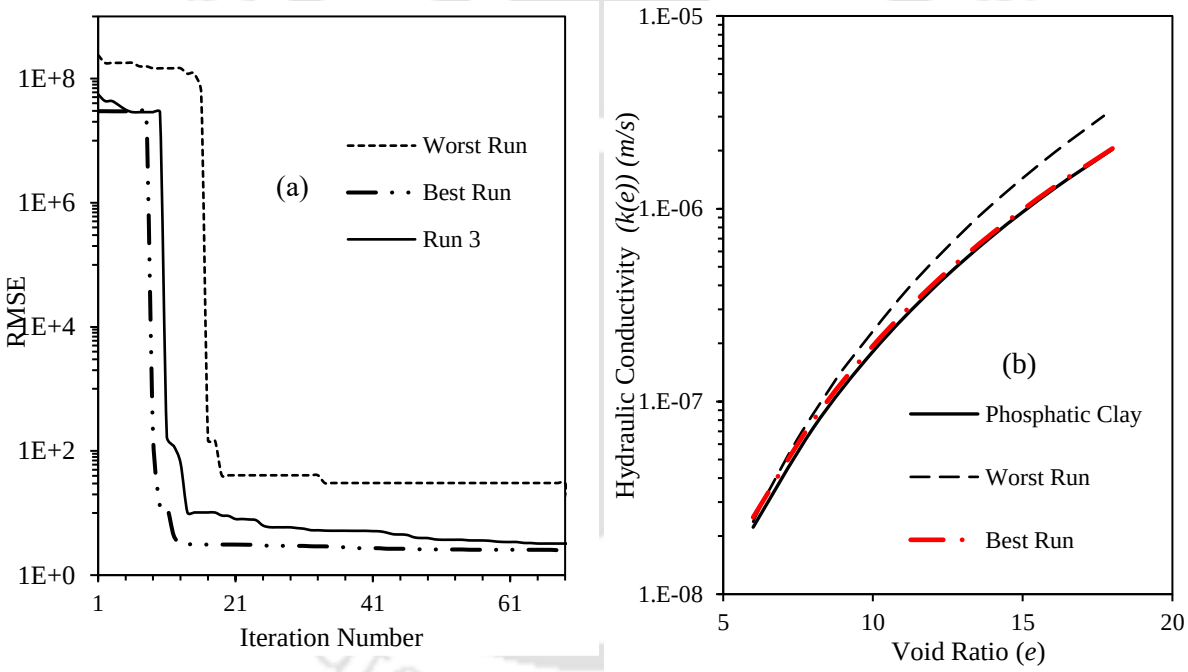


Figure 8.9. (a) Iteration versus RMSE plotted for three runs of PSO for Phosphatic Clay to show the variation in convergence (b) Comparison of hydraulic conductivity function using the parameters obtained from best and worst runs of PSO with the same from literature for Phosphatic Clay

The corresponding *M* and *P* values are 7.76 x 10^{-12} m/s and 4.48, respectively (Case 1), which does not agree with the actual constitutive function parameters. The choice of the maximum number of iterations is also crucial in ensuring that the predicted parameters are the actual converged results. For example, in the case of Phosphatic Clay discussed above, if the stopping

TH-3534_186104002

criteria were 30 iterations, the corresponding objective function value is 40.6 for the worst run. The corresponding optimised parameter values are M=1.183 x 10^{-12} m/s and P=4.782 (Case 2). The iteration history of M and P values for the best and worst runs are shown in Figures 8.10(a) and (b).

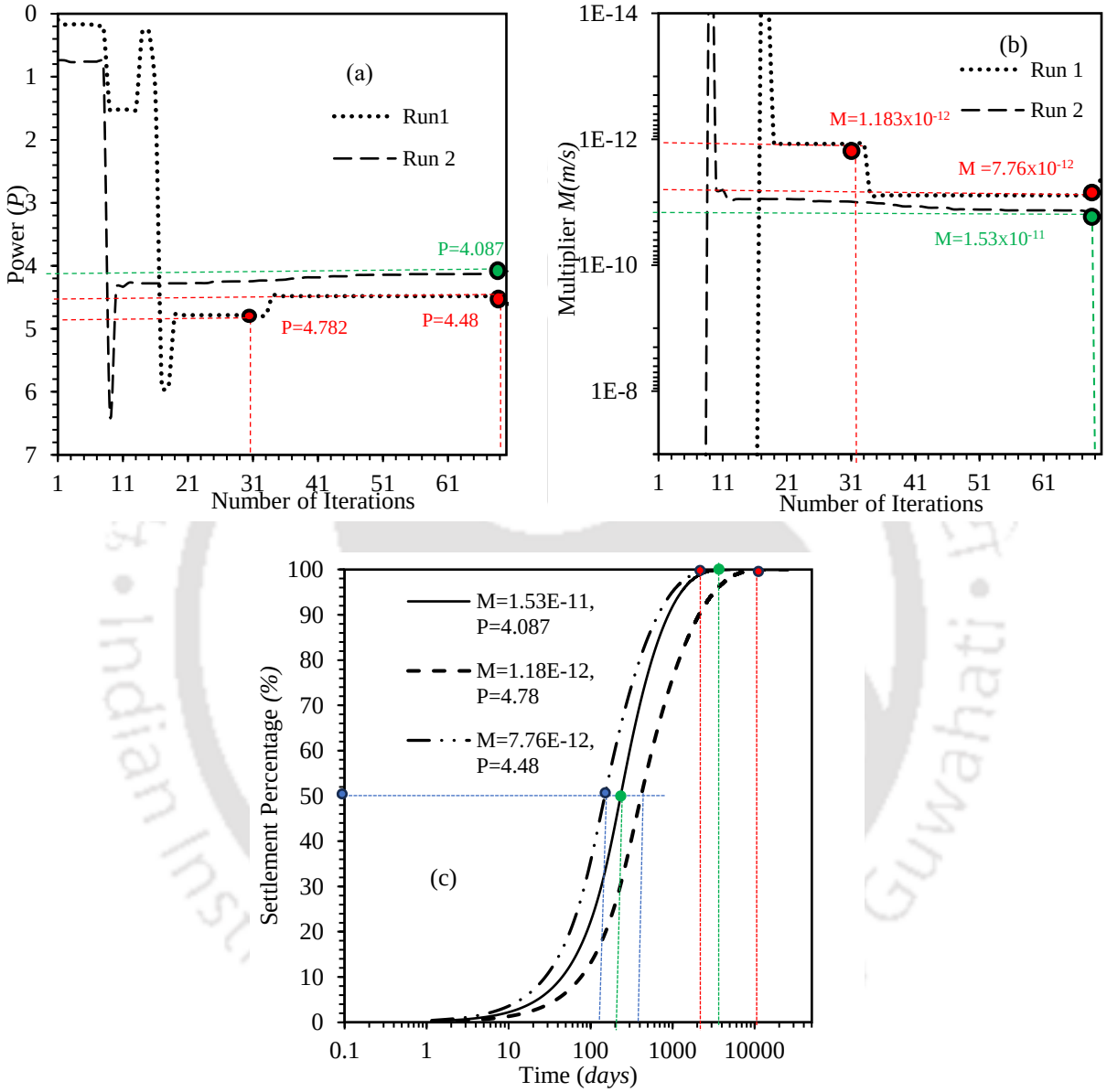


Figure 8.10. For the case of inverse analysis of Phosphatic Clay from settlement data, (a) Iteration history of Power (P) in run 1 (Worst run) and run 2 (Best run) of PSO (b) Iteration history of Multiplier (M) in run 1 (Worst run) and run 2 (Best run) of PSO (c) Influence of erroneous prediction of hydraulic conductivity function parameters on simulated hypothetical field observation of percentage settlement

TH-3534_186104002

A hypothetical case where a Phosphatic Clay layer of 15 m depth was present in a storage facility was considered to illustrate the implications of inaccurate estimation of the hydraulic conductivity function parameters. Other relevant properties were assumed to be the same as those in Table 4.2. The percentage settlement curves simulated using the hydraulic conductivity parameters from Case 1 and Case 2 and the converged values of the best run (Figures 8.10 (c)) were compared. It was observed that the slurry layer was predicted to attain 50% settlement at around 230 days when the optimal parameters from the best run were used for the simulation. Maximum settlement for these parameters were at 2200 days. The slurry layer was predicted to attain 50% settlement at around 150 days, based on the parameters from Case 1. Completing consolidation based on settlement for this case was predicted to take 1600 days. The same simulations done using the hydraulic conductivity function parameters from Case 2 showed that the slurry layer consolidated at a much slower rate than in the actual case. The 50% consolidation based on settlement was predicted to be achieved in 400 days, while completion of the process based on maximum settlement was predicted to take 5200 days. The differences in the time spans predicted using the erroneous parameters and the best pair of parameters cannot be overlooked.

In the field, new layers of slurry material are dumped over the existing layers based on the total compression and pore pressure conditions of the existing layer. The volume of incoming waste material depends on the available clear head above the current layer, which depends on the settlement achieved by the pre-existing layers. The field decisions made based on wrongly estimated hydraulic conductivity parameters can significantly slow down the deposition process of subsequent layers and eventual reclamation of the land (Case 2). In cases where the predicted consolidation rate is higher than the actual rate at the field (Case 1), this can cause premature deposition of successive layers, which can incite instability in the storage facility, increasing the chances of failure.

8.2.5.3 Influence of iteration ratio on the optimal parameters from hybrid algorithms

The hybrid algorithms were developed to ensure consistency in convergence to the global minima across multiple runs by combining the exploration capabilities of probabilistic algorithms PSO and ABC and the exploitation capability of deterministic algorithms *fmincon* and *fminsearch*. Two factors impact the efficiency of these algorithms: (i) the ratio of the number of iterations allotted for each type of algorithm in every run of the hybrid algorithms and (ii) the number of cycles of each of the algorithms allowed within the total maximum

TH-3534_186104002

number of iterations. In Figure 8.11(a), the iteration history of the runs of the HPSO algorithm, repeated with three ratio combinations, is shown.

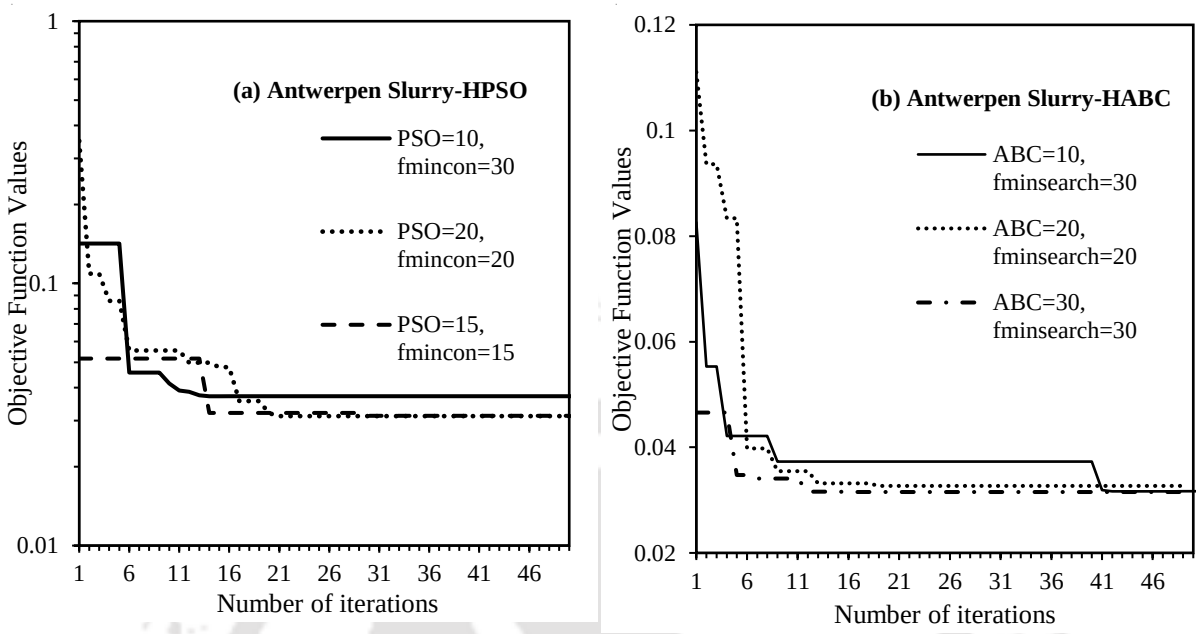


Figure 8.11. Illustration of the effect of choice of the number of iterations on the convergence for Antwerpen Slurry using (a) HPSO (b) HABC

It can be seen that the case with only ten iterations allotted for PSO converged prematurely to a local optimal value. The initial guess values for the optimised parameters provided by PSO after ten iterations were not good enough for *fmincon* to trace the next best value at the end of the first cycle (i.e., at 20 iterations) or at the end of the second cycle (i.e., at 40 iterations), for a total of 50 iterations. In Figure 8.11(b), the combinations used for HABC are 10:10, 20:20, and 30:30. It was observed that for the case of ABC=10 iterations, *fminsearch* successfully guides the solution out of premature convergence in the second cycle. Faster convergence was observed with the other two combinations.

8.2.6 Summary

The section explored six metaheuristic optimization algorithms for the back-estimation of the hydraulic conductivity function coefficients, using FSC settlement data and basic material characteristics as input. Three novel algorithms, HPSO, MABC and HABC, derived from the conventional ABC and PSO algorithms, were introduced. QPSO, an advanced version of PSO, was also applied to the optimization problem. The efficiency of each of these algorithms was compared based on their speed of convergence and the quality of the optimal solutions

TH-3534_186104002

produced. Iteration histories from all the algorithms showed that values of parameters being optimised formed a linear relationship in power versus the natural log of multiplier space, leading to the optimal solution. In several cases, the QPSO successfully converged to the near-optimal solution faster than the PSO. When executed multiple times, the algorithm failed to converge consistently to the same optimal solution in a few of the cases. The proposed MABC was observed to have effectively mitigated the variability in the optimal solutions obtained from consecutive runs compared to the standard (ABC) algorithm. The hybrid algorithms, HABC and HPSO, relied on the assigned number of iterations for their component algorithms. Nevertheless, after selecting the optimal number of iterations, it was noted that these algorithms effectively mitigated the issue of being trapped in local optima, a common challenge encountered by the traditional PSO and ABC algorithms. The hydraulic conductivity function parameters were accurately back-predicted from the synthetic and experimental settlement versus time data obtained from the finite strain consolidation of considered slurries. The settlement versus time curves simulated using the predicted optimal parameter values matched well with the corresponding experimental observations. The proposed approach would be a useful technique for assessing the long-term stability of the mine waste ponds.

8.3 Simultaneous estimation of compressibility and hydraulic characteristics

8.3.1 General

The compressibility function determines the ultimate strain in the slurry during the process of FSC. In this section, a new approach for the indirect estimation of the compressibility function, simultaneously with the hydraulic conductivity function, is presented. The power form of the compressibility function is adopted for the inverse analysis to reduce the complexity of the optimisation landscape. The parameters *M, P, A and B* are being optimised simultaneously and the performance of the algorithms PSO, ABC, QPSO, MABC, HABC and HPSO are compared.

The personal and social learning coefficients for PSO-based algorithms were maintained at constant values of 1.5 and 2, respectively. The initial inertia weight was set at 0.9 and decreased by 1% at the conclusion of each iteration. The population size of 40 was maintained for PSO, QPSO, and HPSO. The shrinkage factor for QPSO is calculated using the values c_1=0.01 and c_2 =0.1. The HPSO employed the same learning coefficients and inertia weight settings as the PSO. The algorithm was set for 50 PSO iterations followed by 50 *fmincon*

TH-3534_186104002

iterations. These parameters were tuned by trial. The number of employed bees, as well as the onlooker bees, were maintained at 50, and the trial limit for improving any source of food was set at 50 for ABC, MABC and HABC. Based on multiple trials, the common ratio of 50-50 *fminsearch* to ABC showed good performance for all the material cases

8.3.2 Back-Estimation Using Synthetic Settlement Data

All algorithms were run three times on these test data sets. The performances of these algorithms were compared based on the "best run" out of the three runs. The performances of algorithms are compared in Table 8.4. The conventional PSO algorithm and HPSO were more dependable than QPSO for the inverse analysis problem considered in this study. The comparison of best runs showed similar performance efficiency for PSO and HPSO. The ABC and its variants showed comparable performance. In a number of cases, repeated runs of PSO, QPSO, ABC and MABC converged to different optimal values prematurely in some cases, as reflected by the worst objective function value and mean of converged values of all three runs. This shows the lack of robustness and emphasises a need to conduct multiple runs of the algorithm to conclude that the converged RMSE is the true minimum. HPSO showed robust convergence to the least RMSE values for the cases of Rutgers and MFT 5, while a slight difference in the mean, worst, and best RMSE was observed in the case of MFT 6.

Responses showed that, for MFT5 and MFT6, PSO converged to local minima when run multiple times, as seen by the variation in the mean, worst, and best objective function values. QPSO suffered from premature convergence in these cases and showed satisfactory responses only in the case of Rutgers. In terms of speed of convergence to reliable values, HPSO and PSO showed comparable performance based on the converged iteration number for the best run. ABC and HABC converged to the same RMSE values, while the converged RMSE value for MABC was 8% higher. In the case of MFT5, MABC improved the converged RMSE value of ABC by 58%. HABC showed the best performance among the ABC-based algorithms. However, the PSO and HPSO had the lowest RMSE. The hybrid algorithms were robust and showed good repeatability. In the case of MFT6, ABC showed improved performance compared to PSO. MFT6 converged to the lowest RMSE when MABC was used for inverse analysis, reducing the value by 20% in comparison with ABC.

HABC was observed to have reduced robustness in this case. These details were observed in Figures 8.12(a-c), which shows the best run-iteration number versus RMSE plots for the synthetic settlement data cases considered. The predicted hydraulic conductivity functions

TH-3534_186104002

from Table 8.4, compared to actual functions as shown in Figures 8.13(a-c), depicted that all the algorithms had achieved good accuracy. The predicted compressibility functions showed slight variations from the actual functions as per Figures 8.14(a-c). Apart from convergence to local, another reason for the observed discrepancy could be the added white noise in the input settlement data used for the inverse analysis. In order to test the accuracy of the optimal values of the parameters further, these were used to simulate the settlement versus time curve by using the MATLAB code for the forward analysis. These simulated curves were then compared with the input settlement data, as shown in Figure 8.15(a-c). The added white noise resulted in input data points that were mildly scattered during the ultimate settlement phase of consolidation.

TH-3534_186104002

Table 8.4. Inverse analysis performance of various algorithms in predicting compressibility and hydraulic conductivity function parameters using synthetic settlement data as the input

Material	Algorithm	RMSE Values			Best Run Iteration Number	Best Run-Predicted Values			
		Best	Worst	Mean		M(m/s)	P	A(1/kPa)	B
Rutgers	**PSO**	0.211	0.282	0.238	135	1.70E-11	6.107	2.825	0.218
	HPSO	0.200	0.200	0.200	149	3.77E-11	5.651	2.799	0.296
	QPSO	0.313	0.596	0.444	7	2.39E-11	5.901	2.752	0.212
	ABC	0.256	0.257	0.257	55	8.66E-12	6.532	2.855	0.188
	MABC	0.277	0.280	0.278	84	1.20E-11	6.336	2.844	0.213
	HABC	0.256	0.257	0.257	150	1.25E-11	6.311	2.843	0.216
MFT5	**PSO**	0.003	0.024	0.010	197	2.53E-11	3.401	3.127	0.250
	HPSO	0.003	0.003	0.003	150	1.52E-11	3.668	3.317	0.180
	QPSO	0.072	0.098	0.081	189	1.69E-11	3.596	3.206	0.223
	ABC	0.012	0.031	0.020	76	1.66E-11	3.630	3.266	0.197
	MABC	0.005	0.038	0.016	135	2.72E-11	3.345	3.253	0.201
	HABC	0.004	0.005	0.004	157	2.43E-11	3.409	3.266	0.197
MFT6	**PSO**	5.05E-04	1.63E-02	1.08E-02	173	1.65E-11	3.689	3.197	0.163
	HPSO	2.74E-04	4.64E-04	3.46E-04	147	1.49E-11	3.764	3.196	0.161
	QPSO	3.08E-02	3.20E-02	3.16E-02	44	2.00E-11	3.622	4.144	0.500
	ABC	4.94E-04	2.01E-03	1.15E-03	159	1.17E-11	3.938	3.194	0.155
	MABC	3.88E-04	1.08E-02	7.23E-03	128	1.22E-11	3.910	3.195	0.157
	HABC	4.47E-04	3.02E-03	1.32E-03	152	1.41E-11	3.804	3.201	0.171

TH-3534_186104002

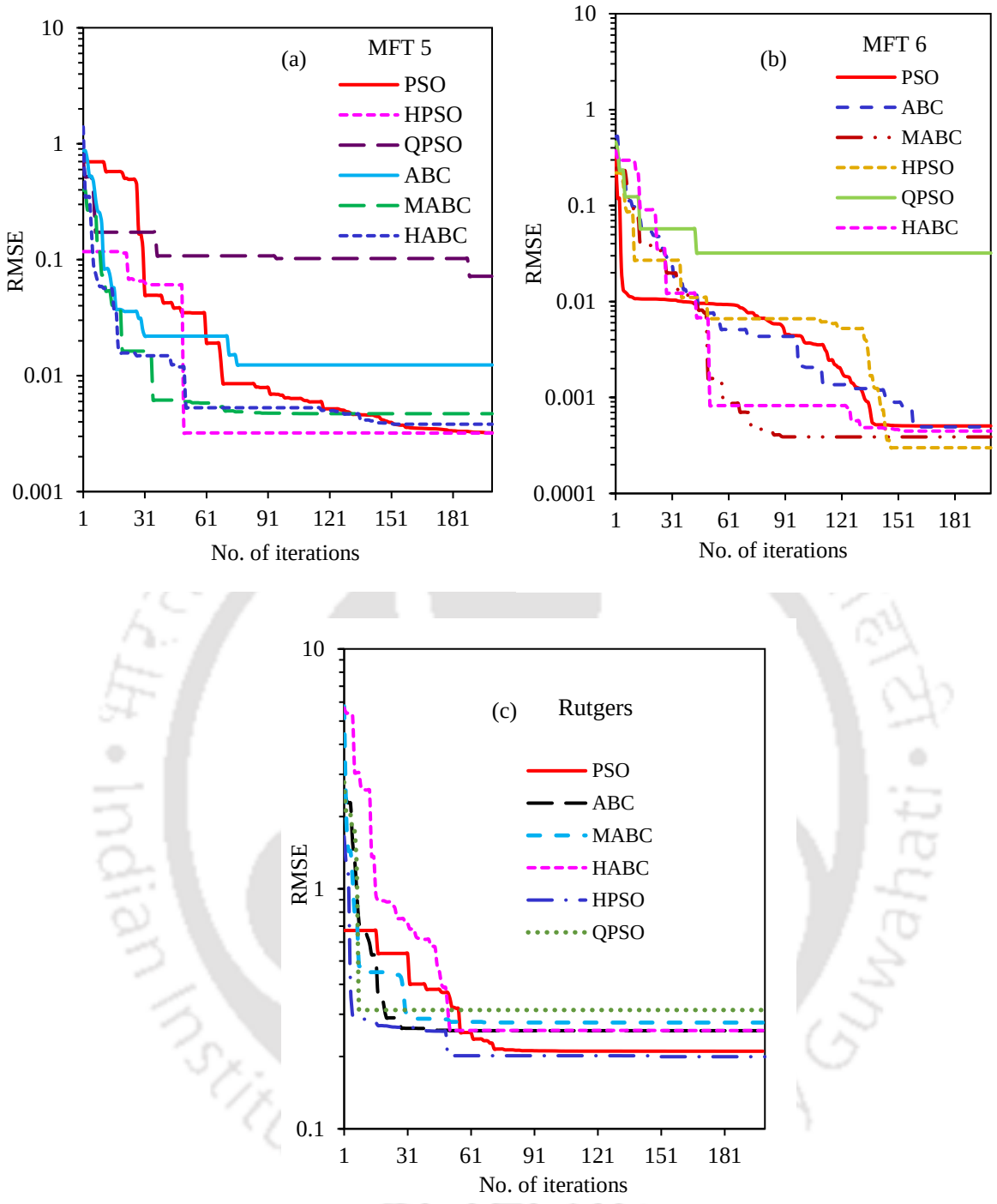


Figure 8.12. Comparison of the objective function value (RMSE) with progressing iterations of the best of three runs of the inverse analysis algorithms using synthetic settlement data cases (a) MFT5, (b) MFT6 and (c) Rutgers

The variation in the compressibility functions tends to influence the overall strain value or the ultimate settlement value of the curves, while the hydraulic conductivity governs the rate of settlement. The overestimation of settlement values indicates that the predicted optimal parameters simulate a settlement value that is higher than the observed/ input settlement value

TH-3534_186104002

at that specific time point. This scenario occurs when the predicted hydraulic conductivity exceeds the actual value, resulting in higher simulated settlement rates than the actual rate. It can also occur when the material is predicted to be more compressible than its original behaviour.

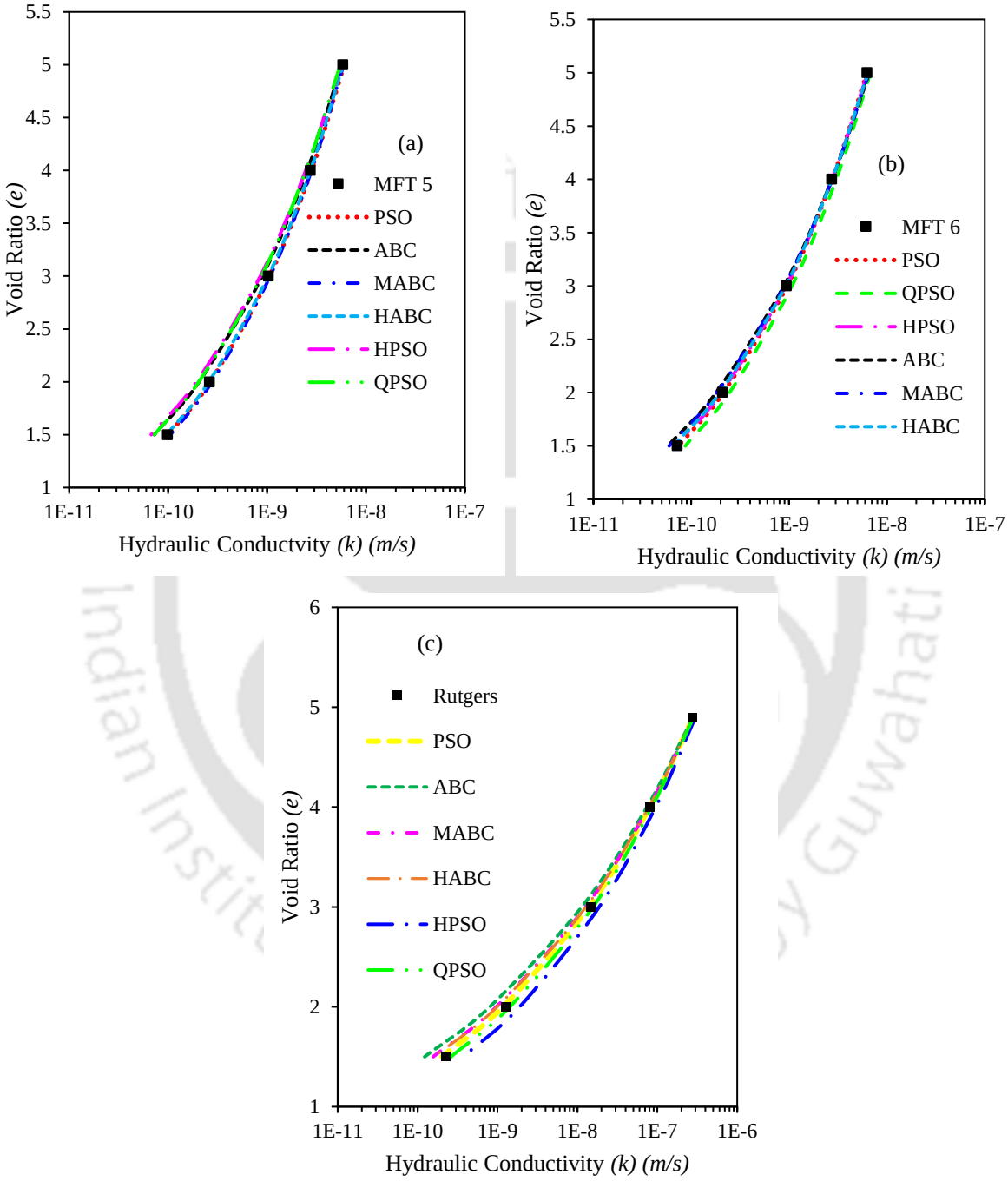


Figure 8.13. Comparison of hydraulic conductivity functions of the synthetic data cases and the same predicted using inverse analysis from the algorithms considered for (a) MFT5, (b) MFT6, and (c) Rutgers

TH-3534_186104002

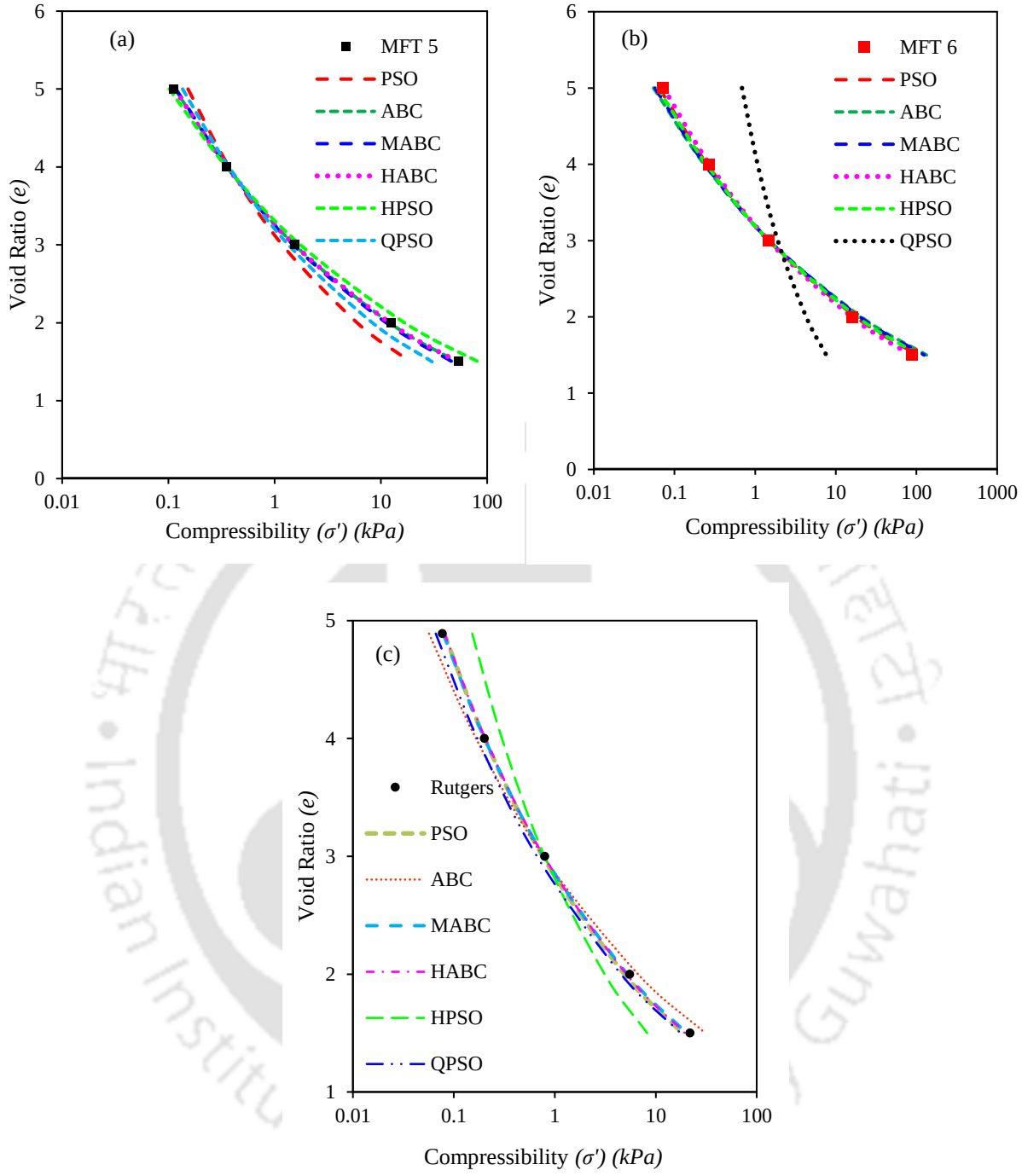


Figure 8.14. Comparison of compressibility functions of the synthetic data cases and the same predicted using inverse analysis from the algorithms considered for (a) MFT5, (b) MFT6 and (c) Rutgers

On the other hand, the scenario where the predicted hydraulic conductivity function simulates a lower rate of settlement or the optimal compressibility parameters simulate lower compressibility values results in the under-prediction of the settlement values at any given point.

TH-3534_186104002

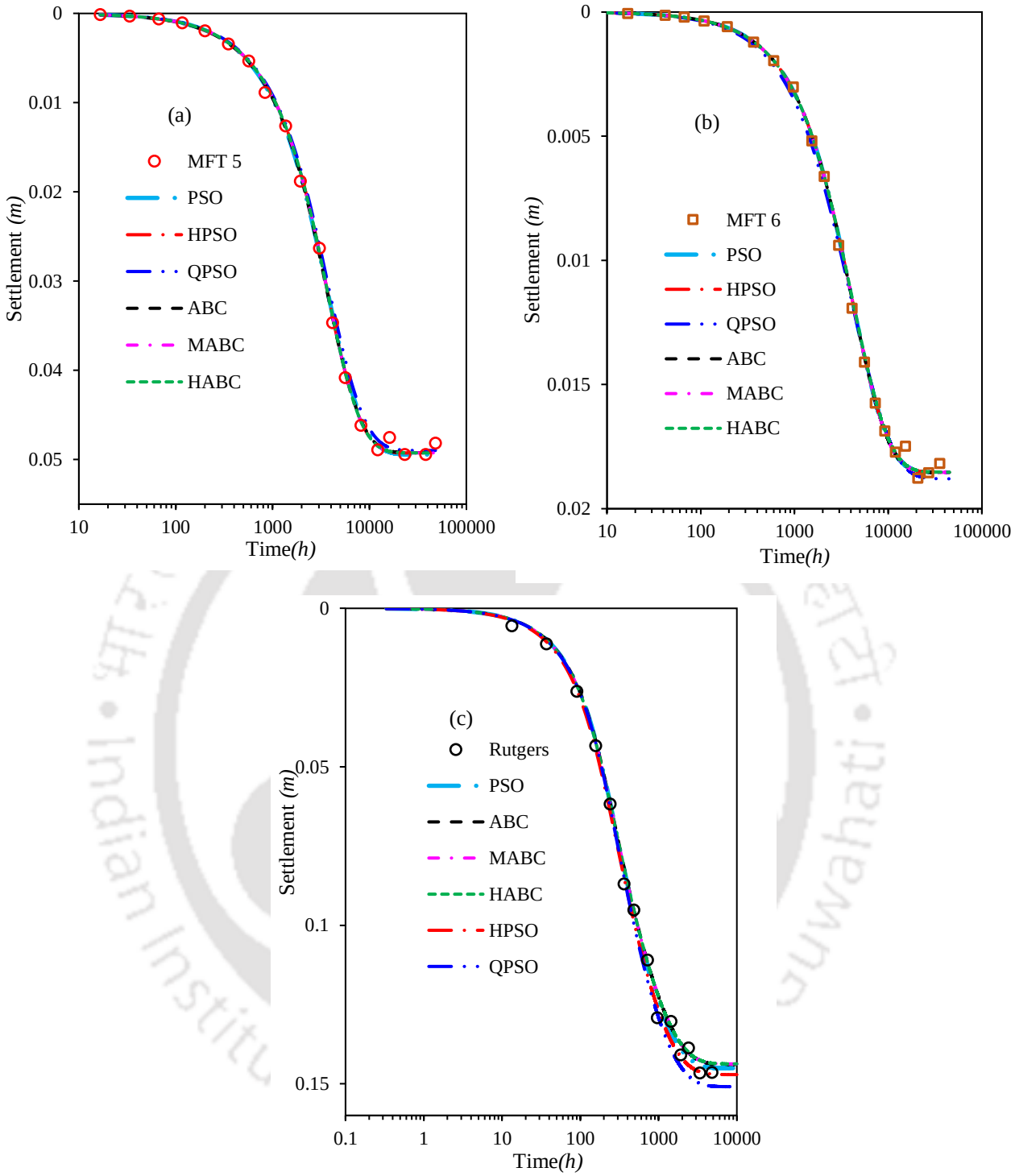


Figure 8.15. Comparison of synthetically generated settlement data points given as input for inverse analysis using the algorithms considered and settlement curves simulated using the constitutive function parameters predicted by inverse analysis for (a)MFT 5, (b) MFT 6, and (c) Rutgers

It was observed that the maximum error, expressed as a percentage, based on the comparison shown in Figures 8.15(a-c), was less than 5% for all the cases. In the case of Rutgers, the over-

TH-3534_186104002

prediction error was observed to be 0.99% and 2.98% at 4800 hours for PSO and QPSO. Meanwhile, HPSO was observed to show a 1.55% error at 90 hours. The ultimate settlement values of MFT 5 matched well with the simulated curves of HPSO and PSO with overestimation errors as low as 3.22 % and 3.4 %, respectively, at 16110 hours.QPSO was observed to underestimate the ultimate settlement value, resulting in an average variation of 2% in the ultimate settlement phase. The simulated settlement curves showed over-estimation errors of 2% for both PSO and HPSO, while the same was 3.3% for QPSO at 35500 hours. In the case of Rutgers ABC, MABC and HABC, variations were observed as overprediction of settlement by 6.32% at 360 hours, 6.04% at 960 hours and 6.14% at 360 hours respectively. In the case of MFT6, the ABC-based algorithms showed settlement underprediction. The settlement curve simulated using the parameters predicted using ABC resulted in a 4% variation at 2960 hours from the corresponding data point in the synthetic data. MABC and HABC simulations showed 3.08% over-prediction at 4116 hours and 4.32% over-prediction at 2960 hours, respectively. Inverse analysis of parameters in the case of MFT5 showed maximum variation as overprediction of settlement at 16100 hours for ABC, MABC and HABC, amounting to 3.13%, 3.23% and 3.22% variation, respectively.

8.3.3 Back-Estimation Using Experimental Settlement Data

The performances of the algorithms were validated using three FSC settlement data sets from published literature, which included two mine tailings (Phosphatic Clay, PA-MFT) and a clay sediment (Antwerpen Slurry). Figures 8.16(a-c) show the number of iterations versus RMSE plots for these materials. The comparison of the converged values of the parameters and the objective function values is given in Table 8.5. It was observed that HPSO performed better than PSO and QPSO for Antwerpen Slurry. QPSO outperformed the other algorithms in the case of PA-MFT, converging relatively faster to robust outcomes for the repeated runs. HPSO showed intermediate performance while PSO converged to a relatively higher RMSE value. HABC outperformed PSO-based algorithms in the case of Antwerpen Slurry, as shown in Table 8.5. However, HABC had issues with robustness, such as HPSO and other algorithms. The mismatch between the worst and mean values of the RMSE can be attributed to the fact that only three data points are present. These points were insufficient to provide adequate information about the initial and final phases of the consolidation for Antwerpen Slurry. In the case of Phosphatic Clay, all the algorithms converged to RMSE values in the same range, except QPSO. ABC-based algorithms performed better than PSO-based algorithms in the case of PA-MFT and showed faster convergence in comparison. Though HABC showed robustness,

TH-3534_186104002

the converged value of RMSE for best run was larger than all other algorithms. The predicted hydraulic conductivity and compressibility functions are being compared with the corresponding literature data in Figures 8.17(a-c) and 18.18(a-c), respectively.

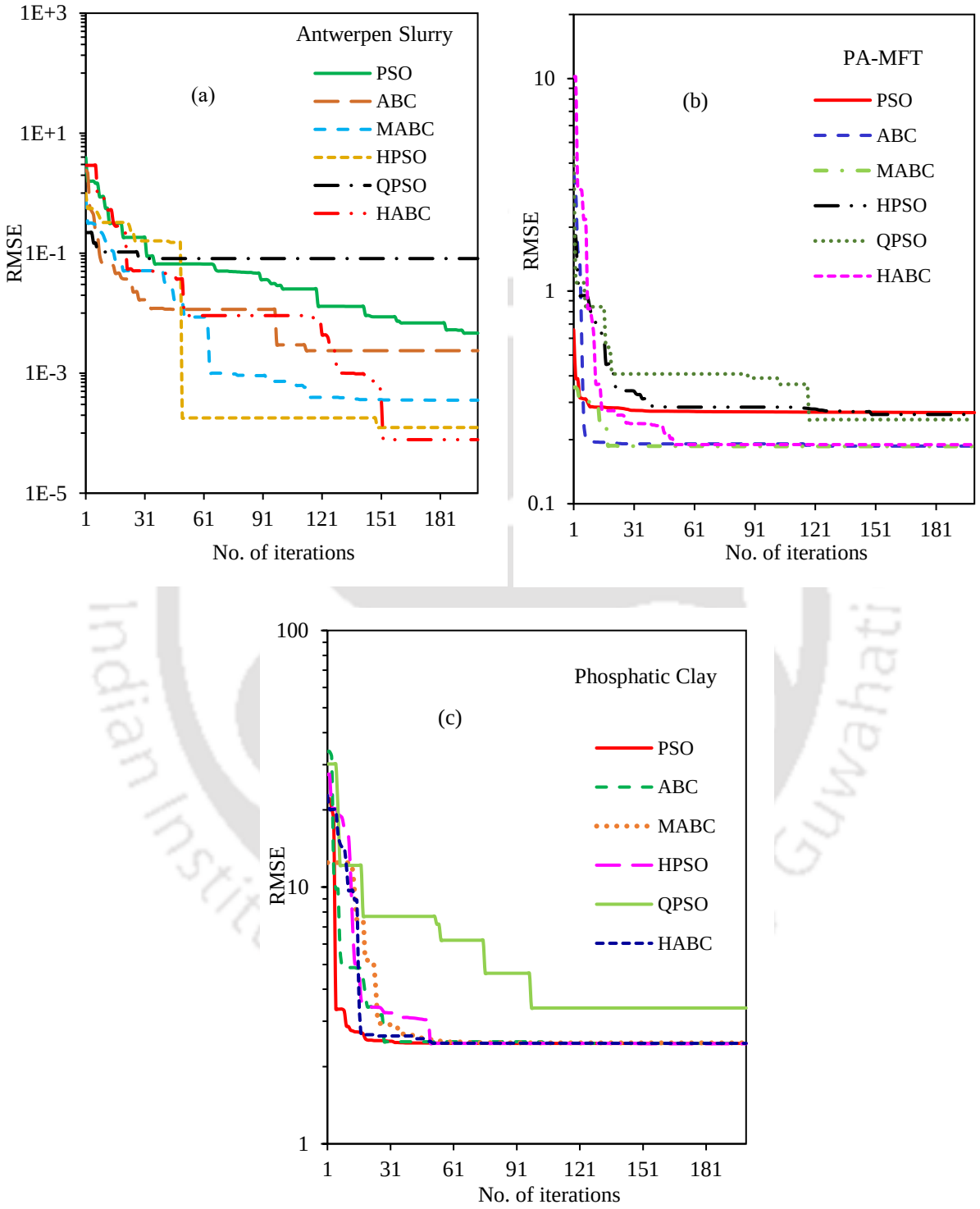


Figure 8.16. Comparison of the objective function value (RMSE) with progressing iterations of the best of three runs of the inverse analysis algorithms using experimental settlement data cases (a) Antwerpen Slurry (b) PA-MFT, and (c) Phosphatic Clay

TH-3534_186104002

Table 8.5 Inverse analysis performance of various algorithms in predicting compressibility and hydraulic conductivity function parameters using experimental settlement data as the input

Material	Algorithm	RMSE Values			Best Run iteration Number*	Best Run-Predicted Values			
		Best	Worst	Mean		M (m/s)	P	A (1/kPa)	B
Antwerpen Slurry	**PSO**	4.65E-03	0.035	0.019	193	5.04E-09	6.927	1.331	0.200
	HPSO	4.66E-05	0.002	0.001	149	2.02E-09	8.004	1.389	0.099
	QPSO	8.14E-02	0.208	0.145	28	6.71E-09	6.949	2.000	0.805
	ABC	2.37E-03	0.006	0.00473	113	1.33E-08	5.783	1.500	0.528
	MABC	3.55E-04	0.010	0.00448	176	4.03E-09	7.174	1.345	0.160
	HABC	2.79E-05	0.0243	0.00811	152	3.70E-09	7.274	1.350	0.151
Phosphatic Clay	**PSO**	2.462	2.504	2.492	96	1.06E-11	4.203	11.661	0.255
	HPSO	2.456	2.457	2.456	62	4.24E-11	3.735	11.158	0.243
	QPSO	3.382	4.212	3.889	98	4.09E-11	3.739	12.503	0.284
	ABC	2.465	2.505	2.478	105	4.14E-11	3.742	12.961	0.339
	MABC	2.474	2.520	2.492	100	1.60E-11	4.065	11.996	0.278
	HABC	2.463	2.478	2.471	152	1.77E-11	4.031	12.110	0.287
PA-MFT	**PSO**	0.268	0.271	0.270	192	9.80E-10	7.809	1.971	0.423
	HPSO	0.263	0.283	0.276	149	6.58E-10	8.286	2.041	0.500
	QPSO	0.249	0.308	0.287	118	2.69E-10	8.881	1.974	0.475
	ABC	0.187	0.199	0.192	128	6.32E-10	8.206	1.966	0.468
	MABC	0.186	0.211	0.195	91	5.56E-10	8.294	1.950	0.419
	HABC	0.190	0.191	0.190	151	6.21E-10	8.242	2.013	0.460

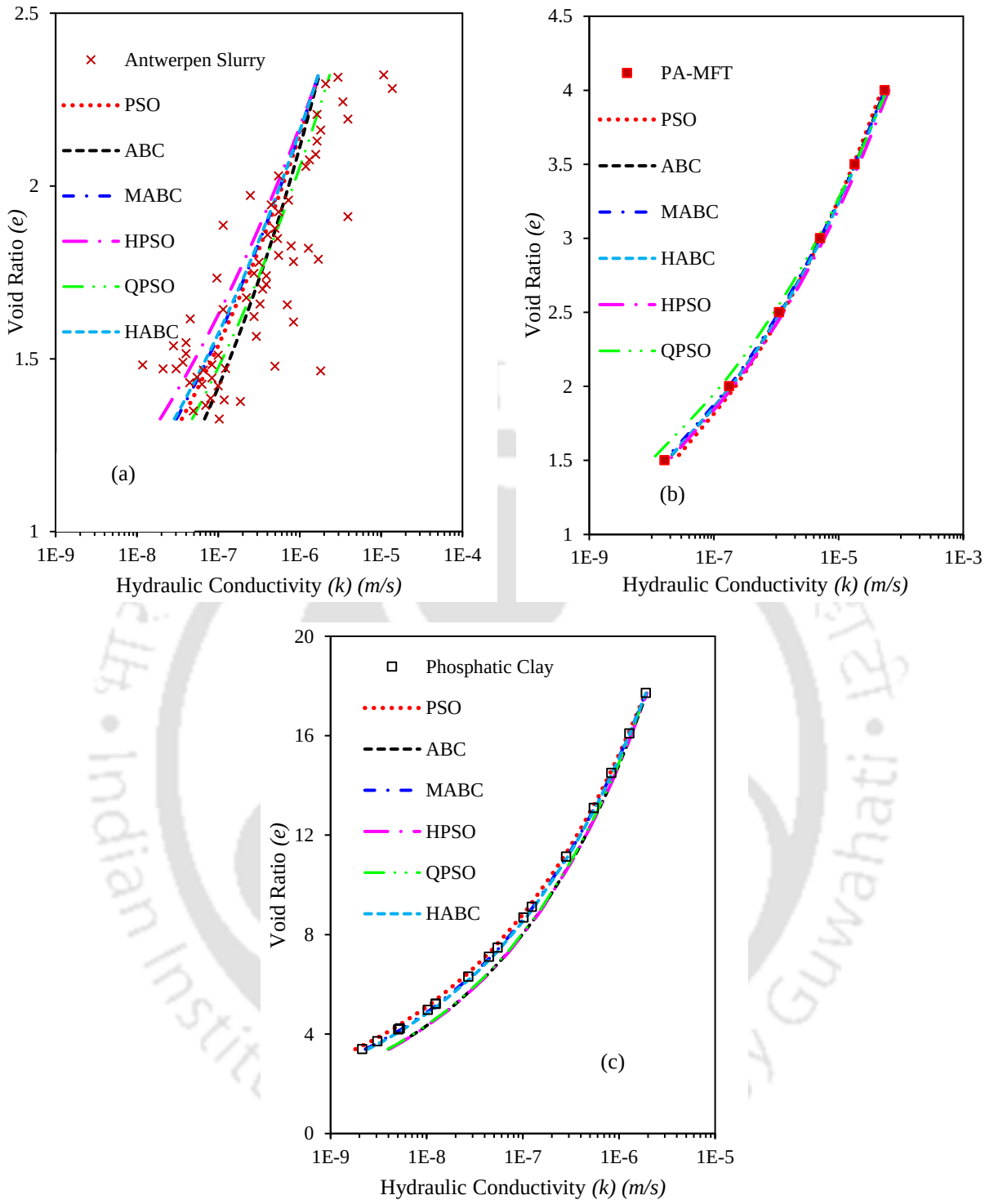


Figure 8.17. Comparison of hydraulic conductivity functions reported in the literature for the experimental data cases and the same predicted using inverse analysis from the algorithms considered for (a) Antwerpen Slurry (b) PA-MFT (c) Phosphatic Clay

The FSC governing differential equation does not include the sedimentation process when the effective stress values are low. Practically, it is not easy to measure these values with reasonable

TH-3534_186104002

accuracy. The effective stress versus void ratio relationship is more reliable at larger effective stress values. Figures 8.19(a-c) show the comparison of the settlement behaviour of the slurries

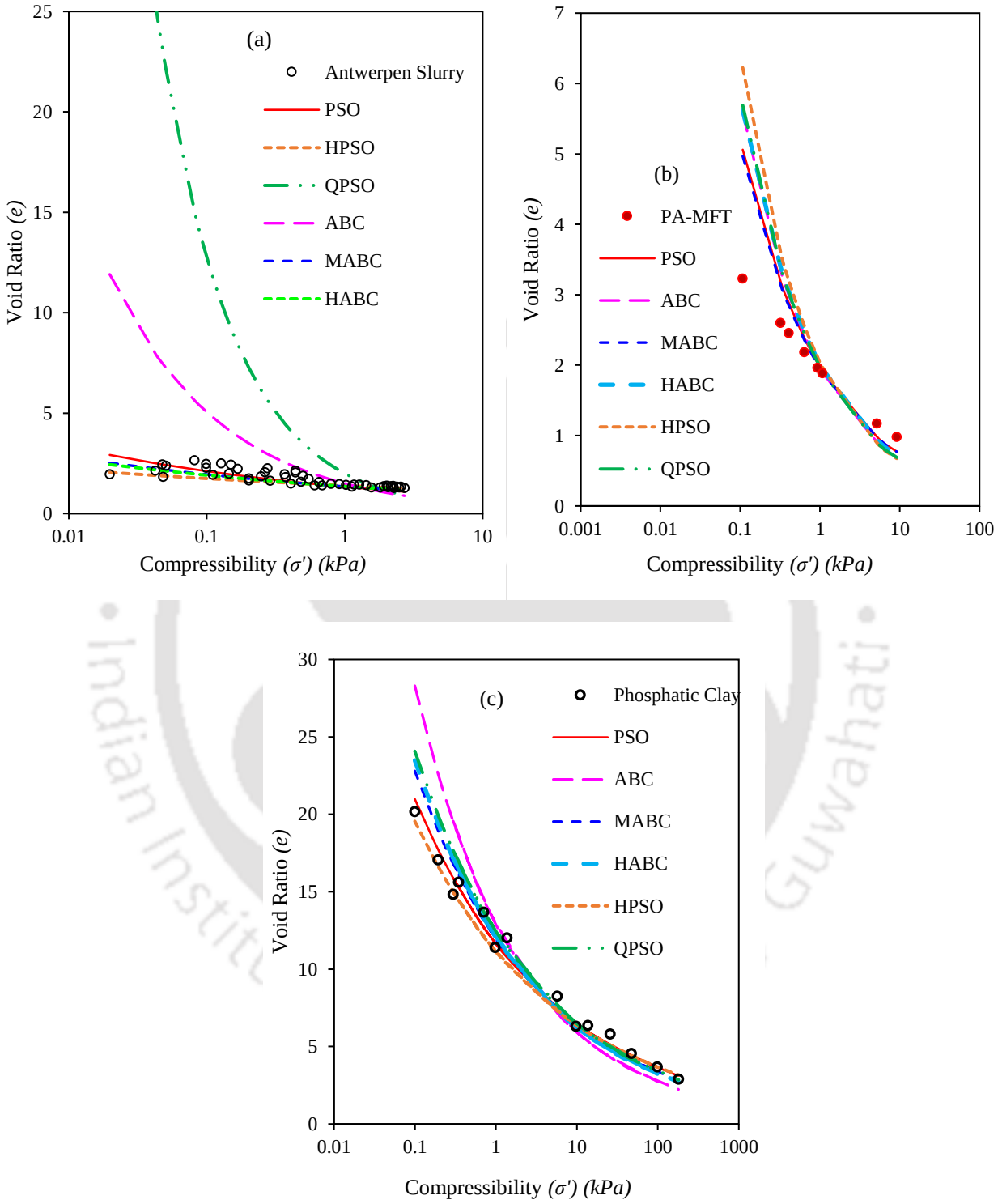


Figure 8.18 Comparison of compressibility functions reported in the literature for the experimental data cases and the same predicted using inverse analysis from the algorithms considered for (a) Antwerpen Slurry (b) PA-MFT (c) Phosphatic Clay

TH-3534_186104002

simulated using the predicted parameters with the experimental data. As a result of the insufficiency of settlement data for inverse analysis during the initial phase of consolidation, each algorithm generated a unique simulation of settlement rates in this phase.

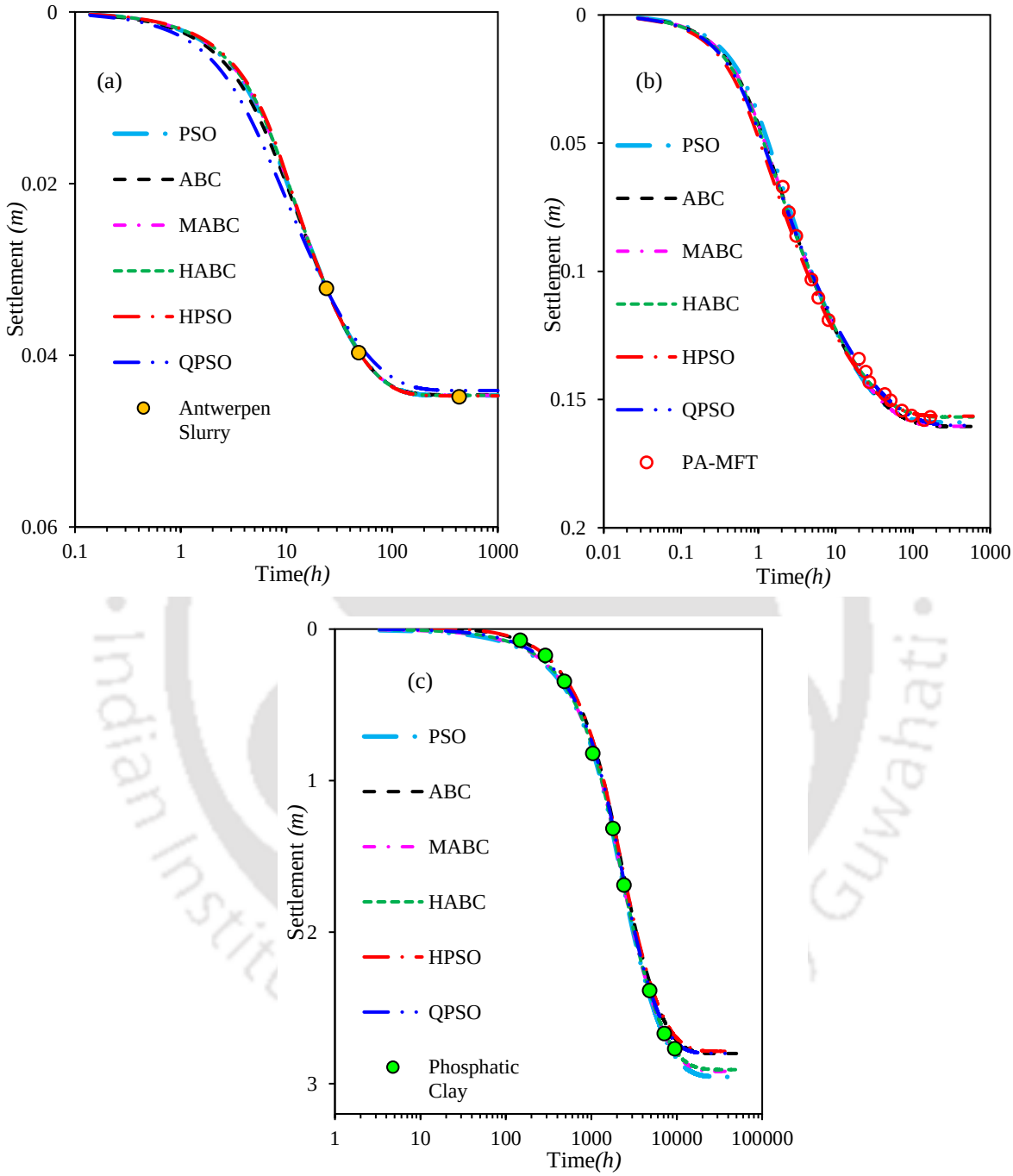


Figure 8.19. Comparison of experimental data points given as input for inverse analyses using the algorithms considered and settlement curves simulated using the constitutive function parameters predicted by inverse analysis for (a) Antwerpen Slurry, (b) PA-MFT, and (c) Phosphatic clay

TH-3534_186104002

When the available data points were compared with the corresponding simulated settlement data points, all algorithms showed slight underestimation. PSO showed an error of 0.3% at 430 hours, while HPSO showed 0.189%, and QPSO showed 2.33% at 49 hours. The sample data set of Phosphatic clay, when compared to the simulated curves, showed that PSO over-estimated the settlement values by 11.3% at 480 hours, while HPSO and QPSO showed over-estimation of 10.2% and 6.5%, respectively, at 1043 hours. The error percentages for PA-MFT were an under-estimation of 3.4% at 8 hours, an over-estimation of the settlement values corresponding to 3 hours by 4 %, and an over-estimation of 3.2 % at 2 hours by QPSO, HPSO, and PSO respectively.

The ABC-based algorithms in the case of PA-MFT showed an over-prediction of settlement of 3.78% at 20 hours for ABC, 3.79% at 20 hours for MABC and 2.87% at 24 hours for HABC. For Phosphatic Clay, under-prediction of 2.573% was observed at 9400 hours, when the settlement curve is simulated using parameters from ABC. The simulated settlement curve from MABC parameters showed an over-prediction of 3.02% at 1000 hours. Meanwhile, an under-prediction of 3.62% was observed at 1040 hours in the case of HABC. In the case of Antwerpen Slurry, the maximum error when compared to available data points was observed at 430 hours, resulting in an underprediction of 0.46%, 0.31% and 0.30% for ABC, MABC and HABC, respectively.

The observed error percentages were within reasonable tolerance levels. The hydraulic conductivity functions were predicted with relative ease. However, increasing the number and spread of settlement data points can improve the prediction of the compressibility function.

8.3.4 Discussion on Significant Observations

8.3.4.1 The linear relationship of P versus ln-M

In the previous section (Section 8.2), the optimisation of hydraulic conductivity function parameters when the compressibility function was known resulted in a linear P versus lnM relationship when the iterative values of the optimised parameters were plotted. It was observed that this relationship held good in the present optimisation landscape as well when both the compressibility and hydraulic conductivity were optimised simultaneously. This shows that the linear relationship is a unique feature of the hydraulic conductivity function parameters in power form, irrespective of the type of optimization algorithm used. It is not affected by the dimension of search space either. The optimization process of hydraulic conductivity function parameters continues independently, unaffected by the search for the compressibility function coefficients. Figures 18.20(a and b) demonstrate this feature for Rutgers and PA-MFT. However, the iteration

TH-3534_186104002

history for the parameters of the compressibility function was found to be random and lacking any such significant distinctive features.

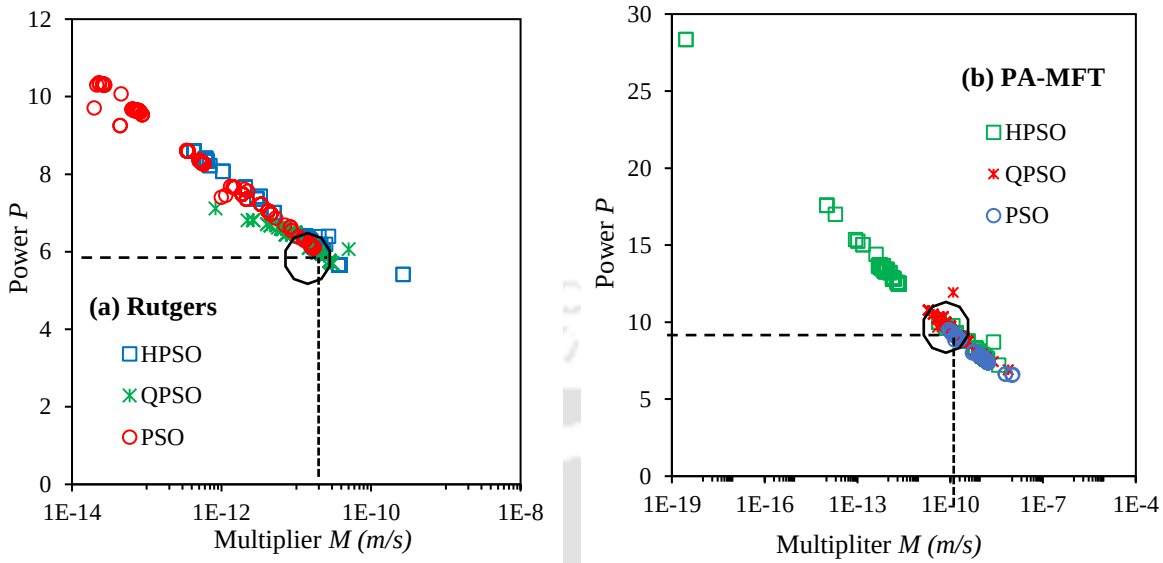


Figure 8.20: The M and P values obtained from consecutive iterations of PSO, QPSO and HPSO forming a linear relationship, finally converging to the optimal pair of values for (a) Rutgers and (b) PA-MFT.

8.3.4.2 Consequences of inaccurate estimation of optimal parameters.

The in-situ void ratio is generally estimated using cone penetration tests and standard penetration tests. The predicted compressibility and hydraulic conductivity functions help to estimate the compressibility and hydraulic conductivity values using the in-situ void ratio values, which in turn can be used for the safe and efficient management of the storage facilities. The impact of error in the predicted hydraulic conductivity was discussed in Section 8.2.5. The erroneous estimation of the compressibility function has several implications. When the predicted compressibility is lesser than the actual compressibility of the material, this results in the under-prediction of overall settlement. Settlement predictions are significant in scheduling the mine closure and finalising the land reclamation strategies. The slurry materials at near-ultimate settlement values possess more shear strength. This aspect is also used for building the dykes of the TSF to increase the reservoir capacity. Under-predicted final settlement can lead to premature land reclamation or lower strength and stability of the underlying material at the time of reclamation. On the other hand, if the overall compressibility is over-predicted, settlement values at any given time point will be overestimated. When the volume of slurry to be dumped in the reservoir is calculated based on these over-predicted settlement values, it can cause the over-dumping of materials to the storage site, where the existing material is expected to have undergone a settlement value much larger than the actual observed

TH-3534_186104002

value in the field. This can cause dangerous consequences such as over-topping or failure due to excessive pore pressure build-up.

8.3.5 Summary

In this study, an innovative procedure for the estimation of constitutive function coefficients using metaheuristic optimization algorithms was explored. The study highlighted the coupling of data from simple settling column tests with the PSO and ABC algorithms and other improved variants to develop an efficient semi-experimental inverse analysis protocol that allows quicker estimation of these relationships. The constitutive function coefficients were successfully back-predicted from three synthetic and three experimental FSC settlement datasets. The unique linear relationship between the power and natural log of the multiplier for the hydraulic conductivity function was found to be independent not only of the type of optimisation algorithm but also of the existence of other decision variables in the optimisation problem. At the same time, no conclusions regarding any unique characteristics were arrived at for the compressibility function coefficients. In the four-dimensional optimisation space, the conventional PSO algorithm showed comparable performance with the HPSO in terms of converged optimal values and the speed of convergence. However, the HPSO results were observed to be repeatable across multiple runs and, therefore, proved to be more reliable. The QPSO algorithm was observed to experience quick convergence to local minima in most cases. Considerable disparity was observed between when the converged optimal values from multiple runs were compared. QPSO, on the other hand, performed better in a two-dimensional search space.

The ABC-based algorithms showed slower convergence in comparison; the MABC was observed to improve the converged values for ABC, while the HABC was observed to be robust in comparison with ABC and MABC. The optimal parameters for the compressibility functions predicted for the synthetic data cases, where the input data points simulated the complete process of FSC, showed better accuracy compared to the experimental data cases. The proposed novel approach expedites the estimation of the constitutive correlations and provides a practical substitute for the laborious conventional experimental procedures frequently used for their determination.

8.4 Strategies for Reliable Optimal Solutions

The work presented in this section shows that optimisation algorithms are indeed a simpler method for the indirect estimation of the constitutive function parameters. However, logically,

TH-3534_186104002

the best performance cannot be guaranteed by a single run of any algorithm when used for the inverse analysis process. Besides, the optimisation landscape itself is dependent on the material properties of the slurry samples considered. Considering this, a sustainable approach to establish reliable results can be devised by combining the insights from the performances of the algorithms in the two- and four-dimensional search space. It is crucial to meticulously identify the optimal number of iterations and the maximum number of repeated cycles necessary to attain reliable outcomes. Several techniques can be employed to guarantee the precision of the outcomes.

An effective strategy would involve executing two algorithms and, after that, evaluating the outcomes for comparison. The second approach involves running a single algorithm multiple times, increasing the maximum number of iterations each time, and choosing the appropriate set of optimal solutions based on the comparison of settlement curves observed and the same simulated using the predicted parameters. The third approach involves establishing the termination criterion as the target RMSE value and running the algorithms until the RMSE requirement is fulfilled. The wide range of compressibility and conductivity characteristics shown by slurry materials pose a significant challenge in the definition of the search space, that is, the setting of the upper and lower limits of the decision variables. Therefore, a certain level of prior knowledge can help to reduce the search space and thereby allow faster convergence to optima. Multiple runs conducted by varying the search space extent can also be incorporated to arrive at the appropriate predictions.

The present chapter established and validated inverse analysis approach for the simultaneous back prediction of constitutive function parameters, using two conventional optimisation algorithms and four newly proposed optimisation algorithms. The approaches were compared for 1g temporal settlement data, which are quite tedious to obtain. In the next chapter, these approaches are tested and validated on the centrifuge data cases.

TH-3534_186104002

9 Inverse AnalysisUsing Ng Settlement Data

9.1 General

The experimental determination of constitutive function parameters is an integral part of tailings storage dam management and is conducted routinely. Conventional experiments take more time and need regular monitoring. Inverse analysis of these parameters from simpler FSC experiments provides an improvement in terms of time and effort compared to the existing methods. In this chapter, the inverse analysis procedure, based on metaheuristic optimisation algorithms, is attempted using centrifuge FSC settlement data. The chapter has two main sections. The first section deals with the inverse analysis of the hydraulic conductivity function for the known compressibility function. In the second section, a simultaneous inverse analysis of compressibility and hydraulic conductivity functions is presented. Three sets of synthetic settlement data (MFT5, MFT6 and Rutgers) were used to test these approaches. Validation was performed using four sets of Ng settlement data from the literature (AL15, Kaolinite, TT50 and TT60). Relevant properties from the Table 4.3 were used. Inverse analysis involves multiple computations of the complex forward analysis problem. Therefore, for the case of synthetic data, the parameters -the initial height of the sample and the initial void ratio- were chosen appropriately so that the estimation process could be expedited. The comparison of performances of PSO, HPSO, QPSO, ABC, MABC and HABC is presented. The suggested method of integrating the Ng FSC test findings with optimisation methods was found to be promising in terms of accurately and efficiently estimating the parameters of the constitutive functions.

9.2 Estimation of Hydraulic Conductivity Parameters

9.2.1 General

The back-prediction of hydraulic conductivity parameters (M and P) for known compressibility functions is presented in this section. Unlike the graphical method of inverse analysis explored in Chapter 7, the approach explored here doesn't involve any rigorous manual computations. Each optimisation algorithm was run thrice, and the best run was selected based on the speed of convergence and the converged RMSE value. The performance of the optimisation algorithms was analysed based on the comparison of predicted hydraulic conductivity with the reported parameter values in the literature, RMSE versus iteration number plots and the comparison of predicted settlement behaviour with the observed behaviour.

TH-3534_186104002

9.2.2 Tuning Parameters

The coefficients for personal learning and social learning were set at 1.5 and 2, respectively, for all the PSO cases. The inertia weight was initially set to 0.9 and then reduced by a factor of 0.99 at the end of each iteration. The population size of the swarm was kept constant at 40 for all the cases. The ABC algorithm used a colony size of 80, which included both employed and onlooker bees. The food number, thus, becomes 40, thereby determining that there are 40 employed bees and 40 onlooker bees. The maximum improvement limit for each solution was kept at 50. When it comes to QPSO, a swarm size of 40 was considered. The values of $\alpha 1$ and $\alpha 2$ were chosen as 0.01 and 0.1, respectively. Throughout the course of the experiment, it was noted that the contraction expansion factor exhibited a range of values, specifically ranging from 0.9901 to 0.01. This variation occurred over a maximum of 100 iterations. The learning coefficients and inertia weight values for HPSO were identical to those mentioned earlier for PSO. A swarm size of 40 was maintained for HPSO. The HPSO algorithms were designed to run PSO and *fmincon* for 50 iterations each, respectively, for synthetic settlement data inputs in each run, based on trial and error. The colony size and improvement limit values used for MABC and HABC were 80 and 50, respectively, for all the cases. The HABC algorithm ran 50 iterations of ABC followed by 50 iterations of *fminsearch* for settlement data cases.

9.2.3 Inverse Analysis Using Synthetic Settlement Data

A centrifuge FSC test takes minutes to hours to complete, depending on the sample size, the speed of rotation, the radius of the centrifuge, and the significant material properties of the sample. These factors govern the stress experienced by the sample. In this study, centrifuges of various drum radii were tested for materials with different compressibility and conductivity characteristics. Beyond 200 iterations, all the algorithms showed no much variation in the converged values. The converged values of RMSE, the worst and mean values, and the iteration number of convergence for the best run are presented in Table 9.1, along with the predicted hydraulic conductivity parameters. A comparison of the best run of MFT5 showed that in terms of converged RMSE, MABC showed the best performance. MABC was robust as well. This was followed by ABC and then PSO. HPSO showed the worst performance in comparison with all the algorithms. HABC and HPSO.

TH-3534_186104002

Table 9.1 Performance of different inverse analysis algorithms using Ng synthetic settlement data as the input for predicting the hydraulic conductivity function coefficients -power (P) and multiplier (M)

Material	Algorithm	RMSE Values			Iteration No.	Best predicted values	
		Best	Worst	Mean		P	M (m/s)
MFT 5	**PSO**	1.64E-05	1.77E-05	1.69E-05	133	3.472	2.16E-11
	HPSO	1.06E-01	1.06E-01	1.06E-01	98	3.649	1.58E-11
	QPSO	8.35E-04	1.13E-03	1.02E-03	78	3.482	2.14E-11
	ABC	1.39E-05	2.55E-05	2.11E-05	18	3.424	2.34E-11
	MABC	7.81E-06	7.81E-06	7.81E-06	66	3.472	2.16E-11
	HABC	6.25E-04	6.25E-04	6.25E-04	51	3.472	2.16E-11
MFT 6	**PSO**	1.14E-05	2.22E-05	1.60E-05	192	3.653	1.78E-11
	HPSO	1.55E-04	2.88E-04	2.01E-04	95	3.557	2.14E-11
	QPSO	1.23E-05	1.52E-05	1.34E-05	46	3.634	1.84E-11
	ABC	1.14E-05	1.15E-05	1.14E-05	17	3.646	1.80E-11
	MABC	1.14E-05	1.14E-05	1.14E-05	48	3.649	1.79E-11
	HABC	1.14E-05	1.14E-05	1.14E-05	51	3.649	1.79E-11
Rutgers	**PSO**	3.50E-04	1.67E-03	7.90E-04	97	6.148	1.69E-11
	HPSO	3.50E-04	3.55E-04	3.51E-04	50	6.148	1.69E-11
	QPSO	3.59E-04	7.51E-04	5.86E-04	42	6.130	1.71E-11
	ABC	3.75E-04	1.71E-03	8.09E-04	95	6.255	1.77E-11
	MABC	3.50E-04	3.50E-04	3.50E-04	49	6.148	1.69E-11
	HABC	3.50E-04	3.55E-04	3.51E-04	50	6.148	1.69E-11

TH-3534_186104002

were robust, but local minima convergence was observed. QPSO showed reasonable performance but was not robust in this case. The iteration number versus RMSE plots of MFT5 are given in Figure 9.1 (a). The predicted hydraulic conductivity function parameters were observed to match well with the actual function, as shown in Figure 9.2 (a).

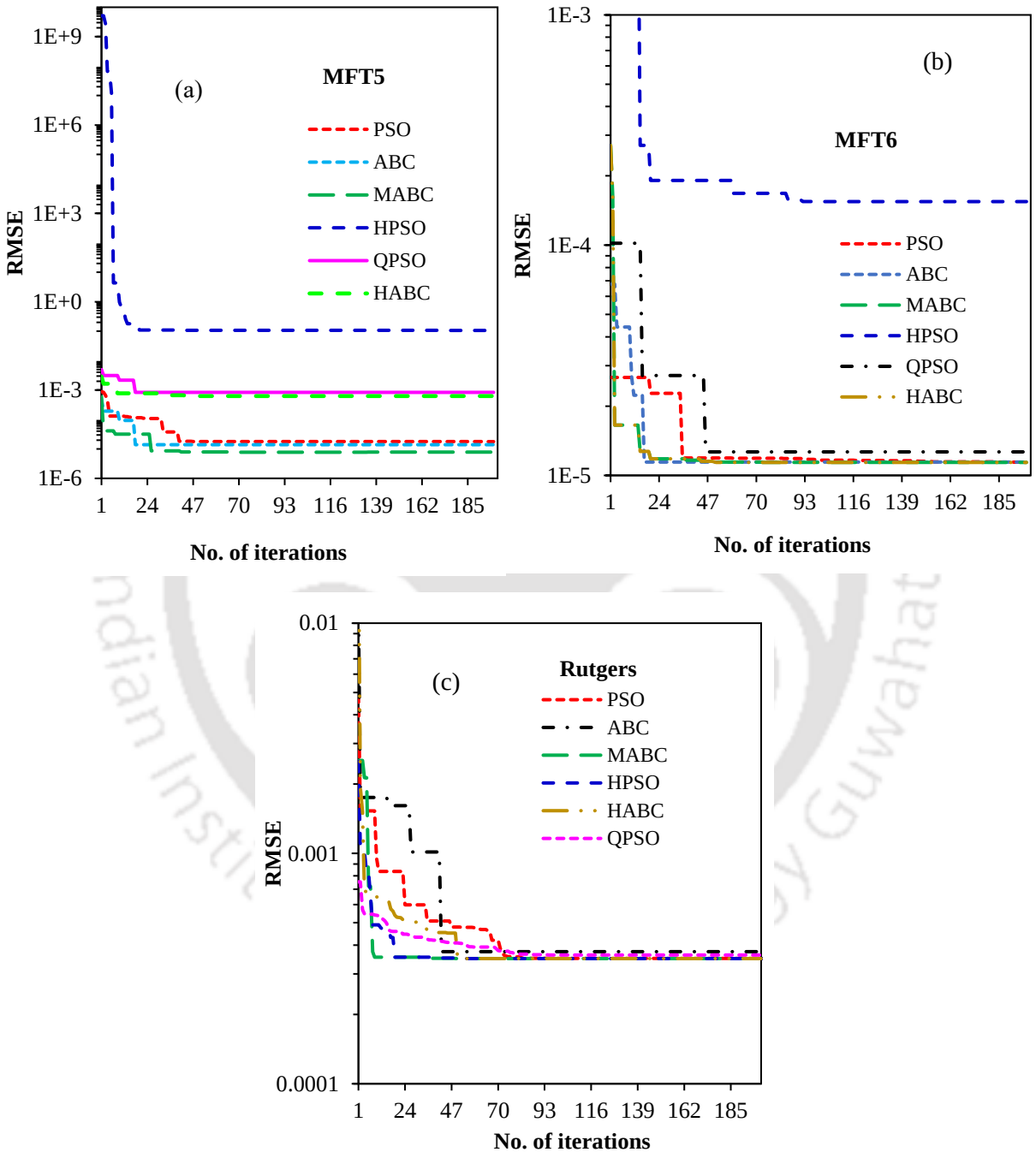


Figure 9.1. The objective function value (RMSE) versus the number of iterations plotted for the best run of each of the algorithms employed for inverse analysis using Ng synthetic settlement data of (a) MFT5, (b) MFT6, and (c) Rutgers

TH-3534_186104002

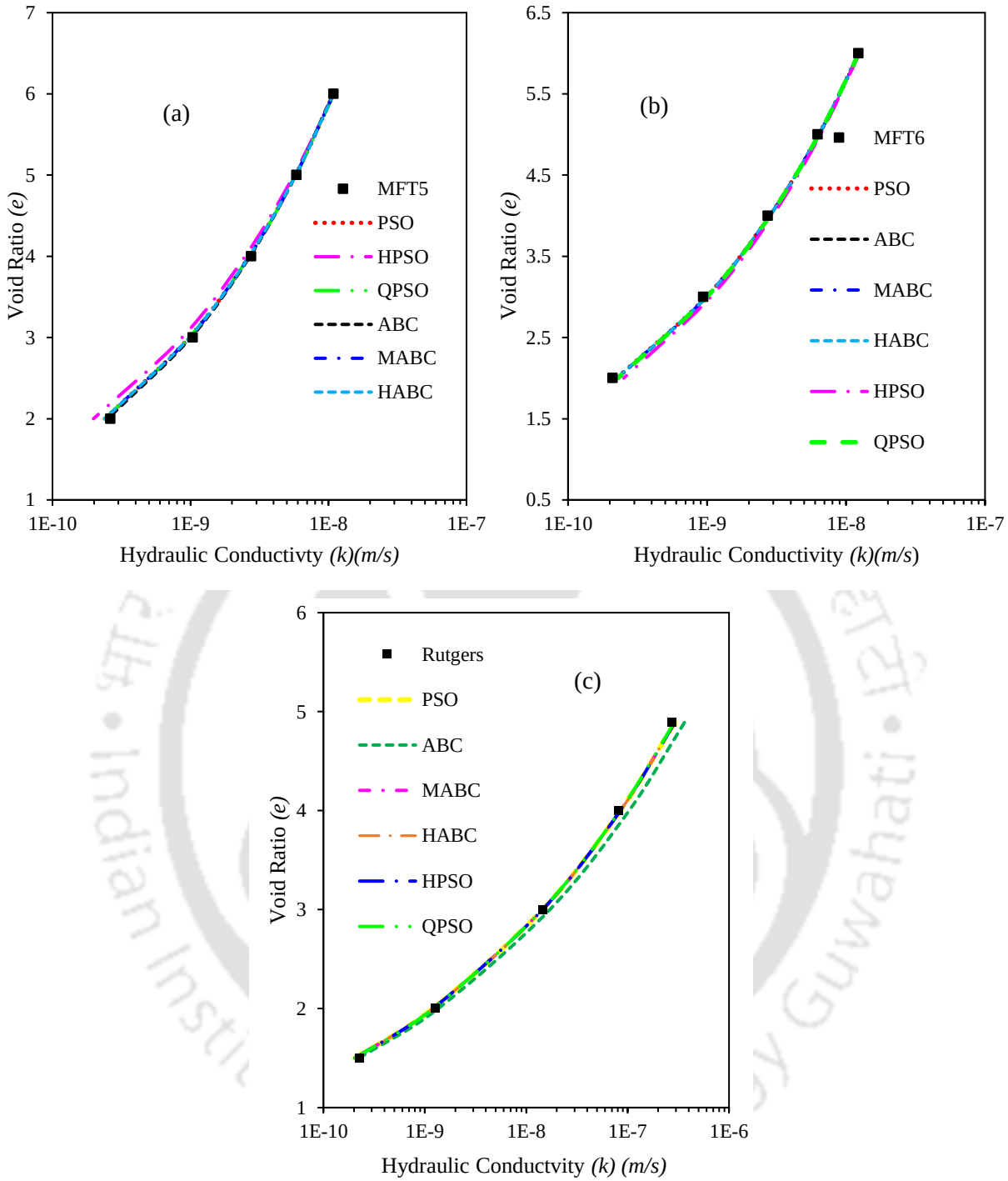


Figure 9.2. Comparison of power (P) and Multiplier (M) values predicted using centrifuge settlement data from various algorithms with the actual parameter values used to generate the synthetic data points for (a) MFT5, (b) MFT6 and (c) Rutgers

The settlement curves simulated using the predicted parameters were compared to the synthetic data used as input in Figure 9.3 (a). The maximum magnitude of error was observed in the final phase of consolidation, which can be attributed to the white noise added to the settlement data.

TH-3534_186104002

MABC, PSO, QPSO and HABC overpredicted the settlement values at 21 hours by a range of 4.75%, while ABC showed an overprediction of 4.78% at 21 hours. HPSO had the maximum error at 51 hours, which is 4.73%.

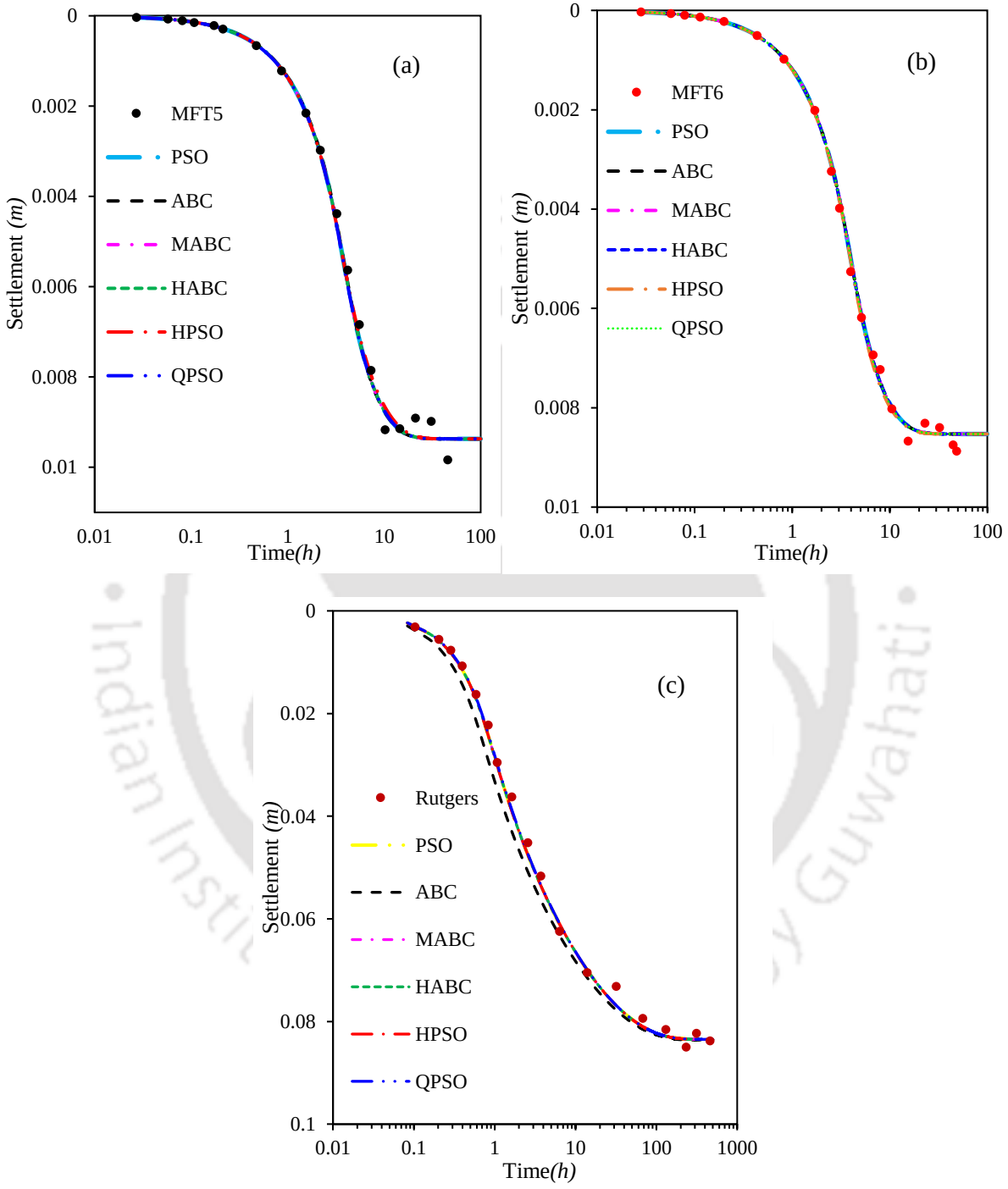


Figure 9.3 Comparison of synthetically generated settlement data points given as input for inverse analysis using the algorithms considered and settlement curves simulated using the hydraulic conductivity function parameters predicted by inverse analysis for (a) MFT5, (b) MFT6 and (c) Rutgers

TH-3534_186104002

HABC and MABC showed the best performance in terms of converged RMSE value in the case of MFT6 (Figure 9.1(b)). These algorithms were robust and reached the optima within 100 runs. In the case of HABC, the convergence happened at 51 iterations, signifying a proper initialisation of the *fminsearch* algorithm after 50 iterations. PSO, ABC and QPSO showed moderate efficiency. The worst, mean, and best converged RMSE values were in the same range and, therefore, satisfactory in terms of robustness. The worst performance was observed in the HPSO case. This can be seen in Figure 9.2(b) as a deviation in the hydraulic conductivity function comparison. Based on Figure 9.3(b), the observed error has larger magnitudes after the data point at 8 hours. PSO showed an under-prediction of 3.75% at 8 hours, while ABC, MABC and HABC showed 3.88% under-prediction at 48 hours. In the case of QPSO, the maximum error value as a percentage was at 15 hours, amounting to a settlement underprediction of 3.42%. HPSO had a 4.83% error at 8 hours.

ABC showed a non-robust performance in the case of Rutgers (Figure 9.1 (c)). It was observed that the converged RMSE for ABC varied by 7%, which resulted in a visible variation in the hydraulic conductivity function, as shown in Figure 9.2 (c). All other algorithms except QPSO converged to the same RMSE value. All algorithms converged within 100 iterations. ABC and QPSO exhibited robustness issues as well. The maximum error in the settlement value observed for ABC was overprediction by 18% at 1.6 hours, based on Figure 9.3(c). The maximum error for all other cases, including QPSO, was an overprediction of 4.5% at 32 hours.

A comparison of the algorithms' performances on preliminary testing showed that the hydraulic conductivity can be successfully back-predicted from synthetic centrifuge settlement data. In the next section, these algorithms are validated using experimental centrifuge FSC settlement data from the literature.

9.2.4 Inverse Analysis Using Experimental Settlement Data

Six algorithms were run three times for a maximum of 200 iterations per run. The tuning parameters were maintained in the same way as the synthetic data cases. The hydraulic conductivity function parameters from the literature were predicted for four slurries. Along with settlement data from centrifuge FSC tests, other relevant properties were given as input based on Table 4.3. The choice of time and space steps for stability and convergence is a challenge for the finite difference method, as these values change from material to material.

TH-3534_186104002

Table 9.2: Performance of different inverse analysis algorithms using Ng experimental settlement data as the input for predicting the hydraulic conductivity function coefficients -power (P) and multiplier (M)

Material	Algorithm	RMSE Values			Iteration No.	Best predicted values	
		Best	Worst	Mean		P	M (m/s)
AL15	**PSO**	1.14E-03	1.54E-03	1.34E-03	195	4.963	1.63E-10
	HPSO	9.96E-04	9.98E-04	9.97E-04	50	4.875	1.78E-10
	QPSO	9.96E-04	1.00E-03	1.00E-03	28	4.875	1.77E-10
	ABC	1.07E-03	1.08E-03	1.08E-03	85	5.021	1.54E-10
	MABC	1.07E-03	1.07E-03	1.07E-03	34	5.021	1.54E-10
	HABC	8.88E-04	8.88E-04	8.88E-04	51	4.456	2.67E-10
Kaolinite	**PSO**	5.85E-04	7.78E-04	6.80E-04	198	6.284	2.68E-10
	HPSO	5.63E-04	2.09E-02	7.33E-03	50	6.295	2.67E-10
	QPSO	5.83E-04	1.21E-03	8.50E-04	120	6.376	2.42E-10
	ABC	5.62E-04	1.39E-03	9.36E-04	198	6.249	2.80E-10
	MABC	5.62E-04	1.39E-03	9.36E-04	100	6.285	2.68E-10
	HABC	5.63E-04	5.63E-04	5.63E-04	50	6.285	2.68E-10
TT50	**PSO**	2.01E-03	3.34E-03	2.45E-03	100	6.734	9.96E-10
	HPSO	9.38E-04	9.38E-04	9.38E-04	51	5.233	1.50E-09
	QPSO	2.65E-02	2.69E-02	2.67E-02	67	6.787	9.70E-10
	ABC	5.62E-04	6.06E-04	5.80E-04	152	6.860	9.57E-10
	MABC	2.01E-03	2.01E-03	2.01E-03	67	6.734	9.94E-10
	HABC	8.94E-04	8.94E-04	8.94E-04	51	5.957	1.37E-09

TH-3534_186104002

Material	Algorithm	RMSE Values			Iteration No.	Best predicted values	
		Best	Worst	Mean		P	M (m/s)
TT60	**PSO**	7.63E-04	3.24E-03	1.60E-03	154	3.894	1.80E-09
	HPSO	2.99E-03	3.82E-03	3.50E-03	40	4.372	1.66E-09
	QPSO	3.36E-03	3.36E-03	3.36E-03	74	5.734	9.94E-10
	ABC	8.82E-04	9.86E-04	9.25E-04	148	3.881	2.09E-09
	MABC	2.98E-03	2.98E-03	2.98E-03	23	4.199	1.64E-09
	HABC	2.01E-03	2.01E-03	2.01E-03	51	4.272	1.74E-09

TH-3534_186104002

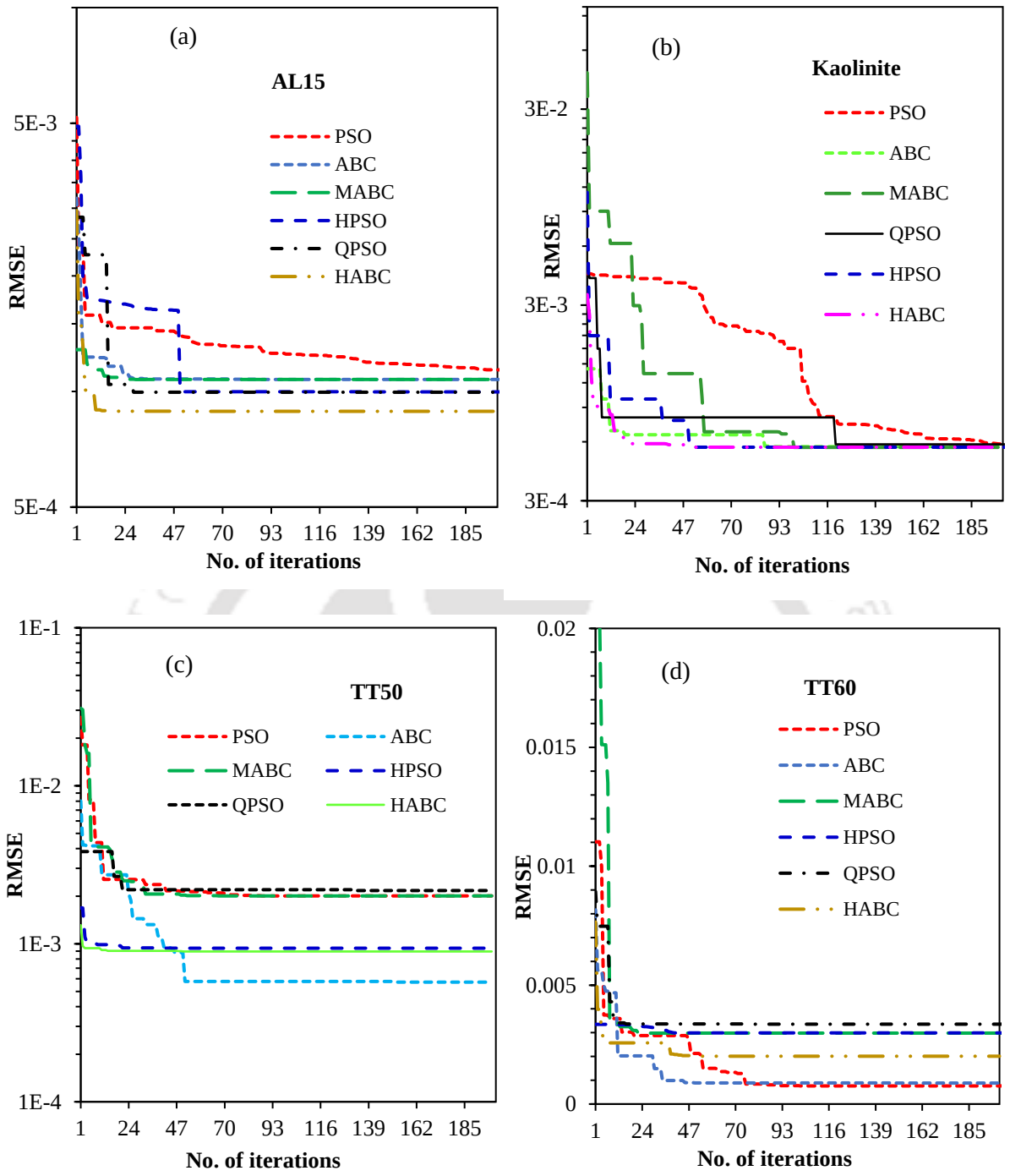


Figure 9.4 The objective function value (RMSE) versus the number of iterations plotted for the best run of each of the algorithms employed for inverse analysis using Ng experimental settlement data of (a) AL15 (b) Kaolinite (c) TT50 and (d) TT60

The comparison of the performances of various algorithms are provided in Table 9.2, and the iteration versus RMSE plots for the best runs are given in Figures 9.4 (a-d). The back-predicted hydraulic conductivity function parameters were compared with the actual values by plotting those as functions alongside the corresponding literature data, as shown in Figure 9.5(a-d).

TH-3534_186104002

These optimal parameters, reported for the best run, were used to simulate the settlement curves for comparison with actual data, as shown in Figure 9.6 (a-d). In the case of AL15, based on the converged RMSE values for the best run given in Table 9.2, HABC showed the best performance.

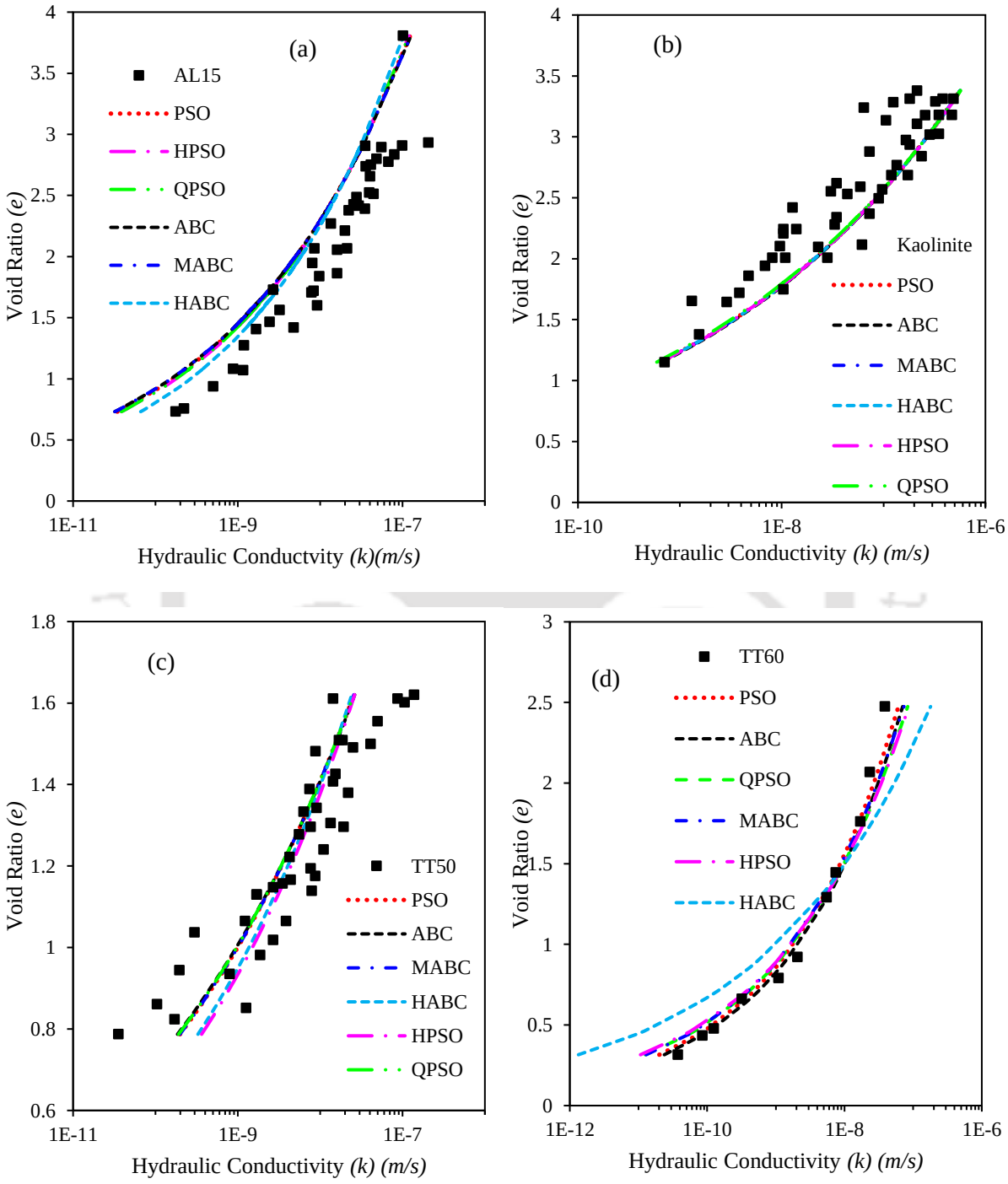


Figure 9.5. Comparison of power (P) and Multiplier (M) values predicted using experimental Ng settlement data as input from various algorithms with corresponding actual values in the literature for samples of (a) AL15, (b) Kaolinite, (c) TT50 and (d) TT60

TH-3534_186104002

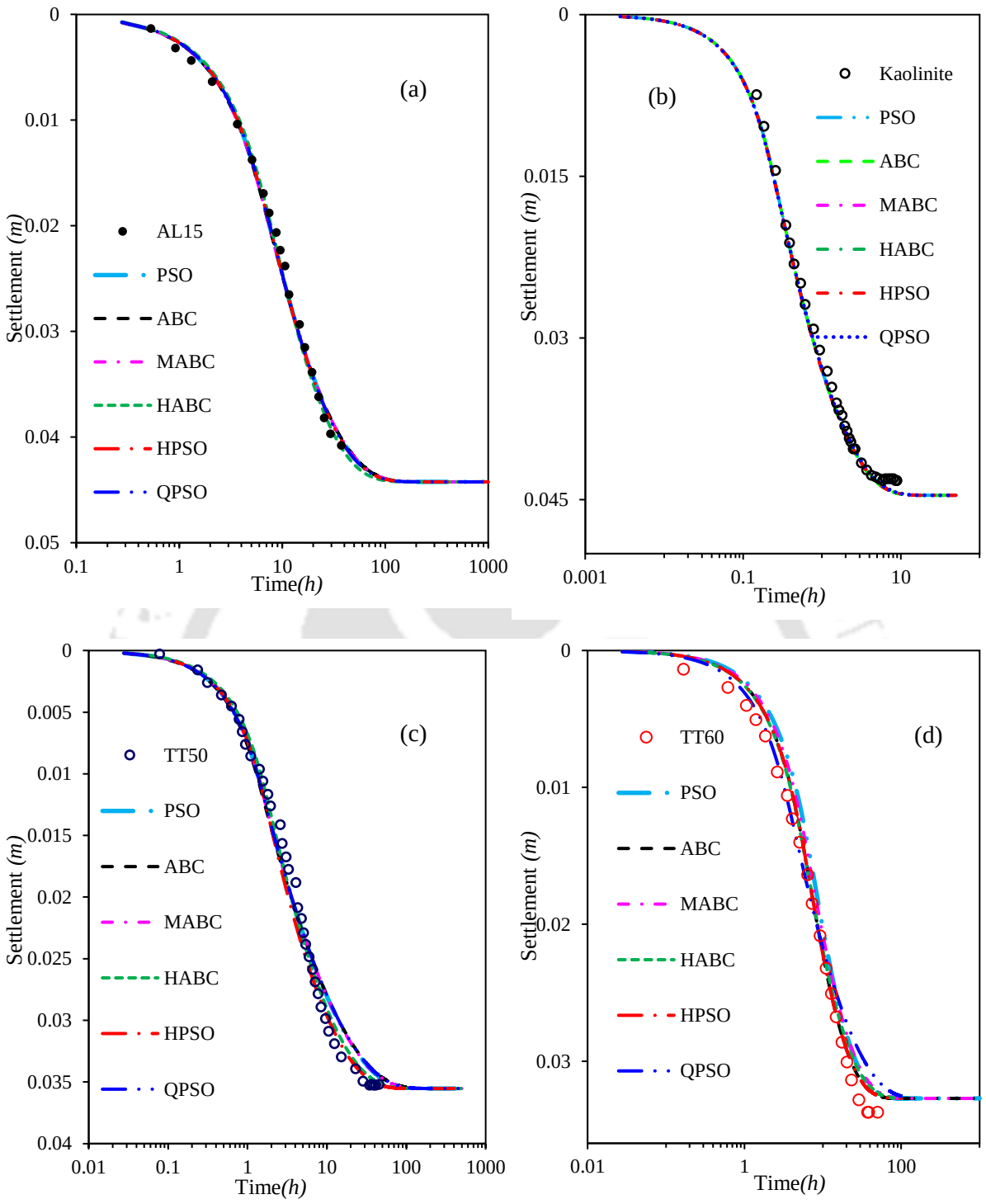


Figure 9.6. Comparison of experimental Ng settlement data points given as input for inverse analysis using the algorithms considered and settlement curves simulated using the hydraulic conductivity function parameters predicted by inverse analysis for (a) AL15, (b) Kaolinite, (c) TT50 and (d) TT60

QPSO and HPSO showed comparable performance, followed by MABC and ABC. It can be seen from Figure 9.4 that within 200 iterations, PSO failed to achieve proper convergence. The

TH-3534_186104002

RMSE at 200 runs from three runs also showed a lack of robustness, as signified by the difference between the mean, worst and best RMSE values. The hybrid algorithms and MABC were robust. The settlement data points for AL15 matched well with the simulated curve. The maximum error for all the cases was at the data point for 10 hours. An over-prediction in settlement by 8.8% was observed at this point.

In the case of Kaolinite, all six algorithms converged to RMSE value in the same range, showing comparable performance. The difference between the smallest and the largest RMSE values was only 4%. ABC and MABC converged to the lowest RMSE value. However, these algorithms were not robust. Only HABC showed repeatability in the results. The PSO algorithm was yet to achieve complete convergence as for the case of AL15, till the maximum iteration number considered, as shown in Figure 9.4(b). Comparison of predicted hydraulic conductivity functions with the literature data showed good matching. (Figure 9.5(c)). Settlement versus time curves simulated using the predicted parameters showed a 2.2% error at the 1.7-hour mark for all algorithms, which is within the tolerance range.

In the case of TT50, all algorithms robustly converged to their best optimal values in all three runs except PSO. MABC, QPSO and ABC were observed to have gotten stuck at local minima values, as shown in Figure 4.5(c). ABC, HABC and HPSO performed better in comparison. Modified algorithms were observed to take fewer number of iterations to converge. Figure 9.5 (c) shows that the predicted hydraulic conductivity functions for HPSO and HABC varied slightly compared to other algorithms. Individual settlement curves simulated using each algorithm was compared with the actual settlement data set. Maximum errors in settlement values were compared as percentages. Under-prediction of settlement value by 7.84% was observed for PSO at 12 hours, while the same was 7.6% for ABC, observed at 15 hours. MABC underpredicted the settlement value at 10.52 by 7.9%. For HABC, the maximum error was the underprediction of 4.5% at 15 hours. HPSO overpredicted the settlement value at 3.4 hours by 7.6%. QPSO was observed to show an overprediction of 8.2% at 12 hours. The observed error values, based on the Figure 9.7 (c), were within the tolerance limit.

Two out of three runs of the PSO algorithm converged to the lowest RMSE value in the case of TT60. ABC showed a comparable convergence. All modified algorithms showed fast convergence within 100 iterations. However, the converged RMSE values were larger than the conventional PSO and ABC results, as seen in Figure 9.4(d). MABC, HABC, ABC, and QPSO showed robust prediction. The hydraulic conductivity predicted using HABC deviated

TH-3534_186104002

noticeably from the predictions given by other algorithms (Figure 9.5(d)). The discrepancy in the initial and final phase of consolidation, when the actual data set and the simulated curves are compared, could be attributed to the compressibility function defined for the material. This is confirmed by a similar variation seen in the final phase of consolidation as well. As a result, in the early phases, PSO underpredicted settlement by 20%, while HPSO showed 25% error. The simulated curve for QPSO showed a reasonably good match in the initial phase. In the final phase, all algorithms were observed to have an error in the range of 5%, corresponding to 37-38 hours.

Though the predefinition of the compressibility function helps in reducing the search space complexity, it was observed to limit the prediction capability of algorithms. On the other hand, all algorithms showed an overall good performance when various cases were compared. The error norm for the algorithms is the RMSE, which gives an idea of the overall mean error in the settlement predicted. Various approaches for improving the performances of these algorithms can be attempted, like increasing the total iteration number or constricting the upper and lower bounds of the variables. The hydraulic conductivity functions were predicted with good accuracy for all the cases considered.

9.2.5 Summary

Centrifuge-based FSC testing promises an expedited approach for the estimation of hydraulic conductivity function parameters. It is evident that the RMSE values are very small. This is due to the fact that the error norm is being determined using centrifuge settlement values expressed in SI units. The model sizes are very small, and the settlement values are even smaller. Therefore, when the root mean square is taken, the value comes out to be in small order. The significance of this error is that it will be magnified in field conditions as the centrifuge models are heavily scaled down. All the algorithms showed comparable performances. Hybridisation was observed to improve robustness to a certain extent. In some cases, the modified algorithm variants converged within a hundred iterations. By carefully defining the time and space steps, setting suitable upper and lower boundaries for the variables, and using well-defined tuning parameters, the suggested optimisation-based methodology, when merged with centrifuge FSC test data, offers a more efficient alternative to existing strategies for the estimation of hydraulic conductivity function.

TH-3534_186104002

9.3 Back-estimation of compressibility and permeability characteristics

9.3.1 General

In this section, a novel approach for the expediated estimation of the compressibility and hydraulic conductivity functions, simultaneously using the settlement data from centrifuge FSC tests, is presented. This approach integrates the speed of the centrifuge testing with the convenience and robustness of six optimisation algorithms to derive a superior technique that can aid in a quick back estimation of the coefficients of compressibility and conductivity functions. An EFDM solution for the governing differential equation for Ng FSC was used for the forward analysis. Inverse analysis using PSO, ABC, QPSO, MABC, HABC and HPSO were tested for three synthetic settlement data cases and validated using four experimental data cases from the literature. The results presented include the comparison of the performance of algorithms in terms of converged RMSE values from best-runs, the iteration number for convergence in these cases and the best-predicted function parameters. In addition, the predicted parameters are compared with actual data, and the settlement behaviour simulated using these parameters is compared with the actual settlement data point and presented for clarity.

9.3.2 Back-estimation Using Synthetic Data

MABC, HABC, and PSO showed comparable performance, which was better than other variants in the case of MFT5. The converged RMSE, in the case of ABC, was within range of these algorithms. However, QPSO and HPSO were observed to get stuck in local minima. In Figure 9.8 (a), it can be seen that the predicted hydraulic conductivity function for the case of QPSO showed a slight deviation from the ones predicted by other algorithms. The comparison of predicted compressibility functions given in Figure 9.9 (a) shows that the predictions deviate from the actual values for lower values of effective stress. The comparison of simulated settlement curves showed that, based on Figure 9.10(a), the maximum error value expressed as a percentage of the corresponding actual value is 4.2% due to underprediction at 30 hours in for PSO. The overprediction error is maximum at 21 hours, equal to 4.8% at 21 hours. For MABC, the under-prediction at 45 hours amounted to 4.78%. HABC showed over-prediction, resulting in an error of 4.93% at 21 hours. HPSO shows under-prediction, resulting in an error of 4.85% at 45 hours. QPSO showed the maximum deviation from the data points in the final phase of settlement. An overprediction of 7.85% was observed in this case at 21 hours.

TH-3534_186104002

Table 9.3 Performance of different inverse analysis algorithms using Ng synthetic settlement data as the input for predicting the constitutive relation coefficients

Material	Algorithm	RMSE Value			Iteration	Predicted parameter values			
		Best	Worst	Mean	No.	Compressibility function		Hydraulic conductivity function	
						A (1/kPa)	C	P	M (m/s)
MFT 5	**PSO**	1.64E-05	1.77E-05	1.69E-05	193	3.201	-0.141	3.431	2.34E-11
	HPSO	3.62E-03	4.49E-03	4.13E-03	152	3.200	-0.172	3.430	2.34E-11
	QPSO	4.56E-05	2.28E-04	1.37E-04	187	3.053	0.160	3.648	1.61E-11
	ABC	1.76E-05	1.89E-05	1.82E-05	36	3.121	-0.171	3.611	1.70E-11
	MABC	1.60E-05	1.96E-05	1.80E-05	72	3.201	-0.174	3.422	2.40E-11
	HABC	1.62E-05	1.71E-05	1.67E-05	152	3.185	-0.161	3.453	2.25E-11
MFT 6	**PSO**	2.16E-04	2.16E-04	2.16E-04	114	4.452	-0.140	3.612	2.24E-11
	HPSO	2.16E-04	2.16E-04	2.16E-04	114	4.449	-0.500	3.605	2.23E-11
	QPSO	1.68E-04	2.01E-04	1.80E-04	26	3.184	-0.160	4.311	5.89E-12
	ABC	1.99E-05	2.17E-05	2.07E-05	124	3.149	-0.140	3.770	1.45E-11
	MABC	1.90E-05	3.04E-05	2.47E-05	94	3.172	-0.160	3.721	1.65E-11
	HABC	1.95E-05	2.33E-05	2.10E-05	152	3.146	-0.150	3.81	1.36E-11
Rutgers	**PSO**	3.13E-04	5.35E-04	4.53E-04	198	2.712	-0.190	6.199	1.52E-11
	HPSO	2.70E-04	2.70E-04	2.70E-04	50	2.682	-0.185	6.141	1.64E-11
	QPSO	9.39E-04	1.59E-03	1.35E-03	39	2.664	-0.175	5.951	2.25E-11
	ABC	3.35E-04	6.73E-04	5.17E-04	63	2.613	-0.173	6.074	1.77E-11
	MABC	2.70E-04	3.70E-04	3.15E-04	140	2.831	-0.206	6.163	1.65E-11
	HABC	2.70E-04	3.70E-04	3.15E-04	141	2.727	-0.192	6.170	1.59E-11

TH-3534_186104002

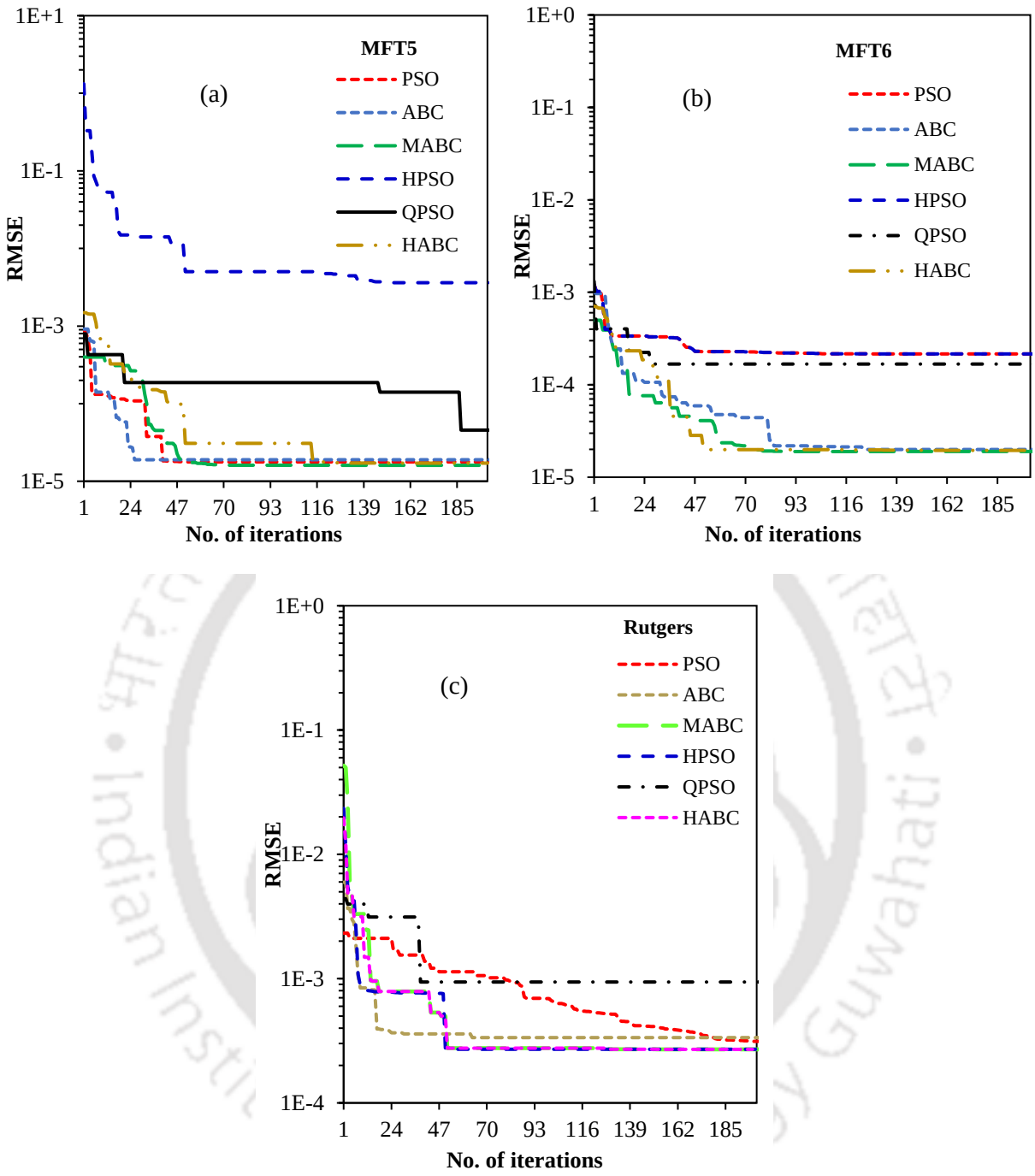


Figure 9.7. The objective function value (RMSE) versus the number of iterations plotted for the best run of each of the algorithms employed for simultaneous back-estimation of constitutive function parameters using Ng synthetic settlement data of (a) MFT5, (b) MFT6 and (c) Rutgers

Though PSO and HPSO showed robust convergence, the converged RMSE values for these algorithms were larger than those of the other algorithms. The best convergence was shown by MABC, HABC, and ABC, though it was not repeatable. Figure 9.8(b) shows that the predicted

TH-3534_186104002

function for QPSO deviated considerably from the actual data points, resulting in a lowering of the conductivity values. This is reflected in Figure 9.10(b) as a slowed-down rate of consolidation, showing a large variation in the simulated settlement behaviour for QPSO.

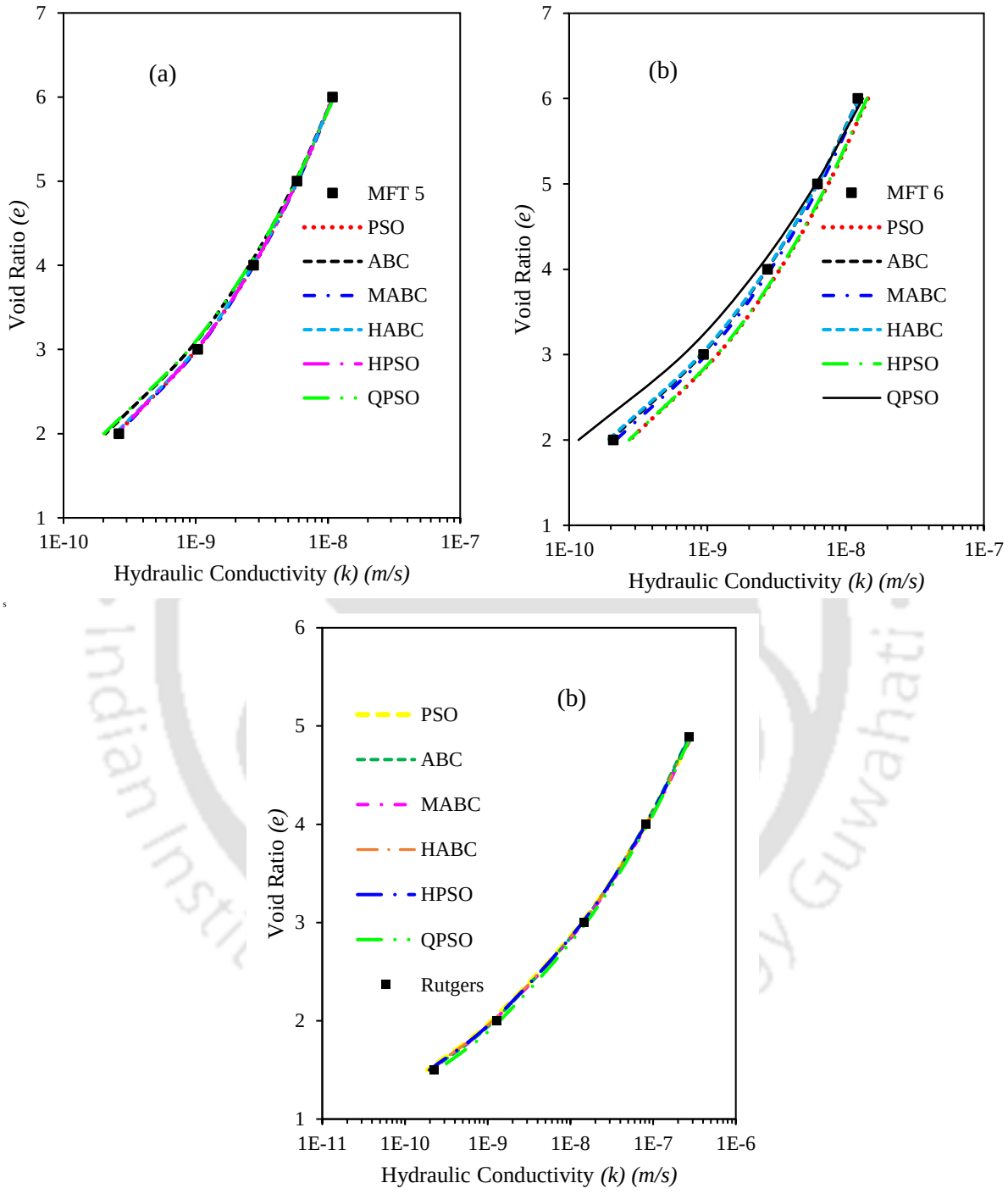


Figure 9.8. Comparison hydraulic conductivity parameters predicted using centrifuge settlement data reported for various algorithms with the actual parameter values used to generate the synthetic data points for (a) MFT5, (b) MFT6, and (c) Rutgers

TH-3534_186104002

PSO predicted a higher value of hydraulic conductivity compared to the actual data, which resulted in faster completion of consolidation in the simulated settlement behaviour. The values of the final settlement simulated by the predicted parameters differ from the actual data points due to the discrepancy in compressibility function parameters.

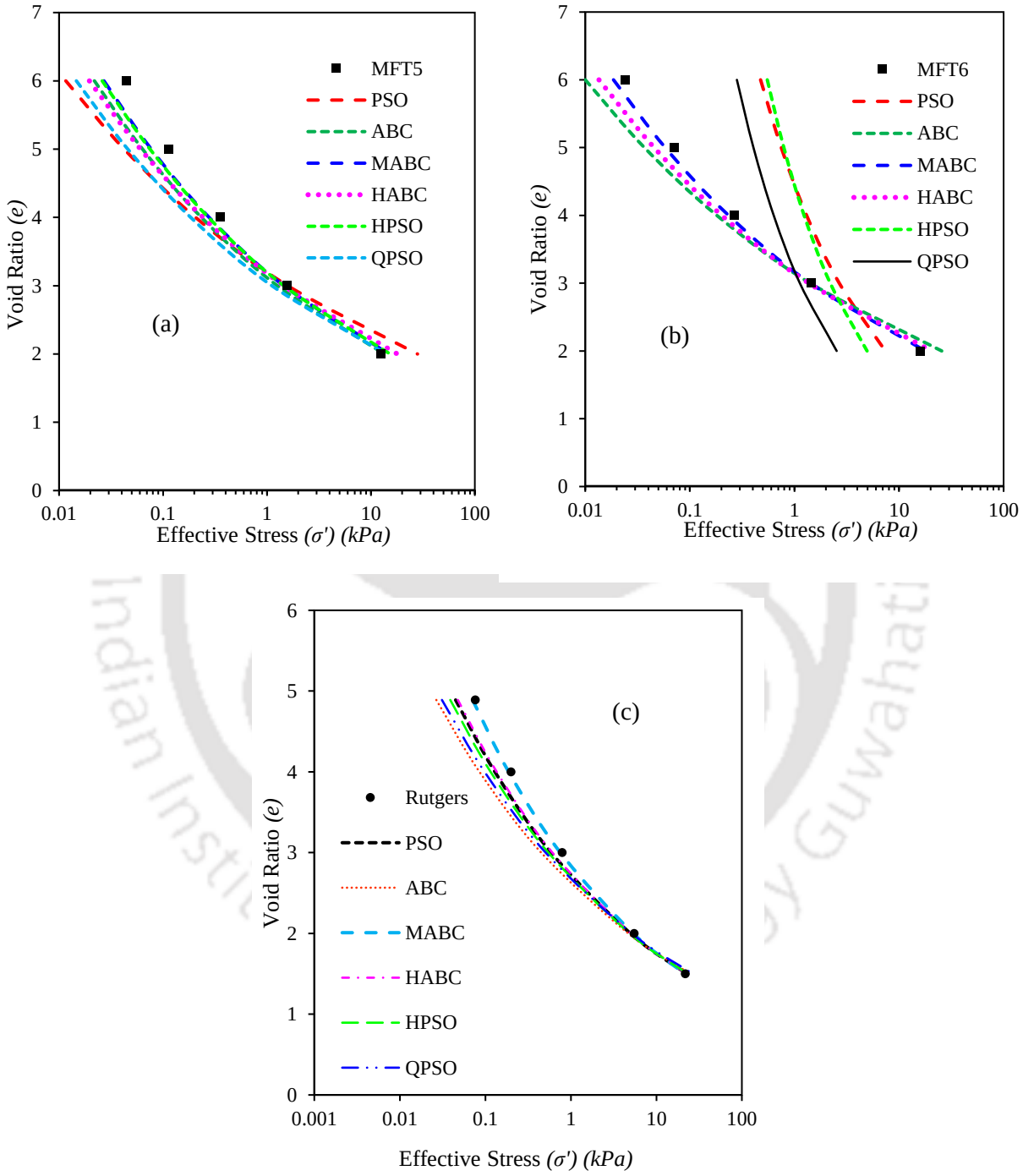


Figure 9.9 Comparison compressibility function predicted using centrifuge settlement data reported for various algorithms with the actual parameter values used to generate the synthetic data points for (a) MFT5, (b) MFT6, and (c) Rutgers

TH-3534_186104002

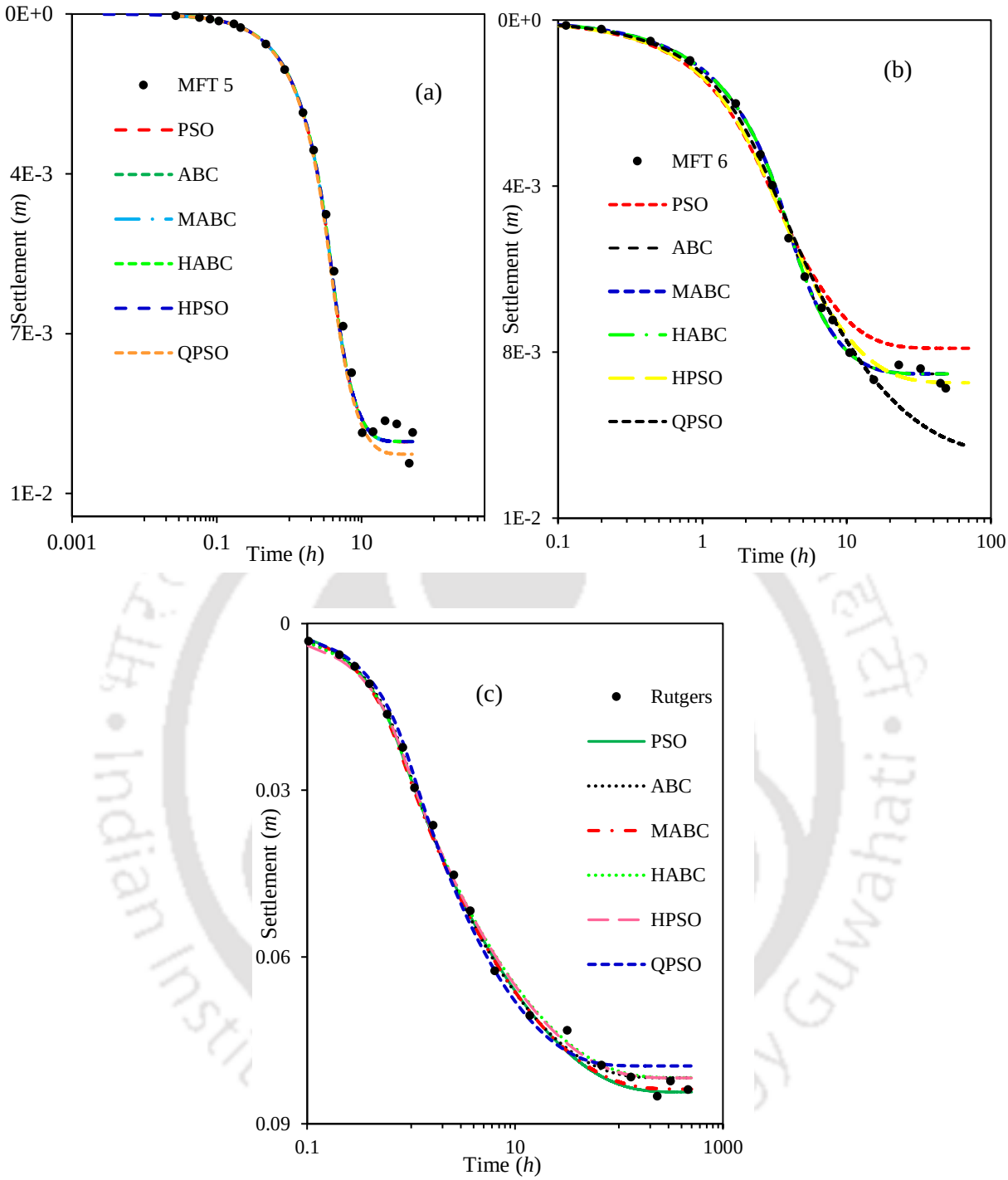


Figure 9.10 Comparison of settlement curves simulated using the predicted constitutive function parameters reported for various algorithms with the observed settlement data from the literature for (a) MFT5, (b) MFT6 and (c) Rutgers

The largest value of error was observed for QPSO at 49 hours. An overprediction of 13.89% resulted from the erroneous prediction of hydraulic conductivity and compressibility functions. In the case of PSO, the error was maximum at 15 hours, having an underprediction value of 10.84%. MABC overpredicted the settlement value at 8 hours by 4.7%, while HPSO, ABC,

TH-3534_186104002

and HABC showed underprediction errors of 3.23%, 3.34% and 3.90%, respectively, at 15 hours' time point.

HPSO showed robust performance while converging to the lowest RMSE value among the six algorithms in the case of Rutgers. Other algorithms failed to converge to the same RMSE value when run repeatedly, as seen from the difference between the best, worst and mean RMSE values. PSO did not achieve complete convergence within the 200 iterations considered in this study. HABC showed a robustness issue for the chosen ratio of ABC and *fminsearch.* Based on the Figure 9.6(c), the predicted hydraulic conductivity matched well with the actual data for all the algorithms. As a result, it can be seen in Figure 9.10© that the simulated settlement curves matched the actual settlement rate dictated by the experimental data points. However, in the final phase of consolidation, the simulated curves showed observable deviation from the observed data. This can be attributed to the variation in actual and predicted compressibility functions, compared in Figure 9.9(c). The simulated settlement curve for QPSO showed 6.4% underprediction at 233 hours. PSO over-predicted the settlement at 130 hours by 1.23%. At 233 hours, HPSO underpredicted the settlement by 3.9%, while HABC showed 4% underprediction at 214 hours. MABC and ABC showed over-prediction at 31 hours, 4.1% and 5% respectively.

Based on the observations using synthetic settlement data as input, QPSO was observed to show less reliable responses. PSO tends to require more than 200 iterations to converge to better optimal values.

9.3.3 Back-estimation using experimental data

The experimental settlement data from AL15, TT50, TT60 and Kaolinite were used for inverse analysis in this part of the study. In the two-parameter optimisation problem for the back-prediction of hydraulic conductivity function parameters, the pre-definition of compressibility function limited the capacity of the algorithms to connect to the actual optimal values to some extent. In this section, the optimisation landscape is four-dimensional, with the compressibility function expressed in power form being back predicted along with the hydraulic conductivity in power form.

Table 9.4 shows the comparison of the predicted parameters and the best, worst and mean values of converged RMSE for multiple runs of the algorithms for various materials.

TH-3534_186104002

Table 9.4. Performance of different inverse analysis algorithms using Ng synthetic settlement data as the input for predicting the constitutive relation coefficients

Materials	Algorithm	RMSE			Iteration No.	Predicted Parameter Values			
						Compressibility function		Hydraulic conductivity function	
		Best	Worst	Mean		A(1/kPa)	C	P	M (m/s)
AL15	**PSO**	8.53E-04	9.20E-04	8.78E-04	125	3.091	-0.29	5.411	1.00E-10
	HPSO	8.88E-04	1.10E-03	1.02E-03	149	3.943	-0.370	5.123	1.38E-10
	QPSO	8.39E-04	1.08E-03	9.60E-04	81	3.164	-0.26	4.101	3.71E-10
	ABC	8.72E-04	8.87E-04	8.79E-04	186	3.082	-0.27	5.031	1.49E-10
	HABC	9.31E-04	9.45E-04	9.37E-04	152	4.035	-0.37	4.972	1.93E-10
	MABC	8.59E-04	9.07E-04	8.89E-04	74	3.058	-0.271	5.161	1.30E-10
Kaolinite	**PSO**	5.68E-04	7.31E-04	6.50E-04	133	4.677	-0.34	5.71	5.57E-10
	HPSO	5.62E-04	1.39E-03	9.36E-04	100	3.361	-0.231	6.169	3.11E-10
	QPSO	9.24E-04	1.21E-03	1.03E-03	36	3.218	-0.21	5.68	5.43E-10
	ABC	5.66E-04	7.31E-04	6.30E-04	50	4.523	-0.33	5.761	5.17E-10
	HABC	5.62E-04	6.04E-04	5.76E-04	152	4.425	-0.32	5.771	5.15E-10
	MABC	5.66E-04	5.96E-04	5.79E-04	70	3.301	-0.22	6.211	2.96E-10

TH-3534_186104002

Table 9.4. Performance of different inverse analysis algorithms using Ng synthetic settlement data as the input for predicting the constitutive relation coefficients (continuation)

Materials	Algorithm	RMSE Values			Iteration No.	Predicted Parameter Values			
						Compressibility function		Hydraulic conductivity function	
		Best	Worst	Mean		A(1/kPa)	C	P	M (m/s)
TT50	**PSO**	1.38E-03	1.38E-03	1.38E-03	195	2.01	-0.241	4.67	2.40E-09
	HPSO	1.27E-03	1.30E-03	1.28E-03	143	2.019	-0.250	5.121	1.99E-09
	QPSO	1.33E-03	1.74E-03	1.51E-03	138	3.016	-0.358	4.454	2.89E-09
	ABC	1.29E-03	1.30E-03	1.29E-03	108	1.719	-0.21	5.521	1.63E-09
	HABC	1.33E-03	1.37E-03	1.34E-03	150	1.751	-0.201	5.131	1.91E-09
	MABC	1.14E-03	1.15E-03	1.15E-03	84	2.008	-0.249	5.121	1.99E-09
TT60	**PSO**	6.13E-04	6.74E-04	6.50E-04	180	2.403	-0.300	4.228	1.62E-09
	HPSO	1.12E-03	1.22E-03	1.16E-03	141	2.001	-0.230	3.850	2.02E-09
	QPSO	7.22E-04	1.26E-03	9.44E-04	191	5.020	-0.500	4.383	1.71E-09
	ABC	7.71E-04	1.01E-03	8.68E-04	67	2.101	-0.241	4.115	1.78E-09
	MABC	8.55E-04	9.57E-04	9.23E-04	148	4.987	-0.481	3.911	2.20E-09
	HABC	8.82E-04	9.86E-04	9.25E-04	152	2.021	-0.259	4.002	1.99E-09

TH-3534_186104002

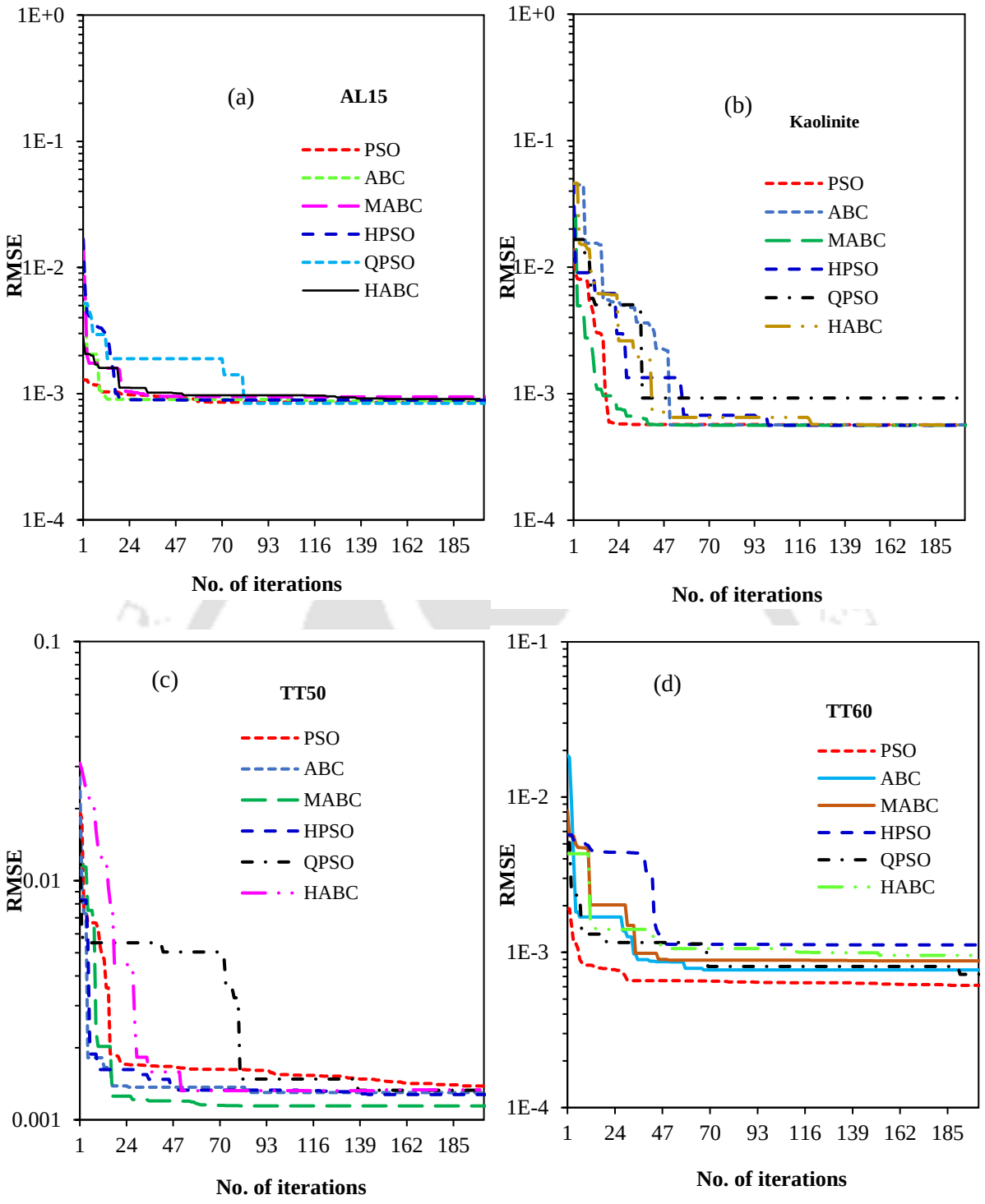


Figure 9.11 The objective function value (RMSE) versus the number of iterations plotted for the best run of each of the algorithms employed for inverse analysis using Ng experimental settlement data of (a) AL15 (b) Kaolinite (c) TT50 and (d) TT60

QPSO converged to the least RMSE value reported within 81 iterations in the case of AL15. The maximum difference observed in the converged RMSE is 11%, which is for the case of

TH-3534_186104002

MABC. For all other algorithms, this error was less than 5%, which essentially suggests that the converged RMSE values were within the same range.

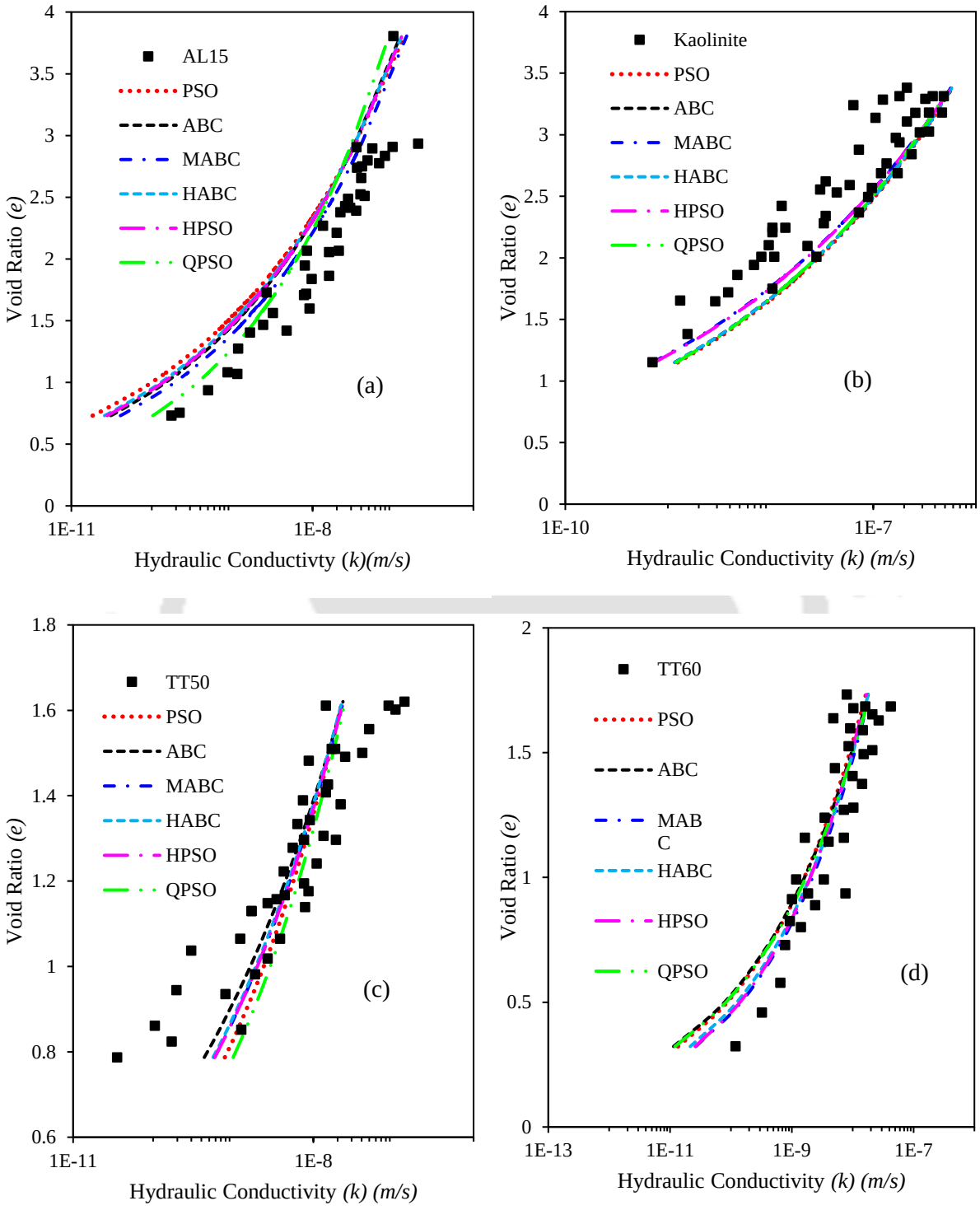


Figure 9.12. Comparison of hydraulic conductivity functions predicted using experimental Ng settlement data as input from various algorithms with corresponding actual values in the literature for samples of (a) AL15, (b) Kaolinite, (c) TT50 and (d) TT60

TH-3534_186104002

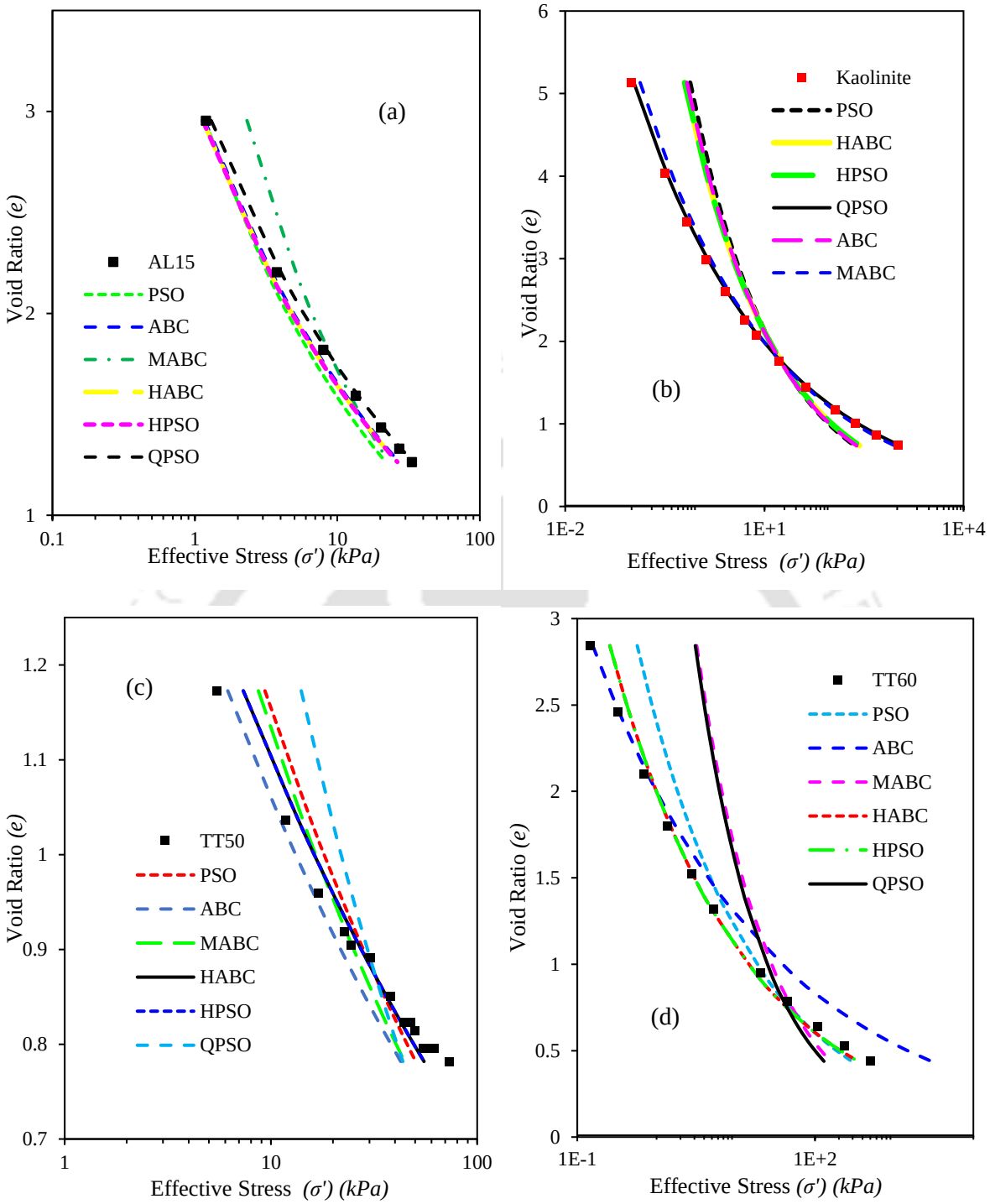


Figure 9.13. Comparison of compressibility functions predicted using experimental Ng settlement data as input from various algorithms with corresponding actual values in the literature for samples of (a) AL15, (b) Kaolinite, (c) TT50 and (d) TT60

These results are presented in Table 9.4. The considered data points were insufficient to show the final phase of consolidation, which resulted in pronounced variation in the compressibility function predictions (Figure 9.13 (a)).

TH-3534_186104002

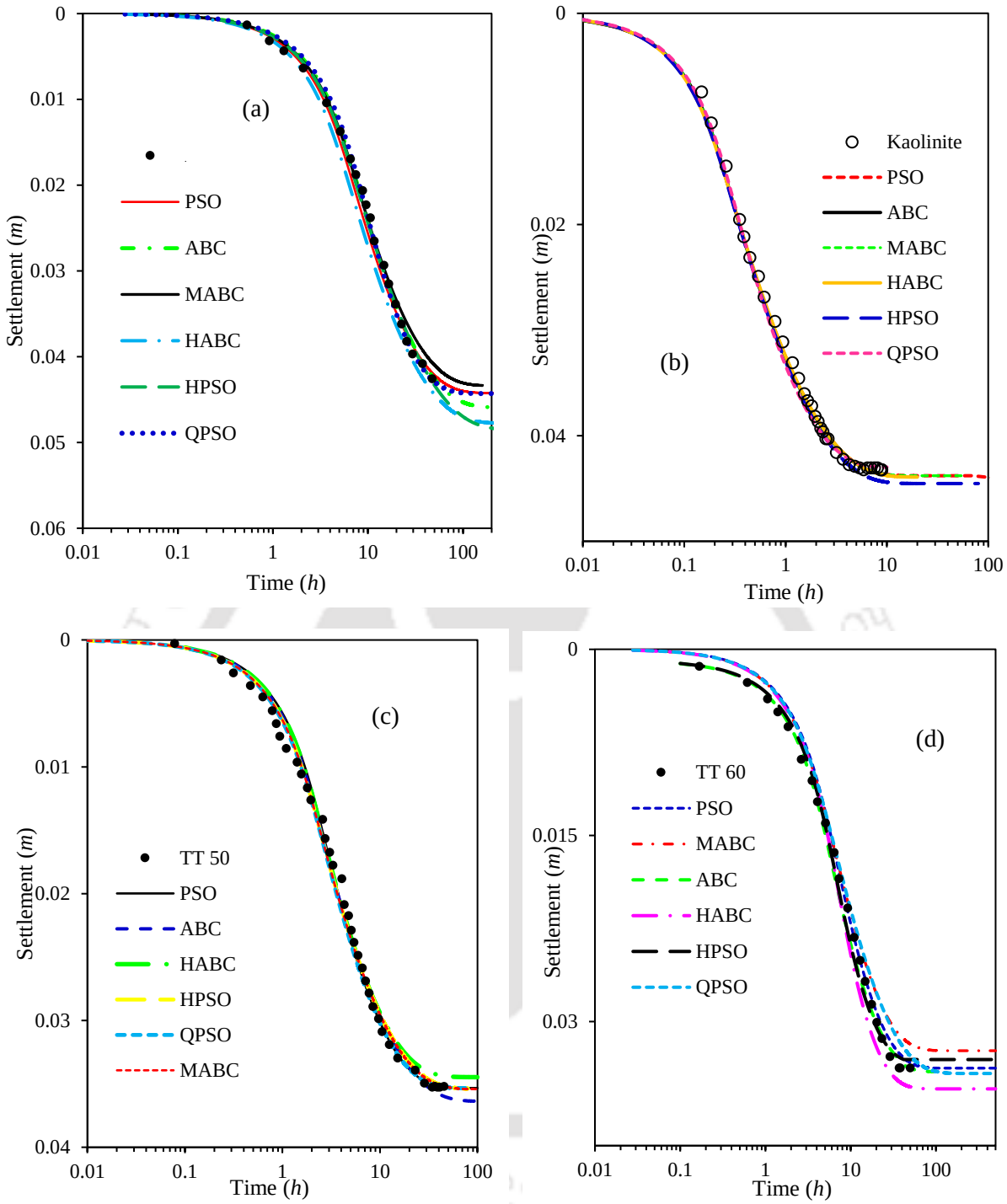


Figure 9.14. Comparison of experimental Ng settlement data points given as input for inverse analysis using the algorithms considered and settlement curves simulated using the constitutive function parameters predicted by inverse analysis for (a) AL15, (b) Kaolinite, (c) TT50 and (d) TT60

These variations were reflected in the simulated settlement behaviour (Figure 9.14 (a)). The predicted hydraulic conductivity function from QPSO was observed to match with a few of the reported points from the literature, while there was a deviation in the case of other predicted

TH-3534_186104002

functions. The percentage error in settlement values were high in certain cases. In the case of PSO, overprediction of 1.25% was experienced at 8.5 hours. For HPSO and QPSO, the error percentages were underprediction of 2.37% and 11.7% at 30 hours and 4 hours respectively. For HABC, ABC and MABC, these error values were 20% underprediction, 12% overprediction and 4.5% underprediction at 2 hours, 10 hours and 48 hours, respectively.

In the case of Kaolinite, a comparison of best-run RMSE showed that MABC and HPSO performed well compared to other algorithms. The worst RMSE value was that of QPSO. (Figure (9.11(b))). Only HABC showed robustness in the prediction of parameters. The hydraulic conductivity function, as shown in Figure 9.12(b), showed that the predicted hydraulic conductivity functions were comparable. In the Figure 9.13(b), the predicted compressibility functions were compared. Other than MABC and QPSO, predictions from all other algorithms deviated considerably from the actual data points. The percentage error in the case of PSO and ABC was at 0.15 hours, which is an over-prediction of 7.8% and 10%, respectively. The overprediction error for QPSO and HPSO are 10.5% and 4% at 1.2 hours and 9 hours, respectively. At 0.74 hours, MABC simulated 1.5% underprediction in the settlement behaviour of kaolinite, while at 3 hours, HABC underpredicted the settlement data by 1.42%.

The converged RMSE value for MABC was the lowest compared to the other five algorithms in the case of TT50 (Figure 9.11(c)). The largest converged RMSE value was reported for PSO. HABC and PSO showed reproducibility in results in this case. In the case of QPSO, reported RMSE values for three runs varied by large margins. The predicted hydraulic conductivity function values were within the same range (Figure 9.12(c)). However, considerable deviations were observed in the case of effective stress predictions in comparison with the actual data (Figure 9.13(c)), mainly in the case of QPSO. The predicted compressibility function, when not matching with the low effective stress values, is reflected as the variation in the initial settlement phase in the settlement curve. In case the predicted compressibility function mismatches with the actual data points for larger values of effective stress, then the final settlement phase of the simulated curves shows deviation from actual behaviour. (Figure 9.14(c)). Overprediction of settlement was reported for PSO, HPSO and QPSO at 4 hours by 9.5%, 10.6% and 11%, respectively. In the case of HABC, the maximum error was reported at 30 hours, resulting in an underprediction of 3.1%. MABC overpredicted the settlement values at 2.5 hours by 11.3%. The final settlement values simulated using the parameters from ABC overpredicted by 2.56% at 45 hours.

TH-3534_186104002

All the algorithms except QPSO showed a negligible difference between the mean, best and worst values of converged RMSE. It was observed that QPSO was yet to converge properly within the 200 iterations considered as shown in Figure 9.11(d). The predicted hydraulic conductivity functions were in the same range (Figure 9.12 (d)). However, the compressibility functions (Figure 9.13(d)) predicted deviated significantly from the actual value in the lower effective stress range for PSO, QPSO and HABC. This resulted in large deviations as high as 22% in the initial settlement phase, that is, up to 2.5 hours for these cases, as shown in Figure 9.14(d). Beyond this, the maximum error percentage for PSO was observed at 38 hours. The settlement value at this time point was underpredicted by 3.3%. MABC, on the other hand, overpredicted the settlement value at the same point by 7.12%. At 11 hours, HPSO overpredicted the settlement by 8.7%. While at 9 hours, ABC over-predicted the settlement by 8.65%. QPSO and HABC overpredicted the settlement values corresponding to hours and hours, respectively, by 7% and 4.75%.

These observations suggest that the proposed approach is reliable mainly for the accurate prediction of hydraulic conductivity parameters. However, further improvements can be made in the algorithms and objective function to focus specifically in the initial and final settlement phase so that the compressibility function can also be back-predicted with the same ease. In some cases, both the constitutive function parameters were accurately estimated by some algorithms.

9.3.4 Summary

The expedited approach for the back estimation of the constitutive function parameters was explored in this part of the study. All the algorithms were observed to showcase comparable performances. ABC-based algorithms were more consistent and robust than PSO-based algorithms. MABC was observed to show improved performance in comparison with conventional ABC, while HABC was seen to provide robust converged RMSE values. The same iteration ratio for *fminsearch* and ABC was used for all the cases. Varying this ratio appropriately can further improve the performance of this algorithm. QPSO was observed to converge more quickly than PSO and HPSO. However, certain predicted results deviated considerably from the observed values when QPSO was employed. HPSO, though faster than PSO and showed good consistency, has the potential to be further improved by varying the iteration ratio for *fmincon* and PSO. In certain cases, PSO and QPSO failed to converge within the maximum iteration number considered.

TH-3534_186104002

9.4. Strategies for Reliable Optimal Solutions

Based on the observations from sections 9.2 and 9.3, it is understood that the performance of individual algorithms doesn't guarantee proper convergence to the most optimal solution set. Consistent convergence of any algorithm to the best possible solution set for all the materials considered is an ideal scenario.

Some of the aspects that can be considered to improve the performance of these algorithms include the consideration of an improved objective function, which magnifies the contribution to the error from the initial and final settlement phases so that compressibility functions can be appropriately predicted. During data collection from centrifuge optimisation, it is possible that a few initial points are lost due to the time consumed by the instrument to attain balance. These points can be appropriately replaced by curve fitting methods before inverse analysis. An increased number of iterations and multiple run cycles can be adopted to arrive at the best possible set of solutions, provided sufficient computational resources are available. The hybrid optimisation algorithms discussed in this study showed good reliability. These algorithms can be efficiently used by running multiple runs with varying iteration ratios. A more reliable approach would be running two algorithms simultaneously and arriving at the optimal solution set by comparing the predictions from these algorithms.

The present chapter tested and validated inverse analysis of constitutive function parameters from centrifuge-based temporal settlement data, using six optimisation algorithms. The efficient optioins from these six optimisation algorithms are used in the next chapter for inverse analysis exercise, considering the pore pressure dissipation data as input.

TH-3534_186104002

10 Inverse Analysis Using Pore Pressure Data

10.1 General

In this chapter, the hydraulic conductivity function parameters are back predicted using the pore pressure variation data from the FSC tests. These data can be easily obtained using pore pressure transducers or piezometers attached to specific locations in the testing cylinder. Chapters 7 to 9 discussed various graphical and optimisation algorithm-based approaches for back estimation of hydraulic conductivity characteristics from the settlement versus time data points. In the present Chapter, these methods were applied to excess pore pressure or total pore pressure dissipation data for the base of the settling samples. These approaches are suitable for use when dealing with slurries that exhibit high levels of turbidity, which hinders the precise monitoring of the movement of the settling border. Pore pressure transducers attached to the base of the sample can digitally monitor the pressure data with better accuracy than the manually monitored settlement data.

In the first section of this chapter, the graphical method of inverse analysis is used to back-predict the hydraulic conductivity function parameters from the 1g base excess pore pressure data. In the second section, optimisation algorithms were used for the inverse analysis of the hydraulic conductivity coefficients. Two sets of synthetic cases were used to test these approaches, and two published experimental data sets were used for validation.

The third section presents the back estimation of hydraulic conductivity function parameters from base total pore pressure dissipation data from centrifuge FSC tests. The inverse analysis is performed using metaheuristic optimisation algorithms. Two synthetic and one experimental data case were used to explore the performance efficiency of these algorithms.

10.2 Inverse Analysis Using Graphical Approach

10.2.1 General

The inferences from Chapter 7 showed the superiority of Method 1 when limited data points were available. Therefore, in this section, the graphical approach- Method 1- was used to back estimate hydraulic conductivity function parameters. The method is based on the observation that the geometric features of the pore pressure versus the log-time curve for the base of the column were influenced by the multiplier and power values of the hydraulic conductivity function, expressed in the power form. The shape of the pore pressure dissipation curve was observed to be dependent on the power, while the multiplier value influenced the position of

TH-3534_186104002

the curve along the log-time axis. The graphical method for back analysis was tested on synthetic pore pressure data simulated using the finite difference solution of the concerned governing equation for two slurry materials. The method is relatively simple, robust, computationally inexpensive, and can be used for a quick estimation of hydraulic conductivity function parameters of slurries.

10.2.2 Inverse Analysis Using Synthetic Data

Synthetic excess pore pressure dissipation data were generated for Phosphatic Clay and Antwerpen Slurry using the forward analysis MATLAB code by adding white noise to the simulated data. The data set for the Antwerpen slurry had 12 data points, and the data set for Phosphatic Clay consisted of 13 points. Five pairs of *(M, P)* were used to generate arbitrary dissipation curves for Antwerpen slurry, while four pairs of *(M, P)* values were used in the case of Phosphatic Clay, as shown in Figure 10.1 (a) and 10.1 (b). Other input properties for these cases were taken from Table 4.2.

Table 10.1 Hydraulic conductivity function parameters predicted from synthetic base excess pore water pressure data using the graphical method

Materials	**Initial Guess values**				**Predicted Values**	
	M_1	**P_1**	**M_2**	**P_2**	**M**	**P**
Antwerpen slurry	1E-07	9	1E-11	3	1.998E-09	8.017
	1E-07	9	1E-10	4	1.888E-09	8.088
	1E-07	9	1E-09	5	1.818E-09	8.135
	1E-07	9	1E-08	7	1.671E-09	8.262
			Average of predicted values		1.844E-09	8.125
Phosphatic Clay	1E-08	7	1E-12	3	2.071E-11	3.996
	1E-08	7	1E-10	4	1.097E-11	4.209
	1E-09	6	1E-12	3	1.798E-11	4.041
	1E-09	6	1E-10	4	1.103E-11	4.205
			Average of predicted values		1.517E-11	4.112

The optimal *M* and *P* values were obtained from various combinations of these arbitrary *(M, P)* pairs to check the robustness of the method, as given in Table 10.1. For each of the slurries, four combinations were tested. For each slurry, various combinations resulted in optimal values in close proximity.

TH-3534_186104002

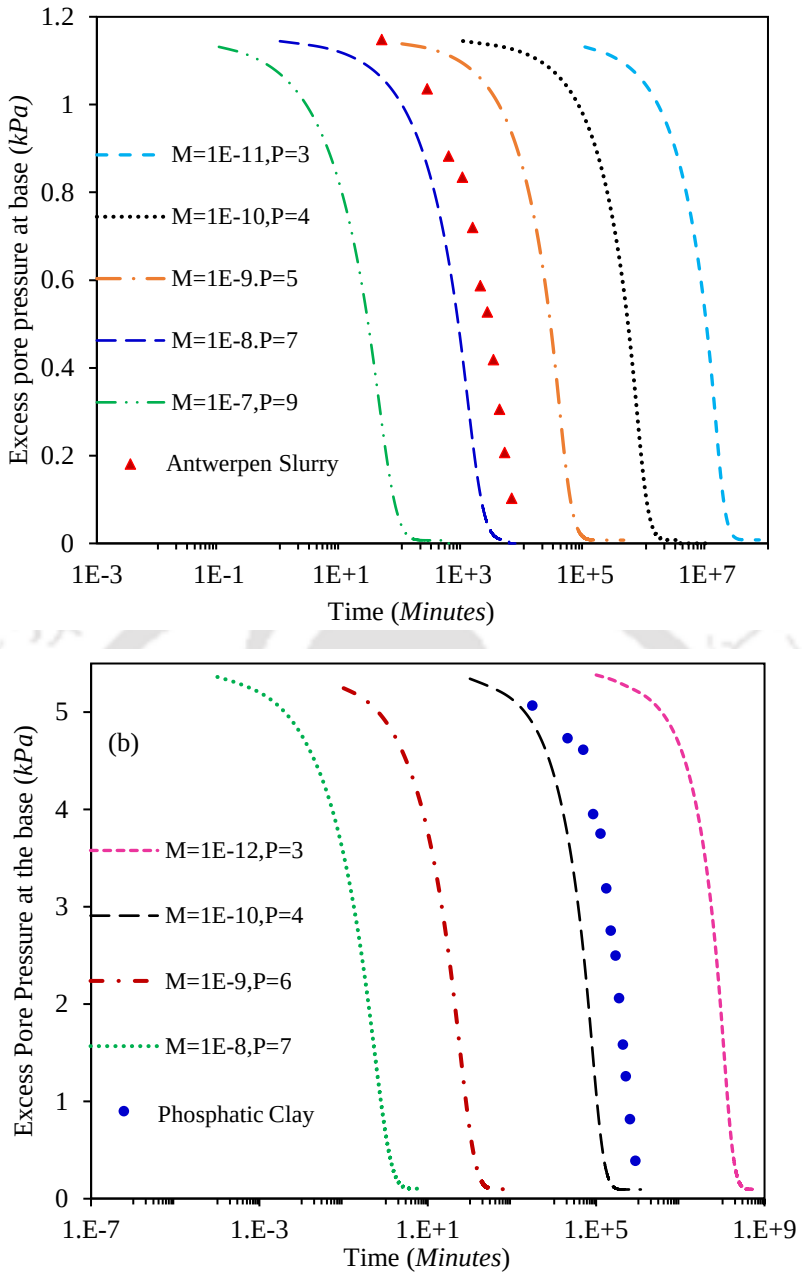


Figure 10.1. Base excess pore pressure dissipation curves simulated using various initial guess values, and the synthetic data sets simulated for (a) Antwerpen Slurry and (b) Phosphatic Clay

The average of optimal values from various combinations was (1.844 x10^{-9} m/s, 8.125) for Antwerpen Slurry and (1.517x10^{-11} m/s, 4.112) for Phosphatic Clay. The average values for the multiplier and power were observed to be almost equal to the parameter values used to generate the simulated curves from which synthetic data sets were derived for both slurries. The average of predicted *M* and *P* values for both cases were used to simulate the base excess pore water pressure dissipation curves. These simulated curves were compared with the synthetic data points used for the analysis, as shown in Figures 10.2 (a) and 10.2 (b).

TH-3534_186104002

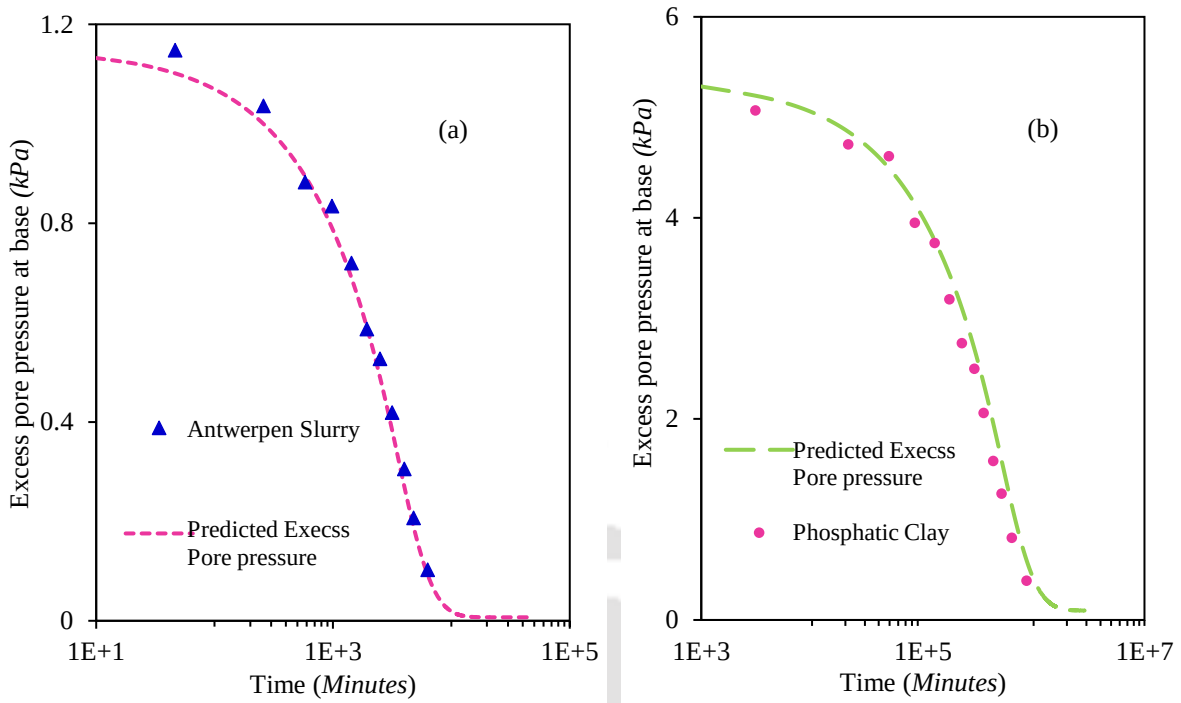


Figure 10.2. Comparison of base excess pore pressure dissipation data simulated using the average of predicted values of hydraulic conductivity parameters with the synthetic data for (a)Antwerpen slurry (b) Phosphatic Clay

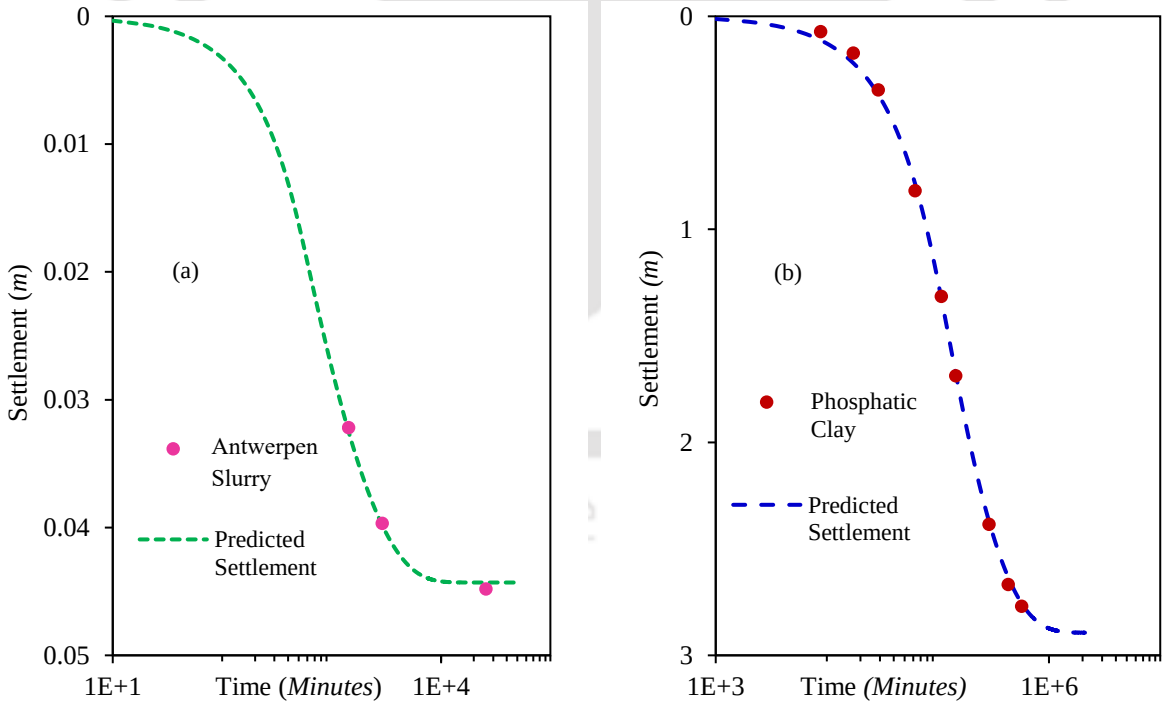


Figure 10.3. Comparison of settlement curve simulated using the average of predicted values of hydraulic conductivity parameters with the settlement data from the literature for (a)Antwerpen slurry and (b) Phosphatic Clay

TH-3534_186104002

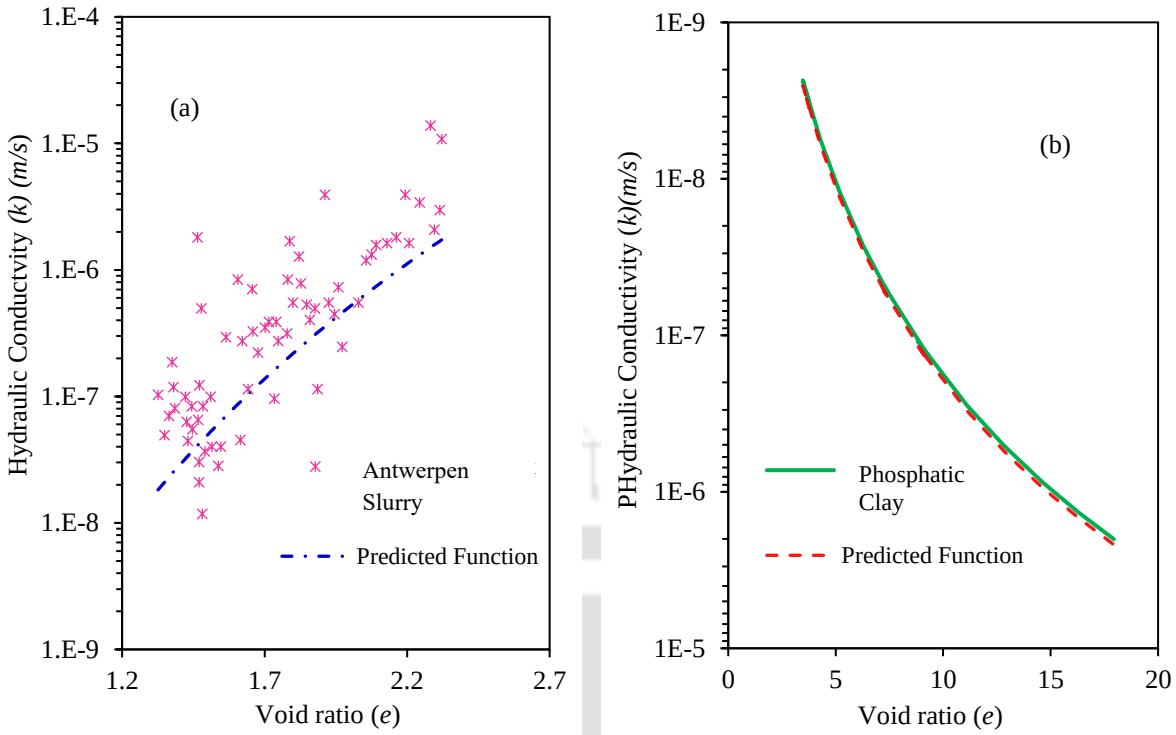


Figure 10.4. Comparison of the average of predicted permeability functions with the data from the literature for (a) Antwerpen slurry and (b) Phosphatic Clay

For both cases, the predicted behaviour showed variation from the synthetic data set in the initial time period. For Antwerpen slurry, an under-prediction of 3.6% of the expected synthetic data value was reported at about 47 minutes. For Phosphatic Clay, a general over-prediction tendency was observed throughout the time of consolidation, having a maximum value of nearly 7% at about 17,000 minutes. These variations could be due to the white noise effect or error during the digitisation of the arbitrary simulated curves used in the analysis. It was observed that the average of predicted M and P values could appreciably simulate the settlement behaviour of the slurries. The comparison between the settlement data from the settling column test on the slurries from the literature and the settlement curves obtained by numerical simulation using the average of predicted M and P values obtained using the graphical method showed a good matching (Figures 10.3 (a) and 10.3 (b)). Figure 10.4 (a) shows the comparison of the predicted hydraulic conductivity function using the average optimal values of M and P with the data points from the literature for Antwerpen slurry. The predicted function was observed to represent the general trend of the observed data set. The hydraulic conductivity function fitted to constant strain rate test data given in the literature was compared with the predicted hydraulic conductivity function in Figure 10.4 (b) for the Phosphatic Clay. A good correlation was observed in the comparison.

TH-3534_186104002

10.2.3 Inverse Analysis Using Experimental Data

The increase in settlement is also associated with a simultaneous reduction in excess pore pressure data. Therefore, the pore pressure dissipation for any given point in a sample plotted against time during the process of consolidation should also show similar behaviour as that of settlement curves. The advantage of considering the excess pore pressure values over settlement values is that the measurements can be made free of personnel errors as the measurement of pore pressure is fully digitised (pore pressure transducers can be used).

Table 10.2 Hydraulic conductivity function parameters predicted from experimental base excess pore water pressure data using the graphical method

Materials	Initial Guess values				Predicted Values	
	M_1	P_1	M_2	P_2	M	P
AS-II	5.70E-09	6	5.70E-07	3	2.69E-08	5.321
	5.70E-09	7	5.70E-07	3	2.03E-08	5.692
			Average of Predicted Values		2.36E-08	5.507
Gold Tailings	3.50E-08	5	3.50E-06	3.3	3.27E-07	3.912
	3.50E-08	5	3.50E-06	2	3.55E-07	3.821
			Average of Predicted Values		3.41E-07	3.865

In this study, the excess pore pressure variation with time observed at the base of settling column tests was used to estimate the hydraulic conductivity. The study used two experimental data taken from the literature- AS-II and Gold Tailings. The variation of excess pore pressure with time at the base of the sample was considered for this study.

The pore pressure curve was simulated using three different combinations of *M* and *P* as an initial guess, and two sets of output values of *M* and *P* were obtained to validate the result. Initial guesses of *M* and *P* were selected such that the curves simulated using these lie on either side of the experimental curve. The initial values used for the simulation of M and P and the final values obtained for *M* and *P* are given in Table 10.2. The simulated curve with guessed values of *M* and *P* are presented in Figure 10.5. The final obtained values of *M* and *P* are reported as the average of the values obtained from two combinations of initial guess values.

TH-3534_186104002

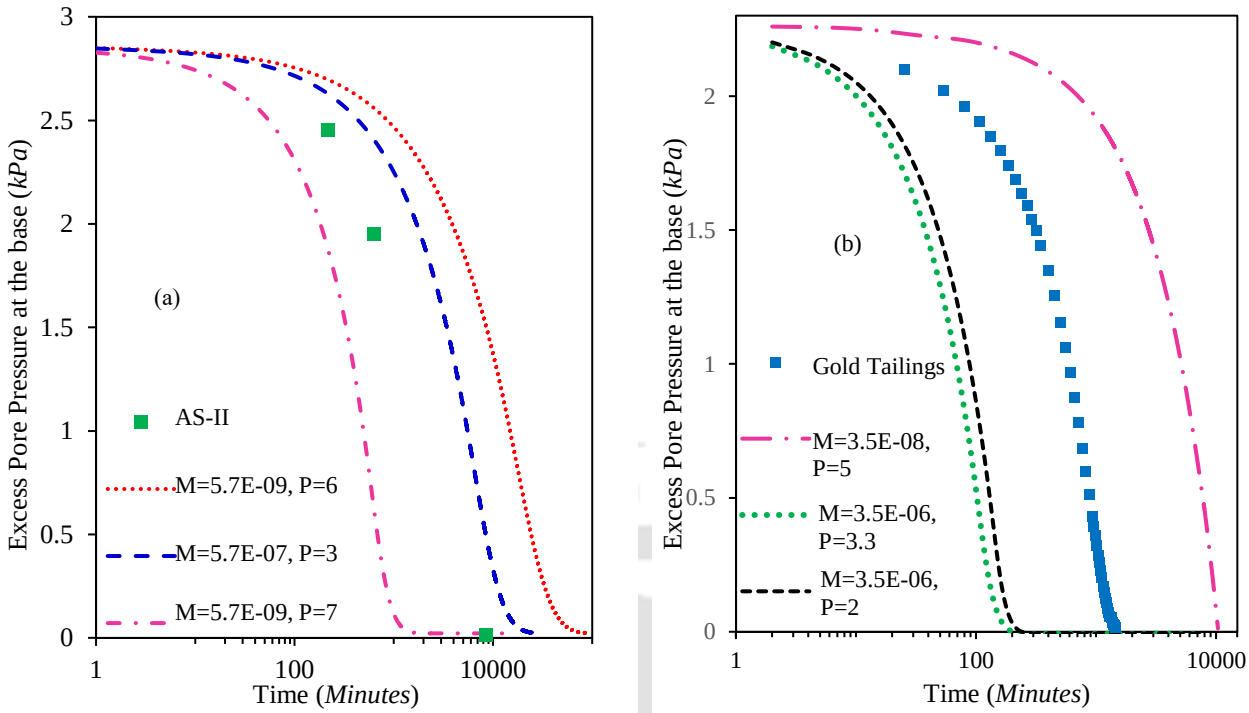


Figure 10.5 Base excess pore pressure dissipation curves simulated using various initial guess values and the synthetic data sets simulated for (a) AS-II (b) Gold Tailings

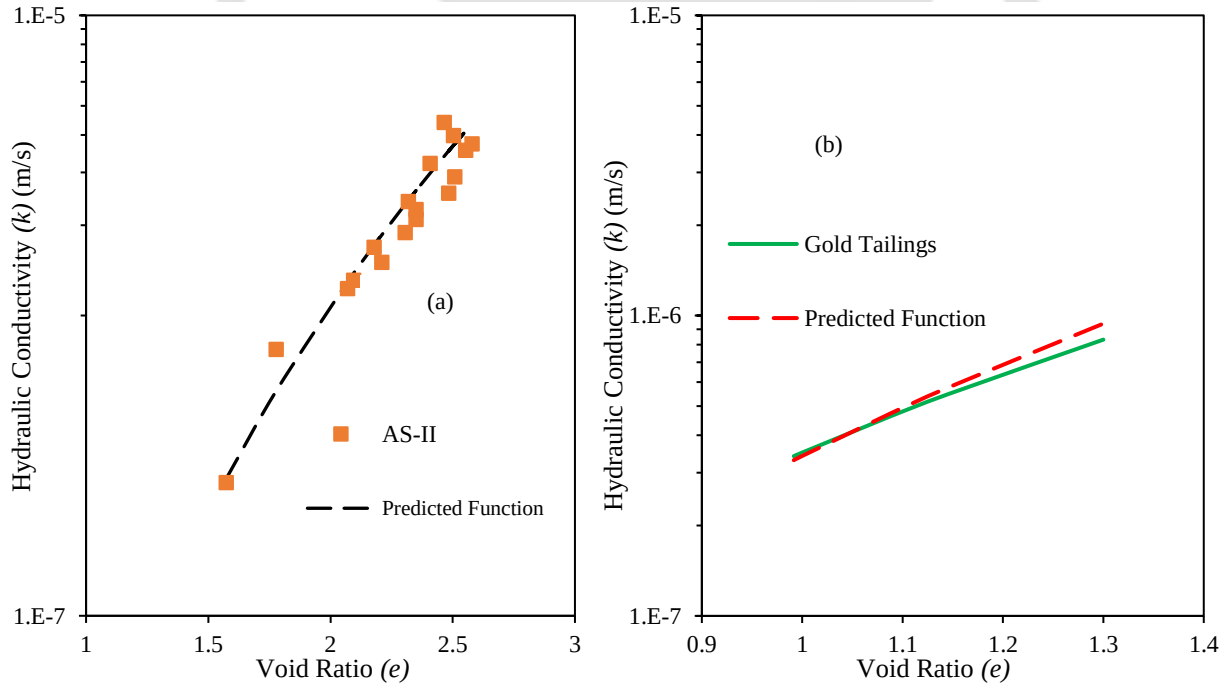


Figure 10.6 Comparison of the average of predicted permeability functions with the data from the literature for (a) AS-II and (b) Gold Tailings

TH-3534_186104002

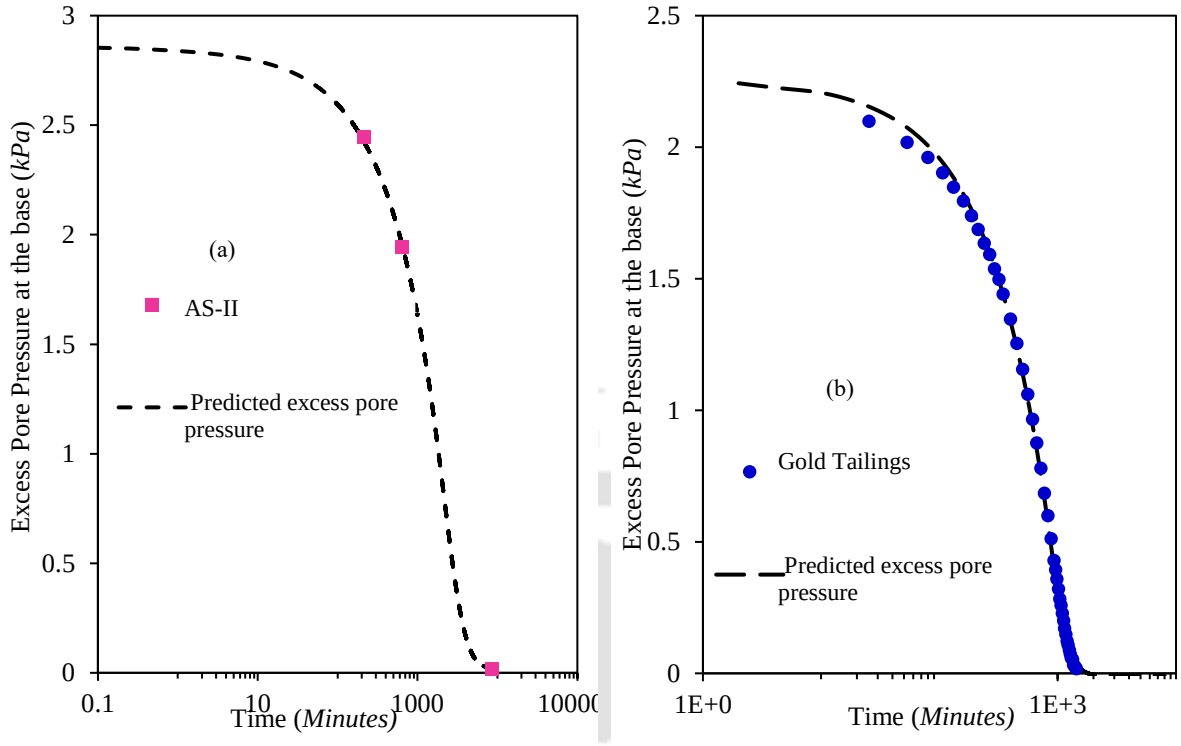


Figure 10.7 Comparison of base excess pore pressure dissipation data simulated using the average of predicted values of hydraulic conductivity parameters with the experimental data for (a) AS-II (b) Gold Tailings

Using the obtained value of *M* and *P*, hydraulic conductivity functions were plotted and compared with the actual data in Figure 10.6. The excess pore pressure dissipation curves for AS-II and Gold Tailings were simulated using the predicted parameters and compared in Figure 10.7 (a) and (b). In the case of AS-II, the predicted pore pressure curve matched the actual data well. In the case of Gold Tailings, the simulated pore pressure curve slightly varied in the initial phase of consolidation.

10.2.4 Summary

At the base of a slurry sample undergoing self-weight consolidation, excess pore water pressure variation with time was found to have features similar to the settlement versus time curve. The position and shape of the dissipation curve with respect to the logarithm of the time axis are influenced by the multiplier (*M*) and power *(P)* values, respectively. Optimal multiplier and power values are obtained with as little as two forward analyses using arbitrary initial guess parameters without requiring optimisation or objective function computations. The settlement curve and excess pore pressure dissipation curves simulated using predicted hydraulic

TH-3534_186104002

conductivity functions showed good matching with the experimental data and synthetic data, respectively. The predicted hydraulic conductivity functions showed a good fit with experimental data for one case and excellent matching with corresponding data from the literature. The graphical method of inverse analysis is a quick and robust technique for the estimation of hydraulic conductivity function parameters from simple laboratory measurements.

10.3 Back-estimation using Optimisation Algorithms

10.3.1 General

In this section, the hydraulic conductivity function coefficients are back estimated using PSO, ABC, HABC, MABC, HPSO and QPSO. These algorithms were successful in the optimisation landscape based on settlement data. In this section, the base excess pore pressure dissipation data from two synthetic data sets and two experimental data sets were used to test and validate the approaches. The comparison of the performance efficiency of the algorithms considered was also presented.

10.3.2 Configuration of tuning parameters

The forward analysis function utilised for calculating the objective function values is computationally costly. Hence, the optimisation algorithms aim to achieve strong convergence in the fewest iterations by utilising smaller populations. A study was conducted on the performance of six algorithms, focusing on the objective function values and the convergence. Each of the material cases underwent three runs of each algorithm. The search space was defined by maintaining suitable upper and lower limits. All of the PSO and HPSO cases retained their respective personal learning and social learning coefficients of 1.5 and 2, respectively. The inertia weight was initially set at 0.9. The population size of the swarm was consistently maintained at 40 for all instances. The ABC, MABC, and HABC algorithms employed a colony size of 80, which included both employed and observer bees for all circumstances. The maximum improvement threshold for each solution was set at 50 for ABC. The performance-related, user-defined parameters for QPSO encompass the swarm size and the contraction expansion factor. The number of individuals in the swarm that was taken into account was 40. The contraction expansion factor was computed using Equation (4.49). The values of $\alpha 1$ and $\alpha 2$ for this computation were selected as 0.01 and 0.1, respectively.

The maximum number of iterations was 70. Additional trials were conducted with larger numbers of iterations. However, the findings demonstrated minimal improvement in most cases

TH-3534_186104002

beyond 70. The PSO and *fmincon* algorithms were run for 20 iterations each in the case of HPSO. The number of iterations for ABC and *fminsearch* algorithms were both set to 20 for HABC.

10.3.3 Back-prediction Using Synthetic Pore Pressure Data

Two sets of synthetic data points were generated by adding white noise to the excess pore pressure dissipation data simulated for Antwerpen Slurry and Phosphatic Clay samples. The properties of these materials are given in the Table 4.2. The boundary conditions considered were free drainage at the top and impervious boundary at the bottom. The void ratio at the top solid-liquid boundary is assumed to be constant throughout. The impermeable boundary experiences no relative movement of solid and fluid particles, while no excess fluid pressure exists in the free-draining boundary.

Table 10.3. Performance of different inverse analysis algorithms using synthetic excess pore pressure data as the input for predicting the Power (P) and Multiplier (M) parameters

Materials	Algorithms	RMSE Value			Iteration	Predicted values	
		Best	Worst	Mean	No.	P	M (m/s)
Antwerpen Slurry	PSO	0.0165	0.0201	0.0183	17	7.644	2.20E-09
	ABC	0.0165	0.0377	0.0239	10	7.544	2.31E-09
	QPSO	0.0168	0.0196	0.0181	38	7.378	2.55E-09
	HPSO	0.0164	0.0181	0.0171	43	7.627	2.22E-09
	MABC	0.0165	0.0173	0.0179	10	7.628	2.21E-09
	HABC	0.0166	0.0176	0.0169	23	7.627	2.22E-09
Phosphatic Clay	PSO	0.0945	0.0952	0.0946	42	3.745	3.29E-11
	ABC	0.0947	0.0951	0.0946	15	3.740	3.33E-11
	QPSO	0.0953	0.1305	0.1090	11	3.813	2.75E-11
	HPSO	0.0943	0.0981	0.0959	8	3.748	3.27E-11
	MABC	0.0950	0.0976	0.0964	5	3.749	3.26E-11
	HABC	0.0949	0.0993	0.0971	9	3.748	3.27E-11

The objective function values for inverse analysis were calculated using Equation (4.41). The errors were calculated using the settlement values in meters. Among the three runs of each

TH-3534_186104002

algorithm, the best run was determined as the one in which the algorithm achieved convergence to the lowest possible objective function value within the fewest number of iterations.

The performances of various algorithms were compared based on the best, worst, and mean RMSE values and the speed of convergence of the best run. The excess pore pressure measurements for the materials considered for the study based on settlement data were not available in the literature. Therefore, for comparison and for testing the efficiency of the proposed approaches, two synthetic data cases were formulated using the material properties of Antwerpen Slurry and Phosphatic Clay.

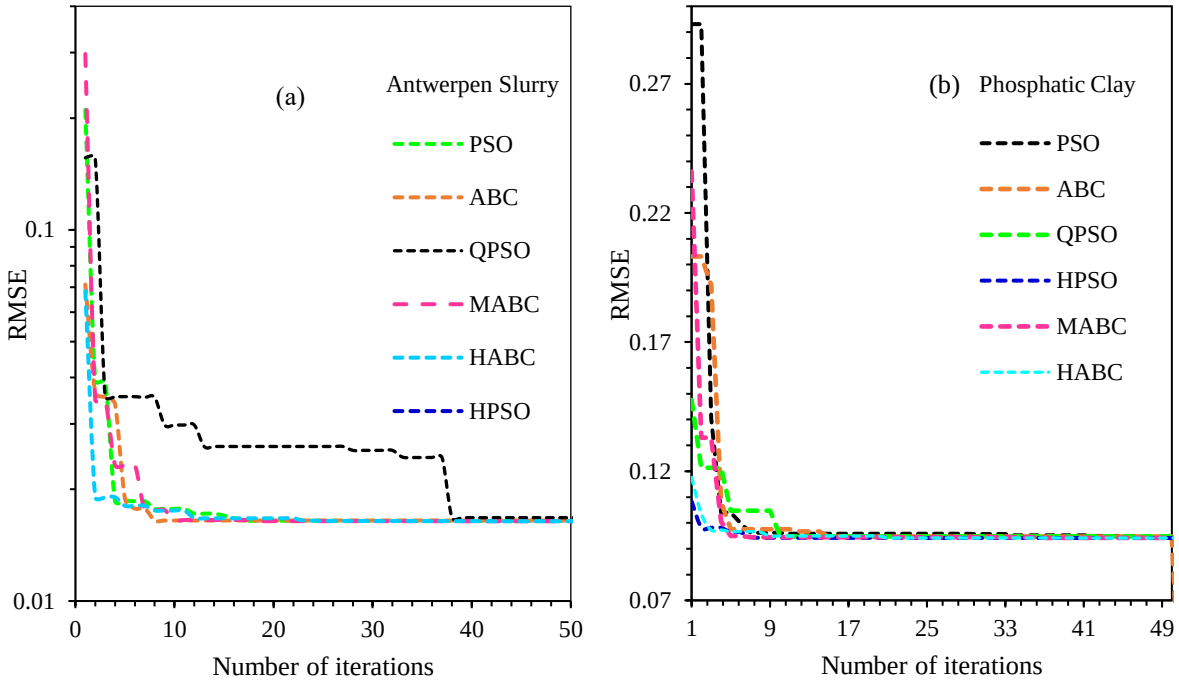


Figure 10.8. Comparison of the objective function value (RMSE) with progressing iterations of the best of three runs of the inverse analysis algorithms using synthetic excess pore pressure data for (a) Antwerpen Slurry and (b) Phosphatic Clay.

The excess pore pressure values at the base of the sample, at different time intervals, were first simulated using known material properties. Sufficient data points were taken from the simulated continuous dissipation curve, and the corresponding excess pore pressure values were tweaked by 5% so that the resultant data set could represent experimental data. These data were used as input for the inverse analysis algorithms.

Mean, worst, and best objective function values calculated using Equation (4.49) were compared for all the algorithms for these cases in Table 10.3. The objective function values are in kilopascal. For each slurry, the best RMSE values obtained by all the algorithms were

TH-3534_186104002

comparable. The worst objective function value for Antwerpen Slurry was twice the lowest RMSE, and the mean value was around 1.5 times the best value when ABC was used for inverse analysis. The worst RMSE value was 1.4 times the best value for Phosphatic Clay when QPSO-

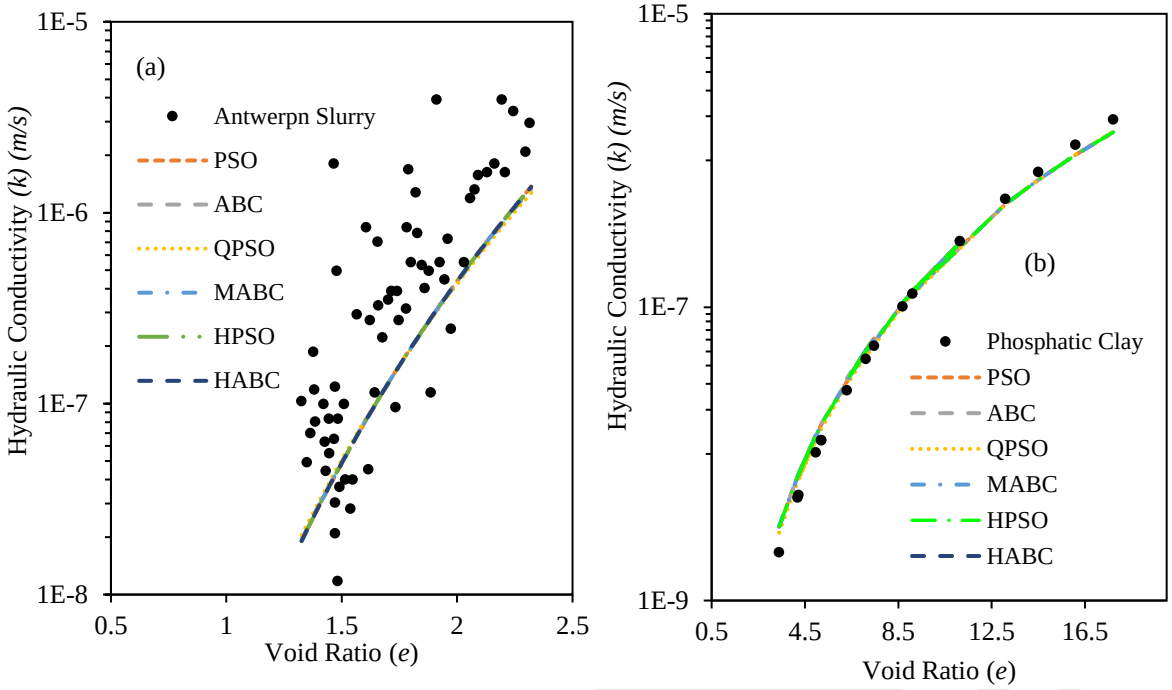


Figure 10.9 Comparison of hydraulic conductivity functions for synthetic excess pore pressure data cases (a) Antwerpen Slurry (b) Phosphatic Clay

was used. These instances indicate premature convergence to local optima in the corresponding runs. The HABC and HPSO gave robust results in all cases. The plots for convergence with iteration number are shown in Figures 10.8(a) and (b). The optimal values of *M* and *P* were plotted as hydraulic conductivity functions and compared with the corresponding literature data, as shown in Figures 10.9 (a-b). The comparison demonstrated a strong correlation. The optimised values of *M* and *P* were in the same range as predicted using the experimental settlement data of these materials. These parameters were used to simulate settlement curves and pore pressure dissipation curves for Antwerpen Slurry and Phosphatic Clay. Figures 10.10(a-b) compare the predicted excess pore pressure dissipation curves with the synthetic data points taken as the input for inverse analysis. The simulated dissipation curves from all the algorithms underpredicted the excess pore pressure value at 3700 hours by nearly 8.5% (equivalent to 0.24 kPa) for Phosphatic Clay. The ABC algorithm overpredicted the dissipation data at 32 hours by 6.8% (equal to a difference of 0.04 kPa), while the other algorithms overpredicted by 6.5% (equal to a difference of 0.037kPa) in the case of Antwerpen Slurry.

TH-3534_186104002

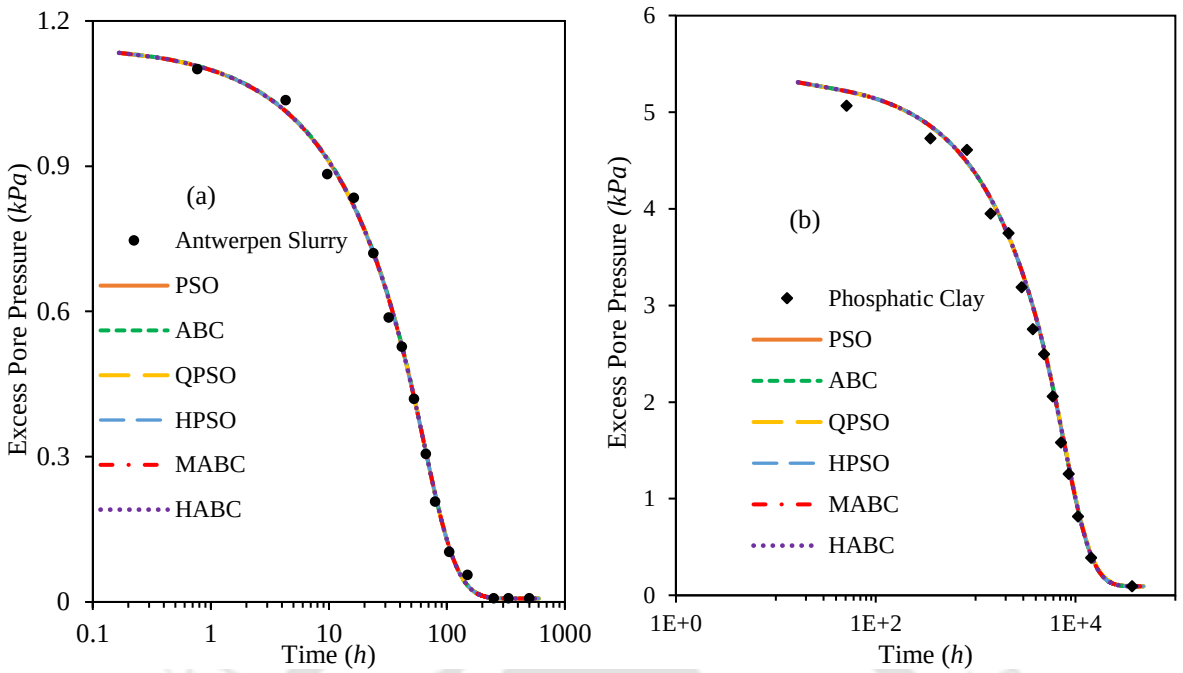


Figure 10.10. Comparison of settlement versus time data in the literature and the curves simulated using the hydraulic conductivity function parameters predicted by inverse analysis from excess pore pressure data for (a) Antwerpen Slurry and (b) Phosphatic Clay

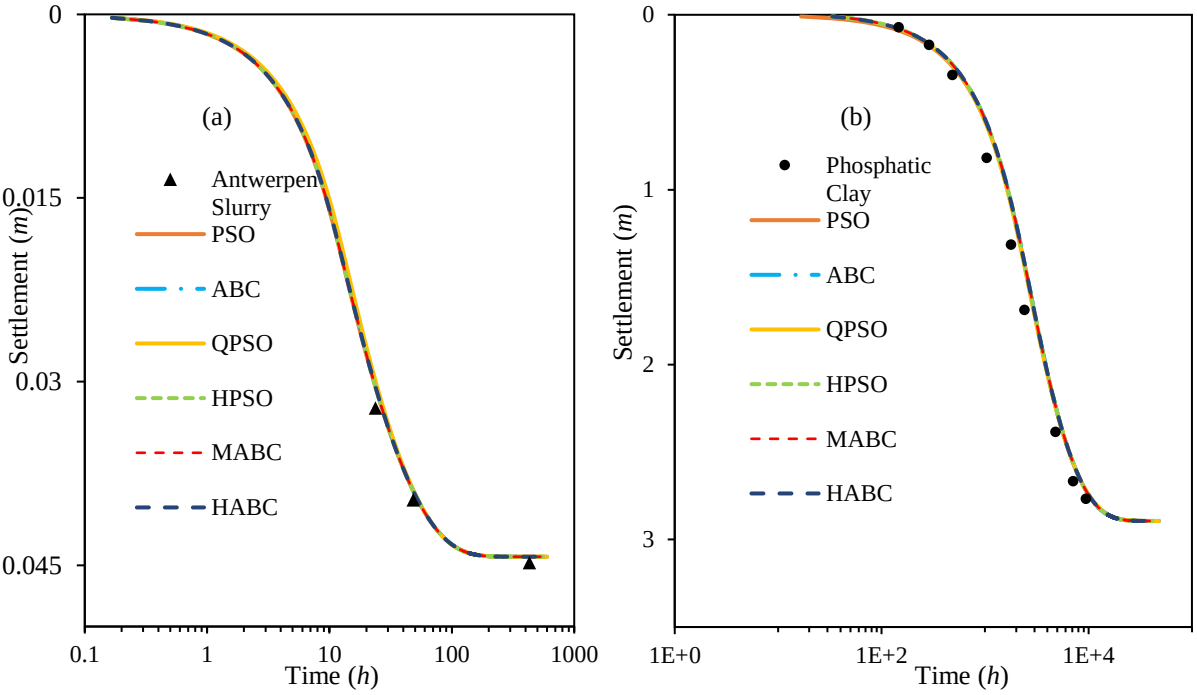


Figure 10.11. Comparison of excess pore pressure dissipation data points given as input for inverse analyses and the curves simulated using the hydraulic conductivity function parameters predicted by inverse analysis for a) Antwerpen Slurry, (b) Phosphatic Clay, (c) Gold Tailings and (d) AS-2

TH-3534_186104002

The settlement versus time curves were simulated using the optimised hydraulic conductivity function parameters. The resulting curves are compared with the experimental settlement data in Figure 10.11 (a-b). It was observed that though an overall matching persisted between the predicted settlement curves and the observed data points, the maximum percentage error values were higher in this case compared to the same in the case of inverse analysis using settlement data. The parameters from QPSO generated an under-prediction of 8.5%, while the same from ABC resulted in an under-prediction of 7.6%, and the other algorithms under-predicted by 7% for the time point of 23 hours in the case of Antwerpen Slurry. The error was as high as around 14% in the case of Phosphatic Clay when parameters from QPSO were used, while the same was around 15% for all the other algorithms at 2400 hours, resulting in under-prediction of settlement values.

10.3.4 Inverse Analysis Using Experimental Pore Pressure Data

The pore pressure data for the base of AS-2 and Gold Tailings were used for inverse analysis. The comparison of resulting objective function values for various algorithms is presented in Table 10.4. The RMSE values at different iterations for these materials are shown in Figure 10.12 (a-b). The algorithms HPSO, HABC, and MABC were giving robust results.

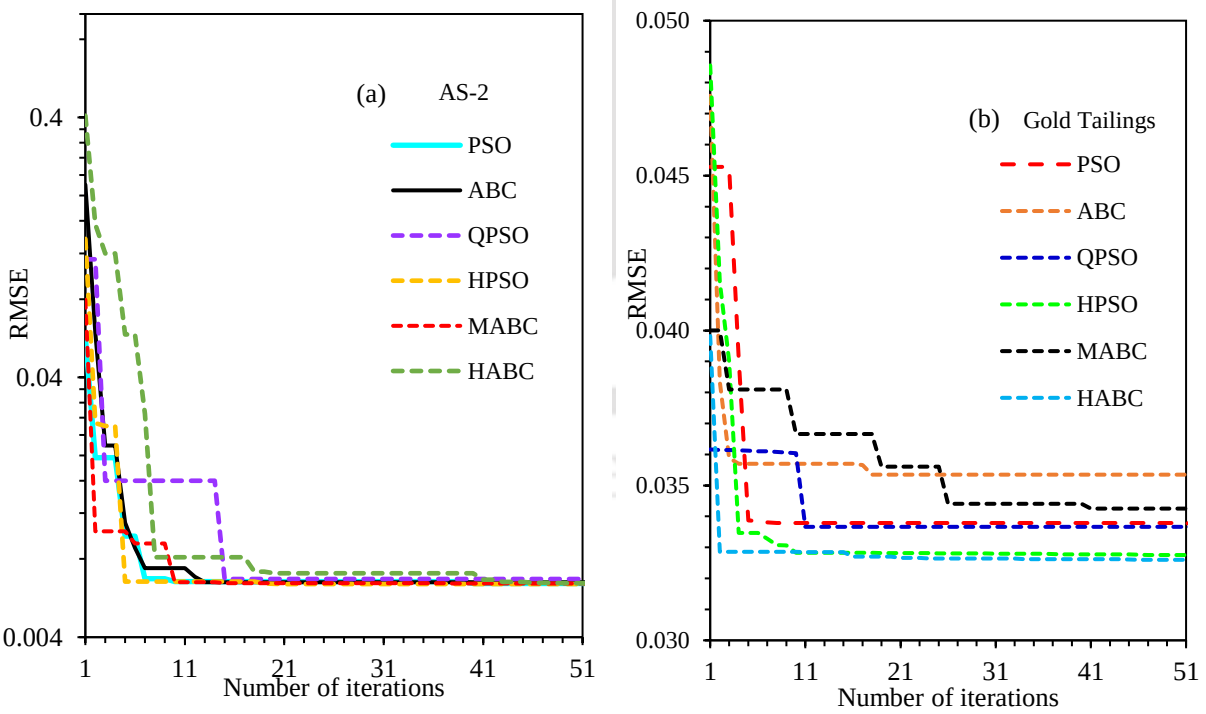


Figure 10.12. Comparison of the objective function value (RMSE) with progressing iterations of the best of three runs of the inverse analysis algorithms using experimental excess pore pressure data for (a) AS-2 and (b) Gold Tailings

TH-3534_186104002

Table 10.4 Performance of different inverse analysis algorithms using experimental excess pore pressure data as the input for predicting the Power (P) and Multiplier (M) parameters

Material	Algorithm	RMSE Value			Iteration No.	Predicted values	
		Best	Worst	Mean		P	M (m/s)
Gold Tailings	PSO	6.40E-03	1.31E-02	9.70E-03	41	3.616	3.18E-07
	ABC	6.50E-03	6.70E-03	6.60E-03	16	3.784	3.08E-07
	QPSO	6.70E-03	1.17E-02	9.90E-03	15	3.585	3.20E-07
	HPSO	6.40E-03	6.70E-03	6.60E-03	24	3.643	3.17E-07
	MABC	6.40E-03	6.50E-03	6.50E-03	40	3.646	3.16E-07
	HABC	6.50E-03	6.50E-03	6.50E-03	42	3.581	3.20E-07
AS-2	PSO	3.36E-02	3.67E-02	3.48E-02	10	3.13	1.42E-07
	ABC	3.53E-02	3.60E-02	3.57E-02	18	3.51	1.03E-07
	QPSO	3.36E-02	1.06E-01	5.97E-02	11	2.948	1.65E-07
	HPSO	3.28E-02	3.40E-02	3.34E-02	28	2.575	2.25E-07
	MABC	3.42E-02	3.42E-02	3.42E-02	41	2.488	1.05E-07
	HABC	3.27E-02	3.27E-02	3.27E-02	23	2.463	2.47E-07

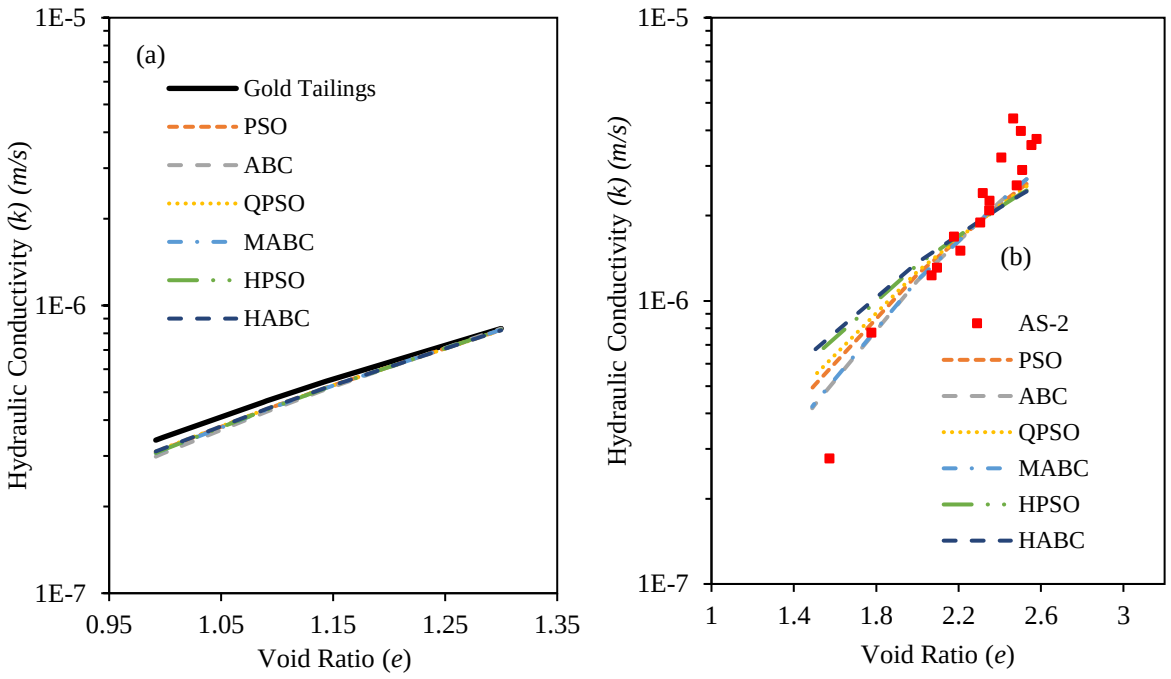


Figure 10.13: Comparison of hydraulic conductivity functions for experimental excess pore pressure data cases (a) Gold Tailings and (b) AS-2

TH-3534_186104002

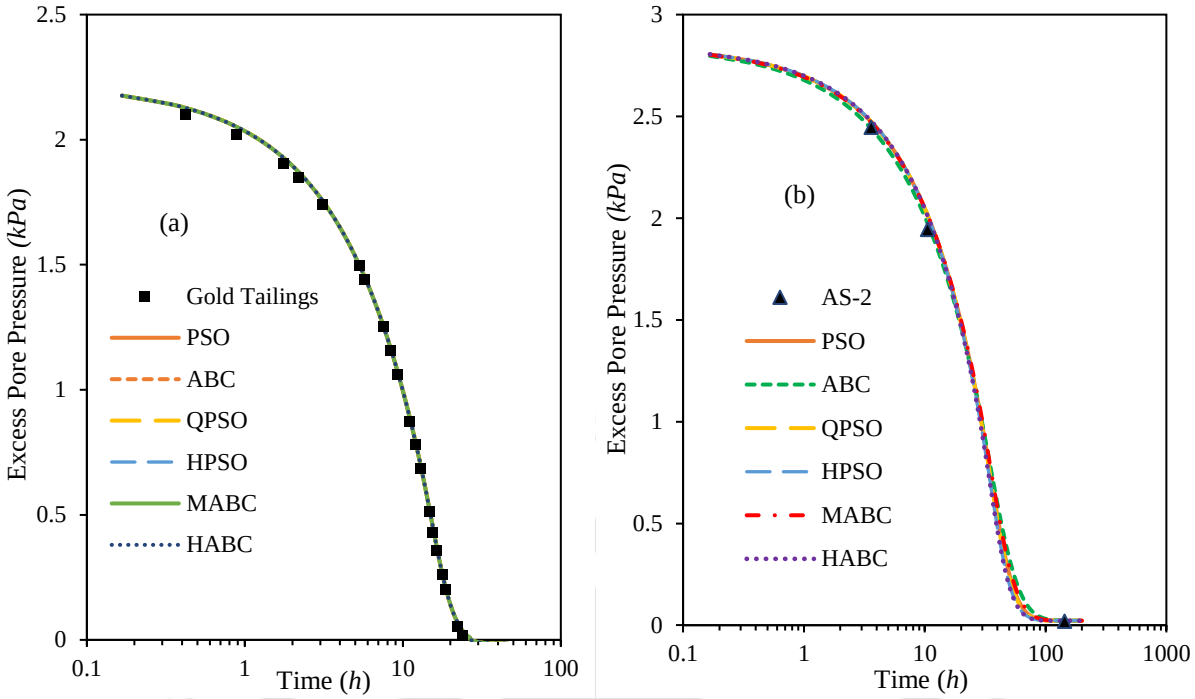


Figure 10.14. Comparison of settlement versus time data in the literature and the curves simulated using the hydraulic conductivity function parameters predicted by inverse analysis from excess pore pressure data for (a) Gold Tailings and (b) AS-2

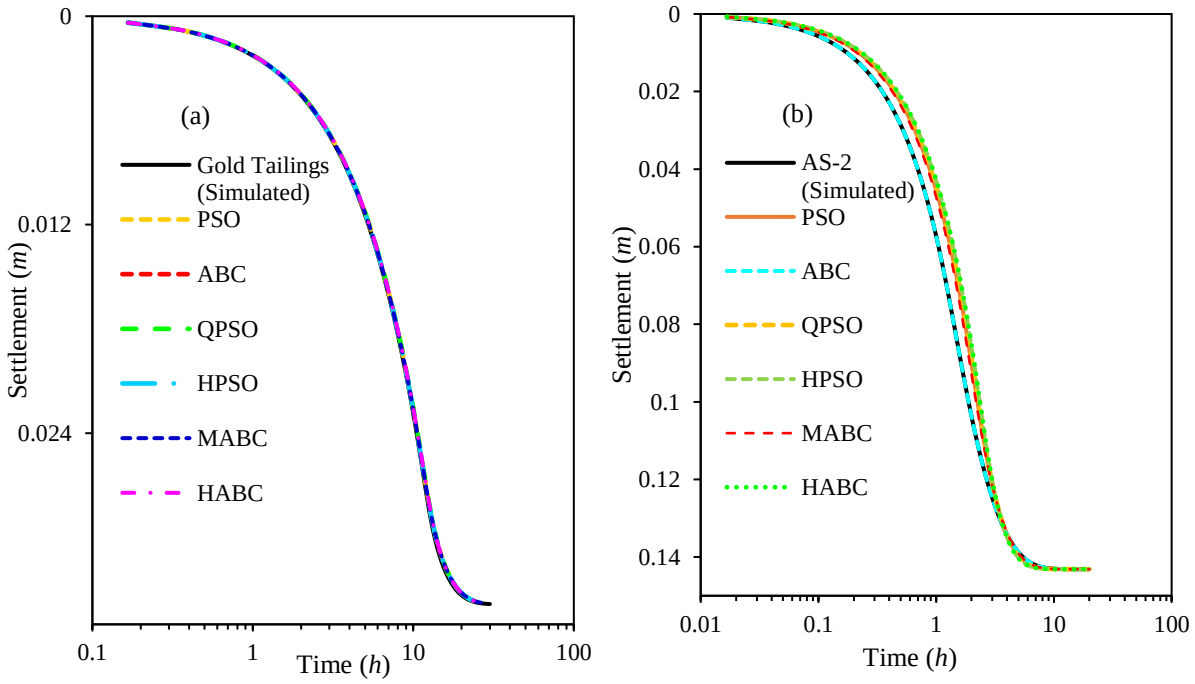


Figure 10.15. Comparison of excess pore pressure dissipation data points given as input for inverse analyses and the curves simulated using the hydraulic conductivity function parameters predicted by inverse analysis for (a) Gold Tailings and (b) AS-2

TH-3534_186104002

The worst RMSE for Gold Tailings was twice the best value, and the mean RMSE was 1.5 times the best value for PSO. In the case of AS-2, the worst converged RMSE was thrice the best value, and the mean was twice the best value for QPSO. The predicted optimal *M* and *P* parameters compared with the corresponding observed data are shown in Figures 10.13(a-b). The comparison was made with the fitted hydraulic conductivity function from the literature in the case of Gold Tailings. It was observed that the predicted hydraulic conductivity values for Gold Tailings show a negligible variation from the actual function. All the algorithms showed slight variation in the predicted hydraulic conductivity function when compared with the experimental data for AS-2. However, when these predicted parameters were used to simulate excess pore pressure dissipation curves, the simulated curves showed appreciable matching with the experimental data, as shown in Figure 10.14(a-b). The maximum error for Gold Tailings was a 2.1% over-prediction at 0.4 hours (equal to 0.04 kPa) from all the algorithms. The ABC algorithm predicted the excess pore pressure values closely in the case of AS-2, resulting in a maximum over-prediction of 1.7% (equal to 0.03 kPa), while the other algorithms gave 3.8% (equal to 0.07 kPa) over-prediction error at 11 hours.

Since the experimental settlement data were not available in the literature, these curves were simulated using the known material properties given in Table 4.2 for AS-2 and Gold Tailings. These curves were compared with the same, simulated using optimised *M* and *P* values, as shown in Figures 10.15(b-c). While the predicted behaviour showed excellent with the simulated original behaviour of Gold Tailings, with an error percentage of less than 1%, the predicted settlement values for AS-2 showed a larger difference from the simulated original behaviour. Only the optimal parameters from ABC captured the settlement behaviour appreciably in this case. The discrepancies observed in the case of AS-2 could be attributed to the fact that the inverse analysis process was carried out using only three input data points. In the synthetic data cases, the errors are possibly incurred due to the randomly added white noise present in the input-data.

10.3.5 Discussion on Significant Observations

10.3.5.1 The linear relationship between power (P) and natural logarithm of multiplier (ln M)

The hydraulic conductivity function parameters get optimised after several forward analysis steps at each iteration. The iteration history of *M* and *P* values obtained from the stochastic algorithms, when plotted, aligned to form a straight line in the *ln M* versus *P* space. This peculiar behaviour was observed by Qi and Simms (2020) when the optimisation was carried

TH-3534_186104002

out using the Nelder Mead Simplex algorithm, using settlement data as input. This was also observed in the inverse analysis using excess pore pressure data, as shown in Figure 10.16(a) for Phosphatic Clay, for all the optimisation algorithms considered. The excess pore pressure dissipation data were used to generate three-dimensional error surfaces for the inverse analysis problems (Figures 10.16(b)), which demonstrated a valley formation with different pairs of *M* and *P* in the iteration history forming straight lines in the *ln M -P* space. In Figure 10.15(a). Each algorithm begins at different sets of random initial populations of *M* and *P* values within the search area and eventually travels along the same straight line in the *ln M* versus *P* space, leading to the perfect pair of *M* and *P*.

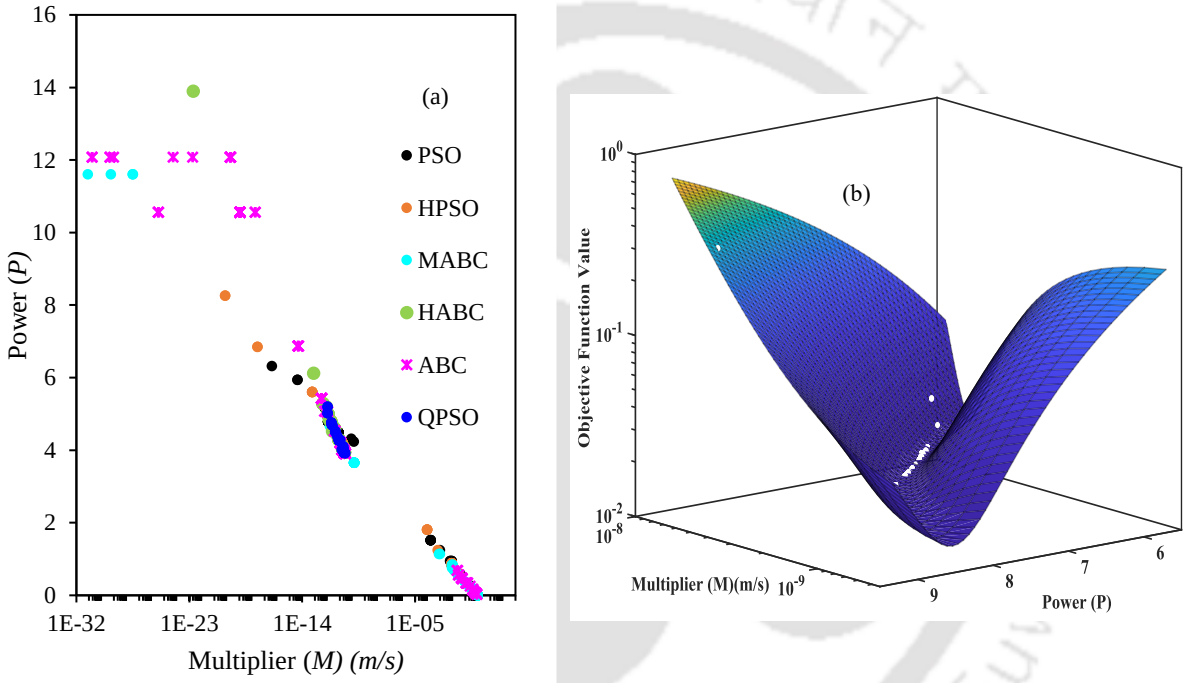


Figure 10.16. (a) M and P values from successive iterations converged to a straight line, leading to the optimal pair of values when base excess pore pressure dissipation data for Phosphatic clay was used for inverse analysis. (b) Error surface showing the valley and straight-line formation in ln M versus P plane for inverse analysis using excess pore pressure dissipation data for Antwerpen Slurry

10.3.5.2 Consequences of inaccurate estimation of optimal parameters

In the field, new layers of slurry material are dumped over the existing layers based on the total compression and pore pressure conditions of the existing layer. The volume of incoming waste material depends on the available clear head above the current layer, which depends on the settlement achieved by the pre-existing layers. Excess pore pressure within the settling slurry

TH-3534_186104002

is monitored continuously in the field to ensure the dam's stability. The time required to achieve the maximum dissipation of excess pore pressure or maximum settlement value is crucial for planning mine closure and associated land reclamation. The field decisions made based on wrongly estimated hydraulic conductivity parameters can significantly slow down the deposition process of subsequent layers and eventual reclamation of the land (Case 2). In cases where the predicted consolidation rate is higher than the actual rate at the field (Case 1), this can cause premature deposition of successive layers, which can incite instability in the storage facility, increasing the chances of failure.

10.3.5.3 Comparison of approaches using settlement and excess pore pressure data

The decision between using settlement data or excess pore pressure data as input values is influenced first and foremost by the availability of the necessary experimental data from column tests. Pore pressure data extraction demands additional instrumentation, such as pore pressure transducers attached to the settling column without leakage. Excess pore pressure dissipation data for the bottom of the sample is the appropriate choice for slurries that do not allow proper observation of the solid-liquid boundary at any point in time due to the smearing effect on column walls or poor visibility resulting from excessive pore fluid turbidity. Internal channels formed within the slurry during the column test can result in faster dissipation of excess pore pressure and an accelerated settling rate. When such data is utilised as input for inverse analysis, it can produce conclusions that differ from the hydraulic conductivity reported using direct measurement methods.

The proposed algorithms successfully predicted the optimal parameters using settlement data as well as excess pore pressure dissipation data. It was seen that three data points were sufficient for predicting the hydraulic conductivity function parameters through inverse analysis from settlement data (Antwerpen Slurry). Comparing the two types of input cases for Antwerpen Slurry and Phosphatic Clay, it was observed that all the algorithms converged to optimal solutions at a lesser number of iterations when excess pore pressure was used as the input.

10.3.6 Summary

In this section, the inverse analysis approach integrating the optimisation algorithms PSO, ABC, QPSO, HPSO, MABC and HABC with base excess pore pressure dissipation data was explored. The synthetic data simulated using Antwerpen Slurry and Phosphatic Clay were used to test these approaches, while the experimental data for AS-2 and Gold Tailings were used to validate the methods. The hydraulic conductivity functions were considered in power form,

TH-3534_186104002

while the compressibility functions of these materials were assumed to be known time invariants. The efficiency of each of these algorithms was compared based on their speed of convergence and the quality of the optimal solutions produced. Iteration histories from all the algorithms showed that values of parameters being optimised formed a linear relationship in power versus the natural log of multiplier space, leading to the optimal solution in the case of pore pressure data, too. All algorithms showed comparable performance. QPSO was observed to converge much faster than other algorithms. The convergence to local minima was observed prematurely in one case for ABC and MABC. The hybrid algorithms showed good performance for the chosen iteration ratios. The hydraulic conductivity function can be back analysed using the excess pore pressure dissipation data for the base of the sample, provided sufficient data points were available. This would be a useful technique for assessing the long-term stability of the mine waste ponds, specifically in cases where the settling materials show a turbid nature.

10.4 Inverse Analysis Using Pore Pressure Data from Centrifuge Test

10.4.1 General

In this section, a back-estimation of hydraulic conductivity function parameters is presented using pore pressure observations from centrifuge FSC tests. The total pore pressure dissipation data at the base of the sample was used as the input. Two synthetic data cases were generated using TT50 and AL15 for faster running of the inverse analysis algorithm. The experimental pore pressure data from the benchtop centrifuge test on the kaolinite sample (Kao-III) was used for the validation. The relevant material properties used for the study are given in Table 4.2.

Based on the results from section 10.2, the algorithms HABC and HPSO were robust and reliable. The convergence speed was relatively better compared to other modified variants, such as QPSO and MABC. The execution time for MABC codes was more due to the opposition-based learning and other additional computations, even though the results were promising. QPSO, on the other hand, was observed to be stuck in the local minima in several instances. Therefore, in the present study, the HABC and HPSO algorithms were used to perform the inverse analysis. The standard ABC and PSO were also implemented to compare with the hybrid variants. The performance and efficiency of these algorithms were compared in terms of convergence speed, robustness and the accuracy of the predicted parameter. The settlement curves and pore pressure dissipation curves were compared with the actual data for further insights.

TH-3534_186104002

The FEM model for the centrifuge FSC was integrated into the inverse analysis procedure. The computational effort was reduced considerably by using the FEM model for the forward analysis steps. This was observed to give more freedom in the selection of time and space steps. The computations were considerably faster than the FDM approach, expediting the execution of the algorithms and thereby reducing the running time required for multiple runs.

10.4.2 Back-estimation using the synthetic and experimental pore pressure data

The synthetic data sets of total pore pressure at the base of the sample were generated for various time points using the material properties of AL15 and TT50. PSO, ABC, HABC and HPSO were run thrice to check the robustness. The personal and social learning coefficients for PSO and HPSO were maintained at 1.5 and 2, respectively.

Table 10.5 Performance of optimisation algorithms for the inverse analysis of hydraulic conductivity function parameters using Ng pore pressure data

Material	Algorithm	RMSE Value			Iteration No.	Predicted Values	
		Best	Worst	Mean		M(m/s)	P
Synthetic Data Cases							
AL15	PSO	5.35E-02	5.62E-02	5.44E-02	125	1.376E-10	5.329
	HPSO	5.35E-02	8.40E-02	6.38E-02	164	1.386E-10	5.318
	ABC	5.35E-02	6.12E-02	5.70E-02	46	1.376E-10	5.329
	HABC	5.35E-02	5.35E-02	5.35E-02	43	1.376E-10	5.329
TT50	PSO	1.08E-01	3.83E-01	2.04E-01	189	2.670E-09	4.562
	HPSO	1.06E-01	1.06E-01	1.06E-01	49	2.664E-09	4.672
	ABC	1.06E-01	1.23E-01	1.12E-01	68	2.666E-09	4.582
	HABC	1.06E-01	1.06E-01	1.06E-01	51	2.664E-09	4.583
Experimental Data Case							
Kao-III	PSO	1.263	2.701	1.761	193	6.757E-10	4.317
	HPSO	1.551	1.551	1.551	182	6.472E-10	4.315
	ABC	1.263	1.551	1.377	141	6.472E-10	4.315
	HABC	1.257	1.315	1.284	50	5.786E-10	4.188

The inertia weight was set to 0.99. The population size for PSO and HPSO was 40, while the number of onlooker bees and employed bees was 40 each, resulting in a colony size of 80. The limit for improving each food source was 50 for ABC and HABC. The iteration ratio for HPSO and HABC was 50:50. The maximum number of iterations was 200, which resulted in two cycles in the case of hybrid algorithms. The predicted parameters are the power (P) and

TH-3534_186104002

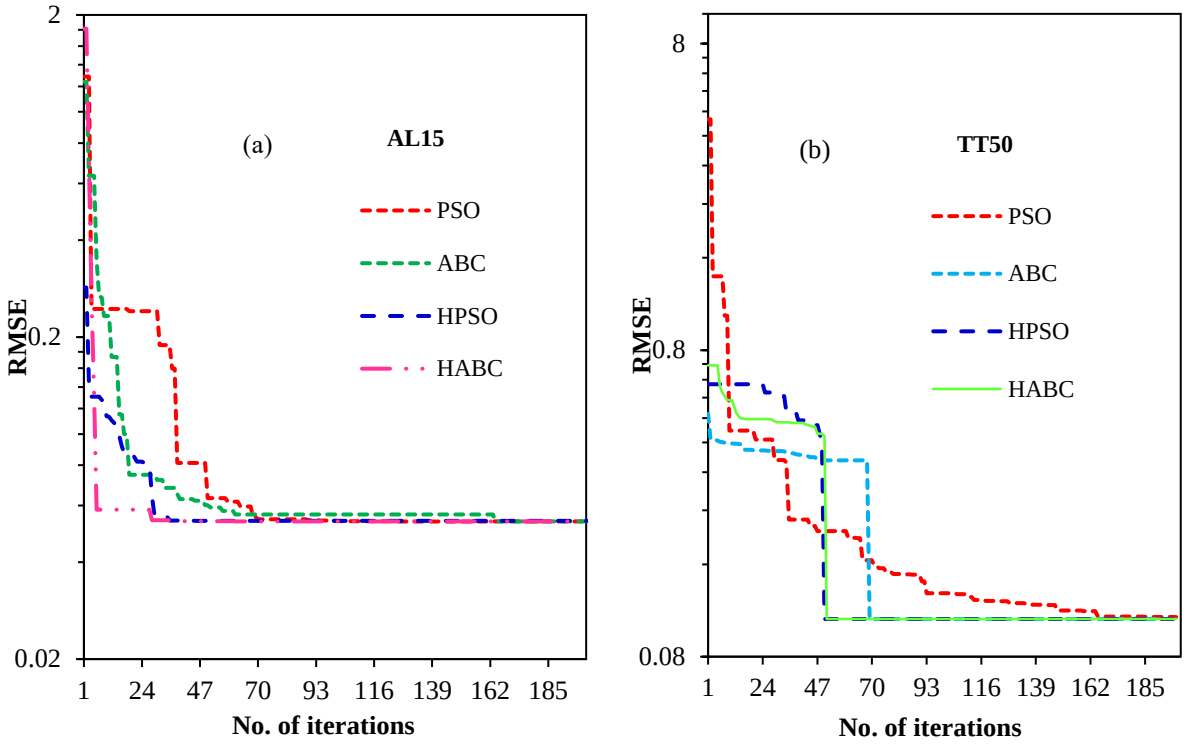


Figure 10.17. Iteration number versus RMSE value plots for the inverse analysis using synthetic pore pressure data set simulated for Ng FSC tests for the cases (a) AL15 (b) TT50

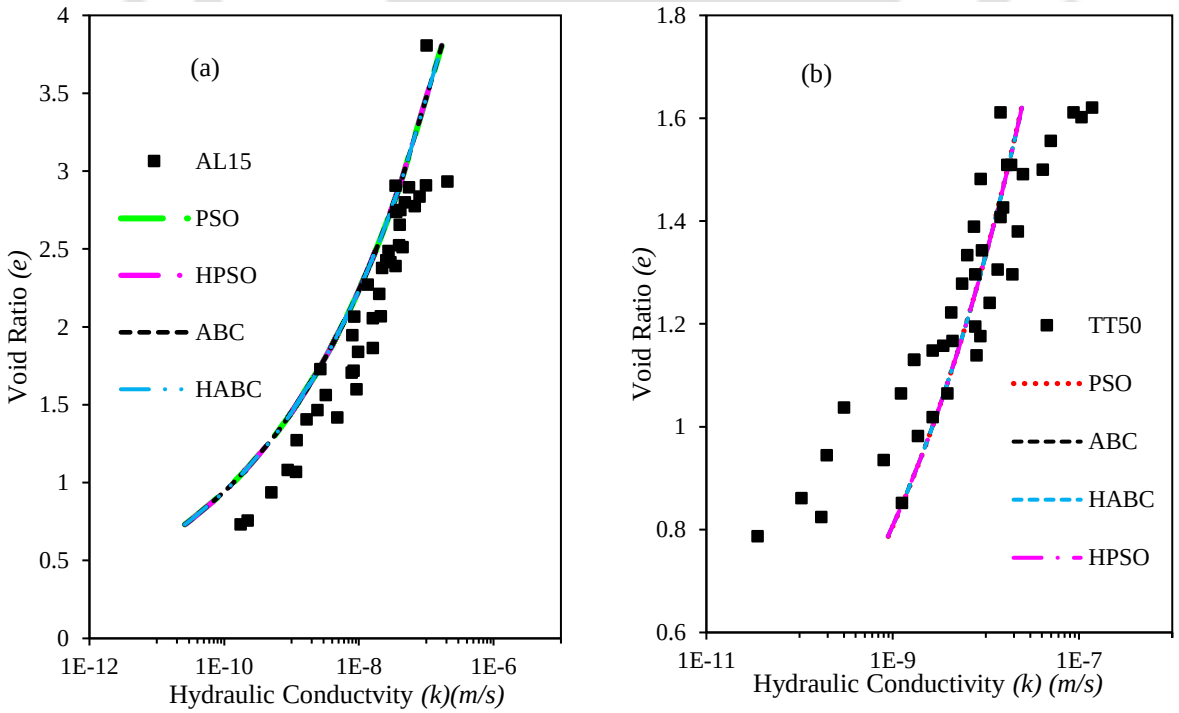


Figure 10.18: Comparison of hydraulic conductivity data reported in the literature with the hydraulic conductivity function parameters predicted using optimisation algorithms through inverse analysis with synthetic total pore pressure data from Ng FSC tests for (a) AL15 (b) TT50

TH-3534_186104002

Multiplier (*M*) values of the hydraulic conductivity function. The *M* and *P* values of the run converging to the lowest RMSE value were reported for each algorithm. Further, the iteration number at which each algorithm converges to the best-run RMSE value is also presented for comparison. The repeatability of the results is checked using the mean, worst and best RMSE values. In order to assess the quality of the results, the predicted parameters were compared with the available hydraulic conductivity data from the literature. The pore pressure behaviours of the slurries were numerically simulated using these parameters and compared with the data used as input for the inverse analysis. Additionally, settlement curves were simulated using these parameters and compared with available literature data. Table 10.5 presents the comparison of the best run conditions of the algorithms.

All the algorithms converged to objective function values in the same range, in the best run, for AL15. In terms of convergence speed, HPSO and HABC performed better than conventional algorithms. When convergence results from three runs were compared, HABC showed consistency. However, in the case of ABC, a 14% difference was present in the best and worst RMSE values. In the worst-run of HPSO, the algorithm got stuck in local minima, which resulted in the convergence to an optimum with the corresponding RMSE value being more than 50% larger than the reported value for the best-run case. The iteration number versus RMSE values for the best run is plotted in Figure 10.17 (a). The predicted hydraulic conductivity function parameters compared with the actual data showed appreciable correspondence in the zone of higher void ratio values (Figure 10.18(a)). The settlement behaviour and pore pressure dissipation plots were predicted using the optimum hydraulic conductivity parameters, which were compared with the actual data for further validation of the solution quality. (Figure 10.19 (a) and Figure 10.20 (a)). The simulated curves were almost the same for all the algorithms since the optimal values for *P* and *M* were in the same range. The comparison showed that the simulated settlement curves showed a faster rate of settlement compared to the actual data. The maximum error in the predicted pore pressure value was 1.7% at 96 hours. In the case of TT50, HPSO, HABC, and ABC converged to the same RMSE value. The predicted *P* and *M* values were in the same range (Table 10.3). These algorithms showed robust performance and faster convergence within 100 iterations in all runs. However, PSO showed considerable variation in the converged values of parameters in the three runs, reflected by the difference in the mean and best RMSE values. Besides, Figure 10.17 (b) shows that PSO did not converge properly within the 200 iterations considered. In Figure 10.19(b), simulated -

TH-3534_186104002

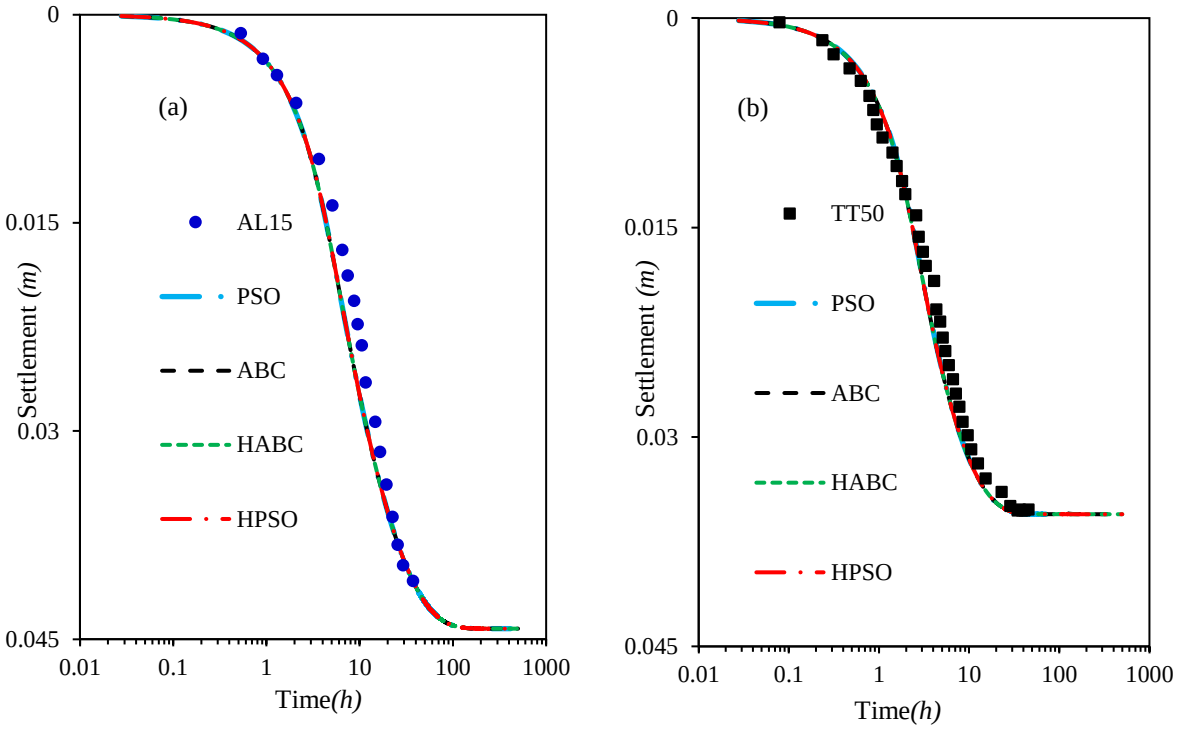


Figure 10.19: Comparison of settlement versus time data in the literature and the curves simulated using the hydraulic conductivity function parameters predicted by inverse analysis from Ng pore pressure data for (a) AL15 and (b) TT50

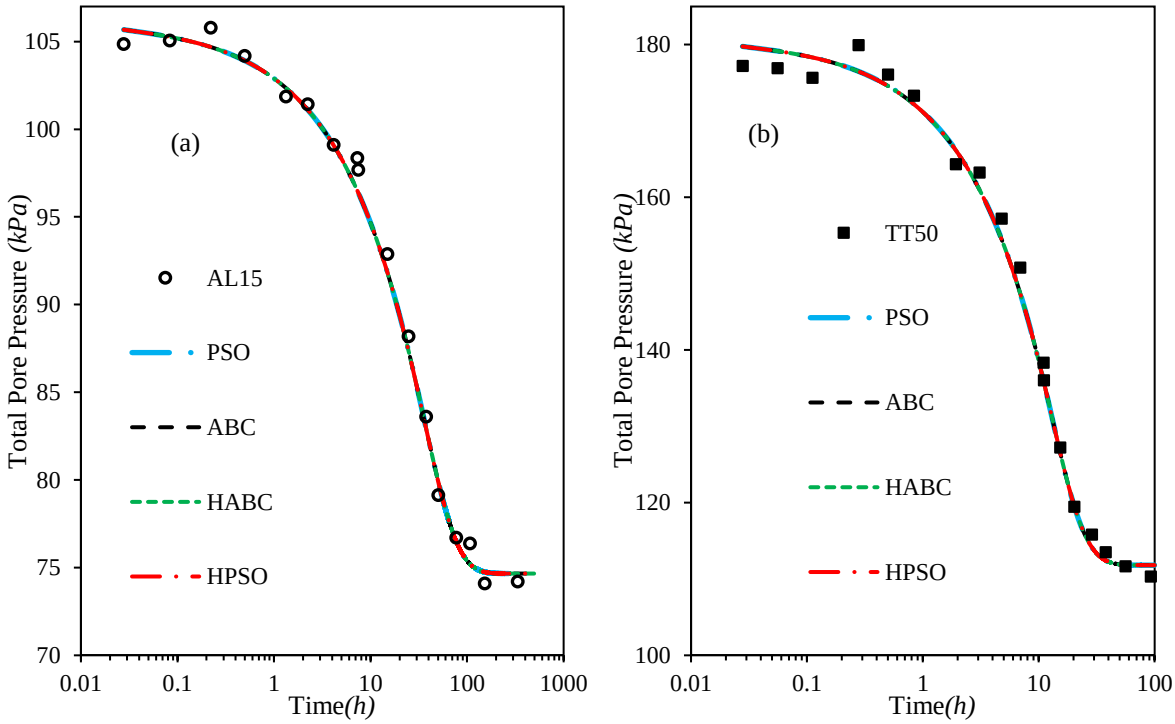


Figure 10.20: Comparison of pore pressure dissipation data generated synthetically and the curves simulated using the hydraulic conductivity function parameters predicted by inverse analysis from Ng pore pressure data for (a) AL15 and (b) TT50

TH-3534_186104002

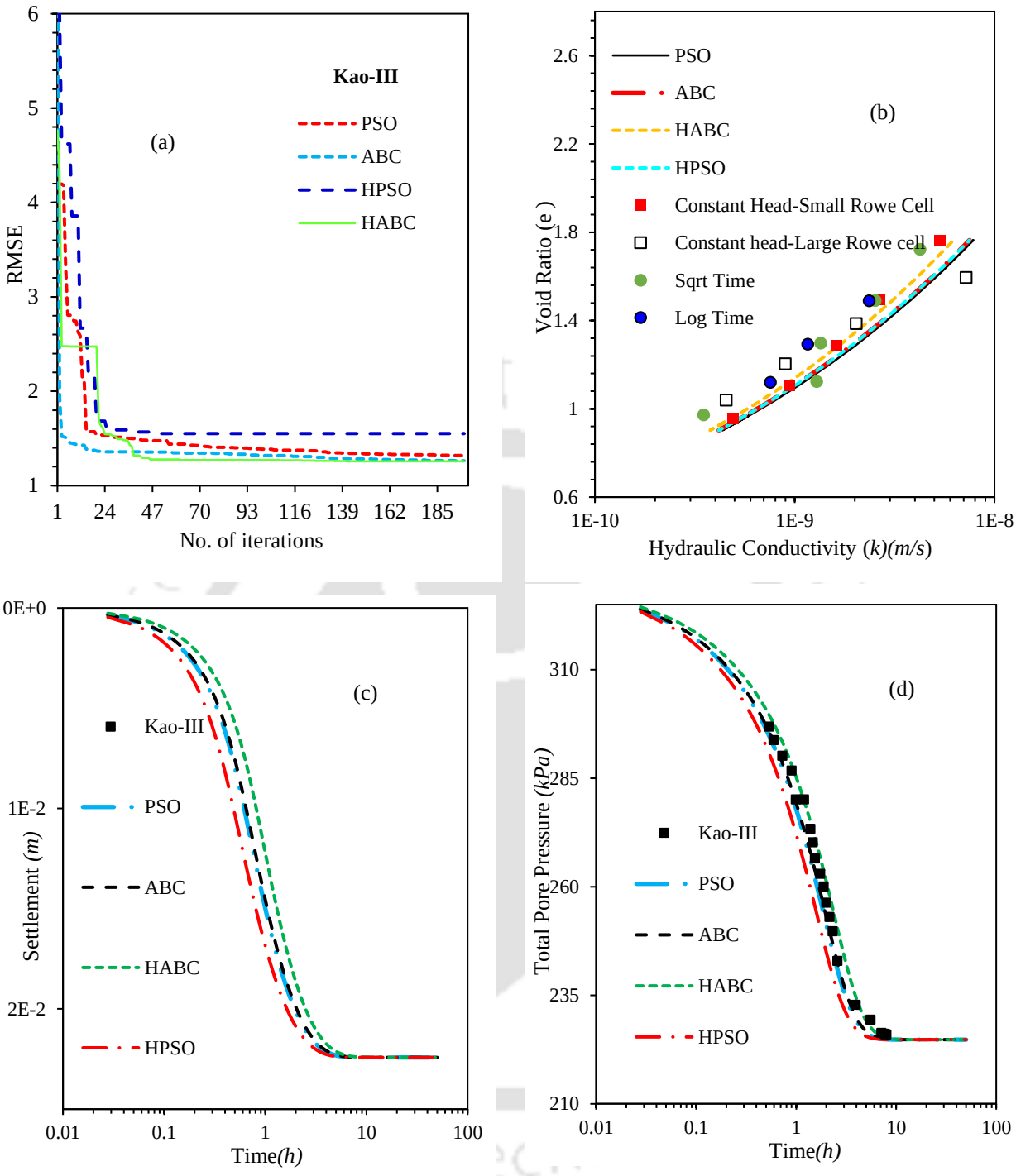


Figure 10.21: Observations from the inverse analysis using experimental pore pressure data from the benchtop centrifuge test on Kao-III: (a) comparison of RMSE versus iteration number plots for various algorithms, (b) comparison of predicted hydraulic conductivity parameters with the available literature data (c) comparison of predicted settlement behaviour and, (d) comparison of simulated pore pressure dissipation curves with the corresponding experimental data

TH-3534_186104002

settlement plots are compared with actual data. 14% error was observed at 4.4 hours when compared with actual data. The settlement rate was observed to be slightly over-predicted after 1.5 hours. Before this point, the settlement rate was underpredicted. Total pore pressure curves were simulated using the predicted parameters. The maximum error for all the cases observed at 0.3 hours, and the corresponding error value was 1.95% underprediction.

The optimisation-based approach for inverse analysis using pore pressure data from centrifuge FSC tests was validated using the experimental data for Kao-III. The material properties are given in the Table 4.3. A benchtop centrifuge was used for the testing in this case. All algorithms were observed to predict the parameters with considerable accuracy. The best response obtained using PSO was not consistent across multiple runs. In the case of ABC, the converged RMSE values varied by a maximum of only 8% and the resulting predicted parameters were in the same range. HPSO and HABC showed robust performance in this case. In the literature, hydraulic conductivity data was measured by constant head test using a small Rowe cell of 76 mm diameter, a large Rowe cell of 150 mm diameter, log-t method and square-root time method, based on Terzaghi's theory. The predicted hydraulic conductivity functions matched best with the constant head test data using the small Rowe cell. Settlement versus time plots were simulated using the predicted values of M and P (Figure 10.21(c)). However, the experimental settlement data was unavailable in the literature for comparison. The rate of settlement predicted by PSO and ABC was observed to match, while HABC predicted a slower rate of consolidation. The predicted consolidation rate of HPSO was faster. For instance, at 0.53 hours, HPSO predicts a settlement value of 0.0108 m, while PSO and ABC predict 0.00808 m. HABC predicts a much lower settlement value of 0.00613 m. The comparison of pore pressure data from the literature with the simulated curves can be seen in Figure 10.21 (d). The dissipation rates of HPSO were faster than ABC and PSO, while the same was slightly slower for HABC. Simulated behaviour for HPSO showed pronounced deviation. Maximum deviation was observed at 1.2 hours, showing an underestimation of total pore pressure value by 14.8 kPa, i.e., 5.3% variation. For PSO and ABC, the simulated curves matched well with available data points. However, a slight deviation was observed at 1.2 hours, resulting in a 2.4% underestimation due to an error of 6.84 kPa. In the case of HABC, the simulated curve matched those data points that PSO and ABC could not match. A general tendency of overestimation was noted. The maximum difference observed was 2.7% due to a pressure difference of 6.7 kPa.

TH-3534_186104002

10.4.3 Summary

The study presented a robust novel inverse analysis method for the back estimation of hydraulic conductivity function using pore pressure data from the FSC test conducted in a benchtop centrifuge. The proposed approach integrated optimisation algorithms with the FEM numerical solution of the governing differential equation. The hydraulic conductivity function coefficients were successfully back-predicted for two synthetic data cases and one experimental data case. Conventional optimisation algorithms showed comparable performance in all three cases considered. PSO showed a slower rate of convergence. In two cases, the algorithm failed to converge properly within the maximum number of iterations considered. Though HPSO showed better robustness of prediction and consistency in converged values, the algorithm got stuck in local minima in one instance, showing the significance of choosing the appropriate iteration ratio and cycles of iteration for *fmincon* and PSO. HABC showed considerable improvement over conventional ABC in terms of consistency and rate of convergence. The settlement and pore pressure curves simulated using the back-predicted hydraulic conductivity function parameters showed appreciable correspondence with the actual data points. Comparison with previous chapters suggests that the hybrid algorithms show reliable performance when centrifuge settlement data was used as input, as well.

Pore-pressure-based inverse analysis using centrifuge test data is a viable alternative to the conventional settlement-based approach. The proposed method can efficiently estimate the hydraulic conductivity function parameters in the case of turbid slurries, reducing the variations resulting from observational errors because of the unclear settling boundary.

The next chapter provides a comprehensive conclusion of the studies conducted as a part of this work.

TH-3534_186104002

11 Conclusions and Future Scope

11. 1 Conclusion

Experimental Analysis of Soft-Soil Consolidation Behavior

1. The compressibility and consolidation settlement behaviour of four soil slurries were experimentally analysed using a conventional oedometer and a modified bench-top centrifuge. The consolidation under step-wise loading in the oedometer was observed to be laborious and time-consuming, lasting for more than 30 days per sample, while the centrifuge tests consumed maximum of 25 minutes for complete consolidation, which was observed for Kao-I at 1000RPM.
2. The assumption of constant hydraulic conductivity was observed to be incorrect for slurries undergoing FSC. The estimated hydraulic conductivity values at the end of each loading step revealed that the hydraulic conductivity value was reduced by at least 90% at the end of the final loading phase.
3. The oedometer tests were significantly constrained by the tendency of slurries to be expelled from the mould during loading. Loading had to be executed with caution to prevent a rapid increase in pore pressure that may lead to spilling.
4. The benchtop centrifuge setup was shown to more effectively capture significant deformations compared to the oedometer, by allowing larger initial height for samples. Comparing the stress conditions in centrifuge testing with oedometer tests, it was found that the maximum settlement was 74.6% at 2000 RPM for Kao-I. In the oedometer data, the closest matching stress condition resulted in a reduction of the sample height by 7.7%. In the case of RS, this comparison demonstrated a significant 41% decrease in height at 2000 RPM, whereas the oedometer only showed a minor drop of 5.7% under identical stress levels. When the sample was subjected to a rotational speed of 2000 RPM, the height of the sample decreased by 44% in the case of MBC. In contrast, when the sample was tested using an oedometer at a pressure of 100 kPa, the drop in height was 11%. In case of BCS, at 2000 RPM, 50% reduction in height was observed, however only 12% reduction was observed in the case of oedometer, at similar stress conditions.
5. The settlement value was proportional to the RPM of the rotation of the centrifuge. The comparison of effective stress relations derived from centrifuge data and oedometer data showed appreciable correspondence for the stress values considered, provided the initial void ratio values for both tests are within the same range.

TH-3534_186104002

6. A tabletop centrifuge provides the convenience of testing slurries with higher moisture content. Higher stress levels may be achieved in a centrifuge by increasing the RPMs. A bench-top centrifuge is a more efficient and viable alternative to a conventional oedometer for the purpose of determining the effective stress-void ratio correlations of slurry materials.

Scaling Effects in Centrifuge

1. Prediction of field settlement behaviour from the centrifuge observation necessitates the appropriate scaling of the settlement and time values to reduce error magnification. Using the N value at the base as the scaling factor for settlement values produces the least error in the ultimate settlement, followed by the scale factor considering effective radius to initial mid-height suggested by Fox. The maximum error was observed in the case of Schoefiled's scale factor.
2. The *Hm/R r*atio influences the difference in ultimate settlement from the simulated prototype curve more than the N_0 value. The influence was greater when the effective scale factors were used. The error in predicted ultimate settlement values was observed to be influenced by the *Hm/R* ratio more than the acceleration scale factor at the base of the sample. Scaling using N at the base was observed to be least affected by the Hm/R ratio and N0 values compared to other cases.
3. The 1g curves obtained using effective radius-based conversion factors show more match to the simulated prototype settlement curve during the initial phase of consolidation. The difference between these converted curves and the simulated prototype curve increases and comes to the maximum at the ultimate settlement. The initial phase of consolidation was observed to vary from prototype behaviour when the N_0 *i*s used as the conversion factor. This variation was observed to increase with the increase in *Hm/R* value.
4. The exponent of the time scaling factor is not exactly equal to the theoretical value of 2. It was observed to vary with the *Hm/R, N* value, and degree of consolidation. The main noticeable pattern is a decline in the time scale factor exponent values as the *Hm/R* increases.
5. The data indicates that the values of the time scale exponent typically rise as the degrees increase for all *Hm/R* ratios, suggesting a positive link between degrees and the exponent. Higher *Hm/R* values show a more consistent increase in the time scale exponent with degrees compared to lower *Hm/R* values.

TH-3534_186104002

Graphical Estimation of Hydraulic Characteristics

1. The change in the position of the settlement versus time curve along the log *t*-axis with the change in the multiplier of the hydraulic conductivity function observed for 1*g* self-weight consolidation is applicable for consolidation tests in a centrifuge environment and is useful for predicting the optimum value for the multiplier. The shape and spread of settlement versus time curves of centrifuge tests obtained from centrifuge consolidation tests showed dependency on power value similar to the consolidation in the 1*g* environment. This observation helped to predict the optimal *P* value.
2. The FSC settlement curves for the centrifuge environment based on the predicted multiplier and power values are in very good agreement with both the corresponding synthetic and real settlement versus time data. The proposed Method 1 and Method 2 are robust for the prediction of hydraulic conductivity characteristics of the slurries from the centrifuge settlement data. The graphical methods are
3. also simple for analysing the centrifuge data due to the requirement of only a limited number of FSC simulations, although several arithmetic calculations are required. Thus, the graphical methods are quicker, simpler, and more robust when compared with the optimisation algorithms for the inverse analysis.
4. The graphical methods for predicting hydraulic conductivity characteristics from the centrifuge data are applicable for both the beam centrifuge and bench-top centrifuge, as well as various initial void ratios and compressibility functions.
5. The prediction of hydraulic conductivity parameters by Method 1 is accurate compared with Method 2 when the centrifuge data in limited time intervals are only available. As Method 2 depends on the variance of the measured settlement versus time data, the partly available consolidation data are inadequate to represent the complete dispersion of the settlement curve.

Inverse Analysis Using 1g Settlement Data

1. Back estimation of constitutive function parameters was explored using metaheuristic optimisation algorithms. A back-estimation approach for the simultaneous prediction of coefficients of hydraulic conductivity and compressibility function from conventional FSC settlement was proposed in this study. Based on both synthetic and experimental settlement versus time data, the hydraulic conductivity function parameters and compressibility function coefficients were predicted with good accuracy. The hydraulic conductivity parameters were back-predicted with ease. The accurate estimation of the compressibility

TH-3534_186104002

function required sufficient settlement data points to represent the complete consolidation process.

2. In comparison to the conventional PSO, the QPSO algorithm exhibited a faster convergence to near-optimal solutions. However, the QPSO algorithm showed unstable performance by occasionally failing to converge to the same optimal solution consistently across multiple executions.
3. In comparison to the conventional ABC algorithm, the MABC algorithm effectively reduced the variability in optimal solutions derived from consecutive runs.
4. An optimal number of iterations for their component algorithms ensured that the hybrid algorithms, HABC and HPSO, effectively mitigated the issue of getting stuck in local optima. These hybrid algorithms were able to conduct a better exploration of the solution space and avoid premature convergence as a result of an effective iteration management approach.
5. The hydraulic conductivity function parameters exhibited a characteristic linear relationship between the power and the natural log of the multiplier. This relationship was determined to be unaffected by the optimisation algorithm employed and the presence of other decision variables. The corresponding experimental observations were in good agreement with the settlement versus time profiles simulated using the predicted optimal parameter values.
6. The simultaneous optimisation approach provided a four-dimensional optimisation space, where the conventional PSO algorithm demonstrated comparable performance to HPSO in terms of the speed of convergence and the converged optimal values. However, the HPSO algorithm was proven to be more dependable as a result of its consistent results across multiple runs.
7. The QPSO algorithm demonstrated superior performance in a two-dimensional search space. However, it frequently reached local minima when compressibility and hydraulic conductivity parameters are simultaneously optimised. This performance disparity implies that, although QPSO is effective for simpler problems, it may necessitate modifications or enhancements to manage more complex optimisation tasks effectively.
8. ABC-based algorithms showed slower convergence speed but a consistent performance in both two-dimensional and four-dimensional search space, showcasing better robustness and reliability.

TH-3534_186104002

Inverse Analysis Using Ng Settlement Data

1. An expedited inverse analysis approach was proposed based on the settlement data from centrifuge FSC tests. Using synthetic and experimental settlement data, the approach for estimation of hydraulic conductivity for known, time-invariant compressibility function was established successfully.
2. Simultaneous inverse analysis of compressibility and hydraulic conductivity functions from centrifuge settlement data using ABC, PSO, HPSO, HABC, QPSO and MABC showed promising results. The predicted functions showed good correspondence to the experimental values.
3. All the algorithms showed comparable performances. Hybridisation was observed to improve robustness to a certain extent. By carefully defining the time and space steps, setting suitable upper and lower boundaries for the variables, and using well-defined tuning parameters, the suggested optimisation-based methodology, when merged with centrifuge FSC test data, offers a more efficient alternative to existing strategies for the estimation of constitutive function parameters.
4. The ABC-based algorithms showed better performance in this optimisation landscape in both two- and four-dimensional search space. MABC reduced the converged RMSE values, while HABC improved the reliability of solutions by consistently converging to the same optimal set of parameters.
5. QPSO was observed to converge more quickly than PSO and HPSO. However, certain predicted results deviated considerably from the observed values when QPSO was employed. HPSO, though faster than PSO and showed good consistency, has the potential to be further improved by varying the iteration ratio for *fmincon* and PSO. In some cases, PSO and QPSO algorithms failed to achieve convergence within the maximum number of iterations considered.

Inverse Analysis Using Pore Pressure Data

1. Inverse analysis for hydraulic conductivity function parameters were carried out using the pore pressure data from 1g FSC tests and centrifuge tests. Testing and validation of graphical and optimisation-based approaches using synthetic and experimental data showed promising results.
2. At the base of a slurry sample undergoing self-weight consolidation, pore water pressure variation with time was found to have features similar to the settlement versus time curve.

TH-3534_186104002

The position and shape of the dissipation curve with respect to the logarithm of the time axis are influenced by the multiplier (*M*) and power *(P)* values, respectively.

3. The Graphical method- Method 1 successfully back-predicted the optimal multiplier and power values from 1g base excess pore pressure dissipation data, with as little as two forward analyses using arbitrary initial guess parameters, without requiring optimisation or objective function computations. The settlement curve and excess pore pressure dissipation curves simulated using predicted hydraulic conductivity functions showed good matching with the experimental data and synthetic data, respectively.
4. The inverse analysis approach integrating the optimisation algorithms PSO, ABC, QPSO, HPSO, MABC and HABC with base excess pore pressure dissipation data from 1g FSC test showed good results for synthetic and experimental data cases.
5. Iteration histories from all the algorithms showed that values of parameters being optimised formed a linear relationship in power versus the natural log of multiplier space, leading to the optimal solution in the case of pore pressure data as well.
6. All algorithms showed comparable performance. QPSO was observed to converge much faster than other algorithms. The convergence to local minima was observed prematurely in one case for ABC and MABC. The hybrid algorithms showed good performance for the chosen iteration ratios. The hydraulic conductivity function can be back analysed using the excess pore pressure dissipation data for the base of the sample, provided sufficient data points were available.
7. An optimisation-based inverse analysis approach was proposed using centrifuge-based total pore pressure dissipation data, which successfully back-predicted the hydraulic conductivity characteristics for experimental and synthetic data cases.
8. Conventional optimisation algorithms showed comparable performance in all three cases considered. PSO showed a slower rate of convergence. In a few cases, the algorithm failed to converge properly within the maximum number of iterations considered. Though HPSO showed better robustness of prediction and consistency in converged values, the algorithm got stuck in local minima in one instance, showing the significance of choosing the appropriate iteration ratio and cycles of iteration for *fmincon* and PSO.
9. HABC showed considerable improvement over conventional ABC in terms of consistency and rate of convergence. The settlement and pore pressure curves simulated using the back-predicted hydraulic conductivity function parameters showed appreciable correspondence with the actual data points.

TH-3534_186104002

10. Pore-pressure-based inverse analysis using centrifuge test data is a viable alternative to the conventional settlement-based approach. The proposed method can efficiently estimate the hydraulic conductivity function parameters in the case of turbid slurries, reducing the variations resulting from observational errors because of the unclear settling boundary.
11. This would be a useful technique for assessing the long-term stability of the mine waste ponds using base pore pressures in cases where the settling materials show a turbid nature.

11.2 Future Scope

- The study proposes various approaches for the inverse analysis of constitutive function parameters using settlement data or pore pressure data. A multi-objective optimisation approach can be explored, using both data sets simultaneously to improve the accuracy of prediction further.
- The effective radius-based scale factors and time scale exponents need further exploration. The idea of integrating optimisation strategies to minimise the scaling error can be considered. As a part of this, a time-dependent dynamic scale factor can be defined to reduce the error in predicted field settlement behaviour.
- The present study assumes a time-invariant nature for the compressibility function. The study can be extended to include varying compressibility functions frequently observed due to the phenomenon of creep.
- The initial balancing phase of the instrument limited the settlement data from the centrifuge tests reported in this study. Incorporating the initial sedimentation phase in the inverse analysis program can allow the slurry to be placed in the centrifuge right after mixing without waiting for the onset of the self-weight consolidation phase. This can help reduce initial data loss and influence the quality of the results.
- QPSO, out of all the algorithms, showed the fastest convergence. However, the premature convergence to local minima was observed in many cases. A hybrid QPSO can be developed to improve the robustness of the algorithm.
- The objective function in this study was based on the values of settlement and pore pressure variation for different time points. Alternate objective functions based on the 'time value' of the observations can be attempted. Increased settlement errors were observed in the initial phases of consolidation in some cases and the final phase in some cases. Tailored optimisation functions, applying appropriate weightage to errors, can be developed to reduce errors in specific phases of consolidation.

TH-3534_186104002

- The flow regime considered within the centrifuge is assumed to follow Darcy's law. The case for possible non-Darcian flow regimes can be explored.
- Improvement of the performance of optimisation algorithms through hyperparameter tuning can be explored.

TH-3534_186104002

Appendix

(i) Pseudocode for PSO

Begin

Load settlement data *(S, t)* for inverse analysis

Initialize *Population, Iter_Max, upper_bound, lower_bound, dimension*

Initialize w, w_{damp}, c_1 *and* c_2

For each particle of the population

Initialize *position* randomly within the *upper and lower bounds*

Initialize *velocity* of particle as zero

Evaluation of fitness using Equation (4.41)

Set P_{best} as the current position

Set G_{best} based on values of P_{best}

End of for

Set *iteration =0;*

Do

For each particle

Update velocity using Equation (4.42)

Update position using Equation (4.43)

Evaluate fitness for updated positions using Equation (4.41)

Update P_{best}

Update G_{best}

End of for

Update *iteration*

Set *w=w*wdamp*

While (*iteration <Iter_Max*)

End of begin

TH-3534_186104002

(ii) Pseudocode for QPSO

Begin

Load *settlement data (S, t)* for the inverse analysis

Initialize *Population, Iter_Max, upper_bound, lower_bound, dimension*

Initialize $\propto_1$ *and* $\propto_2$

For each particle of the population

Initialize *position* randomly within the *upper and lower bounds*

Evaluation of objective function using Equation (4.41)

Set P_{best} as the current position

Set G_{best} based on values of P_{best}

End of for

Set *iteration =0;*

Do

For each particle

Calculate $\propto$ *using* Equation (4.49)

For each variable

Calculate M_{best} from the P_{best} using Equation (4.44)

End of for

Calculate local attractor using Equation (4.45)

Calculate β using Equation (4.48)

Update *position* using Equation (4.47)

Evaluate objective function for updated positions using Equation (4.41)

Update P_{best}

End of for

Update G_{best}

Update *iteration*

While (*iteration <Iter_Max*)

End of begin

TH-3534_186104002

(iii) Pseudocode for HPSO

Begin

Load *settlement data (S, t)* for the inverse analysis

Initialize *Population, Iter_Max, upper_bound, lower_bound, dimension*

Initialize n_1, n_2, w, w_{damp}, c_1 and c_2

For each particle of the swarm

Initialize *position* randomly within the *domain*

Initialize *velocity* as zero

Evaluate objective function value using equation (4.41)

Set P_{best} as the current position

Set G_{best} based on values of P_{best}

End of for

Set *iteration =0;*

Do

For iteration <n_1

For each particle

Update *velocity* using equation (4.42)

Update *position* using equation (4.43)

Evaluate objective function for updated positions using Equation (4.41)

Update P_{best}

Update G_{best}

End of for

Update *iteration*

Set *w=w*wdamp*

End of for

If (*iteration* + n_2) > *Iter_max*

n_2= *Iter_Max* - *iteration*

End if

Run *Fmincon* using the initial value as G_{best} for n_2 iterations

Update G_{best}

Update *iteration*

TH-3534_186104002

While (*iteration* < *Iter_Max*)

End of begin

(iv) Pseudocode for ABC

Begin

Load data for inverse analysis

Input *colony size, upper and lower bounds, limit, Maxcycle, N*

Set *FoodNumber=colony size/2*

Initialise *Foods* randomly as matrix of shape *[FoodNumber, N]*

For each *Foods*

Evaluate *Fitness* using Eq (4.52)

End of For

Memorise the best *Foods*

Set g_{best} = *Foods* with minimum *ObjVal*

Initialise *k, trial* =0 and *iteration* =1

Set *prob= ones (1, FoodNumber)*

Do

For each *Food*

Produce a *NewFood* from *Foods* (x_i)(based on x_k, $i \neq k$) using Eq (4.51)

Evaluate *Fitness* of *NewFoods using eq(4.41)*

Greedy selection between *NewFoods* and *Foods* to replace *Foods*

Set *trial=trial+1*, if no improvement of *Foods* at location cosidered

End of For

Evaluate *prob* for each *Foods* using equation (4.50)

Set *t*=0

Do

For each *Food*

If rand < *prob(t)*

Produce a *NewFood* from *Foods* (based on x_k, $i \neq k$) using Eq (4.51)

Evaluate *Fitness* of *NewFoods using eq(4.52)*

TH-3534_186104002

Greedy selection between *NewFoods* and *Foods* to update *Foods*

Set *trial=trial+1*, if no improvement of *Foods* at *iloc*

Set *t=t+1*

End of if

End of for

Set g_{best} = *Foods* with minimum *ObjVal*

Set *Index*=location of *Foods* with maximum value of *trial*

If *trial (index)> limit*

Generate *NewFood* randomly

Set *Foods(index)=NewFoods*

Set *trial* of *Foods* =0

End of if

Update *iteration* as *iteration+1*

While *(t < FoodNumber)*

Update g_{best}

While *(iteration < Maxcycle)*

End of begin

(v) Pseudocode for MABC

Begin

Load data for inverse analysis

Input *colony size, upper and lower bounds, limit, Maxcycle and N*

Set *FoodNumber=colony size/2*

Initialise *Foods* randomly as a matrix of shape *[FoodNumber, N]*

For each *Foods*

Evaluate *Fitness* using Eq (4.52)

Generate opposite points using Eq (4.53)

Evaluate *Fitness* of opposite points using Eq (4.52)

End of for

Memorise the best *Foods*

TH-3534_186104002

Set g_{best} = *Foods* with minimum *ObjVal*

Initialise λ, *k, trial* =0 and *iteration* =1

Set *prob= ones (1, FoodNumber)*

Do

If *iteration* > *Maxcycle/10*

Evaluate λ using equation (4.55)

Produce a *NewFood* from *Foods* (x_i)(based on x_k, $i \neq k$) using Eq (4.54)

End if

For repeat the following for each *Food*

Evaluate *Fitness* of *NewFoods using eq (4.52)*

Greedy selection between *NewFoods* and *Foods* to update *Foods*

Set *trial=trial+1*, if no improvement of *Foods* at *iloc*

End of For

Evaluate *prob* for each *Foods* using equation (4.56)

Set *t*=0

Do

For each *Food*

If rand < *prob(t)*

Evaluate neighbourhood found based on eq (4.57)

Produce a *NewFood* from *Foods* (based on x_k, $i \neq k$) using Eq (4.54)

Evaluate *Fitness* of *NewFoods using eq(4.52)*

Greedy selection between *NewFoods* and *Foods* to update *Foods*

Set *trial=trial+1*, if no improvement of *Foods* at a location

Set *t=t+1*

End of if

End of for

While *(t < FoodNumber)*

Set g_{best} = *Foods* with minimum *ObjVal*

Set *Index*=location of *Foods* with maximum value of *trial*

If *trial (index)> limit*

Generate *NewFood* randomly

Set *Foods(index)=NewFoods*

TH-3534_186104002

Set *trial* of *Foods* =0

End of if

Update *iteration* as *iteration+1*

Update g_{best}

While *(iteration < Maxcycle)*

End of Begin

(vi) Pseudocode for HABC

Begin

Load data for inverse analysis

Input *colony size, upper and lower bounds, limit, Maxcycle, N,n,m*

Set *FoodNumber=colony size/2*

Initialise *Foods* randomly as matrix of shape *[FoodNumber, N]*

For each *Foods*

Evaluate *Fitness* using Eq (4.52)

End of For

Memorise the best *Foods*

Set g_{best} = *Foods* with minimum *ObjVal*

Initialise *k, trial* =0 and *iteration* =1

Set *prob= ones (1, FoodNumber)*

Do

For *iteration < n*

For each *Food*

Produce a *NewFood* from *Foods* (x_i)(based on x_k, $i \neq k$) using Eq (4.51)

Evaluate *Fitness* of *NewFoods using E*q(4.52)

Greedy selection between *NewFoods* and *Foods* to replace *Foods*

TH-3534_186104002

Set *trial=trial+1*, if no improvement of *Foods* at location cosidered

End of For

Evaluate *prob* for each *Foods* using equation (4.50)

Set t=0

Do

For each *Food*

If rand < *prob(t)*

Produce a *NewFood* from *Foods* (based on x_k, $i \neq k$) using Eq (4.51)

Evaluate *Fitness* of *NewFoods using* Eq(4.52)

Greedy selection between *NewFoods* and *Foods* to update *Foods*

Set *trial=trial+1*, if no improvement of *Foods* at *iloc*

Set *t=t+1*

End of if

End of for

While *(t < FoodNumber)*

Set g_{best} = *Foods* with minimum *ObjVal*

Set *Index*=location of *Foods* with maximum value of *trial*

If *trial (index)> limit*

Generate *NewFood* randomly

Set *Foods(index)=NewFoods*

Set *trial* of *Foods* =0

End of if

Update *iteration* as *iteration+1*

Update g_{best}

End of For

If *iteration + m > Maxcycle*

m= maxitr - iteration

End of if

Run *Fminsearch* using the initial value as g_{best} for m number of iterations

TH-3534_186104002

Update g_{best}

Update iteration

While *(iteration < Maxcycle)*

End of begin

TH-3534_186104002

List of Publications

List of Journal Publications

1. Bharat, T. V., Vasudev, A., Kundu, S., & Ubaid, M. (2020). Reply to the discussion by Liu and Lei on "Analytical model for consolidation settlements under centrifuge environment". *Canadian Geotechnical Journal*, *57*(3), 467-468.
2. Vasudev, A., & Bharat, T. V. (2022). Prediction of hydraulic conductivity parameters of slurries from centrifuge consolidation settlements. *Canadian Geotechnical Journal*, *59*(11), 1981-2001.
3. Vasudev, A., & Bharat, T. V. (2025). Prediction of permeability characteristics of mine slurries and sediments using finite-strain framework by optimisation algorithms. *Expert Systems with Applications*, *261*, 125495.
4. Srinivasulu, D., Vasudev, A., Tadikonda, B. V., & Nandy, A. K. (2025). Centrifuge Consolidation Analysis of Slurries and Tailings Using Finite-Element Modeling. *International Journal of Geomechanics*, *25*(1), 04024313.

List of Journal Publications Currently Submitted for Review / under preparation.

1. Vasudev, A., & Bharat, T. V. (2024). Simultaneous estimation of hydraulic and compressibility characteristics of mine tailings and dredged sediments. *Computers and Geotechnics.* (under review)
2. Vasudev, A., & Bharat, T. V. (2024). Inverse analysis for finite strain consolidation characteristics of soft soil using optimisaiton algorithms *(Manuscript under preparation)*
3. Vasudev, A., & Bharat, T. V. (2024). Optimisation-Based Prediction of Hydraulic Characteristics of Mine Tailings And Dreged Slurries Pore Pressure Data. *(Manuscript under preparation)*
4. Vasudev, A., & Bharat, T. V. (2024). Inverse analysis for Hydraulic conductivity of Slurry Wastes Using Centrifuge Settlement Data in finite-strain framework *(Manuscript under preparation)*
5. Vasudev, A., & Bharat, T. V. (2024). Prediction of compressibility and hydraulic conductivity characteristics using centrifuge finite strain consolidation data *(Manuscript under preparation)*

TH-3534_186104002

6. Vasudev, A., & Bharat, T. V. (2024). Experimental analysis of consolidation characteristics of soft soils using benchtop centrifuge in a finite-strain framework *(Manuscript under preparation)*
7. Vasudev, A., & Bharat, T. V. (2024). Scale Effects in Numerical Prediction of Prototype Consolidation Using Centrifuge Data *(Manuscript under preparation)*

List of Conference Publications

1. Vasudev Akhila., Kaushik Himanshu., Bharat, T.V. (2021). "Hydraulic Characteristics of Mine Tailings by Metaheuristics Approach" *Proceedings, International Conference on Mining Geotechnics and Geotechnical Engineering,* Part 1, Rome, Italy.
2. Vasudev Akhila., Bharat, T.V. (2022). "Scale Effects in Centrifuge Modelling". *Geo-Congress. North Carolina. American Society of Civil Engineers.*
3. Vasudev, A., & Bharat, T. V. (2022 November). Prediction of hydraulic conductivity parameters of slurries from Large-Strain Consolidation Data. *In proceedings of the 26th international conference on tailings and mine waste. Denver, Colorado*
4. Vasudev, A., & Bharat, T. V. (2022 December). Prediction of Hydraulic Conductivity Function Parameters of Slurries Using Hybrid Metaheuristics Approach. *In Indian Geotechnical Conference, Kochi*
5. Vasudev, A., & Bharat, T. V. (2023 June). Prediction of hydraulic conductivity characteristics of slurries using inverse analysis. *10th European Conference on Numerical Methods in Geotechnical Engineering, London*

TH-3534_186104002

References

Abdelkader, E. M., Moselhi, O., Marzouk, M., & Zayed, T. (2022). An exponential chaotic differential evolution algorithm for optimizing bridge maintenance plans. *Automation in Construction, 134*, 104107. https://doi.org/10.1016/j.autcon.2021.104107

Abdel-Kader, R. F. (2011). Hybrid discrete PSO with GA operators for efficient QoS-multicast routing. *Ain Shams Engineering Journal, 2*(1), 21–31.

Abu-Hejleh, A. N., Znidarčić, D., & Barnes, B. L. (1996). Consolidation characteristics of phosphatic clays. *Journal of Geotechnical Engineering, 122*(4), 295-301. https://doi.org/10.1061/(ASCE)0733-9410(1996)122:4(295)

Adamo, N., Al-Ansari, N., Sissakian, V., Laue, J., & Knutsson, S. (2020). Dam safety: The question of tailings dams. *Journal of Earth Sciences and Geotechnical Engineering, 11*(1), 1–26.

Agapito, L. A., & Bareither, C. A. (2018). Application of a one-dimensional large-strain consolidation model to a full-scale tailings storage facility. *Minerals Engineering, 119*, 38-48.

Ahmed, I. S., & Siddiqua, S. (2014). A review on consolidation behavior of tailings. *International Journal of Geotechnical Engineering, 8*(1), 102–111.

Akay, B., & Karaboga, D. (2012). A modified artificial bee colony algorithm for real-parameter optimization. *Information Sciences, 192*, 120-142. https://doi.org/10.1016/j.ins.2010.07.015

Anderson, C., Sivakumar, V., & Black, J. (2015). Measurement of permeability using a bench-top centrifuge. *Géotechnique, 65*(1), 12–22.

Antonaki, N., Abdoun, T., & Sasanakul, I. (2018). Centrifuge tests on comixing of mine tailings and waste rock. *Journal of Geotechnical and Geoenvironmental Engineering, 144*(4), 04017099.

Antonaki, N., Sasanakul, I., Abdoun, T., Sanin, M. V., Puebla, H., & Ubilla, J. (2014). Centrifuge modeling of deposition and consolidation of fine-grained mine tailings. In *Proceedings of the Geo-Congress 2014: Geo-characterization and Modeling for Sustainability, Atlanta, Georgia, USA, 23–26 February 2014*.

TH-3534_186104002

Aubertin, M., & Bussière, B. (2001). Meeting environmental challenges for mine waste management. *Geotechnical News, 19*(3), 21–26. https://www.lrl.mn.gov/docs/2013/other/131247.pdf

Azam, S., & Li, Q. (2010). Tailings dam failures: A review of the last one hundred years. *Geotechnical News, 28*(4), 50-54. https://ksmproject.com/wp-content/uploads/2017/08/Tailings-Dam-Failures-Last-100-years-Azam2010.pdf

Babaoglu, Y., & Simms, P. (2018). Estimating saturated hydraulic conductivity from compression curves for fluid fine tailings. In *Canadian Geotechnical Conference*, Edmonton.

Babaoglu, Y., & Simms, P. (2020). A rapid measurement method to determine hydraulic conductivity of tailings under self-weight consolidation. In *Proceedings of the 24th International Conference on Tailings and Mine Waste*, Fort Collins, CO, USA, 15–18.

Bartholomeeusen, G., Sills, G. C., Znidarčić, D., Van Kesteren, W., Merckelbach, L. M., Pyke, R., & Masala, S. (2002). Sidere: Numerical prediction of large-strain consolidation. *Géotechnique, 52*(9), 639-648. https://doi.org/10.1680/geot.2002.52.9.639

Bassett, R. (1973). Centrifugal model tests of embankments on soft alluvial foundations. In *Proceedings of the 8th International Conference on Soil Mechanics and Foundation Engineering*, Moscow, Russia, 6–11 August 1973.

Beasley, D., & James, R. (1976). Use of a hopper to simulate embankment construction in a centrifugal model. *Géotechnique, 26*(2), 220–226.

Been, K. (1980). Non-destructive soil bulk density measurement using x-ray attenuation. *Geotechnical Testing Journal*, 169–176.

Been, K. (1980). Stress strain behaviour of a cohesive soil deposited under water (Doctoral dissertation). Department of Engineering Science, University of Oxford, Oxford, UK.

Been, K., & Sills, G. C. (1981). Self-weight consolidation of soft soils: An experimental and theoretical study. *Géotechnique, 31*(4), 519-535. https://doi.org/10.1680/geot.1981.31.4.519

Beiranvand, V., Hare, W., & Lucet, Y. (2017). Best practices for comparing optimization algorithms. *Optimization and Engineering, 18*, 815-848. https://doi.org/10.1007/s11081-017-9366-1

Benzaazoua, M., Bussière, B., Demers, I., Aubertin, M., Fried, E., & Blier, A. (2008). Integrated mine tailings management by combining environmental desulphurisation and

TH-3534_186104002

cemented paste backfill: Application to mine Doyon, Quebec, Canada. *Minerals Engineering, 21*, 330–340. https://doi.org/10.1016/j.mineng.2007.11.012

Berilgen, S. A., Berilgen, M. M., & Özaydın, K. (2005). Determination of consolidation behaviour of Haliç dredged material by using a seepage-induced consolidation test. *Management of Environmental Quality: An International Journal, 16*(6), 681-690. https://doi.org/10.1108/14777830510623745

Bharat, T. V. (2008). Agents based algorithms for design parameter estimation in contaminant transport inverse problems. In *IEEE Swarm Intelligence Symposium* (pp. 1–7), SIS 2008, St. Louis, MO, United States. https://doi.org/10.1109/SIS.2008.4668312

Bharat, T. V. (2017). Selection and configuration of sorption isotherm models in soils using artificial bees guided by the particle swarm. *Advances in Artificial Intelligence*. https://doi.org/10.1155/2017/3497652

Bharat, T. V., & Sharma, J. (2011). Prediction of compression and permeability characteristics of mine tailings using natural computation and large-strain consolidation framework. In *Geo-Frontiers 2011: Advances in Geotechnical Engineering* (pp. 3868-3877).

Bharat, T. V., & Sharma, J. (2011). Prediction of compression and permeability characteristics of mine tailings using natural computation and large-strain consolidation framework. In *Geo-Frontiers 2011: Advances in Geotechnical Engineering*, Dallas, Texas, USA, 13–16 March 2011 (pp. 3868–3877). ASCE Special Geotechnical Publication 211. http://dx.doi.org/10.1061/41165(397)395

Bharat, T. V., & Sharma, J. (2012). Metaheuristics for improved estimation of hydraulic properties of unsaturated soils. *GEOMANITOBA, 65*, 1-8.

Bharat, T. V., & Ubaid, M. (2019). Analytical model for consolidation settlements under centrifuge environment. *Canadian Geotechnical Journal, 56*(4), 484-494.

Bharat, T. V., Das, P., & Srivastava, A. (2019). Insights into contaminant transport modeling through compacted bentonites. *Frontiers in Geotechnical Engineering*, 101-120.

Bharat, T. V., Sivapullaiah, P. V., & Allam, M. M. (2008). Accurate parameter estimation of contaminant transport inverse problem using particle swarm optimization. In *IEEE Swarm Intelligence Symposium* (pp. 1–7). https://doi.org/10.1109/SIS.2008.4668334

Bharat, T. V., Sivapullaiah, P. V., & Allam, M. M. (2008a). Swarm intelligence based inverse model for laboratory double-reservoir diffusion experiments. In *Proceedings of the 12th*

TH-3534_186104002

International Conference of International Association for Computer Methods and Advances in Geomechanics, Goa, India.

Bharat, T. V., Sivapullaiah, P. V., & Allam, M. M. (2009a). Swarm intelligence based inverse model for characterisation of groundwater contaminant source. *Electronic Journal of Geotechnical Engineering, 14*(B), 1-14.

Bharat, T. V., Sivapullaiah, P. V., & Allam, M. M. (2009b). Swarm intelligence-based solver for parameter estimation of laboratory through-diffusion transport of contaminants. *Computers and Geotechnics, 36*(6), 984-992. https://doi.org/10.1016/j.compgeo.2009.03.006

Bharat, T. V., Sivapullaiah, P. V., & Allam, M. M. (2012). Robust solver based on modified particle swarm optimization for improved solution of diffusion transport through containment facilities. *Expert Systems with Applications, 39*(12), 10812-10820. https://doi.org/10.1016/j.eswa.2012.03.013

Black, J. A. (2014). Development of a small scale teaching centrifuge. In *Physical Modelling in Geotechnics-Gaudin & White* (pp. 187–192). Taylor & Francis Group.

Bloomquist, D. (1982). *Centrifuge Modeling of Large Strain Consolidation Phenomena in Phosphatic Clay Retention Ponds (Florida)*. (Doctoral dissertation, University of Florida).

Bloomquist, D. G., & Townsend, F. C. (1984). Centrifuge modelling of phosphatic clay consolidation. In *Sedimentation Consolidation Models—Predictions and Validation*. Edited by R. N. Yong & F. C. Townsend. ASCE, New York, USA, pp. 565–580.

Bonin, M. D., Nuth, M., Dagenais, A. M., & Cabral, A. R. (2014). Experimental study and numerical reproduction of self-weight consolidation behaviour of thickened tailings. *Journal of Geotechnical and Geoenvironmental Engineering, 140*(12), 04014068.

Bromwell, L. G. (1984). Consolidation of mining wastes. In *Sedimentation Consolidation Models—Predictions and Validation*. ASCE, Reston, VA, USA.

Burland, J. B. (1990). On the compressibility and shear strength of natural clays. *Géotechnique, 40*(3), 329-378. https://doi.org/10.1680/geot.1990.40.3.329

Cacciuttolo, C., & Cano, D. (2022). Environmental impact assessment of mine tailings spill considering metallurgical processes of gold and copper mining: Case studies in the Andean countries of Chile and Peru. *Water, 14*(19), 3057. https://doi.org/10.3390/w14193057

TH-3534_186104002

Caldwell, J. A., Ferguson, K., Schiffman, R. L., & Van Zyl, D. (1984). Application of finite strain consolidation theory for engineering design and environmental planning of mine tailings impoundments. In *Sedimentation Consolidation Models—Predictions and Validation*. ASCE, Reston, VA, USA.

Cargill, K. (1982). Consolidation of soft layers by finite strain analysis. *MP-GL82-3*. Geotechnical Laboratory, U. S. Army Engineer Waterways Experiment Station, Vicksburg, Miss. http://hdl.handle.net/11681/10139

Carrasco, J., García, S., Rueda, M. M., Das, S., & Herrera, F. (2020). Recent trends in the use of statistical tests for comparing swarm and evolutionary computing algorithms: Practical guidelines and a critical review. *Swarm and Evolutionary Computation, 54*, 100665. https://doi.org/10.1016/j.swevo.2020.100665

Carrier III, W. D., Bromwell, L. G., & Somogyi, F. (1983). Design capacity of slurried mineral waste ponds. *Journal of Geotechnical Engineering, 109*(5), 699-716.

Celorie, J. A., Vinson, T. S., Woods, S. L., & Istok, J. D. (1989). Modeling solute transport by centrifugation. *Journal of Environmental Engineering*, *115*(3), 513-526. https://doi.org/10.1061/(ASCE)0733-9372(1989)115:3(513)

Chambers, D. M. (2015). A review of the "Report on Mount Polley Tailings Storage Facility Breach, Independent Expert Engineering Investigation and Review Panel". Center for Science in Public Participation.

Chapuis, R., & Aubertin, M. (2003). On the use of the Kozeny - Carman equation to predict the hydraulic conductivity of soils. *Canadian Geotechnical Journal, 40*(3), 616-628. https://doi.org/10.1139/t03-013

Chen, C. F., Ju, Y. R., Chen, C. W., & Dong, C. D. (2017). Metal distributions in the Kaohsiung ocean dredged material disposal site, Taiwan. *Desalination and Water Treatment, 63*, 366–374.

Chu, J., & Guo, W. (2016). Land reclamation using clay slurry or in deep water: challenges and solutions. *Japanese Geotechnical Society Special Publication, 2*(51), 1790-1793.

Chun-Feng, W., Kui, L., & Pei-Ping, S. (2014). Hybrid artificial bee colony algorithm and particle swarm search for global optimization. *Mathematical Problems in Engineering, 2014*. https://doi.org/10.1155/2014/832949

Cooke, B. (1991). Selection of operative centrifuge radius to minimize stress error in calculations. *Canadian Geotechnical Journal, 28*(1), 160–161. https://doi.org/10.1139/t91-017

TH-3534_186104002

Croce, P., Pane, V., Znidarcic, D., Ko, H. Y., Olsen, H. W., & Schiffman, R. L. (1985). Evaluation of consolidation theories by centrifuge modelling. In *Proceedings of the International Conference on Applications of Centrifuge Modelling to Geotechnical Design* (pp. 380–401). Balkema, Rotterdam, the Netherlands.

Das, Dhanesh Singh. (2022). Behavior of Bentonite and Kaolin Clays at Different Particle Interactions under Chemical, Hydraulic, and Mechanical Loadings. PhD Thesis. Indian Institute of Technology Guwahati. https://gyan.iitg.ac.in/handle/123456789/2469

Das, S. K., Biswal, R. K., Sivakugan, N., & Das, B. (2011). Classification of slopes and prediction of factor of safety using differential evolution neural networks. *Environmental Earth Sciences, 64*, 201-210. https://doi.org/10.1007/s12665-010-0839-1

de Lillis, A., Rotisciani, G. M., & Miliziano, S. (2020). Numerical investigation of the behaviour of hydraulically dredged fine-grained soils during and after filling of the containment facility of the port of Gaeta. *Geotextiles and Geomembranes*.

Derrac, J., García, S., Molina, D., & Herrera, F. (2011). A practical tutorial on the use of nonparametric statistical tests as a methodology for comparing evolutionary and swarm intelligence algorithms. *Swarm and Evolutionary Computation, 1*(1), 3-18. https://doi.org/10.1016/j.swevo.2011.02.002

Dorleon, G., Rigaud, S., & Techer, I. (2024). Management of dredged marine sediments in southern France: Main keys to large-scale beneficial re-use. *Environmental Science & Pollution Research*, 1-24. https://doi.org/10.1007/s11356-024-33129-9

dos Santos Coelho, L. (2010). Gaussian quantum-behaved particle swarm optimization approaches for constrained engineering design problems. *Expert Systems with Applications, 37*(2), 1676-1683.

Dromer, J. B., Aubertin, M., Kennedy, G., Pedroni, L., & Bussière, B. (2004). A new testing system to investigate the sedimentation and consolidation of sludge and slurry. In *Proceedings of the 57th Canadian Geotechnical Conference*, Québec, QC, Canada, 24–26 October 2004.

Dunmola, A., Wang, N., Lorentz, J., Chalaturnyk, R., Zambrano, G., & Song, J. (2018). Comparison of geotechnical beam centrifuge predictions to field data from 10m deep FFT centrifuge cake columns. In *Proceedings of the 6th International Oil Sands Tailings Conference*, Edmonton, AB, Canada, 3 June 2018 (pp. 290–298).

TH-3534_186104002

Eftimov, T., & Korošec, P. (2022). Introduction to statistical analysis. In *Deep Statistical Comparison for Meta-Heuristic Stochastic Optimization Algorithms* (pp. 23-31). Cham: Springer International Publishing.

El Mkadmi, N., Aubertin, M., & Li, L. (2011a). The effect of transient drainage on the stress state in backfilled mine stopes. *Proceedings of the 2011 Pan-Am CGS Geotechnical Conference*, Toronto, Canada, October, University of Toronto, Paper 1139.

Elloumi, W., El Abed, H., Abraham, A., & Alimi, A. M. (2014). A comparative study of the improvement of performance using a PSO modified by ACO applied to TSP. *Applied Soft Computing, 25*, 234-241.

El-Shall, H., Moudgil, B., & Bogan, M. (1996). Centrifugal modeling of the consolidation of solid suspensions. *Mining, Metallurgy & Exploration, 13*(2), 98–102.

Engelbrecht, A. P. (2007). *Computational Intelligence: An Introduction*. Hoboken, NJ: Wiley.

Estepho, M. (2014). *Seepage induced consolidation test: Characterization of mature fine tailings* (Doctoral dissertation, University of British Columbia).

Etor, A., Josu, C., Irurozki, E., & Aritz, P. (2023). On the fair comparison of optimization algorithms in different machines. *Annals of Applied Statistics*. Retrieved from https://hal.science/hal-04253742

Fang, W., Sun, J., Ding, Y., Wu, X., & Xu, W. (2010b). A review of quantum-behaved particle swarm optimization. *IETE Technical Review, 27*(4), 336-348.

Fang, W., Sun, J., Xie, Z. P., & Xu, W. B. (2010a). Convergence analysis of quantum-behaved particle swarm optimization algorithm and study on its control parameter. *Acta Physica Sinica, 59*(6), 3686–3693.

Fourie, A. B., & Papageorgiou, G. (2001). Defining an appropriate steady state line for Merriespruit gold tailings. *Canadian Geotechnical Journal, 38*(4), 695-706.

Fox, P. J. (1996). Analysis of hydraulic gradient effects for laboratory hydraulic conductivity testing. *Geotechnical Testing Journal, 19*(2), 181–190. https://doi.org/10.1520/gtj10340j

Fox, P. J., & Baxter, C. D. P. (1997). Consolidation properties of soil slurries from hydraulic consolidation test. *Journal of Geotechnical and Geoenvironmental Engineering, 123*(8), 770–776.

TH-3534_186104002

Fox, P. J., & Berles, J. D. (1997). CS2: A piecewise-linear model for large strain consolidation. *International Journal for Numerical and Analytical Methods in Geomechanics, 21*(7), 453–475. https://doi.org/10.1002/(SICI)1096-9853(199707)21:7<453::AID-NAG887>3.0.CO;2-B

Fox, P. J., Lee, J., & Qiu, T. (2005). Model for large strain consolidation by centrifuge. *International Journal of Geomechanics, 5*(4), 267–275. https://doi.org/10.1061/(ASCE)1532-3641(2005)5:4(267)

Gao, H., Shi, Y., Pun, C. M., & Kwong, S. (2018). An improved artificial bee colony algorithm with its application. *IEEE Transactions on Industrial Informatics, 15*(4), 1853-1865. https://doi.org/10.1109/TII.2018.2857198

Gao, W. F., & Liu, S. Y. (2012). A modified artificial bee colony algorithm. *Computers & Operations Research, 39*(3), 687-697. https://doi.org/10.1016/j.cor.2011.06.007

Gao, W. F., Liu, S. Y., & Huang, L. L. (2013). A novel artificial bee colony algorithm based on modified search equation and orthogonal learning. *IEEE Transactions on Cybernetics, 43*(3), 1011-1024. https://doi.org/10.1109/TSMCB.2012.2222373

Gibson, R. E., & McNamee, J. (1963). A three-dimensional problem of the consolidation of a semi-infinite clay stratum. *The Quarterly Journal of Mechanics and Applied Mathematics, 16*, 115–127.

Gibson, R. E., England, G. L., & Hussey, M. J. L. (1967). The theory of one-dimensional consolidation of saturated clays: 1. Finite non-linear consolidation of thin homogeneous layers. *Geotechnique, 17*(3), 261-273. https://doi.org/10.1680/geot.1967.17.3.261

Gibson, R. E., Schiffman, R. L., & Cargill, K. W. (1981). The theory of one-dimensional consolidation of saturated clays. II. Finite non-linear consolidation of thick homogeneous layers. *Canadian Geotechnical Journal, 18*(2), 280-293. http://dx.doi.org/10.1139/t81-030

Gorman, C. T. (1976). Constant-rate-of-strain and controlled-gradient consolidation testing (Research Report No. 448). Kentucky Transportation Center. Available online: https://uknowledge.uky.edu/ktc_researchreports/866 (accessed on January 10, 2023).

Gorman, C. T., Hopkins, T. C., Deen, R. C., & Drnevich, V. P. (1978). Constant-rate-of-strain and controlled-gradient consolidation testing. *Geotechnical Testing Journal, 1*(1), 3–15.

Hajihassani, M., Armaghani, D. J., & Kalatehjari, R. (2018). Applications of particle swarm optimization in geotechnical engineering: A comprehensive review. *Geotechnical & Geological Engineering, 36*(2), 705-722. https://doi.org/10.1007/s10706-017-0356-z

TH-3534_186104002

He, W., Williams, D., & Shokouhi, A. (2017). Numerical study of slurry consolidometer tests taking into account the influence of wall friction. *Computers & Geotechnics, 91*(1), 39-47. https://doi.org/10.1016/j.compgeo.2017.06.014

Helinski, M., Fahey, M., & Fourie, A. (2007). Numerical modeling of cemented mine backfill deposition. *Journal of Geotechnical and Geoenvironmental Engineering, 133*(10), 1308–1319. https://doi.org/10.1061/(ASCE)1090-41(2007)133:10(1308)

Holden, N. P., & Freitas, A. A. (2007). A hybrid PSO/ACO algorithm for classification. In *Proceedings of the 9th Annual Conference Companion on Genetic and Evolutionary Computation*.

Hong, Z. S., Yin, J., & Cui, Y. J. (2010). Compression behavior of reconstituted soils at high initial water contents. *Geotechnique, 60*(9), 691–700. https://doi.org/10.1680/geot.09.P.059

Imai, G. (1979). Development of a new consolidation test procedure using seepage force. *Soils and Foundations, 19*(3), 45–60. https://doi.org/10.3208/sandf1972.19.3_45

Indian Standard Method of test for soils part 15 Determination of consolidation properties.

Indian Standard Methods of test for soils: Determination of liquid limit and plastic limit (second revision), IS 2720: Part 5, Bureau of Indian Standards, (1985) New Delhi.

Indian Standard Methods of test for soils: Determination of specific gravity. Section 1: fine grained soils (first revision), IS 2720: Part 3, Bureau of Indian Standards, (1980) New Delhi.

IS:2720 (part15).1986, Bureau of Indian Standard.

Ito, M., & Azam, S. (2013). Large-strain consolidation modeling of mine waste tailings. *Environmental Systems Research, 2*, 7.

Jadon, S. S., Tiwari, R., Sharma, H., & Bansal, J. C. (2017). Hybrid Artificial Bee Colony algorithm with Differential Evolution. *Applied Soft Computing, 58*, 11-24. https://doi.org/10.1016/j.asoc.2017.04.018

Janbaz, M., & Maher, A. (2017). Consolidation and permeability behaviour of Newark Bay's dredged sediments by seepage-induced consolidation test. *International Journal of Geotechnical Engineering, 11*(2), 120–126. https://doi.org/10.1080/19386362.2016.1195034

Jeeravipoolvarn, S. (2005). *Compression behavior of thixotropic oil sands tailings* (Doctoral dissertation, University of Alberta, Edmonton, AB, Canada).

TH-3534_186104002

Jeeravipoolvarn, S. (2010). *Geotechnical behavior of in-line thickened oil sands tailings* (Master's Thesis). University of Alberta, Department of Civil and Environmental Engineering, Edmonton, AB, Canada.

Jeeravipoolvarn, S., Masala, S., Zhang, C., & Moore, T. (2015). Revisiting the large strain consolidation test for oil sands. In *Proceedings of the Tailings and Mine Waste 2015* (pp. 26–28), Vancouver, BC, Canada.

Jeeravipoolvarn, S., Scott, J., & Chalaturnyk, R. (2009). 10 m standpipe tests on oil sands tailings: Long-term experimental results and prediction. *Canadian Geotechnical Journal, 46*, 875–888.

Jin, Y. F., Yin, Z. Y., Shen, S. L., & Hicher, P. Y. (2016). Selection of sand models and identification of parameters using an enhanced genetic algorithm. *International Journal for Numerical and Analytical Methods in Geomechanics, 40*(8), 1219-1240. https://doi.org/10.1002/nag.2487

Jones, H., & Boger, D. V. (2012). Sustainability and waste management in the resource industries. *Industrial & Engineering Chemistry Research, 51*(30), 10057-10065. https://doi.org/10.1021/ie202963z

Jordan, J., Helwig, S., & Wanka, R. (2008). Social interaction in particle swarm optimization, the ranked FIPS, and adaptive multi-swarms. In *GECCO '08: Proceedings of the 10th Annual Conference on Genetic and Evolutionary Computation* (pp. 49–56).

Kalaiselvi, T., Nagaraja, P., & Abdul Basith, Z. (2017). A review on glowworm swarm optimization. *International Journal of Information Technology, 3*(2), 49–56.

Kang, F., Li, J., & Li, H. (2013). Artificial bee colony algorithm and pattern search hybridized for global optimization. *Applied Soft Computing, 13*(4), 1781-1791. https://doi.org/10.1016/j.asoc.2012.12.025

Karaboga, D. (2005). An idea based on honey bee swarm for numerical optimization (Vol. 200, pp. 1-10). Technical report-tr06, Erciyes University, Engineering Faculty, Computer Engineering Department.

Karaboga, D., & Akay, B. (2009). A comparative study of artificial bee colony algorithm. *Applied Mathematics and Computation, 214*(1), 108-132. https://doi.org/10.1016/j.amc.2009.03.090

TH-3534_186104002

Karaboga, D., & Basturk, B. (2007). A powerful and efficient algorithm for numerical function optimization: Artificial bee colony (ABC) algorithm. *Journal of Global Optimization, 39*(3), 459–471.

Karaboga, D., & Basturk, B. (2007). A powerful and efficient algorithm for numerical function optimization: Artificial bee colony (ABC) algorithm. *Journal of Global Optimization, 39*, 459–471. https://doi.org/10.1007/s10898-007-9149-x

Karaboga, D., & Basturk, B. (2008). On the performance of artificial bee colony (ABC) algorithm. *Applied Soft Computing, 8*(1), 687-697. https://doi.org/10.1016/j.asoc.2007.05.007

Karaboga, D., & Gorkemli, B. (2012, July). A quick artificial bee colony-qABC-algorithm for optimization problems. In *International Symposium on Innovations in Intelligent Systems and Applications*, Turkey (pp. 1-5). IEEE. https://doi.org/10.1109/INISTA.2012.6247010

Kennedy, J., & Eberhart, R. (1995, November). Particle swarm optimization. In *Proceedings of ICNN'95-international conference on neural networks* (Vol.4, pp.1942-1948). IEEE. https://doi.org/10.1109/ICNN.1995.488968

King, G., & McLoughlin, J. (1993). Centrifuge model studies of a cantilever retaining wall in sand. In *Retaining Structures* (pp. 711–720). Thomas Telford Publishing.

Kıran, M. S., & Fındık, O. (2015). A directed artificial bee colony algorithm. *Applied Soft Computing, 26*, 454-462. https://doi.org/10.1016/j.asoc.2014.10.020

Ko, H. Y. (1988). Summary of the state-of-the-art in centrifuge model testing. In *Centrifuges in Soil Mechanics* (pp. 11–18). CRC Press.

Koppula, S. D. (1970). The consolidation of soil in two dimensions and with moving boundaries. National Library, Ottawa, ON, Canada.

Koppula, S., & Morgenstern, N. (1982). On the consolidation of sedimenting clays. *Canadian Geotechnical Journal, 19*, 260–268.

Krizek, R. J., & Somogyi, F. (1984). Perspectives on modelling consolidation of dredged materials. In *Unknown Host Publication Title*. ASCE, Reston, VA, USA, pp. 296–332.

Lawver, J., & Carrier, W. (1983). Mathematical and centrifuge modeling of phosphatic clay disposal systems. In *Proceedings of the SME-AIME Annual Meeting*, Atlanta, GA, USA, 6–10 March 1983.

TH-3534_186104002

Lee, K. (1979). *An analytical and experimental study of large strain soil consolidation*. University of Oxford, Oxford, UK.

Lee, K. (1981). Consolidation with constant rate of deformation. *Géotechnique, 31*(2), 215–229.

Lee, K., & Sills, G. C. (1981). The consolidation of a soil stratum, including self-weight effects and large strains. *International Journal for Numerical and Analytical Methods in Geomechanics, 5*(4), 405–428. https://doi.org/10.1002/nag.1610050406

Lee, S. L., Karunaratne, G. P., Yong, K. Y., Chow, Y. K., & Chew, S. H. (1988). Consolidation of dredged clay in reclamations. *Soils and Foundations, 28*(2), 1-13. https://doi.org/10.3208/sandf1972.28.2_1

Levasseur, S., Malécot, Y., Boulon, M., & Flavigny, E. (2008). Soil parameter identification using a genetic algorithm. *International Journal for Numerical and Analytical Methods in Geomechanics, 32*(2), 189-213. https://doi.org/10.1002/nag.614

Li, L., Alvarez, I. C., & Aubertin, J. D. (2013). Self-weight consolidation of slurried deposition: Tests and interpretation. *International Journal of Geotechnical Engineering, 7*(2), 205-213. https://doi.org/10.1179/1938636213Z.00000000016

Liu, C., Yan, X., Liu, C., & Wu, H. (2011). The wolf colony algorithm and its application. *Chinese Journal of Electronics, 20*(2), 212-216.

Liu, J. C., & Znidarčić, D. (1991). Modeling one-dimensional compression characteristics of soils. *Journal of Geotechnical Engineering, 117*(1), 162-169. https://doi.org/10.1061/(ASCE)0733-9410(1991)117:1(162)

Lu, K. D., & Wu, Z. G. (2022). Genetic algorithm-based cumulative sum method for jamming attack detection of cyber-physical power systems. *IEEE Transactions on Instrumentation and Measurement, 71*, 1-10. https://doi.org/10.1109/TIM.2022.3186360

Lu, K. D., Wu, Z. G., & Huang, T. (2022). Differential evolution-based three stage dynamic cyber-attack of cyber-physical power systems. *IEEE/ASME Transactions on Mechatronics, 28*(2), 1137-1148. https://doi.org/10.1109/TMECH.2022.3214314

Luo, J., Ren, R., & Guo, K. (2020). The deformation monitoring of foundation pit by back propagation neural network and genetic algorithm and its application in geotechnical engineering. *PLOS One, 15*(7), e0233398. https://doi.org/10.1371/journal.pone.0233398

TH-3534_186104002

Luo, J., Wang, Q., & Xiao, X. (2013). A modified artificial bee colony algorithm based on converge-onlookers approach for global optimization. *Applied Mathematics and Computation, 219*(20), 10253-10262. https://doi.org/10.1016/j.amc.2013.04.001

Lyndon, A., & Pearson, R. (1985). *Pressure distribution on a rigid retaining wall in cohesionless material*. A.A. Balkema.

Ma, L., Zhu, Y., Zhang, D., & Niu, B. (2016). A hybrid approach to artificial bee colony algorithm. *Neural Computing and Applications, 27*, 387-409. https://doi.org/10.1007/s00521-015-1851-x

Malengier, B., Peiffer, H., & Di Emidio, G. (2016). One-dimensional model for large-strain consolidation in a bench-scale centrifuge. *Transport in Porous Media, 114*, 675-693.

Marín, O. A., Kraslawski, A., & Cisternas, L. A. (2022). Estimating processing cost for the recovery of valuable elements from mine tailings using dimensional analysis. *Minerals Engineering, 184*, 107629. https://doi.org/10.1016/j.mineng.2022.107629

MATLAB solver, "fmincon". https://in.mathworks.com/help/optim/ug/fmincon.html.

MATLAB solver, "fminsearch". https://in.mathworks.com/help/matlab/ref/fminsearch.html

MATLAB, V (2018). *9.4. 0 (R2018a)*. The MathWorks Inc. Natick, MA: USA.

McDermott, I., & King, A. (1998). Use of a bench-top centrifuge to assess consolidation parameters. In *Tailings and Mine Waste '98*. Routledge.

McVay, M. C., Townsend, F. C., Bloomquist, D. G., & Martinez, R. E. (1987). Reclamation of phosphatic clay waste ponds by capping volume 6: Consolidation properties of phosphatic clays from automated slurry consolidometer and centrifugal model tests. *Florida Institute of Phosphate Research*, Bartow, FL. FIPR Publication no. 02-030-073.

McVay, M., Townsend, F., & Bloomquist, D. (1986). Quiescent consolidation of phosphatic waste clays. *Journal of Geotechnical Engineering, 112*(9), 1033–1049.

Mikasa, M., & Takada, N. (1984). Self-weight consolidation of very soft clay by centrifuge. In *Sedimentation Consolidation Models—Predictions and Validation*. ASCE.

Miller, W. G. (2010). *Comparison of geo-environmental properties of caustic and non-caustic oil sand fine tailings* (Doctoral dissertation, Department of Civil and Environmental Engineering, University of Alberta, Edmonton, Alberta, Canada). https://doi.org/10.7939/R3Z71B

TH-3534_186104002

Mirjalili, S. (2015). Moth-flame optimization algorithm: A novel nature-inspired heuristic paradigm. *Knowledge-Based Systems, 89*, 228-249.

Monte, J. L., & Krizek, R. (1976). One-dimensional mathematical model for large-strain consolidation. *Géotechnique, 26*, 495–510.

Morris, P. (2003). Compressibility and permeability correlations for fine-grained dredged materials. *Journal of Waterway, Port, Coastal, and Ocean Engineering, 129*(4), 188-191. https://doi.org/10.1061/(ASCE)0733-950X(2003)129:4(188)

Morris, P. H., Lochington, D. A., & Apelt, C. J. (2000). Correlations for mine tailings consolidation parameters. *International Journal of Surface Mining, Reclamation and Environment, 14*, 171–182. https://doi.org/10.1080/13895260008953321

Mudd, G. M., & Boger, D. V. (2013). The ever growing case for paste and thickened tailings—Towards more sustainable mine waste management. *Journal of the Australasian Institute of Mining and Metallurgy, 2*, 56–59.

Muir Wood, D. (2017). *Geotechnical Modelling*. CRC Press.

Niu, B., & Li, L. (2008). A novel PSO-DE-based hybrid algorithm for global optimization. In *International Conference on Intelligent Computing*. Springer, Berlin.

Oberender, P. W., & Puzrin, A. M. (2015). Observation-guided constitutive modelling for creeping landslides. *Géotechnique, 66*(3), 232-247. https://doi.org/10.1680/jgeot.15.LM.003

Ortenblad, A. (1930). Mathematical theory of the process of consolidation of mud deposits. *Journal of Mathematics and Physics, 9*(1–4), 73–149. https://doi.org/10.1002/sapm19309173

Ou, X., Yang, J., Yin, X., & Liao, Y. (2011). Experimental study on mechanism for self-weight consolidation of the red mud tailings placed in the karsts. *Applied Mechanics and Materials, 90*, 3102–3107. https://doi.org/10.4028/www.scientific.net/AMM.90-93.3102

Ozturk, C., & Karaboga, D. (2011, June). Hybrid artificial bee colony algorithm for neural network training. In *2011 IEEE Congress of Evolutionary Computation (CEC)* (pp. 84-88). https://doi.org/10.1109/CEC.2011.5949602

Panigrahi, B. K., Ravikumar Pandi, V., & Das, S. (2008). Adaptive particle swarm optimization approach for static and dynamic economic load dispatch. *Energy Conversion and Management, 49*(6), 1407–1415.

TH-3534_186104002

Pham, D. T., Ghanbarzadeh, A., Koc, E., Otri, S., Rahim, S., & Zaidi, M. (2005). The bees algorithm. Technical Note, *Manufacturing Engineering Centre, Cardiff University, UK*, 44-48.

Piciullo, L., Storrøsten, E. B., Liu, Z., Nadim, F., & Lacasse, S. (2022). A new look at the statistics of tailings dam failures. *Engineering Geology, 303*, 106657. https://doi.org/10.1016/j.enggeo.2022.106657

Poli, R. (2007). An analysis of publications on particle swarm optimization applications. *Department of Computer Science, University of Essex*.

Pollock, G. (1988). *Large-strain consolidation of oil sand tailings sludge* (M.Sc. thesis, University of Alberta, Edmonton, Canada).

Puzrin, A. M., Alonso, E. E., & Pinyol, N. M. (2010). Unexpected excessive settlements: Kansai International Airport, Japan. In *Geomechanics of Failures* (pp. 23–43). Springer Dordrecht.

Qi, S., & Simms, P. (2020). Robust methods to estimate large-strain consolidation parameters from column experiments. *Canadian Geotechnical Journal, 57*(5), 683-705. https://doi.org/10.1139/cgj-2018-0870

Qi, S., Chen, X., Simms, P., Zhou, J., & Yang, X. (2020). New method for determining the permeability function parameters of soft soils considering synchronous sedimentation and consolidation. *Computers and Geotechnics, 127*, 103781. http://dx.doi.org/10.1016/j.compgeo.2020.103781

Qi, S., Simms, P., Vanapalli, S., & Soleimani, S. (2017). Piecewise-linear formulation of coupled large-strain consolidation and unsaturated flow. II: Testing and performance. *Journal of Geotechnical and Geoenvironmental Engineering, 143*(7), 04017019.

Qiu, Y., & Sego, D. C. (2001). Laboratory properties of mine tailings. *Canadian Geotechnical Journal, 38*(1), 183–190. https://doi.org/10.1139/t00-082

Rakshith, S., & Singh, D. N. (2017). Utilization of dredged sediments: Contemporary issues. *Journal of Waterway, Port, Coastal, and Ocean Engineering, 143*(3), 04016025.

Reddy, J. N. 2019. *Introduction to the Finite Element Method*. 4th ed. New York: McGraw-Hill Education. https://www.accessengineeringlibrary.com/content/book/9781259861901

TH-3534_186104002

Reid, D., Fourie, A. B., & Watson, S. (2012, April). Accelerated consolidation of soft clays and mine tailings using a desktop centrifuge. In *Paste 2012: Proceedings of the 15th International Seminar on Paste and Thickened Tailings* (pp. 43-52). Australian Centre for Geomechanics.

Riget, J., & Vesterstrøm, J. S. (2002). A diversity-guided particle swarm optimizer—the ARPSO. *EVALife Technical Report* (No. 2002-2).

Robinson, R. G., Tan, T. S., & Lee, F. H. (2003). A comparative study of suction induced seepage consolidation versus centrifuge consolidation. *Geotechnical Testing Journal, 26*(1), 92–101. https://doi.org/10.1520/GTJ11109J

Samarasinghe, A. M., Huang, Y. H., & Drnevich, V. P. (1982). Permeability and consolidation of normally consolidated soils. *Journal of Geotechnical Engineering Division, 108*(6), 835-850. https://doi.org/10.1061/AJGEB6.0001305

Schiffman, R. L. (1980). Finite and infinitesimal strain consolidation. *Journal of Geotechnical Engineering Division, 106*, 203–207.

Schiffman, R., & Cargill, K. (1981). Finite strain consolidation of sedimenting clay deposits. In *Proceedings of the 10th International Conference on Soil Mechanics and Foundation Engineering* (Vol. 1, pp. 239–242), Stockholm, UK.

Schofield, A. N. (1980). Cambridge geotechnical centrifuge operations. *Géotechnique, 30*(3), 227–268.

Scott, J. D., Dusseault, M. B., & Carrier, W. D. (1986). Large-scale self-weight consolidation testing. In *Consolidation of Soils: Testing and Evaluation*. ASTM International.

Scully, R. W., Schiffman, R. L., Olsen, H. W., & Ko, H. Y. (1984). Validation of consolidation properties of phosphatic clays at very high void ratios, predictions and validation. In *Sedimentation Consolidation Models—Predictions and Validation* (Yong, R. N., & Townsend, F. C., Eds.). ASCE, New York, NY, USA, pp. 158–181.

Shi, L., Yin, X., Sun, H., Pan, X., Yuan, Z., & Cai, Y. (2022). A new approach for determining compressibility and permeability characteristics of dredged slurries with high water content. *Canadian Geotechnical Journal, 59*(6), 965-977. https://doi.org/10.1139/cgj-2020-0676

Shi, Y., & Eberhart, R. (1998). A modified particle swarm optimizer. In *1998 IEEE International Conference on Evolutionary Computation Proceedings. IEEE World Congress on Computational Intelligence* (Cat. No.98TH8360) (pp. 69–73). https://doi.org/10.1109/ICEC.1998.699146

TH-3534_186104002

Sills, G. (1998). Development of structure in sedimenting soils. *Philosophical Transactions of the Royal Society of London. Series A: Mathematical, Physical and Engineering Sciences, 356*(1747), 2515-2534.

Silvestri, V., Yong, R. N., Soulié, M., & Gabriel, F. (1986). Controlled-strain, controlled-gradient, and standard consolidation testing of sensitive clays. In *Consolidation of Soils: Testing and Evaluation*. ASTM International.

Solanki, P., Jain, B., Hu, X., & Sancheti, G. (2023). A review of beneficial use and management of dredged material. In *Waste* (Vol. 1, No. 3, pp. 815-840). MDPI.

Soleimani, S., Simms, P., Dunmola, A., Freeman, G., & Wilson, G. W. (2014). Desiccation and consolidation in thin-lift deposition of polymer-amended mature fine tailings. In *Proceedings of the 17th International Seminar on Paste and Thickened Tailings* (Jewell, R., Fourie, A., Wells, P. S., & van Zyl, D., Eds.), Australian Centre for Geomechanics, Crawley, Australia, pp. 307-322.

Somogyi, F. (1980). Large strain consolidation of fine grained slurries. In *Proceedings of the Canadian Society for Civil Engineering* (pp. 29–30), Winnipeg, Manitoba.

Somogyi, F., Carrier, W. D., Lawyer, J. E., & Beckman, J. F. (1984). Waste phosphatic clay disposal in mine cuts. In *Sedimentation Consolidation Models—Predictions and Validation* (pp. 545-564). ASCE.

Sorta, A. R. (2015). *Centrifugal Modelling of Oil Sands Tailings Consolidation* (Ph.D. Thesis, University of Alberta, Department of Civil and Environmental).

Sorta, A. R., Sego, D. C., & Wilson, W. (2015). Physical modelling of oil sands tailings consolidation. *International Journal of Physical Modelling in Geotechnics*. https://doi.org/10.1680/jphmg.15.00006

Srinivasulu, D. (2023). Finite element modeling of finite strain consolidation. Master's thesis. Indian Institute of Technology Guwahati

Sun, J., Fang, W., Wu, X., Palade, V., & Xu, W. (2012). Quantum-behaved particle swarm optimization: Analysis of individual particle behavior and parameter selection. *Evolutionary Computation, 20*(3), 349-393. https://doi.org/10.1162/EVCO_a_00049

Sun, J., Feng, B., & Xu, W. (2004, June). Particle swarm optimization with particles having quantum behavior. In *Proceedings of the 2004 Congress on Evolutionary Computation* (Vol. 1, pp. 325-331). IEEE.

TH-3534_186104002

Sun, J., Xu, W., & Feng, B. (2004). A global search strategy of quantum-behaved particle swarm optimization. In *IEEE Conference on Cybernetics and Intelligent Systems, USA*. https://doi.org/10.1109/ICCIS.2004.1460396

Sun, R., Spelay, R., Kan, J., & Goldszal, A. (2014). Column consolidation testing of oil sands tailings. In *Proceedings of the 2014 International Conference on Oil Sands Tailings*, December 7th-10th 2014, Lake Louise, Alberta. Available from: https://sites.google.com/a/ualberta.ca/iostc2014/

Sun, R., Spelay, R., Kan, J., & Goldszal, A. (2014, December). Column consolidation testing of oil sands tailings. In *Fourth International Oil Sands Tailings Conference* (p. 163).

Sutar, M., & Jadhav, H. T. (2023). A modified artificial bee colony algorithm based on a non-dominated sorting genetic approach for combined economic-emission load dispatch problem. *Applied Soft Computing, 144*, 110433. https://doi.org/10.1016/j.asoc.2023.110433

Suthaker, N. (1995). *Geotechnics of Oil Sand Tailings* (Ph.D. Thesis). University of Alberta, Edmonton, AB, Canada.

Suthaker, N. N., & Scott, J. D. (1996). Measurement of hydraulic conductivity in oil sand tailings slurries. *Canadian Geotechnical Journal, 33*(4), 642-653. https://doi.org/10.1139/t96-089

Takada, N., & Mikasa, M. (1986). Determination of consolidation parameters by self-weight consolidation test in centrifuge. In *Consolidation of Soils: Testing and Evaluation*. ASTM International.

Tavenas, F., Jean, P., Leblond, P., & Leroueil, S. (1983a). The permeability of natural soft clays. Part II: Permeability characteristics. *Canadian Geotechnical Journal, 20*(4), 645–660.

Tavenas, F., Leblond, P., Jean, P., & Leroueil, S. (1983b). The permeability of natural soft clays. Part I: Methods of laboratory measurement. *Canadian Geotechnical Journal, 20*(4), 629–644.

Taylor, R. N. (1995). Centrifuges in modeling: principles and scale effects. In R. N. Taylor (Ed.), *Geotechnical Centrifuge Technology* (pp. 19–33). Blackie Academic & Professional, London, UK.

Terzaghi, V. (1923). Die Berechnung der Durchlässigkeitsziffer des Tones aus dem Verlauf der hydrodynamischen Spannungserscheinungen. *Sitzungsberichte der Akademie der Wissenschaften in Wien: Mathematisch-Naturwissenschaftliche Klasse, Abteilung IIa, 132*, 105-124.

TH-3534_186104002

The MathWorks, Inc. (2021a). https://in.mathworks.com/help/matlab/ref/fminsearch.html, accessed on: 21st July 2021.

The MathWorks, Inc. (2021b). https://in.mathworks.com/help/optim/ug/fmincon.html, accessed on: 21st July 2021.

Thiebot, J., Guillou, S., & Brun-Cottan, J. C. (2011). An optimization method for determining permeability and effective stress relationships of consolidating cohesive sediment deposits. *Continental Shelf Research, 31*(10), S117-S123. https://doi.org/10.1016/j.csr.2010.12.004

Tian, Z., Bareither, C. A., & Scalia, J. (2020). Development and assessment of a seepage-induced consolidation test apparatus. *Geotechnical Testing Journal, 43*(4), 894–917.

TIPC (2018). *Environmental Report: Port of Kaohsiung*. Taiwan International Ports Corporation, Kaohsiung, Taiwan.

Tizhoosh, H. R. (2005, November). Opposition-based learning: A new scheme for machine intelligence. In *International Conference on Computational Intelligence for Modelling, Control and Automation and International Conference on Intelligent Agents, Web Technologies and Internet Commerce (CIMCA-IAWTIC'06)* (Vol. 1, pp. 695-701). IEEE.

Toorman, E. A. (1997). Modelling the thixotropic behaviour of dense cohesive sediment suspensions. *Rheologica Acta, 36*(1), 56-65. https://doi.org/10.1007/BF00366724

Townsend, F. C., & McVay, M. C. (1990). SOAs large strain consolidation. *Journal of Geotechnical Engineering, 116*(2), 147-168.

Townsend, F., & Hernandez, J. (1986). Predictions of phosphatic clay consolidation by numerical and centrifugal models. In *Flocculation, Sedimentation and Consolidation* (pp. 449–455). American Institute of Chemical Engineers.

U.S. Army Corps of Engineers (USACE). (2017). *Inner Harbor Navigation Canal Lock*. https://www.mvn.usace.army.mil/Portals/56/docs/Projects/IHNC/IHNC%20Lock%20Study-%20Eng%20Appendix%20B%20.pdf?ver=2016-12-30-131854-877, accessed on 29 November 2020.

Umehara, Y., & Zen, K. (1980). Constant rate of strain consolidation for very soft clayey soils. *Soils and Foundations, 20*(2), 79–95.

TH-3534_186104002

Ustun, D., Toktas, A., Erkan, U., & Akdagli, A. (2022). Modified artificial bee colony algorithm with differential evolution to enhance precision and convergence performance. *Expert Systems with Applications, 198*, 116930. https://doi.org/10.1016/j.eswa.2022.116930

Van den Bergh, F., & Engelbrecht, A. P. (2002). A new locally convergent particle swarm optimiser. In *Proceedings of the IEEE International Conference on Systems, Man and Cybernetics* (Vol. 3, pp. 94–99).

Van Laarhoven, P. J. M., & Aarts, E. H. L. (1987). Simulated annealing. In *Simulated annealing: Theory and applications* (pp. 7–15). Springer, Dordrecht.

Vasconcellos, J. F. V., Singh, S., & Sivakugan, N. (2010). Sensitivity analysis of time-dependent settlements in hydraulic fills. *Geotechnical and Geological Engineering, 28*, 351–360. https://doi.org/10.1007/s10706-009-9296-6

Wang, B. (2015). A novel artificial bee colony algorithm based on modified search strategy and generalized opposition-based learning. *Journal of Intelligent & Fuzzy Systems, 28*(3), 1023-1037. http://dx.doi.org/10.3233/IFS-141386

Watabe, K., Udaka, K., Nakatani, Y., & Leroueil, S. (2012). Long-term consolidation behaviour interpreted with isotache concept for worldwide clays. *Soils and Foundations, 52*, 449-464. https://doi.org/10.1016/j.sandf.2012.05.005

Weiland, R., Bunnaul, P., & Hogg, R. (1994). Centrifugal dewatering of flocculated clays. *Mining, Metallurgy & Exploration, 11*(1), 37–40.

Wickland, B. E., & Wilson, G. W. (2005). Self-weight consolidation of mixtures of mine waste rock and tailings. *Canadian Geotechnical Journal, 42*(2), 327–339.

World Information Service on Energy (WISE). https://www.wise-uranium.org/ (Accessed on March 30, 2023)

Xie, X.-F., Zhang, W.-J., & Yang, Z.-L. (2002). Adaptive particle swarm optimization on individual level. In *6th International Conference on Signal Processing* (Vol. 2). IEEE.

Xu, G. Z., Gao, Y. F., Hong, Z. S., & Ding, J. W. (2012). Sedimentation behaviour of four dredged slurries in China. *Marine Georesources & Geotechnology, 30*(2), 143-156.

Xu, G. Z., Gao, Y. F., Hong, Z. S., & Ding, J. W. (2012). Sedimentation behaviour of four dredged slurries in China. *Marine Georesources & Geotechnology, 30*(2), 143-156. https://doi.org/10.1080/1064119X.2011.602382

TH-3534_186104002

Xu, G., Gao, Y., Yin, J., Yang, R., & Ni, J. (2015a). Compression behavior of dredged slurries at high water contents. *Marine Georesources & Geotechnology, 33*(2), 99–108.

Xu, G., Gao, Y.-F., & Xu, C. (2015b). Permeability behavior of high-moisture content dredged slurries. *Marine Georesources & Geotechnology, 33*(4), 348–355.

Y. Sun, J. Sun, & L. Ye. (2023). Synthesis of thinned planar concentric circular antenna arrays using a modified artificial bee colony algorithm. *International Journal of Antennas and Propagation, 2023*, Article ID 7735267. https://doi.org/10.1155/2023/7735267

Yang, X.-S. (2010a). A new metaheuristic bat-inspired algorithm. In *Nature Inspired Cooperative Strategies for Optimization (NICSO 2010)* (pp. 65–74). Springer, Berlin.

Yang, X.-S. (2010b). *Nature-Inspired Metaheuristic Algorithms*. Luniver Press, Bristol.

Yang, X.-S., & Deb, S. (2009). Cuckoo search via Lévy flights. In *2009 World Congress on Nature & Biologically Inspired Computing (NaBIC)*. IEEE.

Yao, D. T., & Znidarcic, D. (1997). Crust formation and desiccation characteristics for phosphatic clays: User's manual for computer program CONDES0. Polk County, Florida: Florida Institute of Phosphate Research.

Ye, Z., Zhu, M., & Wang, J. (2018). On modification and application of the artificial bee colony algorithm. *Journal of Information Processing Systems, 14*(2), 448-454. https://doi.org/10.3745/JIPS.01.0025

Yin, Z. Y., Jin, Y. F., Shen, J. S., & Hicher, P. Y. (2018). Optimization techniques for identifying soil parameters in geotechnical engineering: Comparative study and enhancement. *International Journal for Numerical and Analytical Methods in Geomechanics, 42*(1), 70-94. https://doi.org/10.1002/nag.2714

Zeng, L.-L., Hong, Z.-S., & Cui, Y.-J. (2016). Time-dependent compression behaviour of dredged clays at high water contents in China. *Applied Clay Science, 123*, 320-328.

Zhao, B. D., Zhang, L. L., Jeng, D. S., Wang, J. H., & Chen, J. J. (2015). Inverse analysis of deep excavation using differential evolution algorithm. *International Journal for Numerical and Analytical Methods in Geomechanics, 39*(2), 115-134. https://doi.org/10.1002/nag.2287

Zhou, X., Wang, H., Wang, M., & Wan, J. (2017). Enhancing the modified artificial bee colony algorithm with neighborhood search. *Soft Computing, 21*(10), 2733-2743. https://doi.org/10.1007/s00500-015-1977-x

TH-3534_186104002

Znidarcic, D., & Liu, J. C. (1989). Consolidation characteristics determination for dredged materials. In *Proceedings of the 22nd Annual Dredging Seminar* (Vol. 22, pp. 45–65). Center for Dredged Studies, Texas A&M University, College Station, TX, USA.

Znidarcic, D., & Schiffman, R. (1981). Finite strain consolidation: test conditions. *Journal of Geotechnical and Geoenvironmental Engineering, 107* (ASCE 16238 proceeding). https://doi.org/10.1061/AJGEB6.0010708

Znidarcic, D., & Schiffman, R. (1981). Finite strain consolidation: test conditions. *Journal of Geotechnical and Geoenvironmental Engineering, 107* (ASCE 16238 proceeding). https://doi.org/10.1061/AJGEB6.0010708

Znidarcic, D., Croce, P., Pane, V., Olsen, H. W., & Schiffman, R. L. (1984). The theory of one-dimensional consolidation of saturated clays: III. Existing testing procedures and analyses. *Geotechnical Testing Journal, 7*(2), 123–134.

Znidarcic, D., Miller, R., van Zyl, D., Fredlund, M., & Wells, S. (2011). Consolidation testing of oil sand fine tailings. In *Proceedings of the Tailing and Mine Waste Conference*, Vancouver, BC (Canada),6–9. http://hdl.handle.net/2429/38782

Znidarcic, D., Schiffman, R. L., Pane, V., Croce, P., Ko, H.-Y., & Olsen, H. W. (1986). Theory of one-dimensional consolidation of saturated clays: Part V constant rate of deformation testing and analysis. *Géotechnique, 36*(2), 227-237.

Znidarcic, D., Schiffman, R. L., Pane, V., Croce, P., Ko, H.-Y., & Olsen, H. W. (1986). Theory of one-dimensional consolidation of saturated clays: Part V constant rate of deformation testing and analysis. *Géotechnique, 36*(2), 227–237. https://doi.org/10.1680/geot.1986.36.2.227

TH-3534_186104002